London South Bank University

School of Engineering

New Generation of Continuous Hydrothermal Flow Synthesis Materials for Environmental Applications

by

Ioan-Alexandru Baragau

A Thesis submitted

in partial fulfilment of the

requirements for the degree of

Doctor of Philosophy

London, United Kingdom

November 2021

Once we accept our limits, we go beyond them.

Albert Einstein

Acknowledgements

I want to express my gratitude to everyone who assisted, advised, and guided me throughout this fantastic journey.

First, I want to thank my director of studies, my supervisor, and the advisor for my research ideas, Dr Suela Kellici, for offering me the opportunity to work in her team. As a supervisor, she encouraged and gave me the freedom to develop the project and my ideas. She taught me everything I know about CHFS. I sincerely appreciate her encouragement and support in attending national and international conferences, workshops, training, and lectures, which improved my public speaking confidence and aided in my personal development. Without her expertise, experience, and patience, this project would not have been completed.

Special appreciations are given to my second supervisor Professor Sandra Dudley-McEvoy for always encouraging and advising me in a very positive and motivating manner, as well as Dr Nicholas Power from The Open University, who offered me the opportunity to be a visiting researcher in his laboratory, facilitating access to OU facilities, and sharing his synthetic chemistry knowledge. Also, I would like to thank Professor Dr Hari Reehal for providing relevant and valuable feedback during the periodic examinations, as well as Dr Jeremy Ball for the training and discussions at the start of the project.

I would also like to thank the School of Engineering (LSBU) for my scholarship.

I would like to express my gratitude to all current and former members of the Nano2D Lab (my collegues and closest friends, essentially my second family): Zhen Lu, Uthman Alli, Kiem G. Nguyen, Sunil J. Hettiarachchi, Oluwasayo M. Aderogba, Eduardo A. E. Calizaya, Zoe Devlin, Thomas Gaffney, Carlos J. M. Buitrago, Muhammad S. Rafiq, Edvaldo D. G. F. Neto, and Sunday Chiedozie for your collaboration, friendship, support, and help. I hope I was able to give back a tiny piece of the kindness you shared with me.

I would also like to acknowledge all the collaborative opportunities and assistance: Dr David J. Morgan (Cardiff University) for XPS data and assistance, Dr Tobias Heil (Max Planck Institute of Colloids and Interfaces) is thanked for his top-quality TEM imaging (all materials) Special considerations and thanks go to Professor Steve Dunn (LSBU) for help and discussion regarding the TiO_2-hybrid photocatalysts. Dr Tariq Sajjad (LSBU), Dr Stuart Thompson, and

Dr Alistair Rennie (Edinburgh Instruments Ltd) for the support with the TPL measurements and data interpretation for the TiO_2-hybrid nanomaterials, and Mrs Sabina A. Nicolae (QMUL) for UV-Vis measurements of TiO_2-hybrids nanomaterials. I want to thank Professor Maria-Magdalena Titirici, Dr Christopher S. Roberts, and Mr Richard A. Lobo (Imperial College) for AFM and Raman measurements of carbon dots and Dr Igor Kraev (OU) for TEM training and imaging for the CQDs'. Romanian National Institute of Materials Physics (NIMPs) is thanked for allowing access to their materials characterisation facilities. Dr Mihaela M. Trandafir and Dr Aurelian Catalin Galca are thanked for SEM and Raman assistance and training.

For the technical support provided during this project, I want to thank LSBU's technicians Mr Kishore Unadkat, Mr Andrew Ascroft, Mr William Cheung, and OU's technicians Dr Matthew Kershaw and Mr Brett Keith. Without them solving daily technical issues would have been much more complicated.

I want to express my deep gratitude to my high-school chemistry teacher, Carmen Duna, who inspired my passion for Chemistry and Science, to Professor Marius Andruh, Associate Professor Augustin Madalan (University of Bucharest), and Dr Florea Cocu (Research and Development Department of Microsin), who inspired and guided me during the undergraduate and master studies and trained me as a synthetic chemist.

Special thanks to my family for their constant support and love during all my educational stages.

Lastly, and the most important, my overwhelming gratitude goes to my fiancé, Sabina, for her endless support, love, and patience by standing close to me from the beginning to the end of this journey. I dedicate this Thesis to her.

Abstract

The demands for new materials such as carbonaceous nanomaterials and their nanocomposites that are produced in a more efficient, economical, and environmentally friendly manner, as well as the need to integrate them into applications that address global issues, is a current challenge. The focus of this doctoral research project was to develop faster, cleaner synthetic methods to produce materials with superior physical and chemical properties utilising sustainable and/or renewable precursors, ultimately delivering solutions to challenges in environmental applications and beyond. This was accomplished using a continuous hydrothermal flow synthesis approach.

Continuous hydrothermal flow synthesis is an unconventional method that uses supercritical water as a reaction environment, and it was designed for the very fast, continuous flow production of high quality and high quantity nanomaterials, with real-time control over the process parameter (temperature, pressure, precursors concentration, pH, and flow rates). For the first time, by developing and applying CHFS methodologies, carbon quantum dots (CQDs) and nitrogen-doped carbon quantum dots (NCQDs) were synthesized. The CHFS CQDs and NCQDs were produced from biomass-related precursors: glucose and citric acid; the synthetic process can be classified not only as green but sustainable too. The reduction of graphene oxide with a non-corrosive and reusable reducing agent (formic acid) was achieved. The reduced graphene oxide with different oxygen content (17.37 at%, 16.82 at% and 13.3 at%) was synthesised. A new CHFS method to produce nano TiO_2 (anatase) has been developed to pioneer the one-pot synthesis of carbonaceous nanocomposites of TiO_2 with NCQDs and reduced graphene oxide (rGO).

All the materials produced in this study have been characterised and tested in environmental-related applications: a) toxic ions sensing (CQDs, NCQDs) with promising limits of detection for hexavalent chromium (LOD_{CQDs}= 3.62 ppm and LOD_{NCQDs}=0.365 ppm), b) graphene-related membrane-based water treatment with good performances, and photocatalysis where the TiO_2 and its carbonaceous nanocomposites were tested for photodegradation of methylene blue with excellent conversions and rates constants (the best photocatalyst, TiO_2-NCQDs-rGO(1), showed a conversion of 93.45% and a rate constant of 25.24 $x10^{-5}$ s^{-1}). This research project designed and engineered new promising carbonaceous materials, expanding the CHFS portfolio to new frontiers. The as-prepared materials exhibited

superior physical, chemical, and morphological characteristics demonstrating their potential for environmental applications and beyond.

Publications

First author:

Ioan-Alexandru Baragau, Nicholas P Power, David John Morgan, Tobias Heil, Richard Alvares Lobo, Christopher S Roberts, Magdalena Titirici, Steve Dunn and Suela Kellici, *Continuous hydrothermal flow synthesis of blue-luminescent, excitation-independent N-doped carbon quantum dots as nanosensors*, Journal of Materials Chemistry A, 2020, 8, 3270–3279, DOI: 10.1039/C9TA11781D

Ioan-Alexandru Baragau, Zhen Lu, Nicholas P. Power, David J. Morgan, James Bowen, Pedro Diaz, Suela Kellici, *Continuous hydrothermal flow synthesis of S-functionalised carbon quantum dots for enhanced oil recovery*, Chemical Engineering Journal, 2020, 405, 126631. DOI: 10.1016/j.cej.2020.126631.

Ioan-Alexandru Baragau, Nicholas P. Power, David J. Morgan, Richard A. Lobo, Christopher S. Roberts, Magdalena M. Titirici, Vesna Middelkoop, A. Diaz, Steve Dunn, and Suela Kellici, *Efficient continuous hydrothermal flow synthesis of carbon quantum dots from a targeted biomass precursor for on-off metal ions nanosensing, ACS Sustainable Chemistry and Engineering, 9 (2021) 2559–2569. DOI:10.1021/acssuschemeng.0c08594.*

Contributor:

Suela Kellici, John Acord, Katherine E. Moore, Nicholas P. Power, Vesna Middelkoop, David J. Morgan, Tobias Heil, Paolo Coppo, **Ioan-Alexandru Baragau,** and Colin L. Raston, *Continuous hydrothermal flow synthesis of graphene quantum dots*, Reaction Chemistry & Engineering, 2018, 3, 949-958. DOI: 10.1039/C8RE00158H

Vesna Middelkoop, Thomas Slater, Mihaela Florea, Florentina Neațu, Simge Danaci, Victor Onyenkeadi, Katrien Boonen, Basudeb Saha, **Ioan-Alexandru Baragau,** Suela Kellici, *Next frontiers in cleaner synthesis: 3D printed graphene-supported CeZrLa mixed-oxide nanocatalyst for CO_2 utilisation and direct propylene carbonate production*, Journal of Cleaner Production, 214, 2019, 606-614. DOI: 10.1016/j.jclepro.2018.12.274

Conferences and competitions

Ioan-Alexandru Baragau, Suela Kellici, Blue-luminescent carbon quantum dots synthesised using a continuous hydrothermal flow synthesis, London Doctoral Academy Postgraduate Research Summer School, 2018 (Poster Presentation).

Ioan-Alexandru Baragau, Suela Kellici, *Blue luminescent carbon quantum dots as a nanosensor for Cr (VI) ions*, 7th EuCheMS Chemistry Congress, 2018 (Poster Presentation).

Ioan-Alexandru Baragau, Suela Kellici, *Blue luminescent carbon quantum dots as nanosensor*, Barrer Symposium on Separation Materials, 2018 (Poster Presentation).

Ioan-Alexandru Baragau, Suela Kellici, *New generation of membranes for water treatment processes*, London South Bank University, School of Engineering, Research Seminar, 2019 (Oral Presentation).

Ioan-Alexandru Baragau, Suela Kellici, *2D materials as solid membranes for water treatment*, London Materials Society Young Person's Lecture Competition, 2019 (Oral Presentation).

Ioan-Alexandru Baragau, Suela Kellici, *Continuous hydrothermal flow synthesis of blue-luminescent carbon quantum dots as nanosensors for chromium (VI) detection*, London Doctoral Academy Postgraduate Research Summer School, 2020 (Poster Presentation).

Ioan-Alexandru Baragau, Suela Kellici, *Continuous hydrothermal flow synthesis of reduced graphene oxide*, Faraday Discussion: Chemistry of 2-Dimensional Materials: Beyond graphene, 2020 (Poster Presentation).

Ioan-Alexandru Baragau, Zhen Lu, *Is a Carbon World*, NanoArtography, 2020 (Science visual art competition), People's Choice Awarded.

Table of content

List of figures, schematics, and tables

List of abbreviations

FNDs: fluorescent nanodiamonds

FSWCNF: fluorescent single-walled carbon nanotube fragments

CHFS: continuous hydrothermal flow synthesis

N-doped: nitrogen-doped

CQDs: carbon quantum dots

NCQDs: nitrogen-doped carbon quantum dots

GO: graphene oxide

r-GO: reduced graphene oxide

GQDs: graphene quantum dots

CNDs: carbon nitride dots

XPS: X-ray photoelectron spectroscopy

FTIR: Fourier-transform infrared spectroscopy

UV-Vis: ultraviolet and visible spectrophotometry

PL: photoluminescence spectroscopy

QY: quantum yield

HRTEM: high-resolution transmission electron microscopy

SEM: scanning electron microscopy

AFM: atomic force microscopy

BET: Brunauer–Emmett–Teller theory

ppm: parts per million or milligram per litre

ppb: parts per billion or microgram per litre

eV: electron-volt

au: absorbance units

a.u.: arbitrary units

at%: atomic percentages

IFE: The Inner Filter Effect

VAFS: vapour-fed aerosol flame synthesis

CVD: chemical vapour deposition

0D: zero-dimensional

1D: one-dimensional

2D: two-dimensional

3D: three-dimensional

CFNs: carbon fluorescent nanoparticles

SDS: sodium dodecyl sulfate

PEG: polyethylene glycol

OER: oxygen evolution reaction

HER: hydrogen evolution reaction

HTC: hydrothermal carbonisation

LAL: laser ablation in liquid

LASiS: laser ablation synthesis in liquid solution

mJ: millijoule

ms: millisecond

DC: direct current

A: Ampers

kPa: kiloPascal

rpm: rotations per minute

GCNPs: graphitic carbon nanoparticles

NMP: N-methyl-2-pyrrolidone

DMF: N,N-dimethylformamide

Ar: argon

HOMO: highest occupied molecular orbital

LUMO: lowest unoccupied molecular orbital

CBM: conduction band minimum

P25: Degussa (commercial TiO_2)

HPLC: high performance liquid chromatography

FSP: flame spray pyrolysis

HT plasma: high-temperature plasma

LT plasma: low-temperature plasma

CS solution: solution combustion synthesis

LSBU: London South Bank University

BPR: back-pressure regulator

kD: kilodaltons

λ: wavelength

Introduction

The advancement of technology creates a demand for new materials with new or improved properties[1–3], and the negative impact of human activities on the environment[4] necessitates green and eco-friendly approaches to material production and utilisation[5,6].

The nanomaterials and their nanocomposite represent a path to consume fewer resources and deliver optimisations when compared with traditional bulk materials[7]. Carbonaceous nanomaterials such as hydrothermal porous carbon (biochar) or carbon quantum dots derived from biomass, biomass related sources or allotrope forms of carbon such as graphene are considered as a promising alternative in a variety of environmental-related applications, including CO_2 adsorption and conversion, water treatment, toxic ion- or molecule-sensing, photo-energy conversion, and photocatalysis[8,9]. The nanometric-sized TiO_2, which is classified as one of the most efficient photocatalysts, is one of the most promising materials to be engineered for these types of applications[10].

Addressing environmental issues like water pollution is and will continue to be a major challenge for researchers all over the world. Using nanomaterials or nanocomposites such as TiO_2, carbon quantum dots, and graphene produced in green processes completes the principle of solving an environmental problem without generating a new one.

Continuous hydrothermal flow synthesis has proved to be green, tuneable and fast synthetic method for the large-scale production of nanomaterials[11]. The method has been extensively used for nano metal oxides synthesis, and this project broadens the CHFS materials' portfolio to include previously unexplored materials such as carbon quantum dots or TiO_2-carbonaceous hybrids, demonstrating the synthetic approach's tunability in engineering a broader range of nanomaterials and nanocomposites.

The main objectives of this PhD research project were:

- To develop continuous hydrothermal flow synthesis (CHFS) methodologies for producing carbonaceous nanomaterials aiming to deliver materials with new or improved properties.
- To synthesise carbon quantum dots (CQDs), nitrogen-doped carbon quantum dots (NCQDs) from biomass-related carbon sources (glucose and citric acid).
- To synthesise reduced graphene oxide (r-GO) using formic acid as a reducing agent and optimise the CHFS process.

- To synthesise nanocomposites of TiO_2, NCQDs and rGO as photocatalysts for photodegradation of dyes.
- To characterise and analyse the as-synthesised CHFS nanomaterials to understand their optical, electrical, morphological, and surface-chemistry properties to determine their suitability for environmental-related applications.
- To test the as-synthesised materials for their targeted environmental applications.
- To gain a better understanding of the fundamental principles of these materials and deliver a set of knowledge that can be used to inform synthesis optimisation, ultimately leading to a materials-by-design approach.

The Thesis consists of five Chapters, as follows:

Chapter 1 covers the Literature Review, which discusses all the materials synthesised during this project in terms of their synthetic procedures, properties, and applications using previously reported scientific literature. The main aim of this chapter is to provide solid background information about carbon quantum dots, graphene, titanium dioxide, their nanocomposites, and the continuous hydrothermal flow synthesis method so that the reader can understand the experimental part, results, and discussions discussed in the following chapters.

Chapter 2 includes details about the chemicals used, materials devices, experimental setups, procedures, and synthetic methodologies developed and used during this research project. The main aim of this chapter is to provide information on the precursors and synthetic methods (synthetic procedures) used to produce the materials of interest, separation and purification methodologies and the characterisation methods and devices employed to determine the materials' properties and characteristics. This chapter also discusses the experimental setup and methods used to evaluate the performance of the carbon quantum dots, reduced graphene oxide, and TiO_2-hybrid nanocomposites for toxic ion-sensing, water treatment, and photocatalysis applications, respectively.

Chapter 3 is dedicated to the synthesis of carbon quantum dots (from glucose) and nitrogen-doped carbon quantum dots (from citric acid and ammonia as nitrogen source) as well as their application for toxic chromium (VI) ion-sensing, with the explanation of the results and material properties. This chapter is divided into two sub-chapters, each of which discusses the carbon quantum dots, their properties, and their ion-sensing performances separately.

Chapter 4 reports the controlled synthesis of reduced graphene oxide (rGO) with tuneable surface functionalities via a continuous hydrothermal flow synthesis approach where formic acid was used as a reducing agent. This chapter discusses the properties and characteristics of the r-GO materials as indicated by a decrease in oxygen content after CHFS treatment of graphene oxide (the r-GO precursor). The most promising material was used to prepare high-pressure membranes, which were subsequently tested for water treatment processes. The membrane performance is described in this chapter.

Chapter 5 describes the TiO_2-hybrids photocatalyst designed and synthesised in this PhD project. The photocatalysts were successfully tested for dye photodegradation. The synthetic processes for TiO_2-hybrids materials are categorised as 1) one-step CHFS process, where the NCQDs are generated simultaneously with TiO_2 and graphene oxide is reduced, and 2) two-step CHFS process in which NCQDs are pre-synthesised and are then used in combination with titanium dioxide precursor and/or graphene oxide to generate TiO_2 hybrids. This chapter includes the findings and the discussions related to the material characterisation and their photocatalytic performance tests.

In addition, chapters 3, 4, and 5 include recommendations for future experimental works supporting the continuity of the research developed during this project.

Overall, this research project was designed to integrate synthesis, characterisation, and application.

Work reported in Chapter 3 has resulted in two publications, and the work presented in Chapters 4 and 5 has led to the preparation of two additional scientific publications. Parts of the research findings presented in this thesis were presented at national and international conferences, and scientific community feedback was considered.

Chapter 1: A literature review

In this chapter, the focus is to summarise the history, the synthetic procedures developed thus far, the properties and the applications of the materials produced and tested during this doctorate research project, to understand the fundamental principles and properties governing their synthesis and application in the environmental field.

The synthetic route influences the final properties and characteristics of the material; the same material produced using different synthetic methods can have distinct properties due to the surface modifications or the amount and the nature of the defects generated during the synthetic process. During this project, carbon quantum dots, reduced graphene oxide, titanium dioxide, and their nanocomposites were synthesised, characterised, and used in toxic ions sensing, water treatment, and photocatalysis. This literature review will focus on these materials and their properties.

1.1 Carbon quantum dots

1.1.1 Introduction

Carbon is one of the most important chemical elements on Earth, and it is the fourth most abundant element in the Milky Way Galaxy[12]. The usage of carbon materials in human history is related to the beginning of fire usage when partial combustion of wood materials carbon black related materials has resulted. Initially, partially combusted carbon was used as a pigment in inks to decorate various tools or tattoos. Over time, carbonaceous materials were used in an increasing number of applications related to daily human activities[13]. The carbon atoms remain one of the most versatile chemical elements available. It exhibits three possible hybridisations via covalent bonds with other non-metallic elements and has the ability to form ionic bonds generating carbides. The carbon molecules or carbon-based materials can also participate in high or low-energy physical interactions[14]. Even 231 years after its discovery by the French scientist Antoine Lavoisier (1789), there is still much to discover/optimise in its chemistry and physics. At standard conditions, combining carbon with hydrogen and oxygen can produce chemical compounds in all matter states (solid, liquid, and gas). The pure phase

can act as metal or semiconductor depending on the allotrope form. Most of its polymers act as an insulator.

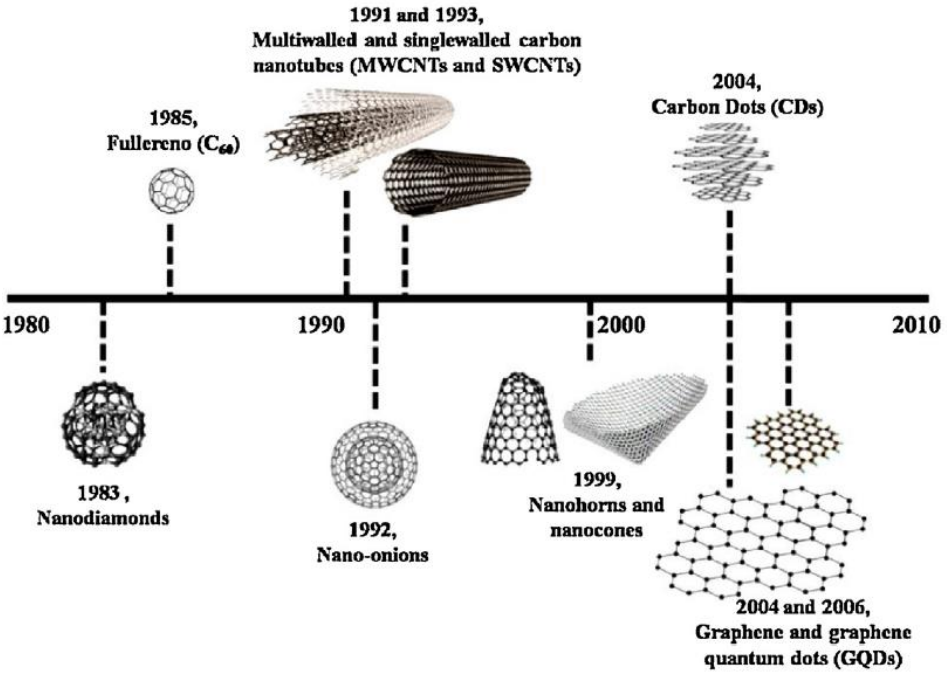

Figure 1.1: Timeline of the recent major discoveries in carbon-based materials family[15]. Reproduced with permission from reference 15. Copyright 2017 Elsevier Masson SAS.

Figure 1.1 illustrates that between 1980 and 2010, nine significant discoveries in the field of carbon-based materials were made, two of which were awarded a Nobel Prize. Fullerenes, discovered by Harry Kroto in 1985, received the Nobel Prize in Chemistry in 1996, and graphene, discovered by Andre Geim and Konstantin Novosolev in 2004, received the Nobel Prize in Physics in 2010. This is a measure of their immediate impact on the field of science.

Carbon quantum dots are an intermediate phase between bulk carbon materials and molecules, being small enough not to be considered a three-dimensional material and big enough not to be classified as a supramolecular structure or molecule. Carbon quantum dots are classified as zero-dimensional (0D) particles (dots), optically active material (fluorescent) with a particle size less than 20 nm, members of the vast carbon materials family.

CQDs were discovered in 2004 by Xu *et al.*[16]. The new material was reported as fluorescent single-walled carbon nanotube fragments (FSWCNF). In 2006, Sun et al.[17] labelled these carbon-based fluorescent dots as quantum-sized carbon dots (QCDs). It is noted that between Xu and Sun's papers (2004-2006), a further two published research, report the synthesis of carbon dots. Yu et al.[18] reported in 2005 the synthesis of “fluorescent nano-

diamonds (FNDs)", however, no connection was drawn between this work and Xu's paper published a year earlier. In 2006 Bottini *et al.*[19], building on the work of Xu *et al.*, expanded the work to graphite, carbon black, and several forms of carbon nanotubes. In addition to carbon precursors, the synthetic method included the use of 1% sodium dodecyl sulfate (SDS) solution and a sonication procedure, with the ultimate aim of dispersing and separating the ultrasmall optically active carbon nanoparticles from the solid mixture. Therein, the researchers were able to successfully isolate fluorescent nanoparticles.

Following the research timeline in the CQDs field, the first three papers used a top-down method, and the fourth paper explored an intermediary between top-down and bottom-up approaches. Sun *et al.* used a pre-treated carbon black precursor in an acidic environment to produce quantum-sized carbon dots, which were optically activated via surface modification with polyethylene glycol (PEG1500N) molecules.

Every year, thousands of publications reporting CQDs related research are published, with a broad range of applications such as optoelectronics[20,21], sensors[22,23], fluorescent inks[24,25], photocatalyst[26–28], electrocatalyst[29–32] (oxygen evolution reaction (OER), hydrogen evolution reaction (HER), and CO_2 reduction), photothermal energy conversion intermediator[33,34], energy storage[35–37], solar cells[38], fuel cells[39], drug delivery[40], bio-imaging[41], and other related nanomedicine applications[42,43].

Among the reported synthetic strategies for producing CQDs, the most promising and eco-friendly route is the use of renewable precursors such as biomass-related carbon sources and a solvents such as water. A hydrothermal method can address these requirements, and a continuous hydrothermal flow approach can solve the challenge of large-scale production (industrialization). Synthesizing CQDs from small molecules like biomass (such as glucose, citric acid, cellulose) can also deliver control over the final product's physical properties and chemical composition. This approach is a significant advantage of the bottom-up synthesis over the top-down approach. A bottom-up method relies on the concept of a constructive process, whereas top-down is more closely associated with a destructive route because it requires reducing the size of a well-defined particle/crystal *via* physical or chemical 'cutting' process[44].

Developing new synthetic routes is required in the CQDs field. The innovative methods must make the materials economically feasible and environmentally friendly for integration into various devices or applications.

1.1.2 Carbon quantum dots: synthesis routes and challenges

Carbon quantum dots were discovered by chance in 2004 by Xu *et al.* when attempting to purify the single-wall carbon nanotubes (SWNTs) from a dispersion derived from arc-discharge soot using an electrophoretic method. He observed that under 360 nm UV light, one of the phases was fluorescent. The phase was described as a mixture of fluorescent nanoparticles derived from the SWNT's[16]. This was the first scientific report in which optical properties were assigned to a material directly derived from a carbon-based phase, with graphene quantum dots (GQDs) discovered in 2006 by Bottini *et al.*. A combination of physical processes (arc-discharge and sonication) with a corrosive chemical treatment (HNO_3) applied on graphite powder were employed. Ultimately, it took nearly four years to develop a single-step chemical process to successfully produce quantum dots of graphene (GQDs) [45].

The fluorescent organic molecules were discovered a long time before CQDs or GQDs. No one predicted the existence of macrostructures with such properties. Following graphene discovery, there was a considerable debate in the scientific community about the theoretical existence of GQD[46–51]. A research race to produce GQDs began between groups working in the related fields all around the world.

There are two main synthetic strategies for producing carbon quantum dots (with a particle size smaller than 10 nm) that can interact with light beams (absorb and emit). These can be classified as top-down and bottom-up approaches.

The top-down strategies involve the use of a pre-made or a pre-existing bulk carbon material which, through the use of chemical or physical processes, is reduced in size to 10 nm or smaller.

On the other hand, the bottom-up methods use small molecules that can react or decompose to generate a bigger particle in size or carbon motives that can assemble into a larger stable structure. The bottom-up methods can never be achieved solely through the physical process because it requires the creation of new chemical bonds between the carbon, oxygen, or nitrogen atoms involved in the synthetic process, which is essential in the process of increasing the size of the CQDs particle. In contrast, the top-down method requires the breaking of chemical bonds to decrease the size. The bottom-up and top-down approaches can be combined with the purpose to increase production. For example, hydrothermal carbonisation (HTC) results in a solid phase containing bulk carbon material, known as hydrochar, and a

liquid phase containing CQDs. The solid phase can be further processed and converted to CQDs.

Bottom-up CQDs perform better in terms of optical properties, stability, and cytotoxicity. The synthetic procedure and surface modification are straightforward when compared to top-down approaches[52]. Also, in terms of the production costs, the top-down method may involve precursors such as fullerenes[53] (buckyballs) or single, multi-walls carbon nanotubes[54] (SWCNT), which are very expensive to produce, purify/isolate, and thus render the entire process not feasible for mass production.

The main synthetic methods for the production of carbon quantum dots will be discussed separately to provide a detailed account of each, including the advantages and drawbacks of using top-down (A) or bottom-up (B) synthetic methods.

A. *Top-down methods*

A process known as 'cutting' is used to achieve a nanometric size starting from a bulk or micro-sized material. This process can be physical, chemical, or a combination of the two. This process requires breaking chemical bonds or soft and strong physical interactions, which unite and keep the macroscopic version of a specific material. The physical processes that use a top-down approach are mechanical milling, laser ablation, arc discharge, microwave, or ultrasonic-assisted. There are very few chemical processes available: oxidative cleavage (or chemical ablation), hydrothermal or solvothermal synthesis, and chemical etching.

A.1 *Mechanical milling*

Mechanical milling is a technique used to convert bulk or crystalline phases into powder or mix different types of solid material (amorphous or crystalline) as a homogenous powder. One of the most explored techniques of mechanical milling nowadays for the top-down synthesis of nanomaterials is high-energy ball milling, which consists of using stainless steel or hard materials balls inside of cylindrical stainless-steel rotating/spinning chamber (see **Figure 1.2**). In general, a powder is a mixture of a broad range of particle size distribution, including particles lower than 100 nm (nanoparticles); mechanical milling (the first ball milling

machine was developed in 1870) has been used a long time before nanomaterials were recognised for their particular properties and characteristics[55] .

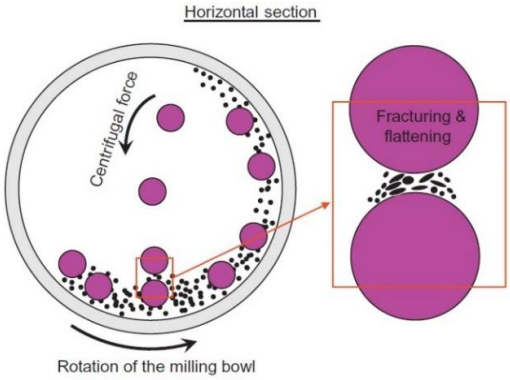

Figure 1.2: Schematic representation of a ball milling process applied for the synthesis of nanomaterials from related bulk starting materials[56]. Reproduced with permission from reference 56. Copyright 2018 Elsevier.

Mechanical milling is an old and extensively used technique[57]. This method has been heavily applied to increase the surface area of carbon-based materials[58,59] in achieving the values required by different applications such as gas absorption[60,61] or energy storage (batteries)[62,63].

Smashing carbon-based materials to generate carbon quantum dots has been explored by Wang *et al.*[64] in developing a ball milling method (dried mechanical milling method) and using a mixture of activated carbon and KOH at 500 rpm for 50 hours. After the isolation and purification of the generated CQDs, the authors reported CQDs with particle sizes in the range of 1.6–2.8 nm with a mean particle size of 2.2 nm. The CQDs exhibited a bright greenish-yellow luminescence under 365 nm UV light and a dual maximum of emission at 490 nm (λ_{ex}=270 nm) with an independent emission between 250-330 nm, and at 540 nm when the excitation wavelengths were between 410-450 nm. The as-prepared carbon quantum dots had a quantum yield of 7.6%. The oxygen content reported was 30.77 wt%, indicating that the activated carbon surface was oxidised by the oxygen from the air during the process. The authors reported traces of metallic iron (0.07 wt%) originated from the stainless-steel balls used during the ball milling process.

A.2 *Laser ablation*

A typical laser ablation process applied for carbon-based materials synthesis entails using a high-energy laser beam to generate localised heating on the surface of the carbon-based particle vaporising the material exposed to the laser beam. The interaction between the surface

carbon atoms and the laser beam generates beam absorption and heat. The energy provided by the laser beam on the surface can break the chemical bonds and cause atomic vaporisation.

When a laser ablation method is applied on carbon-based material, three main parameters can influence the final properties and characteristics of the product: (a) the wavelength of the laser beam, (b) the pulse widths and its repetition rates, and (c) the power density of the used laser.[65] In the most synthetic routes applied for CQDs, the reaction mixture / the final product consists of colloidal solution with fluorescent properties (when exposed to UV light). The reaction system requires a polar solvent (commonly water) to achieve this specific reaction environment, favourable for CQDs dispersion and stabilisation (following production). These synthesis characteristics are also required for other materials such as noble metal nanoparticles[66], metal oxides[67], or ceramics[68]. To fulfil them with a laser ablation method, laser ablation in liquid (LAL)[69] or laser ablation synthesis in liquid solution (LASiS)[70], (where a stabiliser is dissolved in the reaction solvent), have been developed (see **Figure 1.3**).

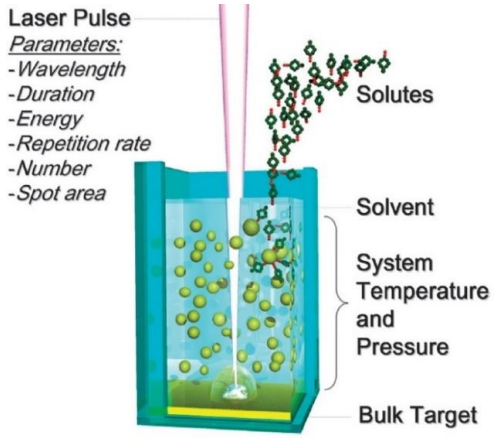

Figure 1.3: Top-down laser ablation synthesis in liquid method representation[70]. Reproduced with permission from reference 70. Copyright 2013 Royal Society of Chemistry.

A similar method was applied by Zhang *et al.*[71] to produce luminescent carbon nanoparticles with controllable oxygen functionalities. The researchers used a graphite disk with a diameter of 5 cm immersed in water, which was exposed for 30 minutes to a KrF pulsed laser (248 nm laser beam) at a repetition rate of 10 Hz with the laser irradiation at a power of 200, 300 and 400 mJ/pulse. In this study, three different carbon quantum dot samples were prepared at three different laser irradiation power (200, 300 and 400 mJ/pulse). CQDs exhibited a diameter of 2 to 5 nm with a graphitic lattice fringe spacing of 0.33 nm. The photoluminescent properties of the as-prepared CQDs shown the strongest emission at 420 nm when the samples were excited at 320 nm. The maximum of emission shifted to 500 nm as the excitation

wavelength increased to 420 nm. The intensity of emission increases when the irradiation power of the laser increase from 200 mJ/pulse to 400 mJ/pulse. From XPS studies, it was noticed an increase of oxygen content from 11.38 wt% (when a 200 mJ/pulse irradiation power was used) to 38.59 wt% (when the irradiation power was increased to 400 mJ/pulse).

Overall, increasing the laser irradiation power resulted in higher quality CQDs materials. This study demonstrated that the quantity of oxygen functionalities present on the CQDs surface (when the CQDs are made of carbon and oxygen only) affects the optical properties, with lower oxygen content resulting in a lower intensity of emission. Hu et al.[72] observed a different relationship between laser parameters and optical properties of CQDs when the laser pulse widths were varied (0.3, 0.9, and 1.5 ms). The researchers successfully tailored the particle size of CQDs in this study: 3.2 nm for 0.3 ms laser pulse widths, 8.1 nm for 0.9 ms laser pulse widths, and 13.4 nm for 1.5 ms laser pulse widths. Overall, the laser ablation method can be a green alternative for the CQDs synthesis. However, in terms of energy consumption and laser maintenance, this method is expensive and requires highly specialised process operators for large-scale production.

A.4 *Arc discharge*

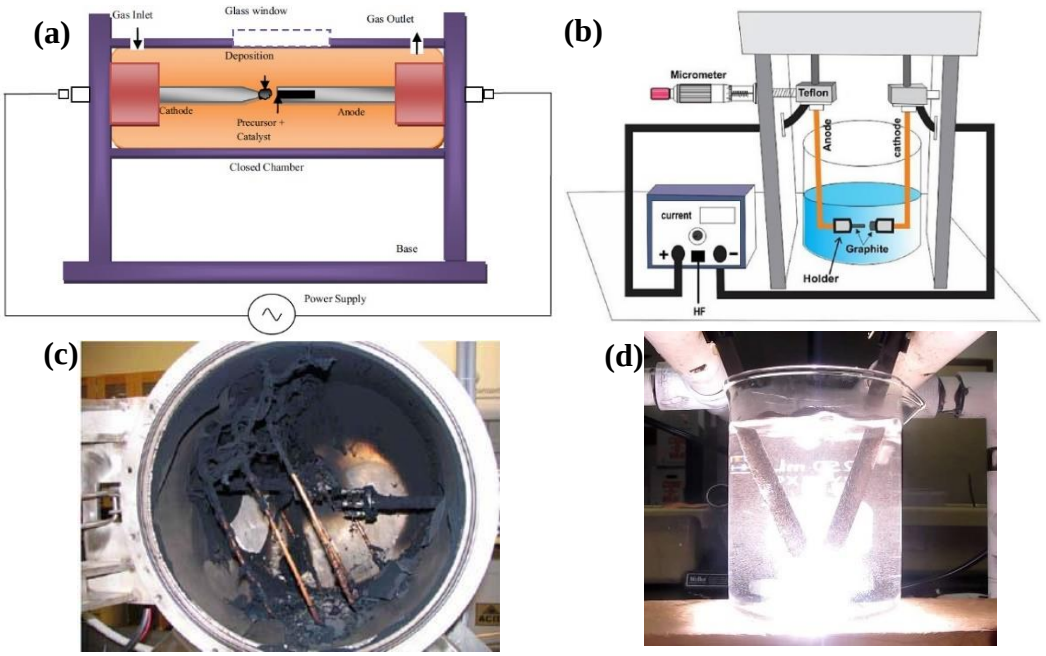

Figure 1.4: The schematic of arc discharge setup based on: (a) gas[73] and (b) liquid[74] technologies employed for the synthesis of carbon nanotubes, and the process view of arc discharge in (c) gas chamber[75] versus (d) liquid environment[76]. Reproduced with permission from references 73, 74 and 75. Copyright 2014 Elsevier, 2018 Springer Nature, and Dr Ya-Ping Sun.

An arc discharge process applied for the synthesis of carbon-based materials consists of an electrical breakdown of gas to generate plasma, vaporisation of carbon atoms from a carbon source located on the anode, acceleration, and reassembly on the cathode into a new form of carbon allotrope (see **Figure 1.4**).

This method has been widely applied in the fabrication of carbon nanotubes (CNTs). It was also used for the synthesis of CNTs which led to their discovery[77] in 1991 by Iilijima. Xu *et al*.[16] discovered carbon quantum dots in 2004 while attempting to synthesise single-walled carbon nanotubes (SWCNTs) using an arc discharge approach and an electrophoretic method to purify the product. This approach appears to be one of the most commonly utilised synthetic methods for producing allotrope forms of carbon. Fullerenes (buckyballs) and buckytubes were discovered by Harold Kroto, Robert Curl, and Richard Smalley in 1985 using a focused laser pulsation method[78]. Graphene was first isolated in 2004 by Andre Geim and Konstantin Novoselov using a scotch tape method[51]. Their findings were published in Science journal, resulting in the most cited paper in the history of carbon-related materials, chemistry, or materials science, followed by Kroto's the research findings on fullerene C_{60}, published in Nature journal (1985). The carbon-based materials (CNTs and CQDs) discovered using the arc discharge method have yet to receive a Nobel prize. Fullerenes work was awarded the Nobel Prize in Chemistry in 1996 and graphene research received the Nobel Prize in Physics in 2010.

CQDs are a by-product of the synthesis of CNTs using an inert gas-assisted arc discharge method. CQDs are extracted from the final product using a wet method consisting of the dispersion of the mixture into a water-based diffusion environment able to form a stable colloidal solution. The CNTs are separated using centrifugation.

Su *et al.*[79] used a DC arc discharge furnace setup consisting of an anode made of sintered graphite rods with a Ni/Y catalyst and a cathode made of pure graphite rods. Having a 2-3 mm gap between anode and cathode, they applied a 90 A current under 50 kPa helium buffer, and the main product was single-walled carbon nanotubes (SWCNTs). The resulted product was dispersed in a 20% sodium dodecyl sulfate solution, sonicated, and centrifuged at 6000 rpm to isolate SWCNTs and the catalyst, followed by another centrifugation step at 9000 rpm to isolate the residual carbon material. This residual carbon material was further used to produce fluorescent graphitic CQDs via refluxing it in a concentrated mixture of H_2SO_4/HNO_3. The resulting CQDs showed independent excitation behaviour at around 502 nm (when the sample was excited between 300-380 nm with the maximum of emission at 300 nm excitation

wavelength), with a quantum yield of 3.2%. The mean particle size of as-synthesised CQDs was found to be 5.6 nm with a size distribution between 3.2-8 nm.

Kiem *et al.*[80] used a wet arc discharge method to synthesise graphitic carbon nanostructures with no optical properties using a 25 V DC arc discharge setup made of 12 mm 99.999 % purity graphite anode and a cathode immersed in deionised water (18.2 MΩ). A current of 1-5 A was applied between the electrodes. At a current intensity higher than 4A, the product is composed of tubular and spherical carbon nanoparticles. Because the plasma zone is formed in water, reactive species (O^+ and O^{2+}) are generated during the process due to the ionising effect of the plasma. These species react with the surface of graphitic carbon nanoparticles (GCNPs), oxidising them. They also found that the degree of GCNPs oxidation is dependent on the current levels during the arc discharge in the water process. The mean particle size of GCNPs was 12.10 ± 3.08 nm, which explains why the material has no luminescent properties. The authors assumed that inside the particle is an open space, approximating the diameter of the open space to be 8.36 ± 2.86 nm, and proposed an open centre onion structure made of graphene-like layers.

If the distance between graphite anode and cathode during the process is large enough to prevent the plasma formation, the method is called electrochemical oxidation. Ming *et al.*[81] used two graphite rods separated by 7.5 cm, immersed in deionised water, and applied a potential between the electrodes to prepare CQDs. The carbon dots exhibited a particle size between 3-6 nm and excitation-dependent photoluminescent properties when the sample was excited in a wavelength range between 300-900 nm. The primary product of this synthetic method is graphite oxide; CQDs were regarded as a by-product.

Overall, due to the multistep synthesis and purification processes, these electrical current-based top-down methods are not a promising option for producing CQDs. Furthermore, none of these methods has resulted in optimisation to achieve CQDs as the main product.

A5. ***Microwave or Ultrasonic Assisted Technique***

An ultrasonic wave is a type of vibration transmitted through an environment with frequencies higher than 20 kHz. A microwave is a type of electromagnetic radiation with frequencies between 300 MHz to 300 GHz. None of these techniques possesses enough energy to break chemical bonds inside a 3D structure, hence decreasing the size of the particle. However, they are efficient at breaking physical interactions such as van der Walls, dipole forces, π-stacking, or π-interaction and hydrogen bonds. In this way, carbon particles smaller

than 10 nm are extracted from a carbon source such as black carbon, activated carbon or graphite, and promoted to diffuse in the liquid environment. This extractive process is specific for a broad range of particle size distribution; further particle size separation processes are required.

The ultrasonic wave-assisted method was employed to produce graphene quantum dots (GQDs) from nano-graphite by Lu *et al.*[82](see **Figure 1.5**). The exfoliation process of graphite via ultrasonic wave assisted process has been used numerous times to produce thin graphene layers[83]. In this study, Lu focused on isolating the optically active particles (less than 10 nm size) from the nano-graphite particles, dispersed in an organic polar solvent (N-methyl-2-pyrrolidone (NMP), and/or N,N-dimethylformamide (DMF)). The nano-graphite powder /solvent mixture was first subjected to low-frequency ultrasonication, followed by one hour of mild ultrasonication (45 W, 59 kHz) step. GQDs consisting of 84 at% carbon, 11 at% oxygen, and 5 at% nitrogen were produced, with a mean particle size of 3 nm and a 2-7 nm particle size distribution. The maximum emission peak was at 465 nm when the sample was excited at 390 nm. The material showed excitation independent emission properties between 310-450 nm and dependent emission properties when the sample was excited between 450-530 nm.

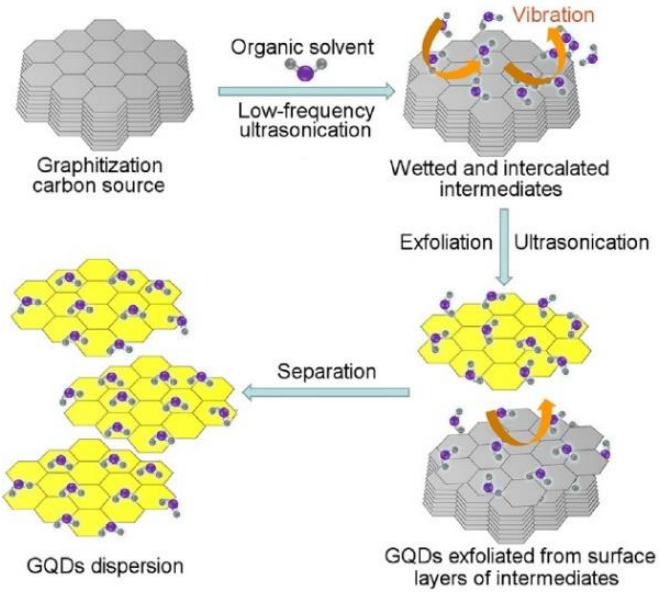

Figure 1.5: Schematic of the top-down ultrasonic wave assisted synthesis process of graphene quantum dots (GQDs) from nano-graphite[82]. Reproduced with permission from reference 82. Copyright 2016 Elsevier.

Starting from a graphene oxide (GO) dispersion in a HNO_3/H_2SO_4 solution (oxidative environment) exposed to 800 W microwave irradiation for one hour, Li *et al.*[84] successfully produced graphene quantum dots. In this study, the authors revealed that microwave irradiation

plays a key role in the process, naming the method ‘a facile microwave avenue’, but in fact, the key parameter was the oxidative environment because the microwave only generate the heat required to accelerate the oxidative chemical cutting of the graphene oxide sheets to small photoactive particles. To date, there have been no studies in which microwave irradiation is used as the primary source to break the physical interactions between the aggregated carbon material, allowing for the dispersion of the small particles into an organic solvent or water. However, the microwave-assisted method is well explored for the bottom-up approaches, where the carbon sources are small organic molecules, and the solvent is water.

A.6 ***Wet chemical methods***

A6.1 ***Oxidation***

Oxidative cleavage is a chemical process that involves the breaking of a carbon-carbon bond and forming a new carbon-oxygen bond instead, relating this type of process to top-down synthesis of CQDs from a larger size carbon source. This means that the carbon particles are chemically cut; the newly formed particles are covered with oxygen functionalities.

Starting from lignite coal, Lu *et al.*[85] successfully synthesised CQDs applying a green route using O_3 and H_2O_2 as oxidation agents. The CQDs have an average particle size of 2.8 nm with a size distribution between 2-4 nm and an oxygen content of 41.89 at% with various functionalities. In terms of optical properties, CQDs are excitation dependent. They have a maximum emission at 460 nm wavelength when the sample was excited at 360 nm, with an emission redshift between 320 to 480 nm excitation wavelength.

A6.2 Extraction

Another top-down wet chemical method is the extraction of carbon quantum dots from carbon black[86] or other non-crystalline carbon phases[87]. It uses a hydrothermal or refluxing treatment in a basic or acidic oxidative environment to break the physical interactions between the different sized carbon particles.

Applying a pure physical extraction method, Han *et al.*[88] demonstrated the natural presence of CQDs in carbon black. They used acetone as an extraction environment, dispersing the carbon black in it for 24 hours, during which time the CQDs diffuses in the solvent and the larger particles settled to the bottom of the flask. The supernatant was collected, and CQDs were isolated and characterised. The optical properties of extracted CQDs revealed an excitation-dependent behaviour with a maximum of emission at 398 nm when the sample was

excited at 345 nm. CQDs exhibited a redshift between 320-440 nm excitation wavelengths. The quantum yield value (19%) obtained for the as-synthesised CQDs is regarded high when compared to other CQDs synthesised via a complex synthetic process. The extracted CQDs had a mean particle size of 2.39 nm, with a particle size distribution ranging from 1.5-2.8 nm. The solvent-extraction was utilised as a particle size separation process. The authors successfully isolated a 1.8 nm CQD's mean particle size with ethanol.

A.7 ***Top-down methods: Conclusion***

It can be concluded that these top-down processes, whether chemical or physical, consume a high amount of energy, can be dangerous or highly corrosive, have multiple steps, and provide poor control over the particle size and distribution, necessitating additional steps for particle size separation in addition to cleaning the precursors and extra reagents used in the process.

B. ***Bottom-up methods***

A typical bottom-up approach applied in CQD synthesis involves the use of organic molecules to 'build-up' the CQD particles via chemical or chemical-physical processes. The organic molecules react with each other, forming a larger structure until it reaches a stable aggregate formation, that is characteristic of the reaction environment and reaction conditions. This method includes carbon sources ranging from very simple and small organic molecules such as hydrocarbons[89] to larger and more complex organic structures like carbohydrates[90] or amino acids[91].

B.1 ***Chemical Vapour Deposition (CVD)***

The CVD method used for carbon-based materials (graphene, graphene quantum dots, carbon nanotubes, fullerenes, and carbon quantum dots) entails using an inert substrate as a template (copper, quartz, etc.), an inert gas as a gas carrier (neon, argon, nitrogen) and a hydrocarbon molecule as a carbon source (methane, ethane, ethene, acetylene, etc.) and high temperature. Some of the hydrocarbon molecules self-assemble during the process, forming new carbon-carbon bonds on the substrate surface as a film of the desired carbon material, and hydrogen and unconverted hydrocarbon molecules are released outside the setup.

Applying a CDV method Cui *et al.*[89] synthesised CQDs starting from acetylene, using argon as a gas carrier and quartz tube heated up at 1000 °C with a C_2H_2 / Ar flow rate of 70/700 mL/min for 2 hours. The resulted powder was dispersed in N,N-dimethylformamide, then the

suspension was filtered on a 0.45 μm PTFE filter, followed by a drying procedure. The as-synthesised CQDs have a 3.5 nm mean particle size with a 2-7 nm particle size distribution. The PL spectrum shows an excitation dependence behaviour between 320-500 nm, and a maximum of emission at 440 nm excitation wavelength. Because the CVD method involves the use of an inert reaction environment and an organic molecule made of carbon and hydrogen, the synthesised CQDs were expected to be oxygen-free, have good solubility in nonpolar solvents such as chlorobenzene, 1,2-dichlorobenzene, and toluene, and a poor dispersion in water. The luminescence in this specific case was attributed to the 'quantum-sized fragment of graphite' existent in the CQD's core.

B.2 ***Microwave-assisted***

When small organic molecules are exposed to microwave radiation, they can undergo intramolecular and/or intermolecular decomposition or condensation, which can lead to the formation of a CQD-like structure.

Shen *et al.*[92] synthesised nitrogen-doped carbon quantum dots with an average size of 5 nm using a microwave technique (750 W and 2450 MHz). The precursors used were carboxylic acid (citric acid) and cyclic amine (cyclen). The N-doped CQDs demonstrated an excitation independent behaviour between excitation wavelengths of 320-380 nm. The maximum of emission was obtained when the molar ratio between the carbon source (citric acid) and the nitrogen source (cyclen) was 1:1; further variations affected the optical properties of the N-CQDs. The authors assumed the photoluminescence origin for their microwave-assisted synthesised CQDs is from the amino functionalities located on the CQD's surface.

B.3 ***Thermal decomposition/carbonisation method***

The thermal decomposition process involves heating carbon precursors without using solvents to produce carbon-based materials such as CQDs. In this process, the mixture of the precursors is heated at a specific temperature and pressure for a period of time. When organic molecules are exposed to heat, they are converted into carbon materials, a process known as carbonisation. The temperature and duration of the precursors' exposure to heat can influence the degree of carbonisation. A complete carbonisation process of the precursors is undesirable for CQD synthesis because it will generate large and optically inactive particles due to the excessive growth of the carbon quantum dots. In the case of thermal decomposition, it is difficult to distinguish between decomposition and carbonisation processes. Similar parameters and reaction mechanisms are used in the synthesis of CQDs.

In 2012 Wang and co-workers reported the synthesis of graphene quantum dots and graphene oxide by tuning the carbonisation degree of citric acid[93], but in 2015 using a similar method, they reported the synthesis of reduced carbon dots[94] where the material was subjected to an additional heat treatment step.

The first step in the synthetic process involved the heat-treatment of citric acid at 200 °C for 30 minutes, followed by CQDs isolation. The isolated CQDs were subjected to an additional heat-treated step at 300 °C for 3 hours to produce optically active reduced carbon dots. These two highly referenced studies mark a milestone in the misidentification between GQDs and CQDs. The reported data (2012)[93], lacks TEM particle size determination. The size and height obtained from AFM could correspond to CQDs (as assigned in a subsequent published work)[94] however, the authors identified the product as graphene quantum dots.

In 2013 by applying a similar method (170 °C for 30 minutes), Zheng and co-workers[95] succeeded to synthesise N-doped CQDs from citric acid and diethylenetriamine. The CQDs were isolated by precipitation with acetone from the main cooled reaction mixture. The precipitate was purified using a 3 kD dialysis bag immersed in water for two days. The CQDs mean particle size was 4 nm, with a size distribution ranging from 3 - 5.5 nm. It was observed an independent excitation behaviour between 300-400 nm in the photoluminescence spectrum. The independent excitation behaviour appears to be a characteristic of CQDs made of citric acid as a carbon source.

B.4 ***Hydrothermal/solvothermal method***

Due to its green and eco-friendly perspectives, the hydrothermal/solvothermal method is one of the most promising synthetic routes applied in CQDs synthesis. It uses water as a solvent, reaction temperatures below 240 °C and parameters that lead to a simple and safer synthetic procedure when compared with other methods available. The reaction environment assures reproducible results, good stability, and dispersion of the products. The CQDs generated via hydrothermal/solvothermal methods are rich in surface functionalities, and most of the materials reported are highly soluble in water at any temperature or pH value. When considering scaling up the process, the method has drawbacks. The limitations are: 1) it requires a large volume of solvent in comparison to the amount of the precursor used, and this is related to the CQDs global production yield (the batch hydrothermal synthetic process is limited in producing a certain amount of CQDs per unit of time), and 2) it takes several hours to several days of reaction time and exposure to temperatures above the boiling point of the

solvent, as well as under pressure which increases the risk of undesirable events. However, the advantages of this method make it very appealing, and many research projects for the production of CQDs have been established.

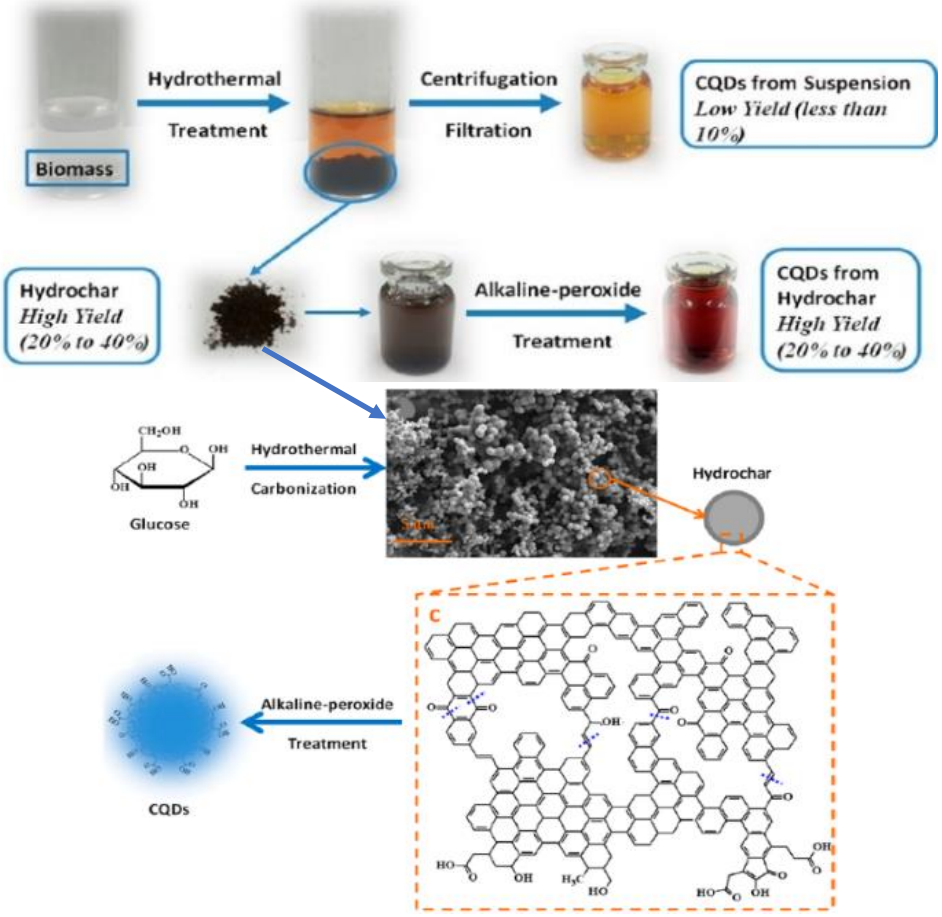

Figure 1.6: Top-down combined with bottom-up method as a process optimisation to maximise the synthesis/production of carbon quantum dots from a renewable source of carbon[96]. Reproduced with permission from references 96. Copyright 2019 American Chemical Society.

Biomass-related molecules or biomass have been successfully used to produce sustainable CQDs[97–100]. The method of producing carbon materials under hydrothermal conditions was named hydrothermal carbonisation in 1913 by Friedrich Bergius and his collaborators[101], and won the Nobel Prize in Chemistry in 1931. The initial goal of the method was to convert cellulose into sugar or coal into petroleum. Early experiments produced a large amount of hydrochar, but the significance of these materials was not recognised at the time. The hydrochar is an intermediate product made of an amorphous oxygen-rich carbon phase. Heat treatment is used to convert biomass into carbon material with specific properties and characteristics. On the other hand, CQDs are produced during the process and do not require

further thermal processing. The possibility of using hydrochar as a CQDs precursor in a top-down method exists, but only a few papers have reported it. For example, Jing et al.[96] established an effective hydrothermal method in which the hydrochar produced as a by-product during the CQDs was used as a precursor to further produce more CQDs (see the process schematic in **Figure 1.6**).

1.1.3 Carbon Quantum Dots Properties

A. *Optical properties: Light absorption and photoluminescence origin*

CQDs have strong ultraviolet absorption and medium to weak visible absorption. The UV absorption is attributed to the core's π-π* transitions, and the visible absorption is assigned to the surface functionalities' n-π* transition.[102]. CQDs are very efficient in harvesting light[103,104]. Due to their electronic structure tunability, CQDs can be tailored to absorb specific wavelength domains required in various application fields including photocatalysis, hydrogen production, water splitting, solar cells and photothermal conversion [105–109].

The light emission properties of CQDs are regarded as one of the most important characteristics of this material. A photoluminescent process involves the absorption of photons that irradiates the surface of a quantum dots particle, causing the transition of valence electrons to a higher energetic state or the conduction band, followed by different and various relaxation processes in which the excited electrons return to their initial energetic state via one or multiple relaxation transitions[110]. Some of these relaxation transitions (known as radiative transitions) generate different types of photons, which are then released into the chemical environment[111].

The origin of emitted light in the case of CQDs can be found in the core and on the surface of the CQDs particle. The CQD's core has a well-defined electronic structure, and it can be compared with the graphite electronic structure because most of the CQD's cores are made of graphitic carbon phase, a crystalline phase with well-defined possible transitions. The CQD's surface electronic structure is more complex due to the variety of functional groups/heteroatom doping and defects present[44,107]. These functional groups/heteroatom doping and defects can either positively affect the final emissive properties by generating intense excitation-relaxation transitions or negatively affect the process by non-radiative transitions, lowering emission-quality[112–114]. Furthermore, the ratio between the core and the surface, the type of the functional groups and their concentration, is consequently reflected in the photoluminescence spectrum[115,116].

B. Surface chemistry and chemical stability

The reaction parameters, for example, the temperature of the synthetic process, the carbon source, doping type, and source, can play an essential role in the final optical and morphological properties of the carbon dots[117].

During the synthetic process, small molecules react together to form an initial polymeric sphere, which is then used to form the CQDs particle. The carbon atoms of the polymeric core accumulate enough energy to further react and to form carbon-carbon bonds between the polymeric chains, generating a graphite-like crystalline structure known the CQD's core. The core continues to grow until the required energy to sustain the formation of sp^2 C-C bonds is higher than what the reaction environment is able to provide[44,118].

Graphene quantum dots (GQDs), carbon quantum dots (CQDs), carbon nano-dots (CNDs), and carbonised polymer dots (CPDs) are examples of CQDs, which are categorised based on their composition and crystalline structure.

GQDs have a well-defined crystalline structure composed of sp^2 carbon. On the other hand, carbon quantum dots have a quasi-spherical or spherical morphology with a distinctly crystalline structure that is primarily composed of sp^3 hybridization, and their size is usually less than 10 nm. CNDs resemble carbon quantum dots (CQDs) in shape and size, but they lack a crystalline structure and have a high degree of carbonization. Finally, CPDs have a carbon core (which can be para-crystalline: having short and/or medium range ordering in their lattice); a hydrated cross-linked polymeric frame; or like CQD/CND, and various functional groups, and polymer chains on the surface. It should be noted that there is no clear distinction in the literature between graphene quantum dots (GQDs) and graphite-like quantum dots.

To summarise, having a graphite-like core and a functionalised surface (the coverage of the core) is one of the most important characteristics of a carbon particle for it to be classified carbon quantum dot[119,120]. The coverage is chemically bonded to the core, and it is rich in oxygen functionalities. The surface formation is shown by the presence of the functional groups as well as sp^3 carbon atoms in the particle. Some of these functionalities are bonded on carbon chains creating chromophore sites that improve the photoluminescent properties of the CQD's particle[116,121]. The surface interacts directly with the environment, and it can create physical or chemical interaction with a different component such as molecules, materials, or other surfaces.

Most CQDs have a high concentration of oxygen functionalities on their surfaces, which makes carbon dots very soluble in polar solvents. When the surface is decorated with nitrogen

functionalities, the solubility increases or remains the same (amine, amide, etc). Except for some oxidation processes that can occur on the hydroxy, phenoxy, some amine, and imine groups, the rest of the CQD's functionalities are chemically stable over time, giving this material long-term physical and chemical stability[26].

Overall, CQD particles offer chemical stability (i.e., not easily decomposed by changing the physical or chemical parameters of the dispersion environment), a variety of properties, and surface composition, and they are classified as biocompatible materials. Several studies have used the material's unique properties in conjunction with their optical properties in bio-imaging processes.[122]

1.1.4 Carbon quantum dots in nano-sensing applications

The optical properties, surface chemistry, chemical and physical stability, and biocompatibility of CQDs make them suitable for a wide range of applications including energy storage, solar cell, photocatalysis, bio-imaging, drug delivery, optoelectronics, luminescent inks, and chemical sensing[20,37,42,109,123–125].

The ability of CQDs to absorb and emit light can be used in chemical photo-sensing applications. The chemical detection of certain species can be assigned to one of two main processes:

a) non-interaction-based sensing and physical or chemical interaction-based sensing. These sensing processes are based on the modification of photoluminescent properties of the CQDs (when they share the same environment with different metal ions and anions or organic molecules)[23]. The section that follows will discuss these in detail. An emission intensity quenching effect based on no interaction between the CQDs and chemical species, called the inner filter effect, consist of photoluminescence quenching of CQDs due to the light absorption competition with the chemical species in solution. A molecule or an ion/anion has a well-defined electronic and chemical structure and a much smaller size than a CQD particle. All these properties confer better dispersion mobility and light absorption capacity to the chemical species in solution, making them more efficient in certain wavelength domain light harvesting. If the absorption domain of the chemical species overlaps with the absorption and/or the PL spectrum of the CQD, it will generate a quenching in the photoluminescence spectrum of carbon quantum dots proportional to the ion/anion/molecule concentration[126–128].

b) An interaction-based quenching in the photoluminescence spectrum is possible due to the surface functional groups, and specific metal ions, anions, or organic molecules can

physically or chemically interact with these functionalities, modifying the surface composition. Physically adsorbed or chemosorbed on the CQD surface, the ions, anions, or organic molecules will modify the electronic structure of the surface, and it can be involved in charge transfer or charge recombination processes. These processes will affect the usual electronic transitions which occur when CQDs absorb light at certain wavelengths, and as a consequence, the emission properties will be influenced (the emission will increase or decrease in intensity depending on the nature of the chemical analysed)[129–131].

Overall, a sensing process based on the inner filter effect can provide a greater sensitivity because it is only concerned with light absorption. In contrast, an interaction-based sensing process can offer enhanced selectivity due to the specific physical or chemical interactions created between the CQDs and chemical species.

1.1.5 Fundamental photonic processes

A photonic process is defined as the result of the interaction between light (photons) and matter. These optical processes include light emission (photon generation), transmission, absorption, detection, modulation, signal processing, switching, amplification, and sensing. During this project, different optical properties of the materials interest were measured, hence for the benefit of the reader, they will be defined[132] as follows:

- **band structure**: the range of energy levels that electrons may have in a material, as well as the ranges of energy that they may not have (band gap or forbidden band). The band structure for semiconductors is composed of three components: a valence band, a conduction band and a band gap between them. The conduction and valence bands are built up of overlapped atomic orbitals. At the ground state, the electrons are located in the valence band, while the conduction band is vacant. Electronic transitions to the conduction band occur when electrons get enough energy (equal or higher than the band gap energy).
- **band gap**: the minimum amount of energy required for an electron to have a transition from the valence band to the conduction band. Normally, the band gap can not be occupied with electrons, except when the material is doped, which creates additional energy levels resulting in p-type or n-type semiconductors materials. If the band gap is large, the energy required for a transition to place is high, the material is classified as an isolator. The energy of the band gap is measured in electron-volts (eV).
- **electron-volt**: is an energy unit, and it represents the energy gained by an electron when the electrical potential increases by one volt. The electron-volt equals 1.602×10^{-19} Joule.

- **light absorption:** the process in which the photons are absorbed by the matter and converted into energy.
- **light emission:** is an optical phenomenon occurring in semiconductors as a result of excited state relaxations, causing the generation and emission of photons with different energies.
- **photoluminescence**: is the phenomenon of light emission from any form of matter due to specific energies photons absorption.
- **wavelength (λ):** is the distance between two waves of a beam (photon), commonly measured in nanometers.
- **excitation wavelength (λ_{ex}):** the wavelength at which a specific chemical species or materials reach the excited state by absorbing photons that have that wavelength.
- **emission spectrum:** is the spectrum of electromagnetic radiation emitted by matter when its electrons have a transition from a high energy state to a lower energy state.
- **excitation spectrum**: is a spectrum recorded for a single emitting wavelength while varying the excitation wavelength.
- **excitation dependent emission**: the emission wavelength has a shift in the emission sprectrum (blue-shift or redshift) when the excitation wavelength is changed.
- **excitation independent emission**: the emission wavelength has no shift in the emission sprectrum (blueshift or redshift) when the excitation wavelength is changed.
- **redshift of emission wavelength**: the emission wavelength is shifted to higher wavelengths in the emission spectrum when the excitation wavelength is changed.
- **blueshift of emission wavelength**: the emission wavelength is shifted to smaller wavelengths in the emission spectrum when the excitation wavelength is changed.
- **quantum yield**: a measure of the photon emission efficiency, calculated as the ratio between the number of photons emitted by the sample to the number of photons absorbed by the sample.

1.1.6 Conclusions

Carbon quantum dots were discovered by chance in 2004, and since then, many distinctive CQDs have been synthesized, characterized, and tested for a wide range of applications.

Various synthetic top-down and bottom-up methodologies have been developed. One of the most promising and versatile methods is the hydrothermal method, which uses a variety of carbon sources to produce CQDs with diverse properties and characteristics. This method

has some disadvantages (is energy and time-consuming), but a continuous flow method can address these problems.

To conclude, possessing excellent optical properties and chemical stability, CQDs are a promising candidate as chemical nano-sensor for water-soluble species, and many studies have confirmed their potential in this field.

1.2 Graphene

1.2.1 Introduction

The history of using carbon materials started with human society. The humans discovered how to use the fire, and they realised that drawing the reality they lived in on the cave walls can be a form of personal development[13].

The year 2004 was excellent for the carbon materials family. Graphene was for the first time isolated, and its electrical properties were measured by Andre Geim and Konstantin Novoselov in their laboratory in Manchester, United Kingdom[51]. In their first report, the newly discovered material was not referred to as graphene, but rather as an atomically thin carbon film. Following this, a new field of research was established and since then, thousands of articles have been published, with graphene being introduced and tested in a wide range of applications. Graphene is made of carbon, an abundant element on Earth, thus it is a low-cost and eco-friendly alternative in practically all industries where this material can replace expensive metals or difficult-to-obtain materials or can be introduced in new applications.

Chemically and physically stable, even in harsh environments, graphene and its derivatives (such as graphene oxide, reduced graphene oxide, and graphene quantum dots) are classified as a biocompatible material and can be safely used in bio-related areas[133,134]. Several studies have shown that some enzymes can biodegrade these materials without causing accumulation in the body, and the resulting products do not exert cytotoxicity[135]. In some selected cases, graphene materials or their bioproducts can help for cell differentiation or/and tissue regeneration[136]. In comparison to other materials used in environmental applications, graphene requires a lower quantity to achieve similar product characteristics, which reduces the environmental impact significantly in related applications. By tailoring the graphene particle size[137] or/and the surface functionalization[138], different types of properties can be easily achieved[139,140].

1.2.2 Graphene: synthesis routes and challenges

Graphene, like most nanomaterials that derive from the carbon family, can be synthesised using two main strategies: a) top-down and b) bottom-up methodologies. The synthetic route and the reaction parameters are very important since it influences the final characteristics and properties of the graphene material. The material characteristics should correspond to a thickness closer to an atomic layer, two-dimensionally (2D) arranged, where the carbon atoms are sp^2 bonded. That is, each carbon atom in the 2D layer is in-plane bonded by three other carbon atoms, except for the edge of the layer where carbon atoms are bonded with just two carbon atoms and one hydrogen atom, stabilizing the material's edges, and preventing the existence of free carbon radical sites on the graphene surface.

Since 2004, the synthetic routes were developed to produce defect-free graphene using both top-down[141] and bottom-up[142] strategies, but the global production cost (per each gram of graphene) was too high for industrialization. On the other hand, the defects inserted on the graphene surface tailor material's properties sufficiently to make graphene suitable for a large spectrum of applications. For example, by manipulating the most common type of defects, the oxygen content, graphene can be transformed from conductor to semiconductor, from hydrophobic to hydrophilic, and from a dark coloured material to a brown coloured material. In addition, the lateral dimensions (length and width) of the graphene layer modify the properties of the material as well. A target-oriented strategy is frequently employed in the development of new synthetic pathways for the manufacture of graphene.

Top-down approaches

The direct three-dimensional correspondent of graphene is graphite. Graphite consists of sp^2 carbon layers of 0.335 nm, held together by van der Waals interactions. A van der Waals interaction is weak physical interaction (approximately 20 meV per carbon atom), but when it is applied to a 2D carbon layered structure, the global energy of these interactions is high.[143] The isolation of pristine graphene from graphite requires breaking the physical interactions between the layers and spatially separating the extracted layer to avoid possible natural self-assembly. The delamination of a single layer of graphene requires a precise physical method to selectively direct the delamination energy between the first and the second layer of the graphite crystal. Andre Geim and Konstantin Novoselov used this method for the first time in 2004 to isolate graphene and is termed as the "scotch-tape method" (mechanical exfoliation).

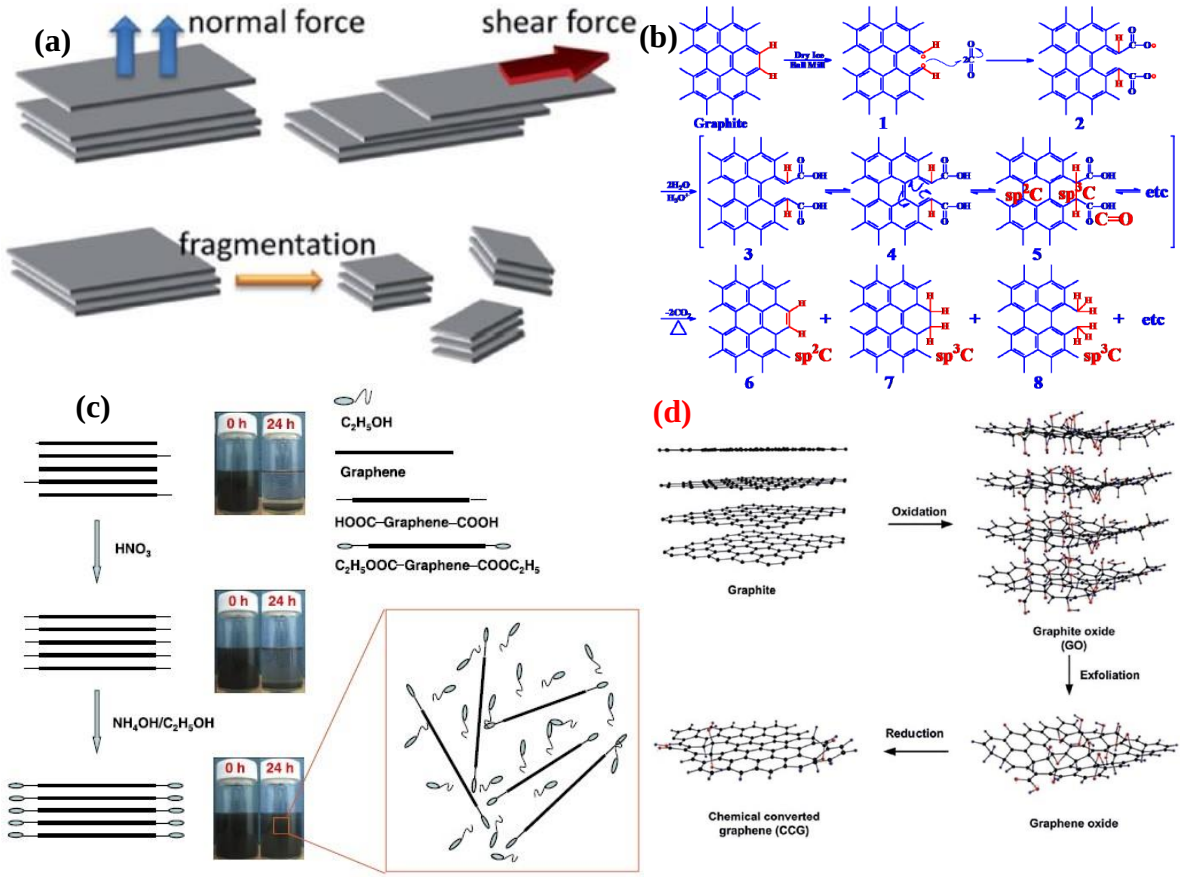

Figure 1.7: (a) The graphical representation of the main process behind the mechanical exfoliation of graphite crystal[144], (b) the reaction mechanism for graphene carboxylation process via dry ice ball milling[145], (c) the process schematic used by Nguyen et al. for wet physical-chemical delamination of graphite[146], and (d) the wet-chemical synthesis method of the reduced graphene oxide *via* Hummers method[147]. Reproduced with permission from references 144, 144, 146, and 147. Copyright 2015 Royal Society of Chemistry, 2012 Proceedings of National Academy of Sciences of the United States of America, 2011 IOP Publishing, and 2011 John Wiley & Sons.

Mechanical exfoliation

This type of method involves two main steps: a) creating a physical interaction/connection between the material/device (which provides the mechanical force) and the graphite crystal and b) applying the force necessary to peel the graphite layer by layer. The applied force can be a normal force or a shear force (see **Figure 1.7**). If the system applies a force higher than required on the graphite crystal, this will cause the crystal to break into small structures, a process known as fragmentation. This process is a side process and implies a decrease in size (length or width of the final isolated graphene sheets), and in some cases, is not desired (when the application requires the isolation of a large surface "one-piece" graphene

layers). Overall, by applying a purely physical process on graphite does not mean that side chemical processes will be avoided, for example oxidation or doping processes can occur.

For example, using a dried ball milling method, Mahmoud et al[148] succeeded to obtain S- and N-doped graphite oxide. Their method involves using a stainless steel or zirconia milling chamber and balls. The experiment was carried out under ambient conditions. The experiment was conducted in atmospheric conditions, rich in molecular oxygen and very rich in microorganisms (bacteria, fungus, viruses), providing the atoms of oxygen, sulfur, and nitrogen required to generate all these chemical side processes (oxidation and doping). Caicedo *et al.*[149] developed a similar ball milling method to produce graphene oxide but in a controlled environment ($KClO_4$ solution in H_2O), assuming the presence of a side chemical reaction during the process. They succeeded to prepare graphene oxide with a particle size distribution between 10 and 120 nm (majority of the particles between 20 and 40 nm) with a variety of oxygen functionalities on the surface. Jeon *et al.*[145] proposed a chemical mechanism for the side reactions during his ball milling experiment caused by CO_2 dry ice (see **Figure 1.7 b**). To avoid oxidation in his ball milling process, Palei *et al.*[150] used a hydrogen atmosphere obtaining low oxygen content reduced graphene oxide (r-GO).

Wet physical and/or chemical exfoliation and delamination of graphite

The exfoliation of graphite to improve the material's overall properties began long before the discovery of graphene. The idea of an unstable 2D related carbon allotrope does not motivate the researchers to look deeper into their processes[151–153]. In 2004 Viculis *et al.*[154] reported graphite exfoliation via potassium intercalation (producing KC_8 phase) followed by water or ethanol exfoliation and extraction of potassium atoms between the graphene layers, thereby increasing the distance between the layers. At that time, the authors referred to this material as graphite nanoplatelets, however they produced graphene. The reaction between KC_8 and water (or other different polar solvents) was later described as a direct method to produce thin graphene layers[155–157]. Potassium graphite (KC_8), which is intensively used as a reducing agent or catalyst in organic chemical processes[158,159], was for the first time synthesized by Fredenhagen and Cadenbach[160] in 1926, and in 1965 G. R. Hennig[161] reported his observation about KC_8 charge transfer between potassium and graphite layers, describing the carbon phase as being negatively charged. Graphene was always there, waiting to be discovered, and for sure, it can be assumed that during different chemical processes, since 1926, graphene sheets have been produced, but no one reported their presence or properties until 2004.

The intercalation of metals[162], metal ions[163], anions[164], organic[165] or inorganic[166] molecules between the graphite layers, followed by a physical process such as microwave irradiation, sonication, heating, or electrical current, have been studied, primarily to achieve graphene precursor delamination/exfoliation. This type of process is on the border between being a chemical or a physical process because these intercalating agents interact with the graphite particle, disperse between the layers, and frequently convert the precursors into new chemical species or form chemical bonds with the graphene layers during exfoliation and/or delamination. All these side chemical reactions are insignificant when compared to the vast majority of chemically unaffected physically delaminated graphene sheets. The majority of these processes are carried out in an aqueous environment (a solvent) where the intercalation compounds are soluble and the graphite particles are dispersed. The small intercalating compounds diffuse between the graphite layers over time, saturating the particles; at this point, the stability of the as-created hybrid graphite particle decreases, and the graphene sheet is separated from the main graphite crystal by fine-tuning the process's physical parameters.

Nguyen *et al.*[146] succeeded to delaminate the graphite by applying a smart chemical-physical method. Their process is divided into three main steps (see **Figure 1.7 c**): 1) graphite crystals expansion through intercalation of sulfuric acid molecules between the layers, followed by a short time exposure (10 s) at 1000 °C where the van der Waals interactions between the layers are broken by energetically vaporising the sulfuric acid molecules. 2) oxidation and esterification of the edges of the expanded graphite layers. The oxidation was done by boiling the material in concentrated nitric acid solution at 80 °C for 36 h, and this process facilitates the oxidation of the edge carbon atoms of graphite to a carboxylic group. The carboxylic edge decorated graphite layers were immersed in ammonia in ethanol solution for three hours, enough time to esterify most of the carboxylic groups, creating micelle-like edges. 3) delamination and isolation of graphene layers via ultrasonication, gravitational decanting of the undelaminated sheets, and separation of the supernatant containing the thin layers of graphene. The thickness of the as-obtained material was found in the range of 2.2 to 3.2 nm, corresponding to less than ten graphene layers. The advantages of this process are the low oxygen content of the final material, the energy required, and the process complexity to reduce the oxygen functionalities are lower than when starting from graphene oxide precursor.

Hummers method is one of the most widely used pure chemical top-down methods for graphene synthesis. This method is divided into two main steps: 1) oxidation of graphite to graphene oxide and 2) reduction of graphene oxide. An intermediate material: graphene oxide,

is generated between the processes. Surprisingly, graphene oxide is a long-known material that has been given various names over the years. The first time was prepared in 1859 by Benjamin Collins Brodie[167] in his laboratory at the University of Oxford when he treated Ceylon graphite in an oxidative mixture of fuming nitric acid and potassium perchlorate. Brodie named his new 'compound' graphitic acid. Later, the name was changed to graphite oxide, and in 1911 Arsem[168] published his work in converting different forms of carbon into graphite, suggesting the graphite is the last pure carbon phase transformation, providing enough fuel to the graphite research field to continue. The work started by Brodie's work was carried on generation after generation until William S. Hummers, Jr., and Richard E. Offeman (1958) published their famous one-page paper[169] where they reported a synthetic method able to fully convert the graphite into graphite oxide.

In 1898, prior to Hummers' development, Staudenmaier[170] optimized the Brodie method. The disadvantages of the method were the strong oxidative environment (potassium perchlorate in concentrated sulfuric and nitric acids), and the high risks posed by the long reaction time (more than 288 hours). Essentially, Hummers and Offeman, modified the method sufficiently to be considered a significant improvement of the previous version. The mixture of concentrated sulfuric acid and fuming nitric acid was replaced with a mixture of concentrated sulfuric acid and sodium nitrate (generating in-situ nitric acid, avoiding possible injuries from handling high volumes of fuming nitric acid). The graphite was immersed in the mixture (Staudenmaier added the graphite at the end after preparing the oxidative reaction environment), allowing the sulfuric acid molecules to diffuse between the graphite layer and to expand the distance between them. The oxidative agent (potassium permanganate) is then added in small amounts to avoid overheating the reaction environment. The synthetic process takes about 2 hours. It is important to notice that the oxidation process generates irreversible defects (holes or edges erosion) in the graphene structure, which can affect the final quality of the material.

A solvent and a reducing agent are used in the wet chemical reduction of graphene oxide (see the schematic in Figure 1.7d). The main purpose of the second step is to clean the graphene oxide surface from the oxygen functionalities; however, this process is unable to reduce/ remove other defects introduced in the first step. Furthermore, due to the nature of the reducing agent, side reactions such as heteroatom doping of the structure are possible.[171–173] To avoid undesired doping, the use of reducing agent/s unable to bound on the surface such as organic

compounds made of carbon, oxygen, and hydrogen[174], metals[175,176], nascent hydrogen[177] or different inorganic reducing agents[178,179] must be used.

The most common wet chemical reduction method employs hydrazine as an effective reducing agent. This method is associated with the nitrogen doping of the final product[180], which is desirable in applications requiring Lewis basic active sites. In the other case, the use of alkali hydride[181] as a reducing agent provides a doped-free process (the final material only loses oxygen functionalities and gains no structural doping atoms or functionalities from the reducing agent).

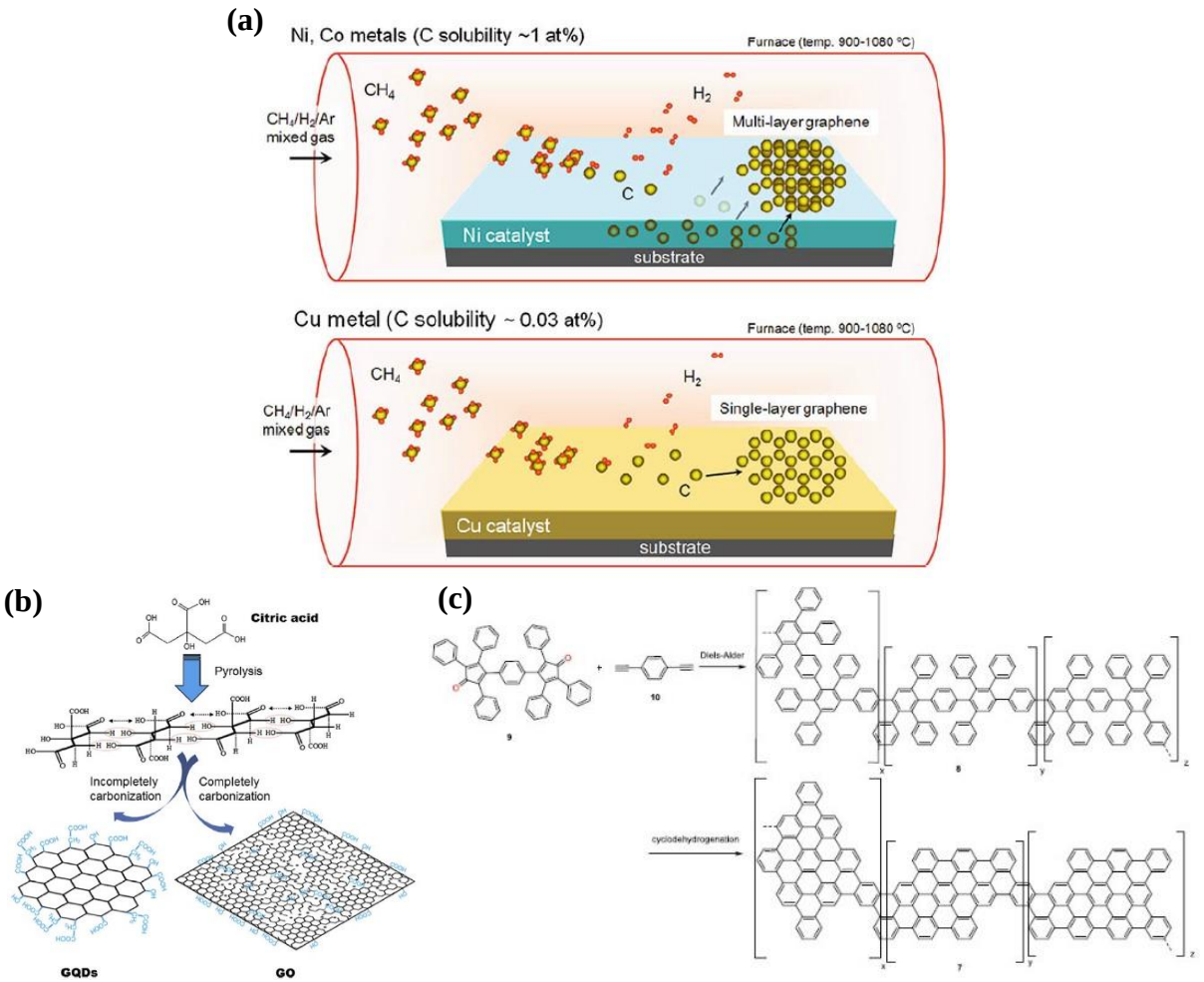

Figure 1.8: (a) CVD process differences between nickel and copper template-assisted graphene synthesis[182], (b) graphene quantum dots and graphene oxide synthesis via controlling the carbonization degree of citric acid[93], and (c) the two steps synthesis of graphene nanoribbons[183]. Reproduced with permission from references 93, 182, and 183. Copyright 2015 Springer Nature, 2012 Elsevier, and 2019 IOP Publishing.

Bottom-up method

This type of method requires small molecules or smaller macrostructures to create the sp^2 atomic thin carbon layers. It requires control over the process parameters in order to avoid the assembly of the as-generated sheets (via van der Waals interactions) into graphite. The nature of the precursor may broaden or narrow the options for obtaining the material via multiple synthetic routes. For example, when comparing methane with glucose, methane can only be used as a carbon source in graphene synthesis via a chemical vapour deposition approach, whereas glucose can be used in a variety of synthetic strategies, ranging from heat treatment under an inert atmosphere to hydrothermal/solvothermal methods. In the case of synthetic methods that use graphite as a graphene source, the amount of produced material is ± equivalent to the mass of the starting material; however, this is not the case for bottom-up methodologies. Due to a large number of possible transformations of a small carbon-based molecule transforming into the desired 2D material architecture, controlling and directing billions of molecules (containing millions of billions of carbon atoms) to assembly into a specific sp^2 bounded atomic thin carbon layer, it is not always easy.

The bottom-up synthetic strategies can be divided into two main categories: template assisted and without template.

Template assisted synthesis of graphene

In this approach, the surface of a particular material is used as a template in the graphene synthesis. Copper is the most widely used template, and chemical vapour deposition (CVD) is the most commonly used method for producing high-quality large surface area single-layer graphene. The CVD method based on copper foil was developed by Li and Rouff[184] in 2009 as an update to the previous methods: SiC template on thermal decomposition of SiC[185], or nickel assisted CVD[186]. Compared to the previously developed methods, Cu-assisted CVD generates ultrathin graphene (single layer), no substrate boundaries, and large flakes of defect-free graphene sheets. The method is one of the most quality efficient because of the high quality of as-made material, but it comes at a cost because it cannot generate large quantities of graphene[187–190]. The traditional CVD involves a flow of methane and hydrogen over a heated copper foil (1000˚C) under an inert atmosphere or vacuum. The low affinity of copper for carbon (to dissolve it at high temperature or to create carbide bounds) makes it one of the best candidates for this method. Metals such as iron, nickel, cobalt tend to interact with the carbon phase at a high temperature during the process, generating undesired defects or carbide phase

(see **Figure 1.8 a**), which can remain in the material as impurity after the metallic etching.[191] Different types of molecules such as ethene, propene, 1-pentene, 1-hexene[192], acetylene[193], hexabromobenzene[194], pyrene[195], or exotic molecule such as 10,10'-dibromo-2,2'-diphenyl-9,9'- bianthracene[196] have been successfully tested for CVD synthesis of graphene on a variety of substrates.

In 2014 Zang *et al.*[197] developed an innovative hybrid template-assisted method. Instead of using metal foils, they used ferric chloride dissolved in water together with glucose to obtain a homogeneous graphene layer. The as-prepared solid was then heated at 700 °C in argon for 6 hours. The hydrochloric acid solution was then used to dissolve the iron compounds in the solid to obtain pure graphene. Since then, this approach has been used to successfully evaluate a variety of biomass-related organic molecules[198].

No template bottom-up graphene synthesis

Synthesizing graphene from small organic molecules is a significant challenge that necessitates extensive synthetic knowledge as well as a well-planned and controlled process. It involves a molecular decomposition and a random combination of carbon atoms into a 2D form, defect-free graphene synthesis has never been achieved by changing basic process parameters (such as temperature, strain, and precursor concentrations).

Dong *et al.*[93] reported the synthesis of graphene oxide by tunning the carbonization degree of citric acid. They claimed to have synthesized graphene quantum dots and graphene oxide by exposing pure citric acid to heat (200 °C) under atmospheric pressure (see **Figure 1.8 b**). Although the bottom-up hydrothermal/solvothermal synthesis of graphene or graphene oxide was never achieved, multiple studies have reported the synthesis of graphene quantum dots[199]. The limitation of bottom-up wet-chemical no-template solvent assisted synthesis (BUWCNTSAS) of graphene can be explained by the three-dimensional growing option available for a sp^3 carbon atom and two-dimensional growing option available for a sp^2 carbon atom. A combination of sp^2 and sp^3 hybridized carbon atoms or even growing above or below the 2D plane of sp^2 hybridized carbon atoms will stop the graphene growing process and will direct the material to carbonaceous material like carbon dots or hydrothermal carbon (HTC)[200].

The rational synthesis was only achieved for graphene nanoribbons, when using a bi-halogen substituted polynuclear aromatic compound or substituted polynuclear aromatic compound capable of undergoing Diels-Alder reaction, which were polymerized and cyclodehydrogenated at high temperatures[183,201,202]. The polymerisation step can be carried out

without the use of a catalyst (see **Figure 1.8 c**), while the cyclodehydrogenation is conducted in the presence of ferric chloride[203]. To achieve the synthesis of nanographene from this type of molecule, gold (111) (as template) is required during the polymerisation and cyclodehydrogenation reactions to spatially assist and direct the 2D growing process[204].

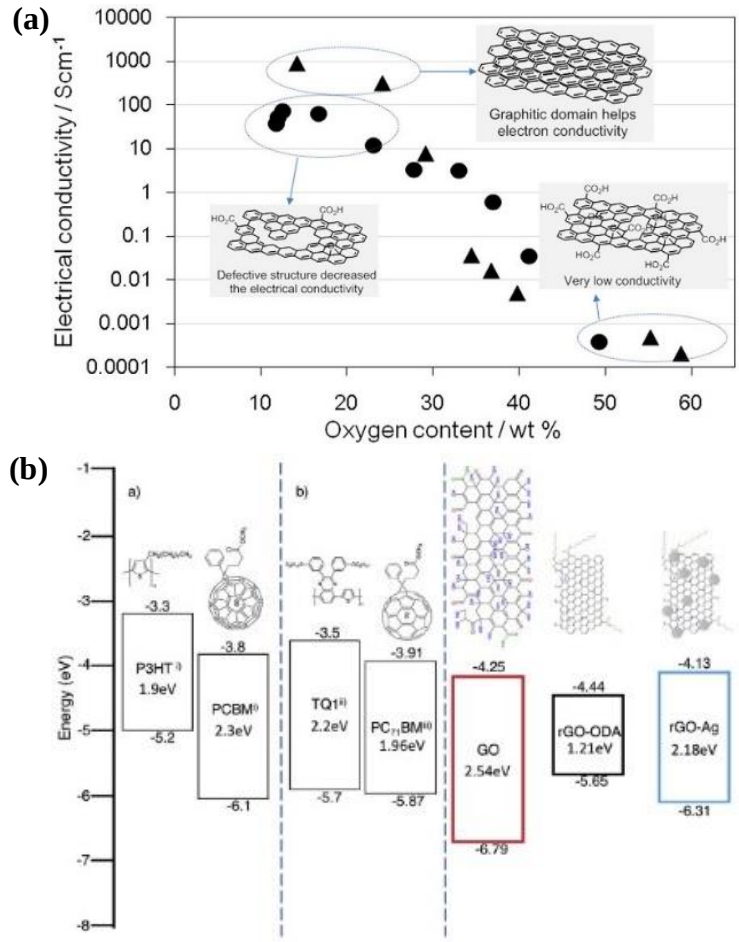

Figure 1.9: (a) Oxygen content versus the electrical conductivity in single layer graphene[205], and (b) HOMO-LUMO energy levels and bandgap diagram of GO and rGO[206]. Reproduced with permission from references 205 and 206. Copyright 2016 Springer Nature and 2019 Elsevier.

1.2.3 Graphene Properties

Being constructed of a 2D network of sp^2 bonded carbon atoms, the properties of graphene can be easily tailored to fit a variety of applications. It was termed as the "amazing" or "miracle" material, not only for its pristine properties but also for its ability to adjust its properties through small changes in its structural and morphological characteristics. The introduced modifications to pristine graphene will generate new properties or will modify the

existing ones, thus when discussing graphene properties, it is important to consider the composition, size, thickness, and morphology.

The first-ever measured properties of graphene were the electronic properties (electric field effect: the modulation of the electrical conductivity of a material by applying an external electric field), which demonstrated the enormous application potential. Geim and Novoselov discovered that graphene exhibits unprecedented metallic-like conductivity and electron mobility even at room temperature, and their experimental data agreed with Dirac equation predictions. Following this, the remaining physical and chemical properties were also measured.

The term ‘graphene' refers to a class of materials that share some properties. The main or starting point of graphene is known as pristine graphene, and it is composed of a single or few layers of sp^2 bound carbon atoms with a very small amount of hydrogen atoms bound on the sheet's edges.

The electronic properties of the material change as the number of layers increases, and the material is referred to as multi-layered graphene; after a certain number of layers, it transforms into graphite flakes, which are semiconductors. When the size of the layer is reduced to less than 10 nm, the optical and electronic properties change, the material gains fluorescence and is known as graphene quantum dots, and if the size is reduced further, the graphene quantum dots will be transformed into organic polynuclear aromatic molecules. The extraction of carbon atoms from the graphene layer will also affect its electronic and mechanical properties. Cutting the sheet into strips produces graphene nanoribbons, and intra-cyclodehydrogenating the parallel edge of graphene produces carbon nanotubes with graphene properties.

The chemical composition of graphene can vary from two elements (carbon and hydrogen) to multi-elemental[207–209]. Most commonly, the graphene 2D network is doped with heteroatoms such as nitrogen atoms, resulting in a material with new properties such as basic active sites, improved light absorption, and improved solubility in polar solvents[210]. This type of doping occurs in network defects (missing carbon atoms from the 2D network), rather than through carbon atoms substitution and, in the same way, it repairs the structural defects in the 2D network, improving its mechanical and electronic properties[211,212].

The presence of oxygen and its functional groups on the graphene surface is not regarded as doping. While other dopants such as nitrogen, sulfur, phosphorous, boron, etc.

improve certain properties[213], oxygen is one of the most undesirable element in graphene. Morimoto et al[205] demonstrated that the lower the oxygen content of single-layer graphene, the higher the electrical conductivity (see **Figure 1.9 a**). Mendez-Romero et al[206] demonstrated bandgap tailoring behaviour using oxygen content and compared the values with different polymers (see **Figure 1.9b**).

Solubility of graphene or the degree of dispersion in different solvents is an essential characteristic; in many cases, this property means easy access to applications where the homogeneous transfer of the material to a surface or an environment is mandatory. Regarding solubility, pristine graphene is considered a nonpolar material that is difficult to disperse in a polar solvent such as water and alcohols[210]. By adding oxygen functionalities to the surface, solubility can be increased, and by controlling the type of oxygen functional group, solubility can be made selective for a specific solvent or a mixture of solvents[214,215].

The mechanical properties of pristine (single layer of a few layers thickness) such as Young modulus and intrinsic strength are superior to strong materials (stainless steel or titanium) because of their much lower density, flexibility, and malleability, able to cover any shape[216,217]. Therefore, each structural defect will negatively affect the mechanical properties, making the material more fragile.

1.2.4 Graphene in membrane technology for water treatment applications

Since 2004 graphene has been tested and used in various applications, including research, industrial, and everyday devices. Graphene, with its excellent mechanical, physical, and chemical properties and ease of functionalisation, modification, or combination with diverse materials, has the potential to replace traditional materials in applications or devices, solving economic, performance, or environmental issues[218–221].

Because of its stability and chemical composition, graphene has been classified as a biocompatible material, allowing it to be used in biological systems. Graphene materials have been tested in a variety of biological, biomedical, and bio-tagging applications[133,222–225]. Also, graphene materials have been classified as environmentally friendly materials, making them an ideal candidate for environmental-related applications such as water treatment and desalination, photocatalysis, photothermal conversion, CO_2 adsorption and conversion, and gas separation[226–228].

By generating/creating holes within the network, single layer or few-layer graphene can be used to prepare membranes for water treatment. The layer will act as a barrier for all ions,

molecules, or particles larger than the hole/pore diameter. To create nanoporous graphene layers, high precision or an elaborated template method is required, which is difficult to achieve, as it requires a high amount of energy and time and is not competitive with zeolite technologies. The hydrophobicity of pure graphene influences the efficiency of the nanofiltration process, and it can favour the adsorption of nonpolar pollutants on the membrane surface, preventing water molecules from passing through the membrane pores.

The functionalized graphene sheets are a promising option as membrane materials, and by layering in a multi-layered configuration, nano-channels can be created between the graphene layers, allowing water molecules to flow. The reduced graphene oxide is the simplest type of functionalized graphene because it contains a low amount of oxygen functionalities. It can be supposed that when the r-GO sheets are assembled into a thicker bed-like film, the distance between the layers is smaller (the nanochannels) than graphene oxide due to the absence of larger volume carboxyl or carboxylate functional groups.

Currently, graphene membrane technologies for water treatment face numerous challenges, and there is no commercially feasible graphene membrane on the market.

1.2.5 Conclusions

Graphene, a single two-dimensional layer of sp^2 bonded carbon atoms, was isolated for the first time in 2004 and has demonstrated enormous potential due to its unprecedented properties. Since its isolation (via a mechanical exfoliation using a scotch tape-based method), many production methodologies have been established. The scientific community has recognised the significance of graphene, and the researchers who isolated the material were awarded the Nobel Prize in Physics in 2010. Exhibiting a diverse range of properties, a large and diverse number of applications were developed, and new and exciting properties of these materials have been observed.

Graphene is still considered a hot research topic today, with thousands of scientific articles, patents, or newspaper articles being published each year. Large-scale production of high-quality graphene materials remains a significant challenge in the field, with new synthetic routes to be explored and old ones to be optimized. Applying graphene in environmental applications can help to reduce the negative impact of human activities on the environment and repair the damage that has already been done to it.

1.3 Carbonaceous nanocomposites of TiO_2 with graphene and carbon quantum dots

I.3.1 Introduction

TiO_2 materials are well known for their superior photocatalytic properties, long-term stability, and low production costs, making them one of the photocatalytic materials with the most reliable perspectives for industrial utilization. To demonstrate photocatalytic activity, the pure TiO_2 phase interacts with UV light resulting in a photoinduced redox reaction on the active sites located on the surface of the material.

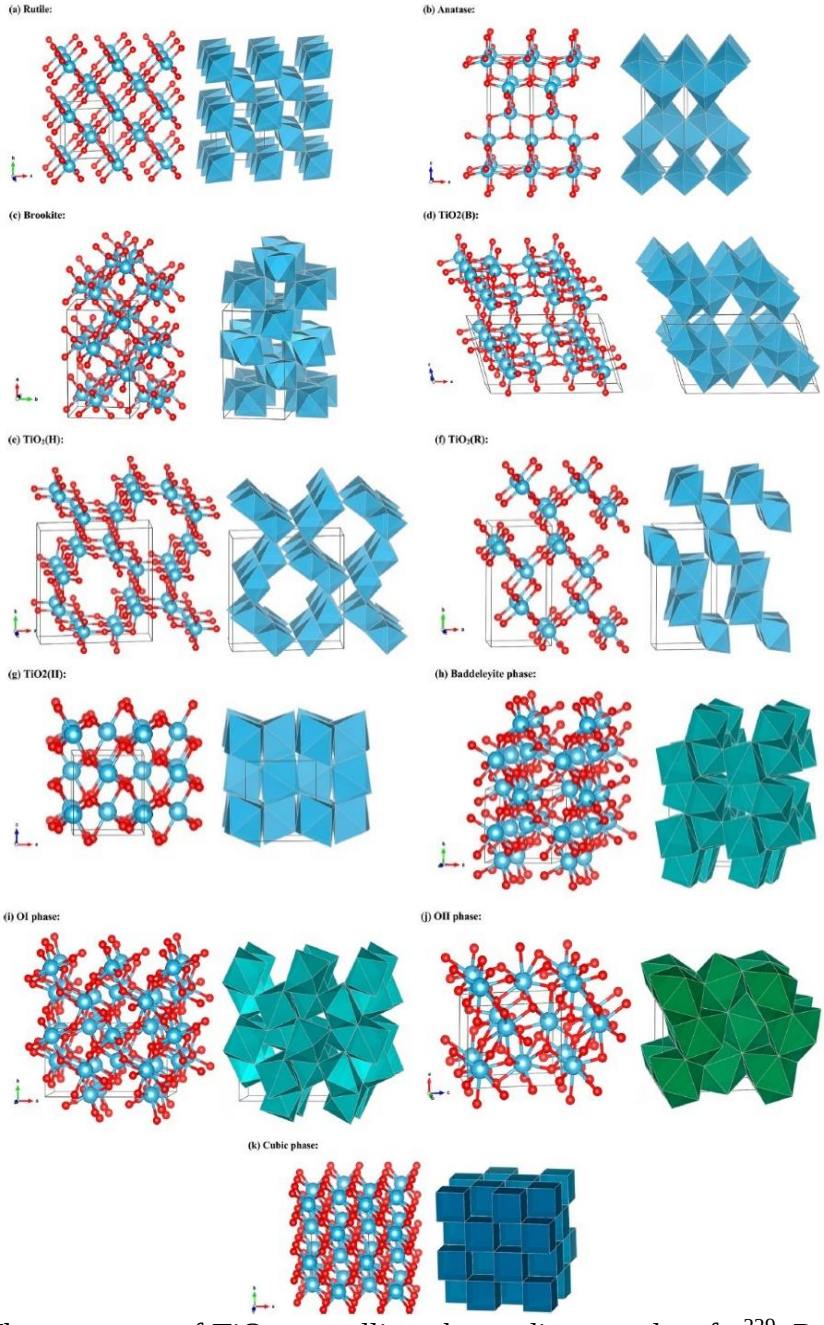

Figure 1.10: The structures of TiO_2 crystalline phases discovered so far[229]. Reproduced with permission from reference 229. Copyright 2014 American Chemical Society.

In nature, titanium dioxide coexists in three crystalline forms: anatase, rutile, and brookite. The material is known from ancient times, and the rutile form has been used as a white pigment, later know as Pigment White 6. Synthetic TiO_2 was first reported in the early twentieth century by dissolving the natural TiO_2 minerals into concentrated sulfuric acid and then recrystallizing the material in smaller crystals suitable for pigment use. Later, TiO_2 was classified as a nontoxic chemical compound, and it was introduced into the food and cosmetic industries. Nowadays, more than eight new synthetic crystalline forms have been reported and characterized (see **Figure 1.10**)[229]. The study of photocatalytic properties of TiO_2 began in the early 1900s in Germany when Eibner[230] observed colour loss in paints (containing TiO_2 and various dyes) when exposed to light. However, it was not until 1956 when Shin-ichi Kato and Fujio Mashio reported in The Annual Meeting of Chemical Society of Japan the photocatalytic activity of TiO_2 by dispersion in different alcohols, which they later published[231].

The photocatalytic activity of TiO_2 is determined by the bandgap, which varies depending on the crystalline form. The bandgap restricts TiO_2 (rutile or anatase) to absorb UV light only, and in order to enhance the material's light absorbance capability, a doping process or a co-catalyst is required[232]. Carbonaceous materials such as reduced graphene oxide and carbon quantum dots can be used to address the TiO_2 issue because they are chemically and physically stable, as well as capable of accepting and transporting electrons. Carbon quantum dots are well known for their ability to interact with the entire domain of sunlight; they can absorb UV, visible, or IR light, implying that the material can generate excited state electrons across the spectrum[233]. Electrons from photoexcited CQDs can be transferred to TiO_2 and used in the redox photocatalytic process.

On the other hand, reduced graphene oxide can transfer electrons between the photocatalyst particles due to its superior properties in electrons conductivity and charge mobility. In the absence of a direct photoactive phase interface, a photocatalytic system containing reduced graphene oxide can (a) exhibit charge transfer, (b) charge separation, and (c) reduce the recombination processes, with r-GO acting as an electron-transfer platform between isolated materials particles. Possessing a large surface area, reduced graphene oxide can act as a solid dispersion environment for TiO_2 particles, providing access to light to more particles and increasing the number of light-harvesting photoactive sites. It can also improve the adsorptive properties of the system, providing a better flux of molecules to the photocatalytic active phase[234,235].

1.3.2 TiO_2-CQDs/Graphene nanocomposites: synthesis and properties

In comparison to a single-phase carbonaceous nanomaterial, a carbonaceous multicomponent nanomaterial (carbonaceous nanocomposite) requires additional steps or more complicated synthetic procedures. The exception is one-pot synthesis, in which all phases are formed and mixed during a single chemical or physical process, but most nanocomposites are made via multi-step synthetic routes, and then mixed all together in the final step of the synthetic protocol. When it comes to nanocomposite materials, some of the reaction parameters of one component can alter the properties of the others, which is why a one-pot synthetic process can be difficult to establish[236].

The TiO_2 anatase has been extensively tested for photocatalytic applications due to its mild synthesis conditions and 3.2 eV bandgap, whereas the rutile with a smaller bandgap (3 eV) requires a more energy-consuming synthetic process. The anatase is more active due to (a) its surface chemistry (exhibiting efficiency in adsorbing molecules on its surface) and (b) the valence and conduction bands position on the energy band diagram. The conduction band minimum (CBM) of anatase is lower than the rutile one, the anatase indirect band gap is smaller than its direct bandgap, whereas, for rutile, they are similar (a smaller indirect bandgap means longer charge carrier lifetimes)[237,238].

In contrast to conventional methods (such as sol-gel or precipitation), which require a heat-treatment step, the TiO_2 anatase can be generated directly using a hydrothermal process. The hydrothermal method has the advantage of allowing the material to be doped in situ[239]. Most of the mild condition synthetic processes generate anatase. The anatase can be transformed in rutile via phase transition by heat treatment at a temperature higher than 400 °C, depending on particle size, shape, surface area, sample volume, heating atmosphere, heating rate[240]. The hydrothermal method can be done via heat or microwave-assisted process, and the advantages comparing with other methods are the homogenous quality of TiO_2 with small particle size and high surface area, and method reproducibility[241,242].

The continuous flow hydrothermal synthesis of TiO_2 anatase was reported in 2006 by Kellici[243] followed by Zhang *et al.*[244] in 2009, and a few months later, Kawasaki *et al.*[245] reported a new efficient CHFS method (TiO_2 anatase made in alkali media), but they utilized a very complicated CHFS setup. The limitations of the traditional hydrothermal method have

been overcome by developing continuous hydrothermal flow synthesis methods to produce TiO_2, and the process has become economically suitable for industrialization.

The first TiO_2-graphene nanocomposite was prepared in 2008 by William *et al.*[246] via TiO_2 anatase photocatalytic reduction of graphene oxide. Essentially, the method was developed to demonstrate the efficiency of TiO_2 as a photocatalyst in the reduction of graphene oxide as an alternative to hydrazine reduction. The charge transfer between the photocatalyst and reduced graphene oxide was also shown in this study. One year later, Akhavan and Ghaderi[247] continued the photoreduction study but tested the nanocomposite for antibacterial properties. Manga *et al.*[248] prepared a multi-layered TiO_2-graphene hybrid and measured the charge transfer and photoconversion properties, noting that the degree of graphene oxide reduction affects performance (higher reduction, better performance), and Lambert *et al.*[249] investigated different methods for TiO_2-graphene in-situ reduction of graphene oxide, measuring the surface area and its stability as a colloidal solution in water and alcohols at different pH values.

Zhan *et al.*[250], applying a hydrothermal method, succeeded to reduce graphene oxide and mixing it with commercial P25 (or Degussa, which is a mixture of TiO_2 anatase and rutile crystallites, with a ratio of 70:30 or 80:20). The nanocomposite showed high photocatalytic performance for methylene blue photodegradation, and they observed the formation of a Ti-O-C bond which revealed the formation of chemically attached TiO_2 particles on the graphene oxide sheets during the hydrothermal process, creating an interface between the nanocomposite phases. The photocatalytic performances were assigned to extended light absorption in the visible domain, better physical adsorption of the methylene blue on the nanocomposite surface, and efficient charge separation and transport. All these enhanced properties of the nanocomposite were attributed to reduced graphene oxide.

Zhu *et al.*[251], for the first time, succeeded to prepare TiO_2-graphene nanocomposites using a one-pot approach starting from graphene oxide and $TiCl_3$ (which acts as TiO_2 precursor and reducing agent for graphene oxide). Sharavath *et al.*[252], using a one-pot hydrothermal method prepared a high-quality TiO_2- nitrogen-doped graphene nanocomposite starting from titanium(IV)-bis-(ammonium-lactato) dihydroxide, graphene oxide, and urea (nitrogen source).

The continuous solvothermal flow synthesis of TiO_2-graphene nanocomposites was reported by Leng *et al.*[253] in 2015 using a counter-flow continuous solvothermal flow reactor

made of two feeds, one of graphene dispersed in ethanol/water and a second one containing titanium isopropoxide solution in ethanol. The graphene feed has been preheated at 350°C and mixed in the counter-flow reactor with the titanium isopropoxide solution. The water from the graphene feed reacted with the titanium precursor and in-situ generated nano-TiO_2, generating a homogenous phase nanocomposite. Different TiO_2:graphene compositions were synthesized and characterized during the study. In the methylene orange photodegradation, titanium dioxide - graphene nanocomposites outperformed pristine TiO_2 and commercial P25 (Degussa).

In 2010 Li *et al.*[26] reported for the first time the synthesis of TiO_2-CQDs nanocomposites, using a two-step process: 1) synthesis of CQDs from graphite via an alkali electrochemical method and 2) the sol-gel preparation of TiO_2-CQDs composite. The material showed good photocatalytic activities on methylene blue photodegradation. This behaviour was attributed to the ability of the CQDs to absorb visible light, and the fact that they are attached to the TiO_2 surface facilitates the formation of electron/hole pairs in metal oxide via electron transfer between the phases, and these pairs then react with the dye molecules absorbed on the surface. Sun *et al.*[254] used a similar method, and their study confirmed the previous observations.

Zhang *et al.*[27] accomplished the synthesis of a nanocomposite from premade nitrogen-doped CQDs and $TiCl_3$ using a hydrothermal approach. They observed a decrease in nitrogen functionalities during the hydrothermal process, as well as a decrease in photocatalytic activity. The electron transfer from excited state CQDs to TiO_2 explains the photocatalytic activity enhancement when compared to pristine titania, and the presence of nitrogen dopants makes the electron transfer more thermodynamically favourable by lowering the work function in NCQDs.

Sharma *et al.* [255] reported a batch hydrothermal method for producing TiO_2-CQDs from titanium isopropoxide and ascorbic acid in a single step. CQDs were found to be homogeneously attached to TiO_2 material, with no isolated CQDs particle found, demonstrating the stability of interface formed between TiO_2 and CQDs. Ti-O-C bond was reported indicating that some CQDs are chemically attached to the TiO_2 particles, which is similar to the observation made for TiO_2-graphene nanocomposites. The photoluminescence spectrum of the nanocomposite was less intense than that of CQDs and TiO_2 pure phase, confirming the electron transfer processes between the components and fewer electron-holes ground state recombination.

To my knowledge, TiO_2-CQDs-Graphene nanocomposites have not been reported, and no continuous hydrothermal flow synthesis method has been reported for the aforementioned hybrid structures.

1.3.3 Applications

TiO_2 is known as one of the most intensively investigated photocatalysts due to its chemical and physical stability. It has been classified as not harmful material to the life system or the environment. The same classification has been made for graphene materials and carbon quantum dots. Combining the high surface area, adjustable surface chemistry, and electronic properties of graphene, visible bandgap, rich and diverse surface chemistry, and tailoring optical properties of carbon quantum dots and ultraviolet light absorption capability of TiO_2 materials, it will generate a nanocomposite able to fit in various application from bio-application to energy production and storage.

The main applications of these nanocomposites can be divided into three main categories: a) environmental-related applications that involve photocatalytic properties of the material and b) energy-related applications such as solar cells and energy storage which involve the property to absorb UV and visible light, and c) bio-related or medical-related applications which involve the biocompatible properties of the nanocomposites.

The photocatalytic application of these nanocomposites includes photodegradation of different organic molecules and inorganic species[236,256–258], hydrogen evolution reaction[259–261], solid membranes for in-flow or stable dispersion for static water and/or wastewater treatment processes[262,263]. In all the studies, the photocatalytic properties of the nanocomposite are superior to the single-phase material (TiO_2, graphene, or CQDs), proving the consistency of the material characteristic.

The energy-related applications include photothermal conversion[264–266], solar cells[27,267,268], batteries[269,270], supercapacitors[271,272] and are based on the nanocomposite's electronic and morphological properties.

The bio-applications and/or medical-related applications such as antibacterial effect[273,274] or chemical sensing[275–277] involve the surface chemistry and electronic properties of the material, but some applications such as enhancing the interfacial bonding in biomaterials[278] are based on the mechanical properties of the nanocomposites.

1.3.4 Conclusions

TiO_2 is one of the most studied metal oxides due to its properties, but more specifically for its UV band gap, which makes it photocatalytic active. Preparing a TiO_2 carbonaceous nanocomposite may be a way to extend its light absorption capabilities to visible or near-infrared domains, while maintaining the biocompatible characteristics.

The superior physical properties of graphene and carbon quantum dots, as well as their high chemical stability, make them ideal candidates for this type of nanocomposite. A variety of synthetic methods are reported and different TiO_2-CQDs and TiO_2-graphene have been prepared. When compared to the individual material, the hybrid demonstrated improved properties in a specific application.

To conclude, new synthetic methods for materials production are still required in order to achieve homogenous quality in high quantities; continuous hydrothermal flow synthesis is a unique alternative to traditional methods.

1.4 Continuous hydrothermal flow synthesis method

1.4.1 Introduction

In the 1970s, the scientific race to make smaller particles, known as nanomaterials (10^{-9} m), prompted the need for new synthetic approaches for materials processing. As the climate change-related phenomenon became a reality on Earth, nanomaterials were seen as part of the solution by using fewer materials and achieving optimised results in various fields of application, interest in the research field grew.

The batch hydrothermal method uses above boiling point and below or near critical point (temperature and pressure) water, and it has demonstrated the ability to produce good quality nanomaterials over time, but it has limitation in real-time control of the reaction evolution over time (the product's quality and quantity are normally evaluated at the end of the process), and the reaction volume is limited at a maximum of 75 % of the reaction vessel volume. Overall, a batch hydrothermal method can produce limited quantities of high-quality nanomaterials while consuming moderate to high amounts of energy and time. By raising the temperature and the pressure above the critical point of water and changing the reactor design from batch to a continuous flow, the time and energy consumption will be reduced while the amount of nanomaterial produced per unit of time will increase exponentially. Water above its critical temperature (374.2 °C) and pressure (22.1 MPa) is referred to as supercritical water. When it is exposed to pressures and temperatures above the critical point, the properties of water change.

The pH, dielectric constant, and polarity of water can be adjusted by tailoring the critical parameters. **Figure 1.11a-b** shows that the density of supercritical water decreases with the temperature at constant pressure, whereas varying the pressure while keeping the temperature constant increases the density. By considering the water density as a result of various types of physical interactions between H_2O molecules, it is possible to conclude that changing the temperature and pressure of the system will affect other properties of water in the same direction (see **Figure 1.11c**). As a result of modifying these water properties, insoluble organic molecules (under normal conditions) become miscible or highly soluble under a supercritical environment. Following the properties and characteristics of supercritical water, when it is used in a reaction environment, it facilitates chemical reaction such as inter- or intramolecular condensations and dehydrations, hydrolysis, decomposition, or redox[279]. At high temperatures or/and pressures, supercritical water becomes highly corrosive and a hazardous element for the

reactor itself, and because most reactors are made of stainless steel, the temperature and pressure variations/combinations must be kept within the safety range. However, there remains a large number of various possibilities to do to achieve the optimal conditions and the process to be considered efficient[280,281]. The synthesis of nanomaterials with supercritical water was initially carried out in batch-type reactors, but the continuous flow method has proven superior in terms of material quality, quantity, energy, and time consumption[282].

One such method has been developed, and it is known as continuous hydrothermal flow synthesis. It is a unique method that employs supercritical water as both a solvent and a reagent (in some specific synthetic processes). Industrial chemical processes and industrial chemical plants were developed using a supercritical water continuous flow reactor, demonstrating the real-world potential and applicability of this unconventional synthetic method[6].

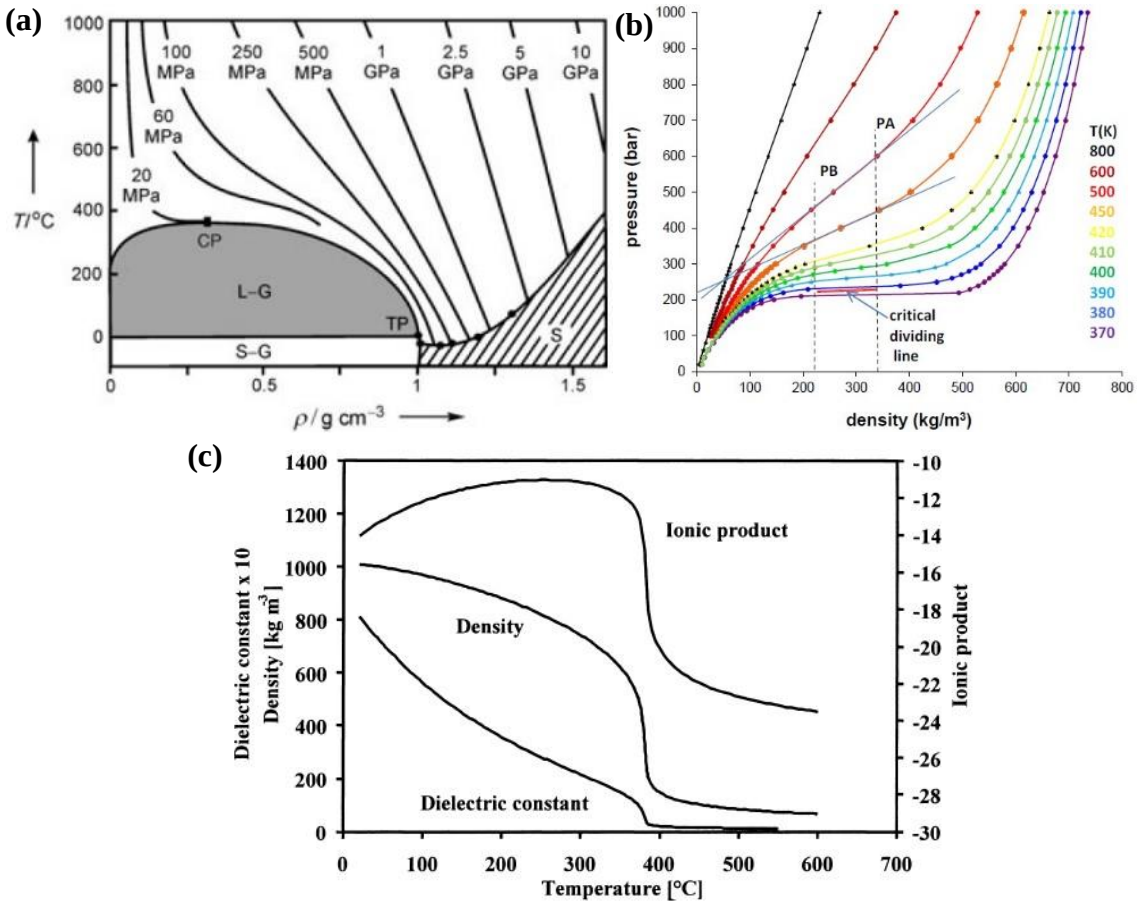

Figure 1.11: Supercritical water (a) isobar[283] and (b) isotherm[284] evolution of density, and (c) the variation of density, dielectric constant, and ionic product with the temperature at 24 MPa[285]. Key: L-G: liquid-gas, CP: critical point of water, TP: triple point of water, S-G: solid-gas, S: solid, ρ: density, K: Kelvin degree, C: Celsius degree, MPa: megaPascal, GPa: gigaPascal. Reproduced with permission from references 283, 284, and 285. Copyright 2004 John Wiley and Sons, 2014 Scientific Research, 1999 Elsevier.

1.4.2 Continuous hydrothermal flow synthesis reactor designs

The main issue with batch hydrothermal industrialization for nanomaterials synthesis was the large volumes of water heated above its boiling point for an extended period of time, which required a large amount of energy, making the entire process unsustainable for the production of high quality and low-cost nanomaterials. The continuous hydrothermal flow reactors involve exposing the water flow at higher temperature than its critical point and keeping the reactor system under high pressures to generate the supercritical conditions. If the precursors are dissolved in the supercritical water flow, they are converted into products; otherwise, the precursors and supercritical water are mixed in the bespoke mixer. The first scenario describes the most basic CHFS reactor which included a high-pressure pump, a furnace, a cooler, a back pressure-regulator, and a reaction mixture collector. All the components are joined together with stainless steel pipes and fittings. The second scenario involved multiple injection sites, a junction for the precursor and additional feeds (where they are all premixed into a single feed), and a mixer where the supercritical water and precursor feed are mixed, and the synthetic process occurs.

The first-ever built CHFS reactor was reported by Adschiri *et al.*[286] in 1992 (see **Figure 1.12a**). The CHFS system consisted of two injectors (HPLC pumps): one water feed and another one for metal salt precursors. The goal of the research was to synthesise metal oxides of α-Fe_2O_3, Fe_2O_3, AlOOH, Ce_2O_3, NiO, ZrO_2, and TiO_2, with the reaction parameters of T= 400 °C and P= 35 MPa. The authors demonstrated that the synthetic approach can directly generate nanosized materials from their metal salts precursors without the need for a post-synthesis heat treatment. In other words, metal oxides can be produced continuously in supercritical water in less than two minutes. According to their findings, larger particle size is generated when the reaction mixture is exposed to high temperatures for a longer period of time and when a higher concentration of precursors is used, implying that parameters such as retention time and concentration play a decisive role in the growing process of the particle.

A year later, the researchers reported two new reactor designs[287](see **Figure 1.12 b-c**) for non-catalytic biomass conversation. The reactor shown in **Figure 1.12b** is a two-evacuation setup designed to investigate the diffusion of the cellulose depolymerisation products with supercritical water flow. The second reactor shown in **Figure 1.12c** was designed to study the glucose decomposition during the supercritical water treatment (they did not discover the CQDs which can be generated during the process).

The CHFS reactors designed by Adschiri had major flaws; most of their setups failed due to blockages in the mixing point area caused by the T-shape connector used to combine the precursor feed, supercritical water feed and the product exit feed from the reaction area. Another issue with their reaction setup was the failure of the back-pressure regulator as a result of the large particles generated during the process. Various research teams attempted to resolve all of these issues, such as preheating the precursors feed to avoid mixing point blockages or adding particle filters before BPR. All of these changes solve some problems while creating new ones. In 2000 the group led by Poliakoff from Nottingham University reported their first CHFS reactor setup[288] built for hetero Ce-Zr oxide.

In 2004 Lester *et al.*[289] studied the diffusion and the mixing of precursors with supercritical water inside the T-shape mixer, using methanol/sucrose simulations to understand how the selected precursors behave during the CHFS process. A new counter-flow design of the mixer/reactor was reported as a result of this study and the observations they made. (see **Figure 1.12e**). In the study, the stability, reproducibility, versatility, and tunability of the new system were demonstrated for a variety of nano-metal oxides (TiO_2, CeO_2, ZrO_2, ZnO, CuO_2, and CuO), nanometals (Ag, Cu), and nanocomposites (CuO_2-CuO-Cu and ZnO-Cu).

The counter-flow CHFS reactor performances and stability have been tested by Darr's research group[290], and later they reported a new mixing point design, a confined jet CHFS reactor (see **Figure 1.12f**). The counter-flow CHFS designed was revolutionary, with upgrades/optimisations reported[291,292] over time. It has been used as a model by Promethean Particles Limited (a UK-based company) for industrial applications of the CHFS method.

A simplified CHFS system schematic (see **Figure 1.12g**) used nowadays for the syntheses of metal oxides, and their nanocomposites includes (a) the premixing of the precursors with additional reagents (which takes place usually into a T-junction), (b) followed by a mixing step between the premixed precursors and superheated water (which takes place into a turbulent or laminar engineered mixer) where the chemical reactions occur and (c) a cooling process of the reaction mixture before being collected at room conditions[11].

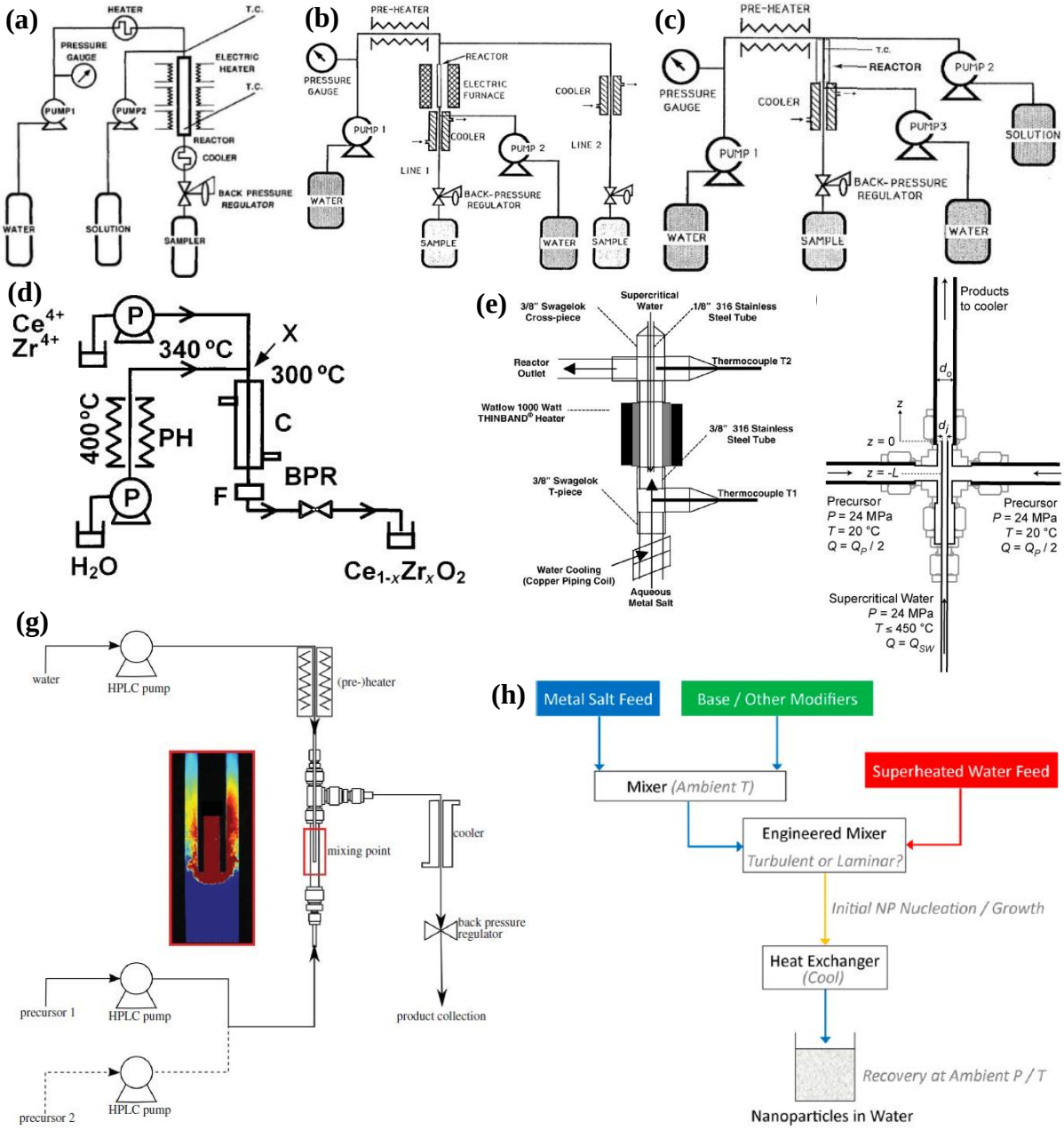

Figure 1.12: (a) The first-ever reported CHFS reactor[286], CHFS setups designed for: (b) cellulose depolymerisation and (c) glucose decomposition during the supercritical water treatment [287], (d) the first CHFS reactor designed by Poliakoff *et al.*[288], (e) the counter-flow CHFS reactor mixing point design by Lester *et al.* in 2006[293], (f) the confined jet CHFS reactor mixing point designed by Darr *et al.* in 2013[294], (g) the upgraded version of counter-flow CHFS reactor[291] and (h) a simplified schematic of a current CHFS reactor designed for the nanomaterials production[11]. Reproduced with permission from references 11, 286, 287, 288, 291, 293, and 294. Copyright 2005 John Wiley and Sons, 1993 J-STAGE, 1997 and 2000 Royal Society of Chemistry, 2006 Elsevier, and 2013 and 2017 American Chemical Society.

1.4.3 Continuous hydrothermal flow synthesis method as a green alternative for nanomaterials production

The CHFS method has two features that differentiate it from other methods: the use of supercritical water and the short reaction time. The supercritical water provides the necessary energy and the environment as the nanomaterials form and grows in a controlled and uniform crystalline phase[295].

Water is described as an ideal solvent in green synthesis[296]. The process is much faster than traditional methods, and the exposure of the precursors to the extreme reaction conditions and their conversion to nanomaterials, as well as the global energy consumption related to the amount of synthesized material and the environmental impact, are much lower.

The life cycle assessment conducted by Caramazana-González *et al.*[297] for the production of nano-TiO_2 demonstrated that, when compared to the solvothermal method, (a) the hydrothermal approach produced homogeneous materials at different temperatures, and (b) different precursors (such as titanium oxysulfate, titanium tetrachloride, titanium isopropoxide, titanium bis(ammonium lactato) dihydroxide and potassium titanium oxide oxalate) generate different environmental impact. The research also indicated that (c) bis(ammonium lactato) dihydroxide is the most efficient precursor available for TiO_2 synthesis using the continuous hydrothermal flow method. Kellici *et al.*[298] also demonstrated that the CHFS method has a lower environmental impact and a higher synthetic efficiency than the traditional batch hydrothermal method for the synthesis of graphene and carbon quantum dots[299].

The speed of a CHFS process is given by the retention time, which is defined as residence time, *i.e.*, how long the reaction mixture stays in the reaction zone, and it is exposed to heat generated by the supercritical water. Considering the reactor is constructed of stainless steel tubes, the retention time is a value given by the volume of the reactor in the reaction area and the flow rate (retention time = reactor volume/flow rate). If at the beginning of CHFS, the retention time was calculated to be ca. 2 minutes[286], due to the influence of supercritical condition over the material quality, nowadays most of the processes last from less than a second to a couple of seconds[11,298]. A fast-synthetic process means that less energy is consumed to maintain the supercritical conditions inside the reactor, and as a first consequence, the process has become more economical than a traditional method.

The study done by Stieberova *et al.*[300] revealed that CHFS is a sustainable synthetic method and is superior to most of the conventional methods in terms of production rate, quality,

variability, cost of inputs, cost of equipment, energy consumption, and CO_2 emission (see the table in **Figure 1.13a**). The industrial production cost for different nanomaterials was estimated in this study (see **Figure 1.13b**), and it was observed that the longer the CHFS reactor is used the lower the global price per nanomaterial kg will be. For example, if the reactor is operated 1600 h/year instead of 400 h/year, the price of TiO_2 drops by 44%, and the price per kg evolution follows a similar pattern for ZrO_2, ZnO, and $LiFePO_4$.

Recently, Bayer *et al.*[301] claimed for the first the continuous hydrothermal flow synthesis of pure phase TiO_2 rutile (rod-like morphology) with different bandgap values (from 3.46 eV to 3.15 eV), specific surface area (from 256 m^2/g to 5.6 m^2/g), and particle size (from 4.89 nm to 19.5 nm in width and from 33 nm to 65 nm in length) by varying the reaction temperature (by 50°C steps from 100 to 450°C) and the retention time (2.4 seconds to 42.5 seconds). The synthesis of anatase TiO_2 via CHFS has been extensively explored in the past two decades[244,245,253,302]. This study reported a method that highlighted the tunability capabilities of the CHFS process; by adjusting the process parameters, different TiO_2 material quality and properties were achieved.

An important step forward in pioneering CHFS methodologies has been made by Kellici *et al.*[303], and for the first time, the CHFS material portfolio has been expanded to include 2D materials. The research involved the continuous reduction of graphene oxide in mild alkaline conditions while avoiding the use of traditional toxic chemicals (such as hydrazine). Starting with a graphene oxide containing 27.23 at% oxygen, the oxygen content was reduced to 17.89% after the CHFS treatment using KOH as a reducing agent (0.2 M solution).

The as-developed CHFS method outperformed the conventional alkali method[304], and the as-synthesized r-GO demonstrated antibacterial activity. This work was expanded to include the functionalization of the 2D substrate with various metal oxides[305] and metal[306] nanoparticles for environmental (CO_2 utilisation) and biological (antibacterial) applications. The CHFS exploration of graphene materials reached a new milestone in 2017 when Kellici *et al.*[307] developed for the first time a method for in-flow synthesis of graphene quantum dots (GQDs).

(a)

Technology/ Criterion	Production rate	Quality	Variability	Cost of inputs	Cost of equipment	Energy Consumption process	Energy Consumption embodied	CO2 emissions
CFHS	High	Very good	Very high	Different	Medium	Low	Different	Low
VAFS	Very high	Good	Low	Low	Very High	Low	Low	Low
Sulfate process	High	Good	Low	Low	High	Low	Low	Low
Altair	High	Good	Medium	Low	Medium	Low	Low	Low
HT plasma	High/medium	Good	High	Different	Medium	Very high	Different	High
FSP	Medium	Good	High	High	Medium	Low	High	Medium
LT plasma	Low	Very good	Medium	Different	Medium	N/A	Different	N/A
CS solution	Low	Very good	High	High	Low	N/A	High	N/A
Sol-gel	Low	Very good	Very high	Different	Low	High	Different	High
Solvothermal	Low	Very good	Very high	High	Medium	N/A	High	N/A
Hydrothermal	Low	Very good	Very high	High	Medium	N/A	High	N/A
Precipitation	Low	Very good	Very high	Different	Low	High	High	High

(b)

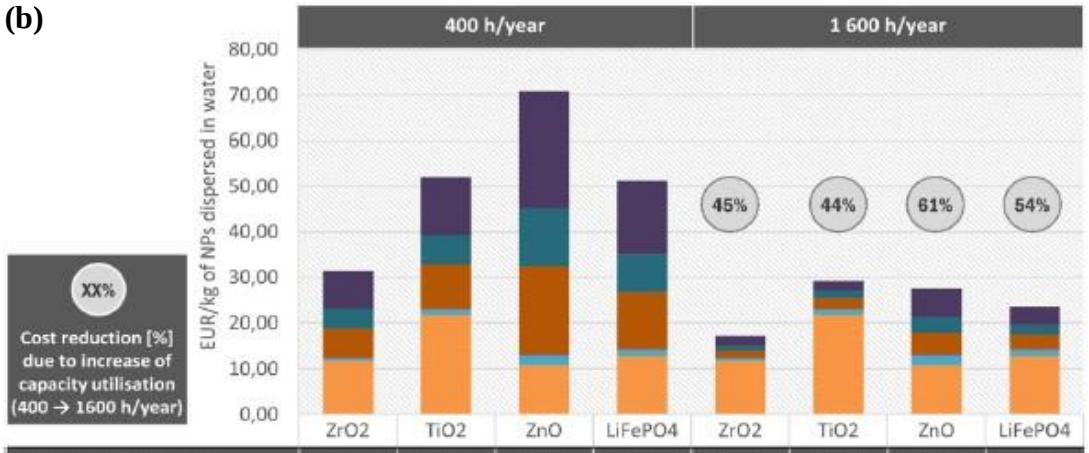

TOTAL UC [EUR/kg]	**31,42**	**52,06**	**70,77**	**51,19**	**17,30**	**29,20**	**27,63**	**23,63**
Costs of equipment	8,37	12,76	25,57	16,15	2,16	2,11	6,39	4,04
SUBTOTAL II [EUR/kg]	**23,06**	**39,30**	**45,20**	**35,04**	**15,14**	**27,09**	**21,24**	**19,59**
Other costs	4,23	6,52	12,79	8,25	1,06	1,63	3,20	2,06
Personal costs	6,33	9,76	19,15	12,35	1,58	2,44	4,79	3,09
Electricity	0,14	0,21	0,41	0,27	0,14	0,21	0,41	0,27
Natural Gas	0,59	1,04	2,04	1,32	0,59	1,04	2,04	1,32
Costs of chemicals and water	11,78	21,77	10,80	12,86	11,78	21,77	10,80	12,86

Figure 1.13: (a) Continuous hydrothermal flow synthesis method versus traditional synthetic methods comparison matrix and (b) the cost evaluation table at industrial scale for different nanomaterials produced via CHFS method[300]. Reproduced with permission from reference 300. Copyright 2019 Elsevier.

The previous CHFS method developed for r-GO synthesis was improved and adapted to achieve the conditions required for the GQDs synthesis. In this study, GO was used as graphene precursor and sulfonated calix[4]arene (at different concentrations ranging 1 mg/mL

to 10 mg/mL) was added to the process as a stabiliser and as a molecular tool, able to control the GQDs functionalities and morphological characteristics shortly after they were generated in the reaction area. The study also demonstrated the effect of sulfonated calix[4]arene (SCX4) concentration over the optical and morphological properties of GQDs; for higher SCX4 concentration, improved optical properties and smaller particle size was obtained. In the study published in 2018[298], the SCX4 molecules were replaced by phosphonated calix[4]arenes (PCX4) for further explorations in continuous hydrothermal flow synthesis of GQDs. The effect of PCX4 concentration on CHFS was reflected in the larger particle size and excitation independent emission (with a maximum of emission at 510 nm).

These studies on graphene materials opened a new avenue in the CHFS explorations, expanding the method capability for the generation of nanomaterials and nanocomposites. The reported synthetic routes were continued, adapted, and improved during this doctoral research project.

1.4.4 Conclusions

Continuous hydrothermal flow synthesis has been developed to update batch hydrothermal method and as an application for supercritical solvent with an enormous industrial potential due to their green perspectives. Even though the flow reactor is an old concept, continuously producing bottom-up nanomaterials has been a real challenge because it requires creating a favourable reaction environment to grow and stabilise crystalline nanometric-sized particles that are well dispersed in the reaction mixture feed.

The initial CHFS reactors designed in the beginning by Adschiri and his collaborators demonstrated that such requirements could be met, but adjustments and optimization were required before the method could be used as an industrial alternative to batch hydrothermal methods. The counter-flow CHFS reactor has solved most of the problems associated with this design's industrial implementation.

Overall, the CHFS method is an efficient, fast, tunable, green, and sustainable alternative for producing high quality and large quantities of nanomaterials.

1.5 Summary: an overall critical view

Materials such as carbon quantum dots, graphene or reduced graphene oxide, and their nanocomposites with TiO_2, have all drawn tremendous scientific and industrial attention in the

last decade. This recognition is attributable to their properties, which allow these materials to be versatile and applicable in a wide range of applications.

The high level of research interest in these materials is also reflected in the range of the synthetic methods, with both top-down and bottom-up synthetic methodologies being the primary manufacturing technologies. Some of these methods, such as chemical vapour deposition, arc-discharge, laser ablation, require a high energy consumption or expensive setups and highly skilled operators. In addition, the nature of the precursors, which can be toxic, highly flammable, or environmentally hazardous, creates safety risks. Considering that the primary aim for investigating these materials is their use in everyday applications, a costly and risky synthetic method will not be a candidate for a possible industrialization process.

The optical and electronic properties of CQDs, graphene and titanium dioxide, combined with chemical and physical stability, and biocompatibility, make them excellent candidates (alone or as nanocomposites), for environmental-related applications such as toxic ion detection, water treatment and photocatalysis. Developing a method that can accommodate the synthetic conditions for all these three nanomaterials will be a significant step forward in the field. The continuous hydrothermal synthesis method employed in this project is an alternative, effective essential option because it is green, tunable, fast and cost-effective, and has already demonstrated its efficiency and capability in the synthesis of nanomaterials.

Chapter 2: Continuous Hydrothermal Flow Synthetic Methodologies

In this Chapter, continuous hydrothermal flow synthesis reaction setup, detailed synthetic approaches, and characterisation techniques used for the production and characterization of materials (carbon quantum dots, reduced graphene oxide, and TiO_2 carbonaceous nanocomposites) are described.

The as-synthesised and characterized materials were tested for environmental applications in ion sensing (carbon quantum dots), water treatment (reduced graphene oxide), and photocatalysis (TiO_2 carbonaceous nanocomposites). The experimental setups, as well as the application methodologies for each, are also presented.

2.1 Continuous hydrothermal flow synthesis (CHFS): general aspects about the method and reaction setup

All the synthetic work in this research project was carried out using the in-house built continuous hydrothermal flow synthesis reactor. The CHFS approaches were developed and adjusted to produce different types of carbonaceous nanomaterials and nanocomposites. A schematic is shown in **Figure 2.1a**. The CHFS reactor, constructed[303] at LSBU, consisted of 1/8" 316SS Swagelok stainless steel fittings and tubing unless otherwise stated. The system is designed to be leak-proof, robust, reproducible, controlled reaction conditions (temperature, pressure, and flow rate), as well as safely conducting reaction chemistry. Three feeds (F1, F2, and F3) CHFS system was used in all the cases and is described in the following section.

F1: a supercritical water feed which plays multiple roles in the CHFS process (solvent, reagent, and local heat provider); **F2:** a precursor/s feed, delivering the chemicals necessary to synthesize the desired products; **F3:** an additional feed delivering auxiliary agents such as doping, reducing agent, or precursors for one or more components of a nanocomposite. The F2 and F3 are premixed at the "T" junction" before reaching the reaction area, generating a single precursor feed mixture which is then delivered to the mixing point, utilising a counter-current reactor (built of ¼' fittings), labelled as "Reactor" in the **Figure 2.1a**.

To inject the precursor/s feed, additional feed, and water into the system, HPLC Gilson 307 pumps, each fitted with a pump head (25 mL water feed and 10 mL for F2 and F3 feed), were used. Water is pumped through an electrically powered heater before entering the mixing zone. The heater consisted of a ¼ inch tubing and was connected to an external temperature controller (Watlow). The water feed enters at 20°C and exits at 450 °C. The 'T' junction

ensures a premixing of the precursor flow with the auxiliary flow, facilitating a reaction environment required in the mixing zone for the materials chemistry to occur.

The counterflow reactor (shown in **Figure 2.1b**) is made of a ¼ inch four-way union, equipped with an industrial mineral insulated K-type thermocouple (RS Components) to monitor the reaction temperature. The supercritical water is delivered through a 1/8" pipe in the reaction area, meeting the precursor/s feed mixture. The chemical process takes place in less than a second[298].

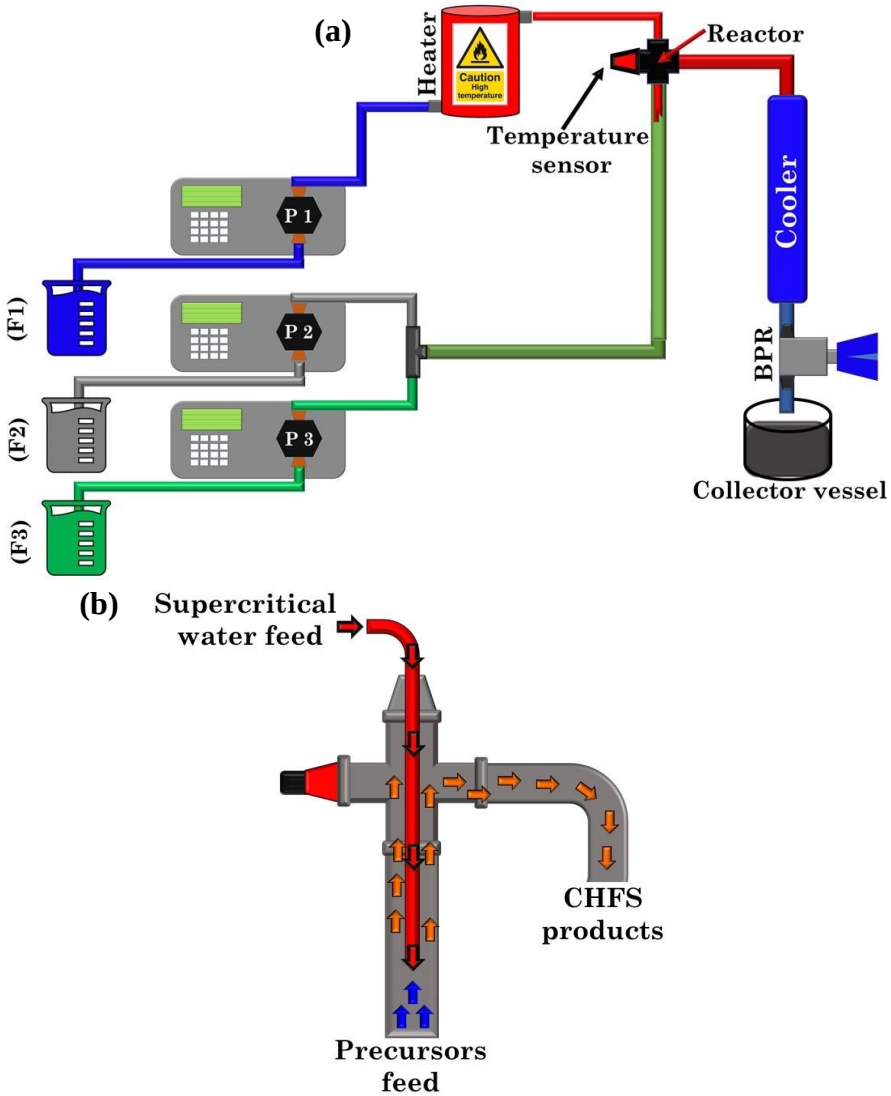

Figure 2.1: The schematics of (a) CHFS reactor setup and (b) CHFS counter-flow reactor mixing point.

The reaction mixture is then passed through a cooler. It is made of a vertical pipe-in-pipe design where the formed reaction mixture containing the reaction products, side products, and unreacted precursors is cooled at a temperature around 20 °C. The cooling process is necessary to protect the back-pressure regulator and to avoid possible accidents caused by the

hot reaction mixture. The back-pressure regulator (BPR, Tescom) maintained a constant pressure in the system. Also, the reactor is equipped with three high-pressure gauges (400 bar, RS Components) and three pressure safety check valves (Swagelok), one per feed. The reaction temperature at the water exits from the heater and at the mixing point was monitored using a temperature logger (Pico) connected to a computer. The as-synthesised materials, after passing through BPR were subjected to cleaning, separation, freeze-drying, and further characterisation.

2.2 Synthesis of carbon quantum dots from biomass related carbon sources (glucose and citric acid)

The aim of this work was to synthesize carbon quantum dots from biomass-related carbon sources aiming to deliver a material with enhanced properties via a green and efficient synthetic technology, CHFS. The reaction environment created during CHFS process is favourable for CQDs to form, grow and stabilize. Furthermore, CHFS provides the ability to modify the reaction media, process parameters, and overall, the product in real-time, offering tunability, characteristic feature of the method. To synthesise CQDs and NCQDs, glucose and citric acid were used as carbon precursors. Ammonia solution was used as nitrogen source in the nitrogen doping of NCQDs samples (using citric acid as carbon source).

The as-synthesized CQDs and NCQDs were characterized and tested for ion-sensing. The chemicals, materials, equipment, and procedures employed are described in detail in the following section.

Chemicals and materials:

All the materials were purchased from commercial suppliers and used without further purification. Deionized water (15 MΩ•cm) obtained from an ELGA Purelab system was used in all experiments. D(+)-glucose anhydrous (purity: 99+%), anhydrous citric acid (purity: 99%), ammonia solution (32%), and potassium chromate (purity: 99.5%) and potassium dichromate (purity: 99%) were purchased from Fisher Chemicals (UK) and used as received.

The solutions of metal ions, used for the nano-sensing experiment, were prepared from their nitrate, acetate, or chloride salts. The chlorides of Na^+, K^+, Mg^{2+} and Ca^{2+}, the acetate of Fe^{2+}, Zn^{2+}, Cu^{2+}, the nitrates of Fe^{3+}, Cr^{3+}, Ce^{3+}, Co^{2+}, Ni^{2+}, $Ag^{+,}$ and sodium: F^-, Cl^-, Br^-, I^-, NO_3^-, SO_4^{2-}, $H_2PO_4^-$, CH_3COO^-, $HCOO^-$, HCO_3^- and CO_3^{2-} were all purchased from Sigma-Aldrich (UK).

Synthetic Procedures:

Adjusted for this study, a three feeds CHFS system was employed:

Synthesis of CQDs:

- **F1:** supercritical water feed, flow rate: 20 mL/min
- **F2:** the carbon precursor: glucose solution (concentration of 70 mg/mL), flow rate: 5 mL/min
- **F3:** deionized water, flow rate 5 mL/min

Synthesis of NCQDs:

- **F1:** supercritical water feed, flow rate: 20 mL/min
- **F2:** the carbon source: citric acid solution (concentration: 70 mg/mL), flow rate: 10 mL/min
- **F3:** nitrogen source: ammonia solution (concentration: 1M), flow rate 10 mL/min

In both cases, the supercritical water feed was heated at 450 °C (lower temperatures of 250 °C and 350 °C have also been explored) and the system pressure was kept constant at 24.8 MPa using a back-pressure regulator. Feeds F2 and F3 were combined in a "T" junction prior to being delivered into the reaction zone (labelled as "Reactor") where it was mixed with the supercritical water feed (F1) where carbon dots were generated. The reaction mixture containing the CQDs or NCQDs was cooled using a straight pipe-in-pipe water cooler (labelled as "Cooler") and then passed through a back–pressure regulator (labelled as "BPR") and collected for further processing (see the CHFS general schematic **Figure 2.1a**).

A 0.2 µm alumina membrane was used for the filtration of the reaction mixture. The filtrate was initially separated using 30 kD membrane in a tangential filtration unit, followed by 1 kD membrane. The resulting solution was concentrated to 1/5 of the initial volume and subjected to further analysis. The sample concentrations were determined by freeze-drying 10 mL of the purified carbon dot sample: CQDs: 1.23 mg/mL and NCQDs: 1.1 mg/mL.

2.2.1 Ion-sensing

Fluorescence and sensing tests:

Fluorescence sensitivity and selectivity experiments of CQDs with Cr (VI) were performed as follows: Cr (VI) solution was prepared by dissolving potassium chromate (K_2CrO_4, 100 mg), deionized water (100 mL) (CQDs) or carbon dots stock solution (100mL)

(NCQDs). CQDs also demonstrated sensitivity/selectivity against Fe (II). The Fe (II) stock solution (1000 ppm) was prepared by dissolving iron acetate ($[Fe(C_2H_30_2)_2]$ 100 mg) in deionized water (100 mL). In each case, a fresh carbon dot solution containing CQDs (with the concentration of 1.23 mg/mL) or NCDQs (concentration 1.1 mg/mL) was placed into a 10 mL standard volumetric flask, followed by the addition of a required volume of 1000 ppm Cr (VI) or Fe (II) stock solutions (in the case of CQDs) to achieve concentrations of 500 ppm, 250 ppm, 100 ppm, 75 ppm, 50 ppm, 20 ppm, 10 ppm, 5 ppm, and 1 ppm. Additional dilutions of Cr (VI) in the ppb concentration range were prepared from Cr (VI) 100 ppm solution giving the following concentrations: 5 ppb, 10 ppb, 20 ppb, 50 ppb, 100 ppb, and 500 ppb. These were tested against NCQDs. In all the experiments, after 3 minutes of incubation and stirring at room temperature, the fluorescence spectra were measured for the quantitative analysis of Cr (VI) and Fe (II). Each experiment was repeated in triplicate. The fluorescence emission spectra for ion-sensing experiments were recorded for excitation at 360 nm with the band-slits of both excitation and emission set as 5 nm. The sensitivity was fixed on high with a response time set at 0.5 s. The emission spectra were recorded, and the fluorescence intensity of CQDs at 446 nm and 441 nm for NCQDs was used for the quantitative analysis of Cr (VI) or Fe (II). For comparison purposes, a range of anions and various metal cations were tested for selectivity and sensitivity using 50 ppm as a standard concentration. Furthermore, stability analysis of the carbon quantum dots (CQDs and NCQDs) in the presence of Cr (VI) or Fe (II) (50 ppm) was made by recording the fluorescence intensity of the mixture when initially exposed continuously at 360 nm excitation.

2.3 Synthesis of reduced graphene oxide (r-GO)

The traditional wet chemical bottom-up synthesis of reduced graphene oxide involves the use of toxic or carcinogenic reducing agents[308,309]. Hydrothermal synthesis is an alternative for the production of reduced graphene oxide[310], but the process has a high energy and time consumption. The continuous hydrothermal flow synthesis method has already proved its ability to produce r-GO[303,306].

The purpose of the current study is to develop a new CHFS method by using an economical, organic reducing agent (formic acid), to characterize the as-synthesized materials and to test it for membrane preparation and testing for water treatment applications.

Chemicals and materials:

All the materials were purchased from commercial suppliers and used without further purification. Deionized water, (15 MΩ • cm) obtained from an ELGA Purelab system was used in all experiments.

Graphene oxide (low acid 25% aqueous paste, Abalonyx AS) was used as stock to prepare 0.5 mg/mL and 2 mg/mL graphene oxide solutions in water. The formic acid (concentration: 98%) was purchased from Fisher Chemicals (UK), and it was used as a stock solution to prepare the 3M formic acid solution. The iron (II) acetate (purity: 99%) was purchased from Sigma Aldrich (UK) and has been used to prepare solutions for the iron catalyst involved in the r-GO synthesis process and the water treatment experiment.

The solutions of pollutants involved in the water treatment experiment were prepared from potassium ferricyanide, iron (III) acetylacetonate, potassium chromate, methylene blue, rhodamine B and cytochrome C, and were all purchased from Sigma-Aldrich (UK). The quartz wool and the extra pure sand used in the membrane preparation were purchased from VWR (UK) and Fisher Chemicals (UK), respectively.

Synthesis of the reduced graphene oxide:

The CHFS system is made of three feeds: supercritical water feed (F1: flow rate: 20 mL/min), a second feed containing graphene oxide dispersion in water (F2: flow rate: 10 mL/min) and a third feed containing 3M formic acid solution (F3: flow rate 10 mL/min). In this investigation, the graphene oxide concentration in the second feed was varied in order to observe the variation of oxygen content and optimise the reaction conditions. The water feed (F1) was heated at 450 °C using a water pre-heater, and the internal pressure was kept constant at 24.8 MPa using a back-pressure regulator (labelled as BPR). Feeds F2 and F3 were combined in a "T" junction mixer and delivered to the reaction area (marked as "Reactor"), where it was combined with the superheated water feed (F1). The thermal decomposition of formic acid in the presence of water generates H_2 and CO_2[311,312]. The in-situ generated H_2 is reactive and rapidly (within fraction of seconds) reduces the oxygen functionalities on the graphene oxide surface.

During this study, two different concentrations of graphene oxide were used 2 mg/mL (sample labelled as r-GO(1)) and 0.5 mg/mL (sample labelled as r-GO(2)). For the process optimization, in-situ generated iron nanoparticles were used as a catalyst for 0.5 mg/mL graphene oxide (sample labelled as r-GO(3)). In all experiments, the formic acid concentration

was constant (3M), and for r-GO (3) experiment, the third feed contained a solution of formic acid (3M) and iron acetate (0.074 M). The iron acetate was used as a precursor for the iron nanoparticle catalyst. The reaction mixture containing the reduced graphene oxide was delivered from the reaction area into a pipe-in-pipe water cooler (labelled as "Cooler"), further evacuated outside the system through a BPR and collected for isolation and cleaning. The reaction mixture was centrifuged for 30 minutes at 6000 rpm, and the resulted black slurry washed with deionized water until it reached pH 6-7. The resulting slurry was freeze-dried, and it was used for characterizations and water treatment testing.

2.3.1 Water treatment processes

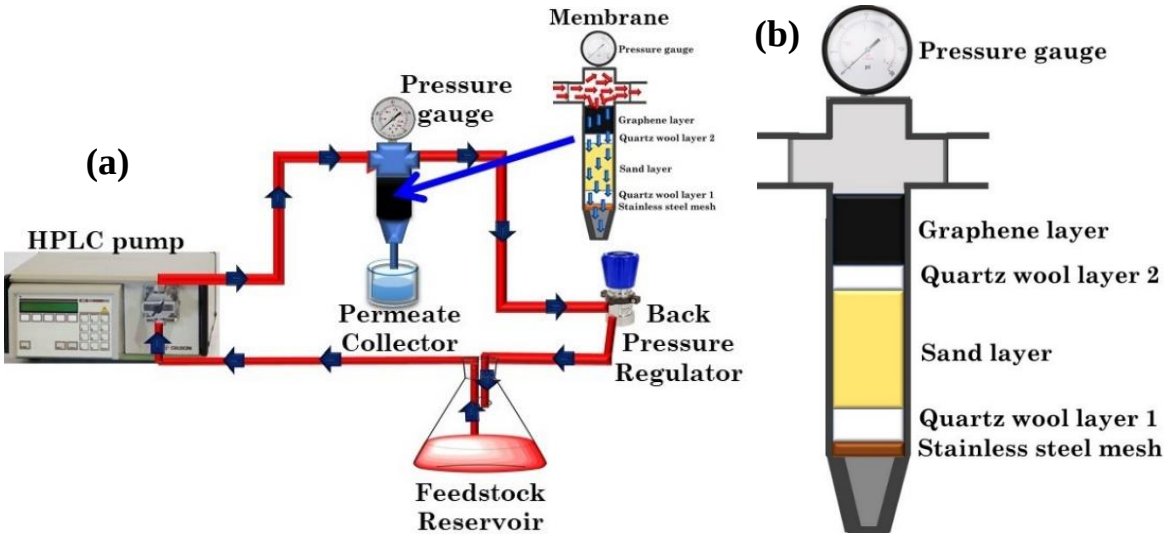

Figure 2.2: (a) Water treatment high-pressure membrane setup schematic and (b) graphene high-pressure membrane representation.

Water treatment setup and process:

The water treatment setup consists of Gilson 307 HPLC pump with a 10 mL pump head connected at the inlet with a feedstock reservoir which contains the pollutant solution and at the outlet with the main membrane body setup. The main membrane body setup is built of a four ways union which connects: the pressure gauge (RS components), the membrane (in-house constructed), BPR (Tescom), and the HPLC pump (see **Figure 2.2a**). Before initiating a water treatment process, DI water was firstly passed through the membrane system in order to determine the volume. This was determined to be 12 mL (from the pump outlet to the BPR outlet in the absence of the membrane). When the pollutant solution was injected into the membrane system, this volume was considered as the volume collected prior to the exchange between the pollutant feedstock reservoir and the water collector. In the feedstock, the reservoir was filled with 100 mL pollutant solution, and this was recirculated through the membrane

system with a flow rate of 10 mL/min and a system pressure of 16.54 MPa until 50 mL of permeate were collected. The permeate pollutant concentration was measured every 10 mL to determine the membrane's performances over time. Following each pollutant test, the membrane system was washed with deionized water, and 50 mL of washing permeate was collected under the same conditions (10 mL/min and 16.54 MPa) until the membrane was deemed clean and ready to be used for another pollutant test.

Membrane preparation:

The graphene membrane (see schematic in **Figure 2.2b**) was built inside of 35 mm length, ¼ inches 316SS Swagelok tube with connector for the inlet and outlet. It contains a 100 μm stainless steel mesh, 20 mg of quartz wool, 400 mg of sand, 10 mg of quartz wool. CHFS synthesised materials were then added: (a) 40 mg of reduced graphene oxide/graphene oxide or (b) 20 mg of graphene oxide and 20 mg of reduced graphene oxide when tested together. The membrane was built by placing the layers one by one inside the Swagelok tube and hand pressing them to a uniform surface before adding the next layer. Following installation into the water treatment set-up and prior to the use, the membrane was wetted with deionized water (in the absence of the pressure), and then washed at 16.54 MPa to generate channels between the reduced graphene oxide or graphene oxide layers.

Membrane performances measurements:

The following performance test experiments were used to determine two important parameters of the as-prepared membranes: the rejection rate and the permeation. The rejection rate was measured to determine the efficiency of the membrane performing as a barrier for the pollutants molecules dissolved or suspended in the simulated wastewater feed and the permeation was determined to demonstrate how fast the graphene-based membranes can perform.

The rejection rate, R(%) was calculated using the following formula:

$$\mathbf{R(\%)} = \frac{C_{stock} - C_{permeate}}{C_{stock}} \cdot 100 \quad \textbf{(Equation 2.1)}$$

Where:

- R(%) is the rejection rate.
- C_{stock} is the stock concentration (the initial concentration).
- $C_{permeate}$ is the permeate concentration.

The permeation was calculated using the following formula:

$$\textbf{Permeation (mL/min)} = \frac{V_{permeate}}{t} \quad \textbf{(Equation 2.2)}$$

Where:

- $V_{permeate}$ is the volume of the permeate.
- t is the time recorded to collect a certain volume of permeate.

2.4 Synthesis of TiO_2-NCQDs-rGO nanocomposites

Chemicals and materials:

All the materials were purchased from commercial suppliers and used without further purification. Methylene blue (pure), anhydrous citric acid ($C_6H_8O_7$) (purity: 99%) and ammonia solution (NH_3 32%) were purchased from Fisher Chemicals (UK); titanium(IV)bis(ammonium lactate)dihydroxide solution ($[CH_3CH(O-)CO_2NH_4]_2Ti(OH)_2$, 50 wt% in water) was purchased from Sigma Aldrich (UK). Deionized water (15 MΩ•cm) (ELGA Purelab system) was used in all experimental work.

Synthetic Methodology:

All materials were synthesised using in-house constructed CHFS set-up[303] operated at 450 °C and at constant pressure 24.8 MPa. The simplified CHFS schematic is shown in Figure 1. It consists of a water pre-heater connected to a temperature controller, three high pressure pumps used for continuous delivery of water and precursors feeds, a 'T' junction (facilitating the mixing of the precursor(s)/auxilary feeds), a counterflow reactor equipped with a thermocouple (where the supercritical water meets the precursors feed and the chemical process takes place), a post-reaction pipe-in-pipe water cooler, a back-pressure regulator (BPR) (that maintains a constant pressure in the system) and a collection vessel (for the collection of the final product aqueous mixture). The reactor is also equipped with three high-pressure gauges (to monitor the pressure in each feed) and three pressure safety checks (one per each feed).

Generally, in each experiment, pre-mixed (at the T-junction) feeds of an aqueous solution of titanium(IV) bis(ammonium lactato)dihydroxide (0.2 M) and a carbon precursor (graphene oxide and/or citric acid or pre-made NCQDs[313] were delivered via the T-junction to meet a concurrently flowing feed of sc-H_2O in the mixing zone (reactor), whereupon formation of nanocomposites occurred. The product mixture was then cooled, evacuated from the reactor

and collected for further isolation, purification and analysis. A summary of the experiments and experimental conditions are given in **Table 2.1**.

Table 2.1: Summary of the experimental conditions employed for the CHFS synthesis of the nanocomposites. All experiments were performed at the following conditions: T = 450 °C and P = 24.8 MPa; flow rates for each corresponding pump were set as Pump 1 = 20 mL min^{-1}, Pump 2 = 5 mL min^{-1}, Pump 3 = 10 mL min^{-1}.

Photocatalyst name	Synthetic Methodology		
	CHFS Pump	Feed content	Concentration
TiO_2	Pump 1	H_2O	Pure
	Pump 2	$[CH_3CH(O^-)CO_2NH_4]_2Ti(OH)_2$	0.2 M
	Pump 3	NH_3	1 M
TiO_2-NCQDs(1)	Pump 1	H_2O	Pure
	Pump 2	$[CH_3CH(O^-)CO_2NH_4]_2Ti(OH)_2$	0.2 M
	Pump 3	$C_6H_8O_7$	70 mg/mL
		NH_3	1 M
TiO_2-NCQDs(2)	Pump 1	H_2O	Pure
	Pump 2	$[CH_3CH(O^-)CO_2NH_4]_2Ti(OH)_2$	0.2 M
	Pump 3	NCQDs	1.2 mg/mL
		NH_3	1 M
TiO_2-Graphene	Pump 1	H_2O	Pure
	Pump 2	$[CH_3CH(O^-)CO_2NH_4]_2Ti(OH)_2$	0.2 M
	Pump 3	Graphene Oxide	1 mg/mL
		NH_3	1 M
TiO_2-NCQDs-Graphene(1)	Pump 1	H_2O	Pure
	Pump 2	$[CH_3CH(O^-)CO_2NH_4]_2Ti(OH)_2$	0.2 M
	Pump 3	Graphene Oxide	1 mg/mL
		$C_6H_8O_7$	70 mg/mL
		NH_3	1 M
TiO_2-NCQDs-Graphene(2)	Pump 1	H_2O	Pure
	Pump 2	$[CH_3CH(O^-)CO_2NH_4]_2Ti(OH)_2$	0.2 M
	Pump 3	Graphene Oxide	1 mg/mL
		NCQDs	1.2 mg/mL
		NH_3	1 M

2.4.1 Photocatalytic test and experimental setup

Photocatalytic experiments:

The photocatalytic activities of titania nanocomposites were evaluated by the photodegradation of methylene blue (MB) in water using the solar-simulator set-up as described above (**Figure 2.3d-e**). Routinely, each photocatalyst (10 mg) was suspended in MB aqueous standard solution (0.02 mM, 50 mL) in a glass beaker (Corning Pyrex Griffin) equipped with a magnetic bead. The solution was stirred in the dark for 30 minutes to ensure the establishment of an adsorption-desorption equilibrium. The reaction mixture was located

at a distance (27 cm) from the light source and stirring was maintained for the whole photocatalytic process period.

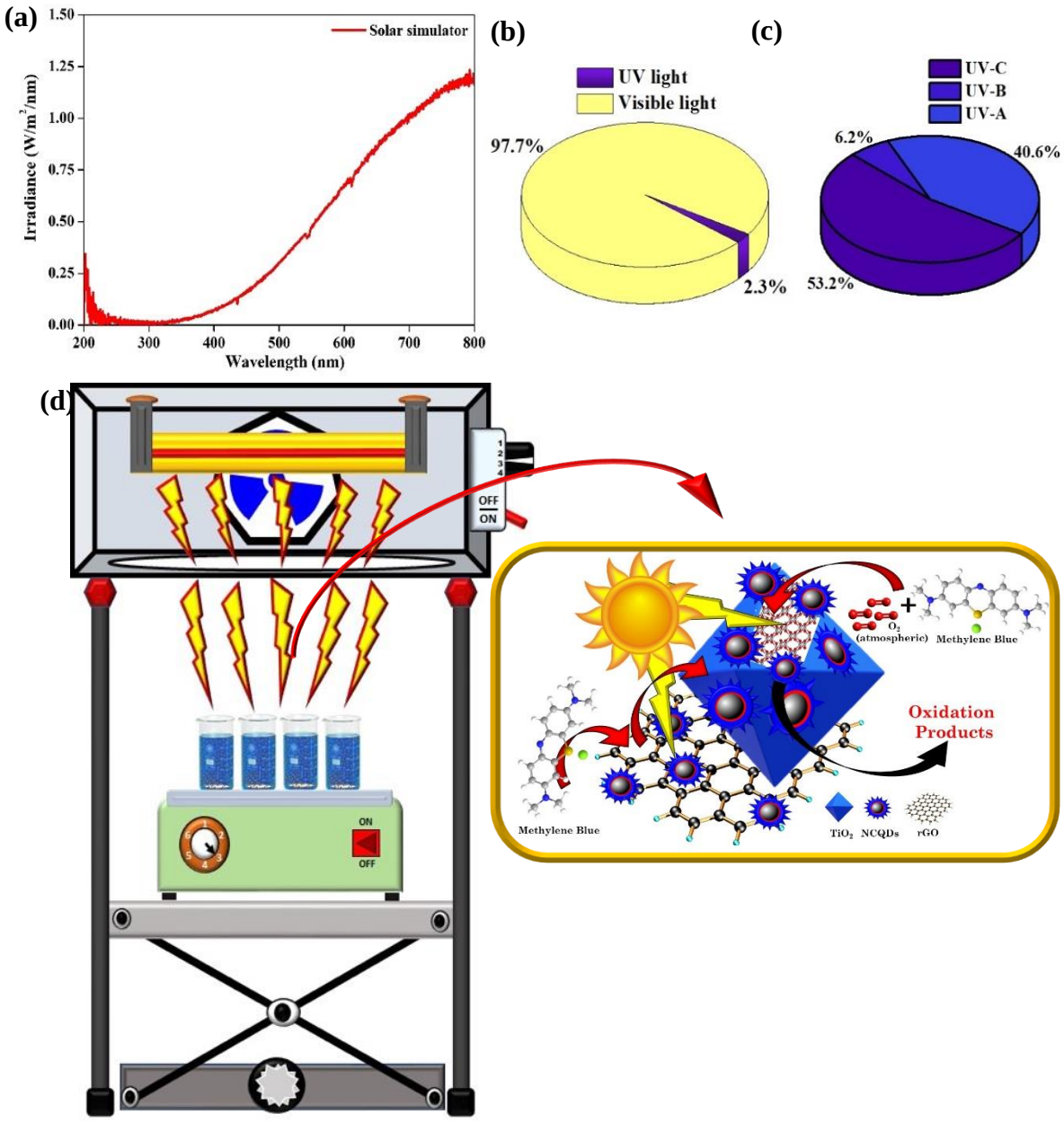

Figure 2.3: The optical properties of the solar simulator light showing (a) the irradiance spectrum, (b) the light composition between 200-800 nm and (c) the ultraviolet radiation composition, (d) solar simulator setup schematic, and (d) the photocatalytic process schematic.

The samples were irradiated for 180 minutes. During the irradiation process, aliquots (10 mL) were collected at 30 minutes intervals, centrifuged to removed particulates (5 mins at 4500 rpm) and analysed with a UV-Vis spectrophotometer (Shimadzu UV-1800) to assess the MB photodegradation by measuring its absorbance change at 660 nm. After the UV-Vis analysis, the centrifuged material was resuspended in the aliquot and returned to the initial reaction mixture. The quantitative determination of MB was calculated using a calibrated

correlation between the measured absorbance and its concentration. Adsorption coefficients (q_t) (shown in **Table 2.2**) were also determined using Langmuir-Hinshelwood model[314].

Table 2.2: Adsorption coefficients of TiO_2 and TiO_2-carbonaceous nanocomposites.

Photocatalyst	q_t
TiO_2	**4.4**
TiO_2-rGO	**14.2**
TiO_2-NCQDs(1)	**5.5**
TiO_2 - NCQDs(2)	**2.4**
TiO_2 –NCQDs-rGO(1)	**11.2**
TiO_2 –NCQDs-rGO(2)	**11.2**

Solar simulator setup:

In-house made consisting of a laboratory jack, a magnetic stirrer, and a quartz tungsten halogen lamp (Osram 1 kW R7s 22000 lm Linear Halogen Lamp) mounted on a light intensity adjustable device cooled by an electric fan (**Figure 2.3**). The lamp performances were verified using Ocean Insight Flame Optical Spectrometer by measuring the tungsten halogen lamp irradiance spectrum between 200 and 800 nm (see the irradiance spectrum in **Figure 2.3a**). This confirmed that the artificial sunlight generated by the device contains 2.3% UV radiation and 97.7% visible radiation (**Figure 2.3b**), and the UV radiation is made of 40.6% UV-A radiation (320-400nm), 6.2% UV-B radiation (280-320 nm), and 53.2% UV-C radiation (200-280 nm) (**Figure 2.3c**). The study confirms that the lamp used in the photocatalytic experiments in its normal parameters generates light like the sunlight, hence simulating a process very close to the solar light, which is required as activation energy in a photocatalytic process.

2.5 Equipment and characterisation methods

Freeze-drying was performed using a Heto PowderDry PL 3000.

Surface area analysis (SA_{BET}):

The BET surface area of the TiO_2 and TiO_2-carbonaceous nanocomposites powders were determined by the Branauer-Emmett-Teller (BET) method using a Micrometrics Gemini

II 2237. The 5-point N_2 adsorption method was used. The powders were degassed prior to analysis at 180 °C for 2 hrs to remove any moisture using a FlowPrep 060 degasser.

X-Ray Photoelectron Spectroscopy (XPS):

The XPS analysis was performed on a Thermo Fisher Scientific K-alpha+ (CQDs) and Kratos Axis Ultra DLD photoelectron spectrometers (used for the characterisation of NCQDs, reduced graphene oxide and titanium dioxide hybrids) utilizing a monochromatic Alka source operating at 144 W. The base pressure of the system was ca. $1x10^{-9}$ Torr rising to *ca.* $4x10^{-9}$ Torr under the analysis of these samples.

Samples in the liquid form (carbon quantum dots) were placed on to gold-coated silicon wafers or conductive carbon tape) and the solution pumped away in the load lock of the spectrometer and repeated until a notable drying pattern was observed. These patterned areas were analysed using a micro-focused monochromatic Al X-ray source (72 W) using the 400-micron spot mode. Whereas samples in the powder form (reduced graphene oxide and TiO_2-carbonaceous nanocomposites) were mounted using conductive carbon tape. The data was recorded at pass energies of 150 eV or 160 eV for survey scans and 40 eV for the high-resolution scan with 1 eV and 0.1 eV step sizes, respectively. The charge neutralisation of the sample was achieved using a combination of both low energy electrons and argon ions.

High-Resolution Transmission Electron Microscopy (HRTEM):

The particle size and morphology of CQDs were observed using JEOL JEM2100 equipped with LaB6 filament. For the investigation, the acceleration voltage was set to 200 kV, and the emission was set to 107 µA.

A double-corrected JEOL ARM200F, equipped with a cold field emission gun, was also employed to analyse NCQDs, reduced graphene oxide and titanium dioxide hybrid materials. For this investigation, the acceleration voltage was set to 80 kV, and the emission at 10 µA.

In all the cases, the samples were prepared by depositing the aqueous dispersions onto a holey carbon-coated Cu-grid (400 µm). The images analysis was performed using ImageJ software.

Scanning Electron Microscopy (SEM):

The SEM images were recorded using a Hitachi SU-70 FEG instrument for TiO_2-carbonaceous nanocomposites, and for the GO and r-GO samples, the images were recorded using a Carl Zeiss AG - EVO® 50 Series instrument.

Fourier-Transform Infrared Spectroscopy (FT-IR):

FT-IR data of CQDs, reduced graphene oxide and titanium dioxide hybrid materials were recorded using a Shimadzu IRAffinity-1S Fourier Transform Infrared Spectrophotometer fitted with a Specac Quest ATR Accessory (diamond 4000-200 cm^{-1}).

Nicolet Avatar 370DTGS FT-IR spectrometer fitted with a Smart Orbit accessory (diamond 4000-200 cm^{-1}) also was used to investigate the composition of NCQDs.

Raman Spectroscopy:

The Raman spectrum of dried CQDs was measured with a Bruker Confocal Raman Microscope SENTERRA II with radiation at 532 nm.

Nitrogen-doped carbon quantum dots, titanium dioxide hybrids and reduced graphene oxide were analysed using a Horiba LabRAM HR Evolution spectrometer with radiation at 514 nm (NCQDs) and 633 nm (TiO_2-hybrids and GO/r-GO samples).

X-Ray Powder Diffraction (XRD):

XRD patterns were recorded using a Siemens D5005 X-Ray Diffractometer using a long fine focus Cu K alpha radiation source (λ = 1.54 Å) operating at 30 kW.

Atomic Force Microscopy (AFM):

In all the samples**,** the images were obtained *via* dynamic mode on an hpAFM with AFM Controller (NanoMagnetics Instruments, UK) using Nanosensor tapping mode probes. The micrographs were then processed with NMI Image Analyser (v1.4, NanoMagnetics Instruments), with plane correction and scar removal using the in-built functions.

Steady-State Optical Characterisation:

UV–Vis spectrophotometry:

Adsorption measurements of CQDs, NQDs, and methylene blue were conducted using a Shimadzu UV-1800 in the range of 200-750 nm in a 10 mm quartz cuvette.

In the case of titanium hybrid powders, the absorption measurements were taken with a Perkin-Elmer Lambda 950 spectrophotometer in the range of 200-800 nm. The instrument was fitted with an integrated sphere. The spectra were converted to Tauc plots, and the band gaps of the materials were calculated for indirect and direct transitions[315].

Photoluminescence spectroscopy (PL):

The fluorescence spectra for all the CQDs and NCQDs samples were recorded with Shimadzu RF-6000 Spectrofluorophotometer. The excitation wavelength was scanned between 300–500 nm (by 20 nm steps) for CQDs, resulting in a maximum of emission of 446 nm at 360nm excitation wavelength, and for NCQDs between 300 – 420 nm (by 20 nm steps), the maximum of emission of 441 nm at 360 nm excitation wavelength.

The fluorescence spectra of titanium dioxide hybrids were recorded with Horiba FluoroMax Plus Spectrofluorophotometer. The PL decays were measured using TCSPC with an FLS1000 Photoluminescence Spectrometer (Edinburgh Instruments, UK) equipped with a double emission monochromator and a high-speed PMT detector (H10720). The TiO_2 hybrids suspensions were excited at 375 nm by a pulsed diode laser (EPL-375), and the decays were measured at an emission wavelength of 450 nm. The decays were fitted using reconvolution analysis with the IRF in the FLS1000 Fluoracle software.

Quantum Yield (QY) determination:

Quantum yield values of carbon quantum dots were calculated (**Equation (2.3)**) by measuring the integrated PL intensity in the aqueous dispersion of dots in comparison with the integrated photoluminescence spectra of quinine sulphate in 0.1 M H_2SO_4 (standard) and was plotted as integrated PL *vs* Absorbance (Figure S1) from which the extracted slopes (the gradient Δ) were obtained.

$$\theta_{QDs} = \theta_S \cdot \frac{\Delta_{QDs}}{\Delta_S} \cdot \left(\frac{\eta_{QDs}}{\eta_S}\right)^2 \quad \textbf{Equation (2.3)}$$

Where:

- θ_{QDs} is the quantum yield of CQDs or NCQDs.
- θ_S is the quantum yield of standard (quinine sulphate 54%).
- Δ_{QDs} is the slope of integrated PL of CQDs.
- Δ_S is the slope of integrated PL intensity of the standard.
- η_{QDs} is the refractive index of water (1.33).
- η_S is the refractive index of 0.1 M H_2SO_4 (1.33).

Isolation and purification:

The CQDs and NCQDs were isolated, purified and concentrated using a KrosFlo®IIi Tangential Flow Filtration System equipped with 1kD and 30 kD membranes.

A centrifugation process was involved in terms to isolate and wash the TiO_2-hybrids and r-GO samples. The centrifugation process was done using a Thermo Scientific Sorvall RC 6 Plus Centrifuge: the isolation process: 10000 rpm for 10 minutes (for TiO_2-hybrids) or 60 minutes (for r-GO), and the washing process (with DI water): 17000 rpm 2 cycles of 240 minutes and 10000 rpm 3 cycles of 30 minutes (each sample has been washed for three times).

2.6 Conclusions

During this PhD research project, fast single- or double-step new continuous hydrothermal flow methods were engineered and developed using water-soluble precursors or water-stable nanomaterials dispersions to produce green materials for environmental-related applications. These methods have a real potential to be scaled-up for industrial explorations, and the as-synthesized nanomaterials and nanocomposites were simply integrated into ion-sensing, membrane preparations for water treatment and photocatalysis.

The CHFS process and the CHFS reactor offer superior performances (faster, greener, real-time control over the process parameters and material quality, and cheaper) when compared with conventional batch hydrothermal.

Chapter 3: Continuous hydrothermal flow synthesis of carbon quantum dots for ion-sensing

3.1 Introduction

This chapter describes the experimental work done to synthesize carbon quantum dots (CQDs) *via* Continuous Hydrothermal Flow Synthesis (CHFS). The CQD were characterized using a variety of characterization techniques and tested as a fluorescent nano-sensor for the detection of Cr(VI). Continuous Hydrothermal Flow Synthesis represents an effective synthetic process to make high quality and high quantity of nanomaterials. Applied to CQDs synthesis, CHFS is a green, fast, and low energy consumption one-step continuous hydrothermal flow synthesis approach using an available, economical and biomass related carbon source.

Carbon quantum dots are fluorescent nanometric particle, smaller than 10 nm, with a quasi-spherical and discrete morphological structure. In the last decade, it has attracted increasing scientific and industrial interest due to their optical properties and chemical and physical stability. A typical carbon quantum dots particle is composed of a graphite core, ended with an amorphous carbon framework (hybridised sp^2/sp^3). The surface chemistry is dependent on carbon source, doping agent, synthetic route, and process parameters. The CQD's surface is rich in functional groups (*e.g.* oxygen or nitrogen moieties), and it can have physical or chemical attached polymers molecules or other derivative species. Due to their properties such as high photostability, good biocompatibility, and excellent optical properties, with low potential for environmental hazards[316,317], CQDs are suitable for various applications including bio-imaging & bio-tagging[318,319], drug delivery[40,320], fluorescent ink[24], ion sensors[321,322], optoelectronics[323], photocatalysis[26], light-emitting devices[324], and solar cells[98].

The usage of biomass or biomass-related molecules such as glucose[118,325], fructose[326], citric acid[327], chitosan[98], cellulose[102] or lignin[328] to produce CQDs *via* intra- and inter-dehydration and, or decomposition processes under hydrothermal conditions[327,329] is a promising bottom-up approach due to the sustainable and eco-friendly perspectives. The *top-down* method is mainly a size reducing process, involving a chemical and physical 'cutting' of larger dimensional pre-made carbon materials such as carbon nanotubes, graphite, or carbon black, aiming to obtain an active photoluminescent material. By applying a *top-down* method for the synthesis of CQDs will raise two significant issues: 1) high consumption of energy and expensive precursors such as carbon nanotubes or carbon black, and 2) are using dangerous chemicals such as strongly oxidizing agents, strongly acidic or alkaline environments or highly

corrosive chemical compounds. In these conditions, *bottom-up* methods remain the main option in the synthesis and large-scale production of CQDs and nanomaterials in general. However, the current *bottom-up* approaches have their own challenges, including lengthy manufacturing time, non-uniformity in CQD particle size distribution, inconsistent reproducibility and high energy costs. Consequently, applying the synthetic approaches to an industrial scale within the current parameters would be limiting. In this regard, it is essential to overcome these challenges in providing a controllable, cleaner, and rapid synthetic process that can be scaled up at the industrial level and deliver high-performance CQDs.

It is in this context, continuous hydrothermal flow synthesis (CHFS) is highlighted[11,298,306,330–333] as one of the most promising methods employed for the *bottom-up* approaches offering significant synthetic advantages over traditional methods, delivering in a cleaner and rapid mode, high-quality nanosized materials. The CHFS method can be classified as either *top-down* or *bottom-up* approach, but in this case, is an efficient bottom-up method for converting small biomass related molecules such as citric acid and glucose into carbon nanoparticle with interesting optical properties. The simplicity and efficiency of the synthetic procedure can be a turning point in the industrial production and mass utilization of CQDs in a broad range of applications. The current work adds further to the development of continuous flow technology of carbon-related quantum dots nanomaterials.

Sensing different analytes such as metal ions, anions, organic molecules, metal nanoparticles and biological samples based on the affinity of CQDs surface functional groups or through interaction with the light beams at certain wavelengths, CQDs can be engineered and designed for sensitive and selective detection for molecular or ionic targets. The nano-sensing process is based on the modification of optical properties when CQDs are in contact with the analyte. Due to their fluorescence stability under neutral mild acidic and basic conditions, the CQDs were successfully tested as a fluorescent nano-sensor for the detection of Cr (VI) ions with good sensitivity and selectivity to other ions and anions.

The CHFS CQDs' chemical composition such as elemental composition and functional groups and carbon hybridization (sp^2/sp^3) were determined using X-Ray Photoelectron Spectroscopy (XPS), Fourier-transform infrared spectroscopy (FTIR) and Raman spectroscopy, the optical properties such as absorption of ultraviolet (UV) and visible (Vis) light, the emission properties and quantum yield (QY) were measured using UV-Vis spectroscopy (UV-Vis) and Photoluminescence spectroscopy (PL) and the structural and morphological properties such as particle's shape, lattice fringes, particle size, and size

distribution were identified using High-Resolution Transmission Electron Microscopy (HRTEM) and Atomic Force Microscopy (AFM). The nano-sensing measurements were performed using PL and the quenching of PL intensity was used to determine the sensitivity and selectivity of CQDs nano-sensors.

3.2 Continuous hydrothermal flow synthesis of carbon quantum dots from glucose

3.2.1 Results and discussions

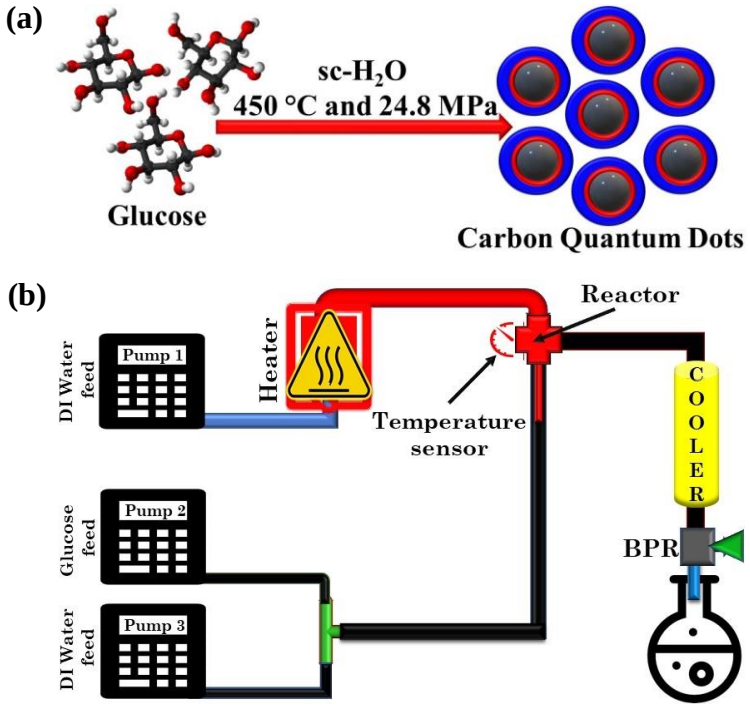

Figure 3.1: Synthesis of carbon quantum dots (CQDs) using Continuous Hydrothermal Flow Synthesis (CHFS) process: (a) illustration of the CHFS synthetic process using glucose as carbon source and supercritical water as solvent and reaction environment and (b) simplified CHFS reactor design.

The synthetic procedure representation and CHFS reactor setup are shown in **Figure 3.1**. The purpose of this study was to develop a CHFS approach for the CQDs continuous production, characterisation and in-depth analysis aiming to understand their properties and to test the as-synthesized material for ion-sensing.

Materials characterisation

The high-resolution transmission electron microscopy images (HRTEM) (**Figure 3.2a, c, and d**) of the as-prepared CQDs display an irregular round shape morphology with an average particle size of 2.3 ± 0.5 nm from a sample population of 150 particles ranging between

1.4 nm to 4.5 nm in diameter (**Figure 3.2b**). Each exhibited the same structural arrangement, indicating consistency in homogeneity for the CHFS synthesized sample. The graphitic core arrangement of the carbon atoms (**Figure 3.2e**) can be clearly identified with an in-plane lattice spacing of 0.22 nm and is consistent with the reported literature data[21,334].

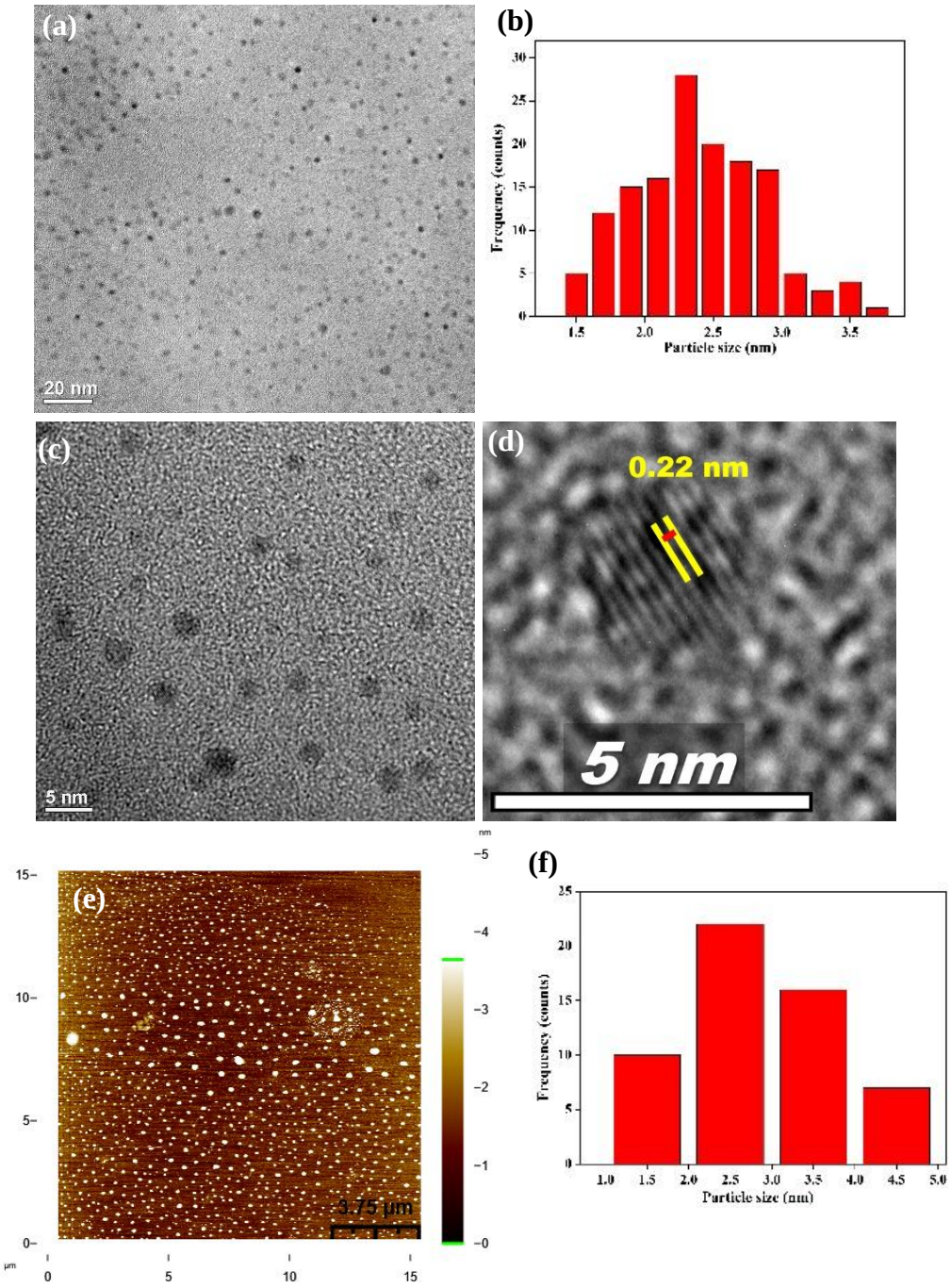

Figure 3.2: HRTEM images of carbon quantum dots at different magnification and scale: (a) 20 nm, (b) TEM particle size distribution histogram with an average particle size of 2.3 ± 0.5 nm (c) 5 nm, (d) graphitic core lattice fringes, (e) AFM image and (f) AFM particle size distribution histogram with an average particle size of 3.7 ± 1.7 nm.

The atomic force microscopy (AFM) image (**Figure 3.2e**) reveals the tomography of the as-synthesised NCQDs, distributed in the range from 1.0 to 9 nm (see **Figure 3.2 f**), with an average value of 3.5 ± 1.7 nm, and is consistent (within experimental error) with data from HRTEM.

X-ray photoelectron spectroscopy (XPS) was used to analyse the surface chemistry of CQDs (**Figure 3.3a**) and it shows peaks characteristic for carbon (*ca.* 286 eV) and oxygen (*ca.* 533 eV). The fitted C1s spectra (**Figure 3.3b**) peaks at 284.9 eV, 286.4 eV, 287.9 eV, and 289.2 eV can be assigned to the carbon atoms in the form of C=C bond (sp^2), O–C–O (sp^3), C=O (sp^2) and O–C=O (sp^2), respectively. Elemental analysis (inset **Figure 3.3c**) shows that CHFS synthesized CQDs contain 41.15 wt% oxygen and 58.85 wt% of carbon, concluding that CQDs are made of oxygen and carbon as it was expected by using glucose only.

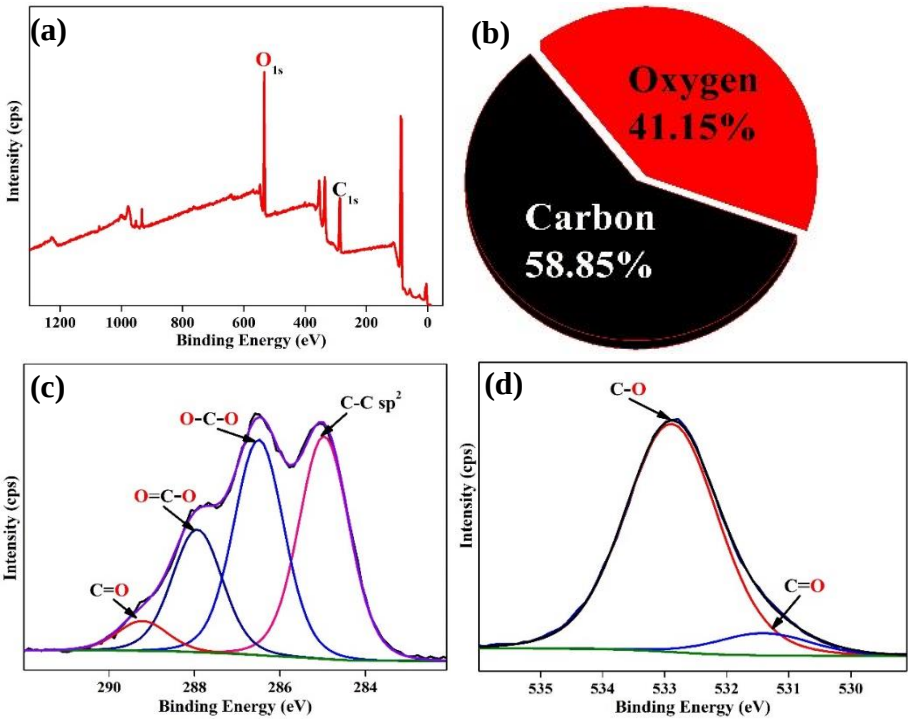

Figure 3.3:(a) XPS survey scans of carbon quantum dots, (b) elemental composition showing C(1s), and O(1s) content of CQDs, and high-resolution spectra of (c) C(1s) and (d) O(1s) regions.

The Raman spectrum of CHFS synthesised CQDs shown in **Figure 3.4a** was recorded to determine the presence of graphitic core (sp^2 hybridized carbon) and the sp^3 carbon. The Raman spectrum displays two broad peaks at 1384 and 1597 cm^{-1}, corresponding to D and G vibrational bands. The G-band is attributed to E_{2g} vibrational mode of graphitic core associated with the vibration of sp^2 hybridized carbon atoms, suggesting the aromatic character of CQDs. Furthermore, the I_D/I_G ratio of 0.83 indicates the predominance of the graphical core in the

CQDs. This I_D/I_G value lies somewhere between the values of thin graphite flakes and graphite oxide[335,336]. A smaller D-band peak indicates the presence of oxygen functionalities on the CQDs surface. The results are in agreement to XPS data which gave a C/O ratio of 1.7 (with (O1s: 36.74 at%).

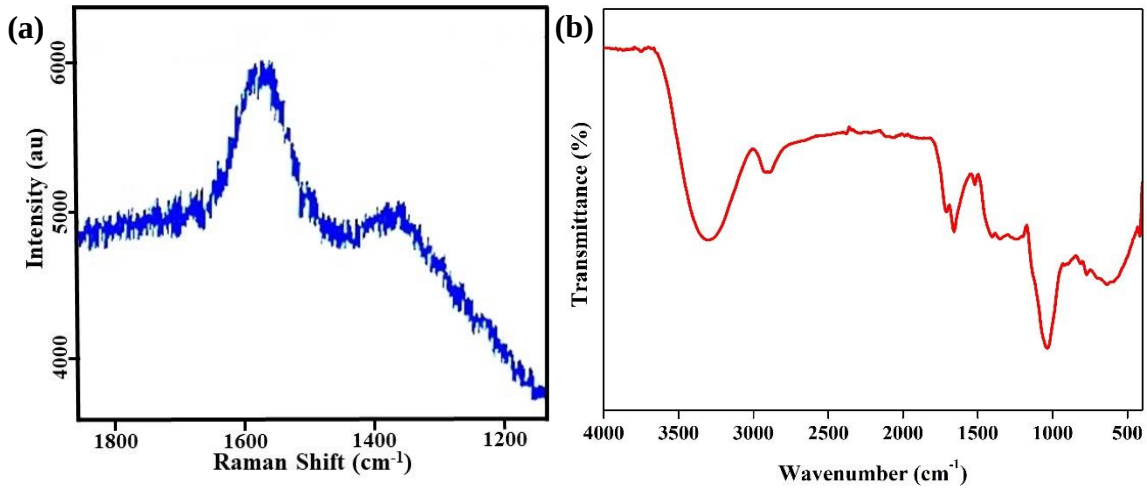

Figure 3.4: (a) Raman and (b) FTIR spectra of CQDs.

The Fourier transformation infrared spectroscopy **(FT-IR)** is shown in **Figure 3.4b** and it supports the XPS analysis. The broad absorptions band at 3302 cm^{-1} and 2900 cm^{-1} can be assigned to overlapping stretches for O–H (R-OH, -COOH), and C-H stretching vibrations, and the aromatic C-H vibrations can be observed at 640 cm^{-1}.The presence of oxygen functionalities on the CQDs surface can be observed in the FTIR spectrum by the following vibrations that could be assigned for stretches at 1712 cm^{-1} and 1658 cm^{-1} of C=O (COOH), and C-O and C-O-C vibrations may be assigned to stretches at 1357 cm^{-1} and 1033 cm^{-1}, respectively.[35]

The CQDs were measured with UV-Vis and the steady-state PL spectrophotometry. The characteristic specific absorption and emission properties recorded from aqueous solutions of CQDs and the pH influence over the emission properties are shown in **Figure 3.5**.

Figure 3.5 (a) shows the strongest absorbance for CQDs produced via CHFS. The UV-Vis spectrum displays two absorption bands that are characteristic of CQDs, the first at ~225 nm and the second peaking at 280nm. The 280 nm band can be ascribed to **π-π*** transitions for aromatic sp^2 domains in the graphitic core and the latter to **n-π*** transitions for C=O in the CQDs. The absorption band displayed at 225 nm can be attributed to the C=C and the C-C bonds[326].

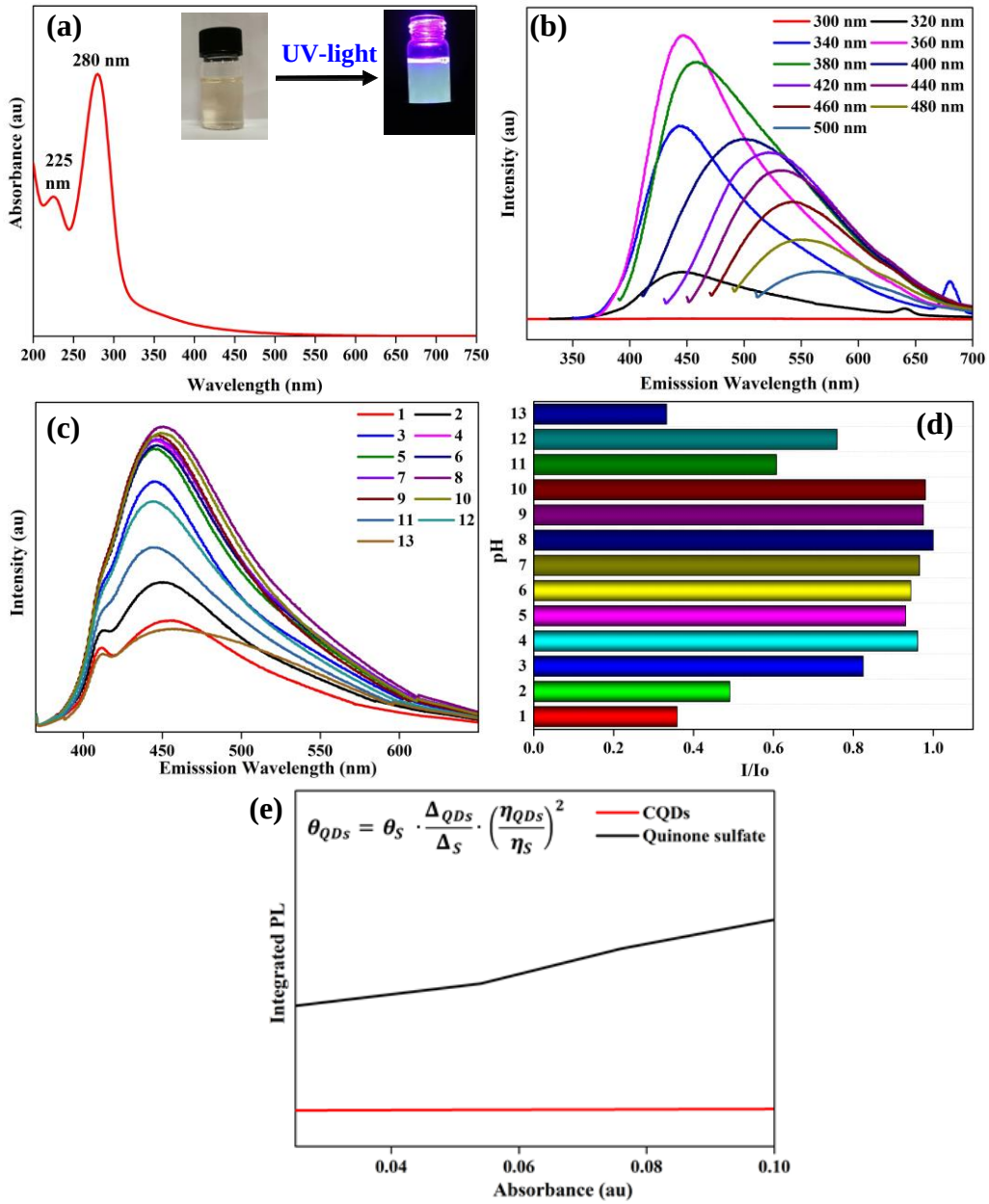

Figure 3.5: (a) UV-Vis absorption spectrum of carbon quantum dots, (b) photoluminescence spectrum of CQDs at excitation wavelengths between 300 – 500 nm showing excitation dependent behaviour. (c) pH influence over the emission intensity, (d) histogram of pH effect on the emission spectrum and (e) quantum yield determination *via* integrated fluorescence intensity vs absorbance plot method.

Photoluminescence (PL) was measured for the as-prepared CQDs under UV-Vis excitation wavelengths between 300–500 nm (see **Figure 3.5b**). The as-synthesized CQDs displayed an optimum excitation at 360 nm corresponding to blue fluorescence emission at 446 nm. A blue-shift and increased PL intensity were observed from 300 nm to 360 nm excitation wavelength. It was further noted that a red-shift and a consecutive decrease in PL intensity was

observed for 360 - 500 nm excitation wavelength (**Figure 3.5b**). The as-prepared CQDs exhibited a usually observed UV-Vis excitation dependent emission behaviour.[326,334] The red-shift character for lower energy excitations, may be ascribed to the π-π* graphitic core transitions of isolated sp^2 clusters[337]. The amount of the defects on the CQDs surface, reflected in the electronic structure and properties of CQDs particle, can be correlated with the oxidation degree which increases proportionally with the oxygen content in the CQDs.

To achieve sensitive and selective detection of different metal ions in different environments, the effect of pH can play an important role. The influence of pH on the fluorescence of CDs was investigated (**Figure 3.5c** and **d**). The fluorescence intensity of CQDs changes slightly within a broad pH range between 3 and 10, indicating that this pH range has a small to negligible impact over the emission properties of the CQDs. However, the fluorescence intensity of the CQDs is significantly reduced in strong acidic (pH=2 and pH=1) and strong basic (pH=13) media to 50% (against control intensity). A small but significant red shift occurs at pH=1 and pH=13. The diminishing intensity is a consequence of protonation of the carboxylate and phenolate groups which are randomly distributed on the CQDs surface. This phenomenon can relate to the missing emissivity, thus allowing emission from the graphitic core to behave prominent over the surface influence and it is reflected by the red shift of the spectrum. The quantum yield value of our sample was measured to be 0.3% (calibrated against quinine sulphate in 0.1 M H_2SO_4 as standard), comparable to most of the CQDs, reported in the literature, made of carbon and oxygen without any surface passivation processes[334,338].

3.2.2 Chromium (VI) and Fe (II) ion-sensing

Due to their fluorescent properties and their stability over a broad pH range (pH 3-10), CQDs have been tested as nano-sensors for chromium (VI) and iron (II) detection. The investigations follow to study their sensitivity for chromium (VI) and iron (II) and their selectivity over a range of environmentally relative anions and cations. These included the metal ions Na^+, K^+, Ca^{2+}, Mg^{2+}, Fe^{3+}, Co^{2+}, Ni^{2+}, Cu^{2+}, Zn^{2+}, Cr^{3+}, Ce^{3+}, Ag^+ and the anions: F^-, Cl^-, Br^-, I^-, NO_3^-, SO_4^{2-}, $HCOO^-$, CH_3COO^-, HCO_3^-, CO_3^{2-}, at concentrations of 50 ppm each in aqueous solutions.

The sensitivity of the CQDs fluorescent probe was investigated for Cr (VI) and Fe (II) detection. As shown in **Figure 3.6** the fluorescence of CQDs at around 446 nm is quenched after the addition of Cr (VI) (**Figure 3.6a, b**) and Fe (II) (**Figure 3.6d, e**), with the emission

intensity shown to be dependent on the concentration of Cr (VI) and Fe (II) species. The fluorescence peaks of [CQDs-Cr (VI)] [CQDs-Fe (II)] systems were stable at 446 nm; no peak shifting was observed. The emission intensity decreased linearly with the concentration of Cr (VI) (**Figure 3.6c**) and Fe (II) (**Figure 3.6f**).

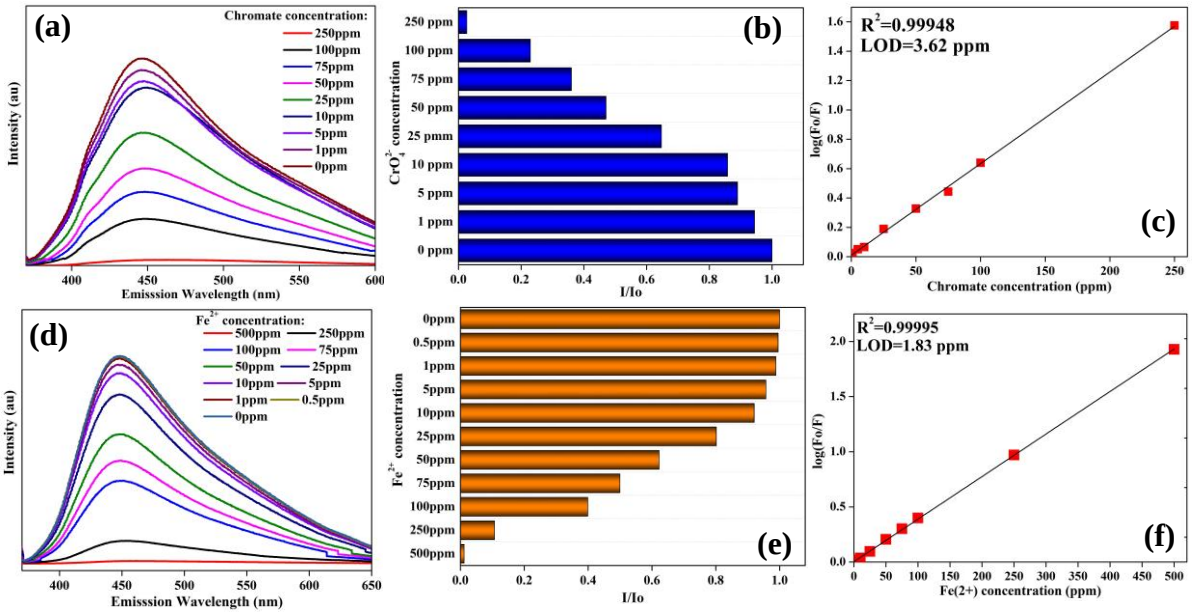

Figure 3.6: Sensitivity of the CQDs based sensor over Cr (VI) and Fe (II) ions. The influence on PL spectrum of CQDs on the fluorescence intensity changes in (a-c) Cr (VI) and (d-f) Fe (II) ppm concentration range with showing Stem-Volmer plot, log(F_0/F) versus concentration.

The Stern-Volmer relation plot showed a good correlation Cr (VI) (R^2 = 0.9994) and Fe (II) (R^2= 0.9999) giving a quenching constant K_{SV} value of 0.00624 (obtained from the slope of the line y = 0.00624x + 0.01108) for chromate anions (Cr (VI)) and a quenching constant K_{SV} value of 0.00386 (obtained from the slope of the line y = 0.00386x + 0.0383) for ferrous ions (Fe (II)).

The limit of detection (LOD) is calculated by using the following equation LOD = 3σ/K_{SV}, where σ is the standard error of the intercept. The LOD obtained value was 3.62 ppm for Cr (VI) (σ=0.00725) and 1.83 ppm for Fe (II) (σ=0.00232). The limit of quantification (LOQ = 10σ/K_{SV}) was 11.6 ppm for Cr (VI) and 6 ppm for Fe (II). Emission intensities at 446 nm for the pure CQDs, [CQDs-Cr (VI)], and [CQDs-Fe (II)] solutions **(Figure 3.7e**) had shown negligible variation over time when the samples were continuously excited at 360 nm for 1200 seconds. This stability of the measured signal over time reflects the suitability of the materials as a sensor for Cr (VI) and Fe (II) detection.

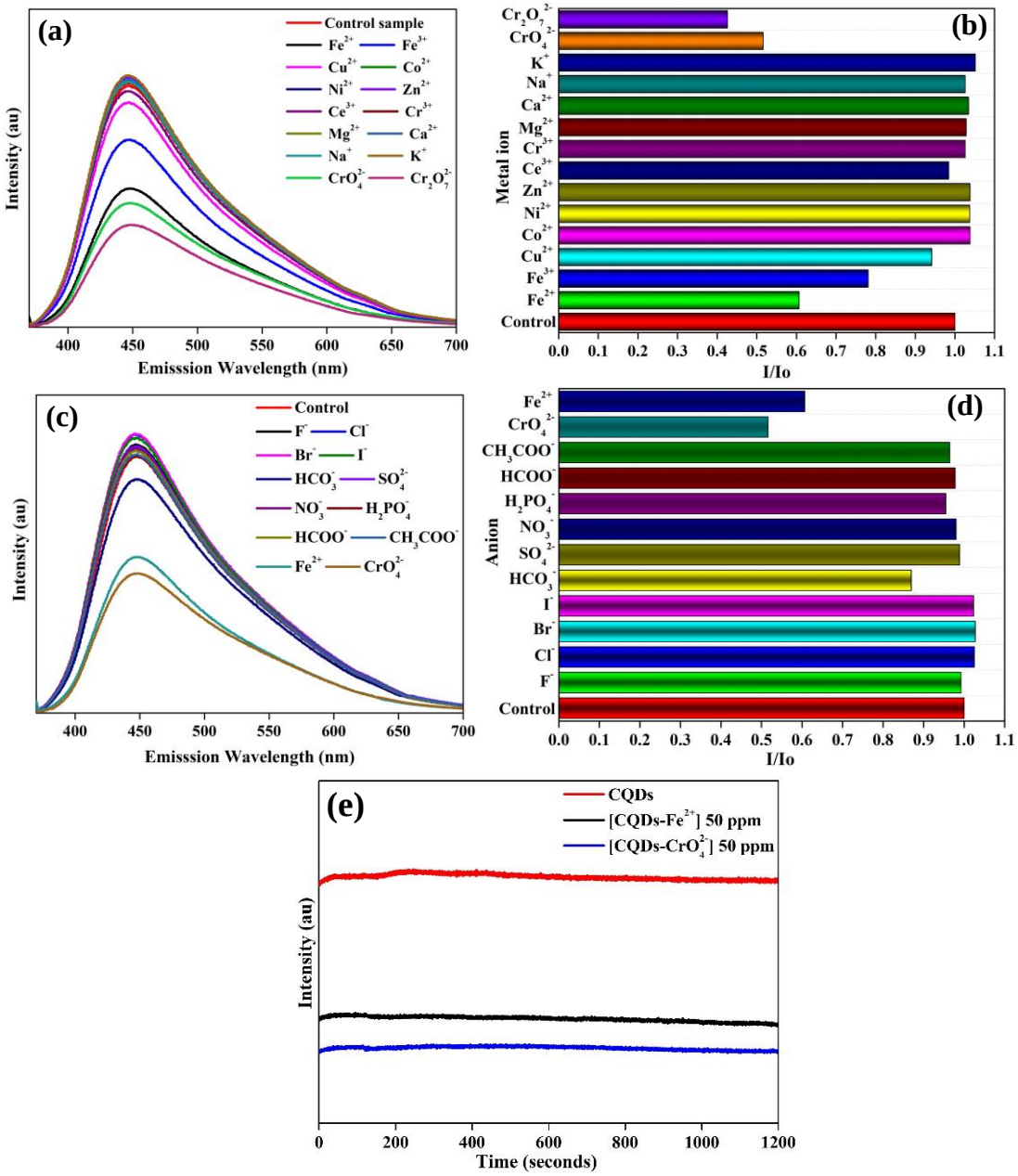

Figure 3.7: Selectivity of the CQDs based sensor over other (a-b) ions, (c-d) anions and (e) stability analysis of the CQDs in presence of Cr (VI) (50 ppm) and Fe (II) were made by recording the fluorescence intensity at 446 nm emission wavelength of the mixture exposed continuously for 1200 seconds (15 minutes) at 360 nm excitation.

The selectivity of CQDs nano-sensors for Cr (VI) and Fe (II) detection was analysed to prove that it has an independent response when it is in contact with other ions and anions (**Figure 3.7b, and d**). The CQDs nano-sensors exhibited limited/negligible quenching effect or fluorescence enhancement with minimal variation over other ions and anions. The selectivity for Cr (VI) and Fe (II) of the fluorescent probe was performed in triplicate for each ion and anion.

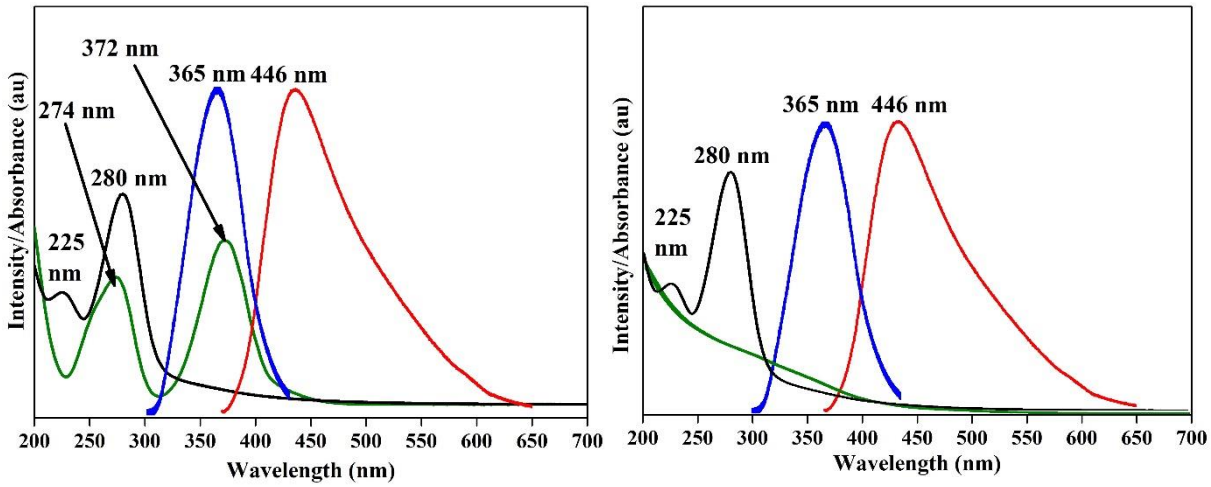

Figure 3.8: The Inner Filter Effect of (a) Chromate (CrO_4^{2-}) and (b) Ferrous (Fe^{2+}) ions representing the spectral overlap between the (a) chromate or (b) ferrous normalised UV-Vis absorption band (green line) CQDs normalised UV-Vis absorption band (black line), CQDs' excitation spectrum (emission wavelength λ_{em} = 446 nm) (blue line), and the emission spectrum (excitation wavelength λ_{ext} = 360 nm) (red line).

Due to the fact that there was no observed red-shift for the detection of Cr (VI) and Fe (II), comparing with the response of the CQDs nano-sensor when modifying with the pH of the environment when a red-shift of CQDs emission was found, it suggests a mechanism other than that involving the interaction of the CQDs surface between the functional groups and Cr (VI) or Fe (II) ions. The selectivity of the nano-sensors for Cr (VI) and Fe (II) can be attributed to a physical phenomenon called the Inner Filter Effect (IFE).

The Inner Filter Effect (IFE) is a physical phenomenon consisting of a spectral overlap of the absorption bands of the analyte (chromate (CrO_4^{2-}) anions or ferrous (Fe^{2+}) ions) with the excitation band and/or emission band of the substrate (CQDs) as described by the **Figure 3.8 a** and **b**. Due to the overlap of the absorption and emission band, fewer photons will reach the light measuring sensor, reflected in a decrease of the emission band intensity proportional to the concentration of the analyte. If the emission band of CQDs is overlapped on the absorption spectrum of the analytes, then most of the emitted photons by the CQDs are absorbed, the IFE having an even major impact on the CQDs PL spectrum.

The excitation spectrum for the CQDs has a maximum of emission bands at 365 nm and with its emission band centred at 446 nm (excitation at 360 nm), whereas the chromate (CrO_4^{2-}) anions have one of its absorption bands centred at 372 nm, with significant overlap of the maximum excitation band of the CQDs. The second absorption band of chromate (CrO_4^{2-})

anions at 272 is overlapped with the CQDs most intense absorption band at 280 nm. In the case of Fe (II) ions, there is a broadband of absorption starting at around 450 nm, with high values when overlap with the excitation and absorption spectra of CQDs.

All of these spectrum overlaps are generating an absorptive competition between the chromate anions ($[CrO_4]^{2-}$) or ferrous ions (Fe^{2+}) and the carbon quantum dots particles inside the same environment due to their well-defined electronic structure, smaller size and higher concentration in the solution comparing with the CQDs, the chromate ($[CrO_4]^{2-}$) anions and the ferrous (Fe^{2+}) ions have a higher efficiency of absorbing the radiation at 360 nm necessary for CQDs to generate the transition to the excited state, but also it can absorb the emitted photons from the CQDs, generating a signal decrease in the CQDs fluorescence intensity. The IFE mechanism has been previously explored and reported as an effective on-off, rapid and enhanced sensitivity approach to chromium (VI) and iron (II) sensing[95,339,340].

3.2.3 Conclusions

In conclusion, a continuous hydrothermal flow synthesis route was developed to synthesise carbon quantum dots starting from glucose as biomass tagged precursor. The photoluminescence studies for the CQDs exhibit an excitation dependent behaviour with a maximum emission peak at 446 nm when the sample is excited at 360 nm. Additionally, we demonstrated that the material displays a high selectivity and sensitivity for Cr (VI) and Fe (II), our new CHFS-produced CQDs suitable for environmental and biological sensing applications.

3.3 Continuous hydrothermal flow synthesis of N-doped carbon quantum dots from citric acid

3.3.1 Results and discussions

Carbon quantum dots are known for their chemical and physical properties, but specifically their optical properties, with an intense fluorescence in the visible range.[24,98,341] However, the materials often exhibit optical and structural heterogeneity as well as limited relevant synthetic approaches that do not readily facilitate large-scale production. We have explored and developed a rapid synthesis approach that delivers in a continuous mode, carbon quantum dots (control) and blue luminescent N-doped carbon quantum dots by simply using citric acid (carbon source), in the absence and presence of ammonia (N-precursor), respectively, both in water under supercritical conditions (24.8 MPa and study reaction

temperatures of 250 °C, 350 °C and 450 °C). The optimal temperature was 450 °C for the NCQDs synthesised using Continuous Hydrothermal Flow Synthesis (a single step approach as shown in **Schematic 4.2**) showing high homogeneity (narrow particle size distribution) and excellent optical properties (excitation independent fluorescence).

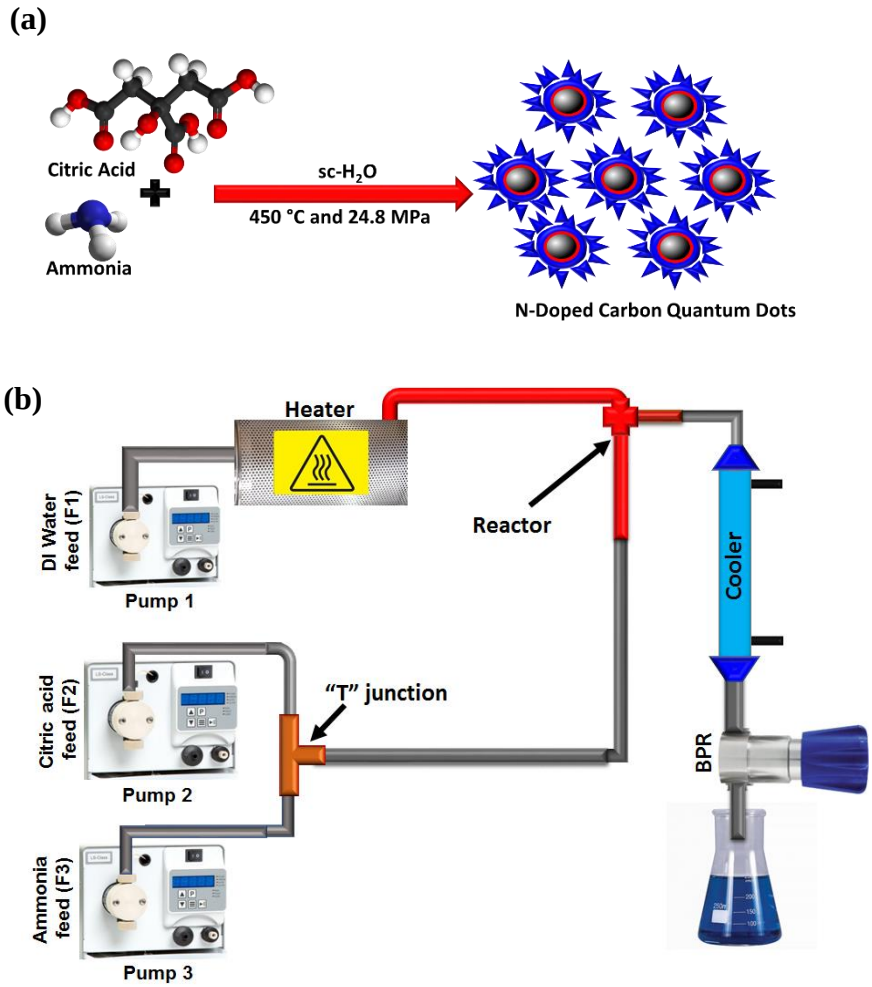

Schematic 3.1: Synthesis of N-doped carbon quantum dots (NCQDs) using Continuous Hydrothermal Flow Synthesis (CHFS) process: (a) illustration of the CHFS synthesis process using citric acid as carbon source and ammonia as N-dopant, (b) simplified CHFS design.

The optimal as-produced NCQDs were characterized using a variety of techniques, including UV-Vis absorption and emission (PL) spectrophotometry to examine the optical properties, FT-IR and Raman spectroscopy to determine electronic properties and functionalities, X-ray Photoelectron Spectroscopy (XPS) to determine the composition and surface chemistry, High-Resolution Transmission Electron Microscopy (HRTEM) analysis and Atomic Force Microscopy (AFM) for particle size analysis and structural morphology.

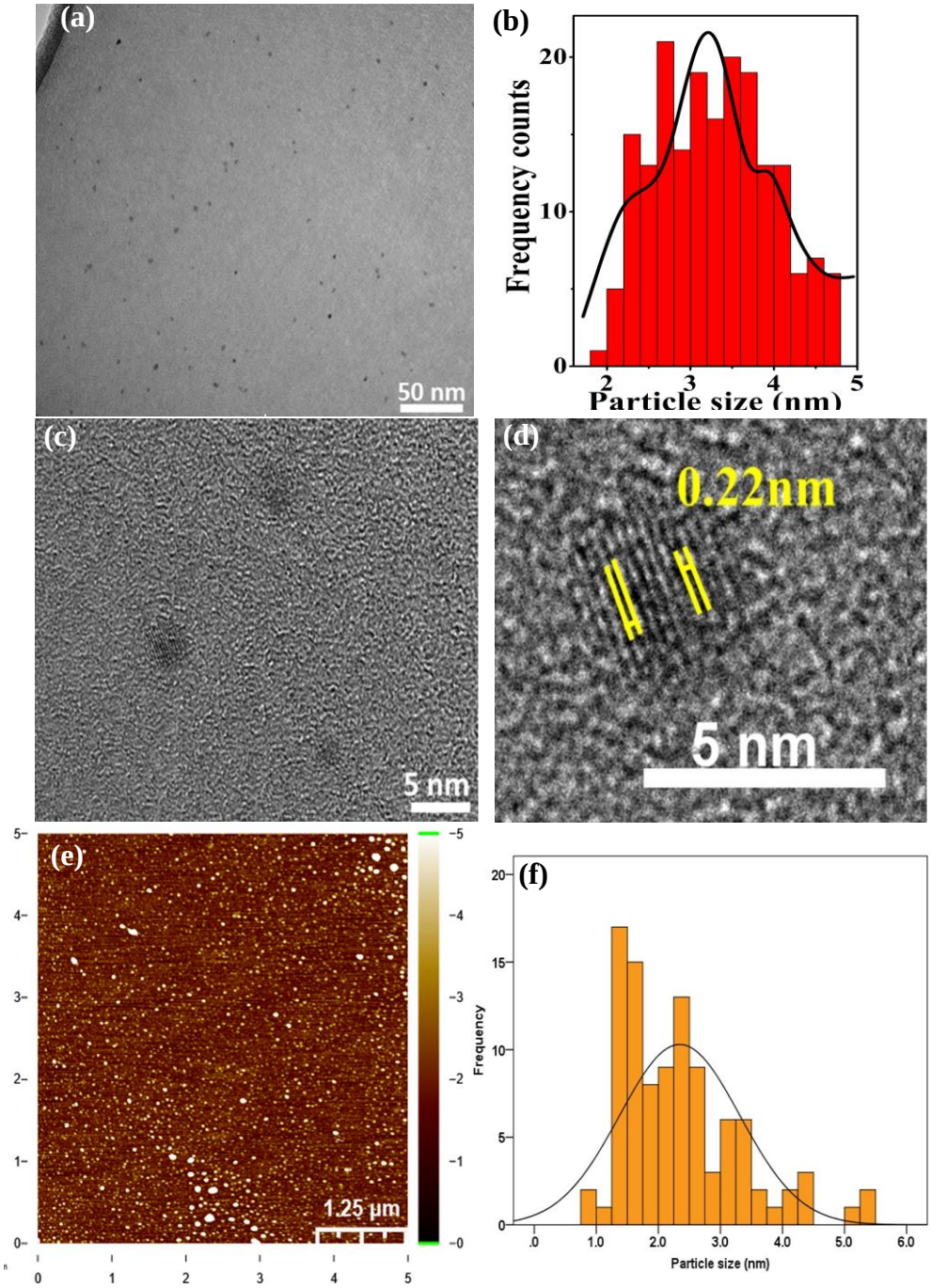

Figure 3.9: HRTEM images of N-doped carbon quantum dots at different magnification and scale: (a) 50 nm, (b) particle size distribution histogram with an average particle size of 3.3 ± 0.7 nm, (c) 5 nm (d) graphitic core lattice fringes, (e) AFM image and (f) inset showing particle size distribution histogram.

HRTEM images (**Figure 3.9a and c**) of the as-prepared NCQDs exhibit a quasi-spherical morphology with an average particle size of 3.3 ± 0.7 nm from a sample population of 190 particles ranging between 1.9 nm to 4.7 nm in diameter (**Figure 3.9b**). Each exhibited the same structural arrangement, indicating consistency in homogeneity for the CHFS

synthesized sample. The graphitic core arrangement of the carbon atoms (**Figure 3.9d**) can be clearly identified with an in-plane lattice spacing of 0.22 nm and is consistent with the reported literature data[342].

The atomic force microscopy (AFM) image (**Figure 3.9e**) reveals the tomography of the as-synthesised NCQDs, distributed in the range from 1.0 to 5.2 nm (**Figure 3.9f**), with an average value of 2.4 ± 1.0 nm, and is consistent (within experimental error) with data from HRTEM.

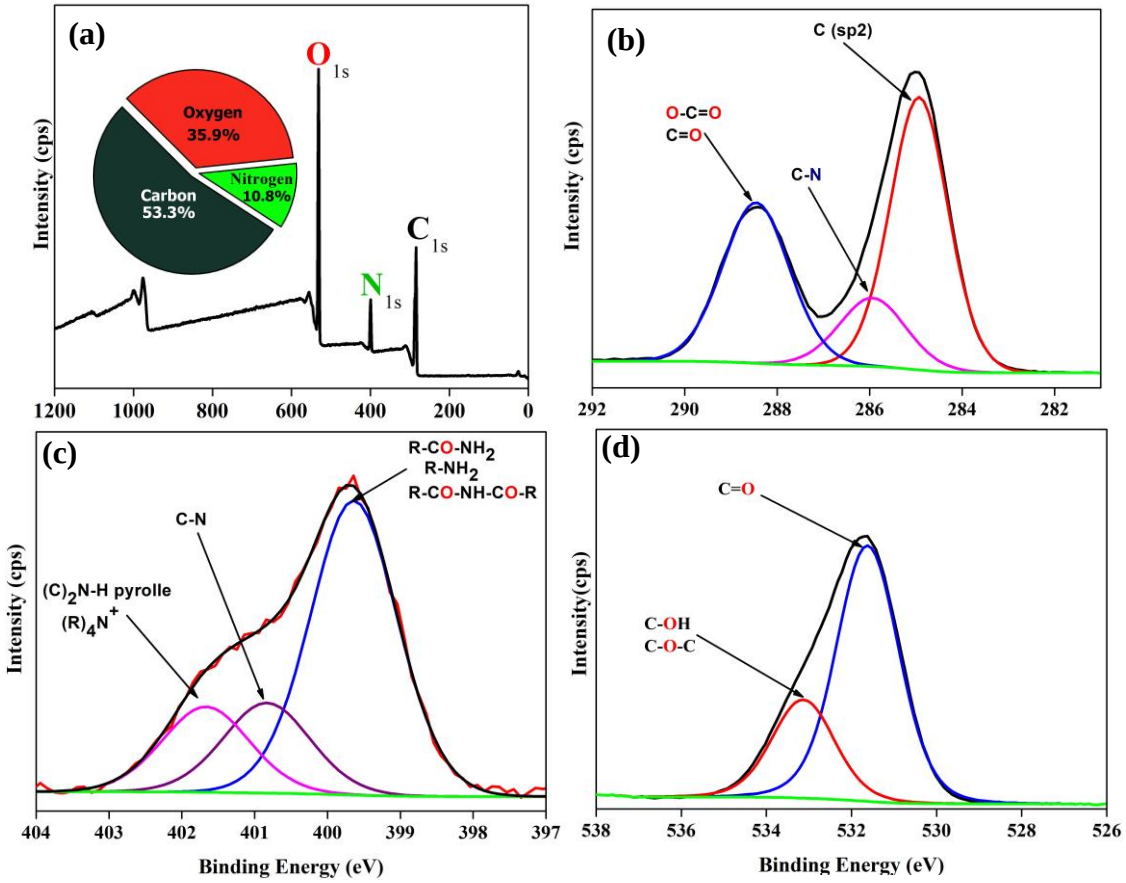

Figure 3.10: XPS survey scans of N-doped carbon quantum dots: (a) survey spectrum showing C(1s), N(1s) and O(1s) core levels, (b) – (d) fitted high resolution spectra of C(1s), N(1s) and O(1s) regions, respectively.

X-ray photoelectron spectroscopy (XPS) measurements were performed for the surface characterization of NCQDs (**Figure 3.10a**) and revealed peaks typical for the presence of carbon (*ca.* 285 eV), nitrogen (*ca.* 399 eV) and oxygen (*ca.* 531 eV). The fitted C1s spectra (**Figure 3.10b**) peaks at 284.9 eV, 285.9 eV, and 288.4 eV can be assigned to the carbon atoms in the form of C=C bond (sp^2), C–N (sp^3), C=O (sp^2) and O–C=O (sp^2), respectively, whilst the fitted N(1s) spectrum (**Figure 3.10c**) exhibits three peaks at 399.7 eV, 400.8 eV, and 401.6 eV, indicating that the nitrogen exists in pyrollic/amino N-H, protonated pyridinic N, and

graphitic-N (sp^3) forms respectively, signifying that the nitrogen atoms were efficiently doped into the structure[343]. Elemental analysis (inset Figure 2a) shows that CHFS synthesised NCQDs contain 35.9 wt% oxygen, 10.8 wt% nitrogen and 53.3 wt% of carbon (see inset **Figure 3.3a**), concluding that NCQDs are nitrogen-doped and carbon-rich.

The Raman spectrum for the NCQDs (**Figure 3.11a**) displayed two broad peaks at 1392 and 1591 cm^{-1} which correspond to the D and G bands, respectively. The G band is attributed to an E_{2g} mode of vibration of sp^2 bonded carbon atoms associated with the graphitic core and is in good agreement with the HRTEM lattice spacing image described previously for the NCQDs (**Figure 3.9d**). The smaller D band peak is due to the presence of a medium level of oxygen content (35.9 wt%) and the presence of sp^3 carbon atoms; the results are complimentary with the XPS data (see **Figure 3.10**). The relative intensity ratio of the observed bands (I_D/I_G) gave a value of ~ 0.76 for the NCQDs, typical of graphene oxide[30].

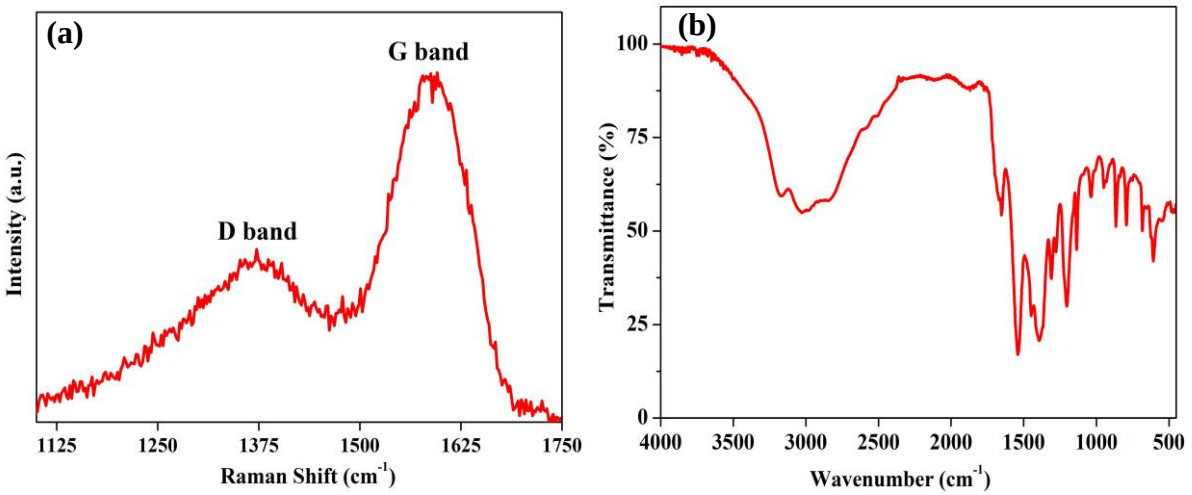

Figure 3.11: (a) Raman and (b) FTIR spectra of N-doped CQDs.

The FT-IR spectroscopy (**Figure 3.11b**) further supports the XPS analysis. A broad absorption band (3450-2400 cm^{-1}) can be ascribed to overlapping stretches that encompass those for O–H (R-OH, -COOH), amine and protonated amine ($N\text{-}H^+$, $N\text{-}H_2^+$, $N\text{-}H_3^+$) stretches, and C-H stretching vibrations (3028 cm^{-1} and 2835 cm^{-1}). The presence of protonated and deprotonated species is plausible with carboxylates and amine groups in proximity on the NCQDs. Other stretches observed include pyridinic C=N at 1652 cm^{-1}, a stretch which could also be attributed to an amino-vibration (-NH or $-NH_2$). The amino vibrations could also be assigned for stretches at 864 cm^{-1} and 792 cm^{-1}, as well as carbonyl (COO-) stretches at 1541 cm^{-1} and 1394 cm^{-1}, asymmetric vibrations for C-NH-C at 1136 cm^{-1}, and C-O and C-O-C vibrations may be assigned to stretches at 1202 cm^{-1} and 1035 cm^{-1}, respectively[343].

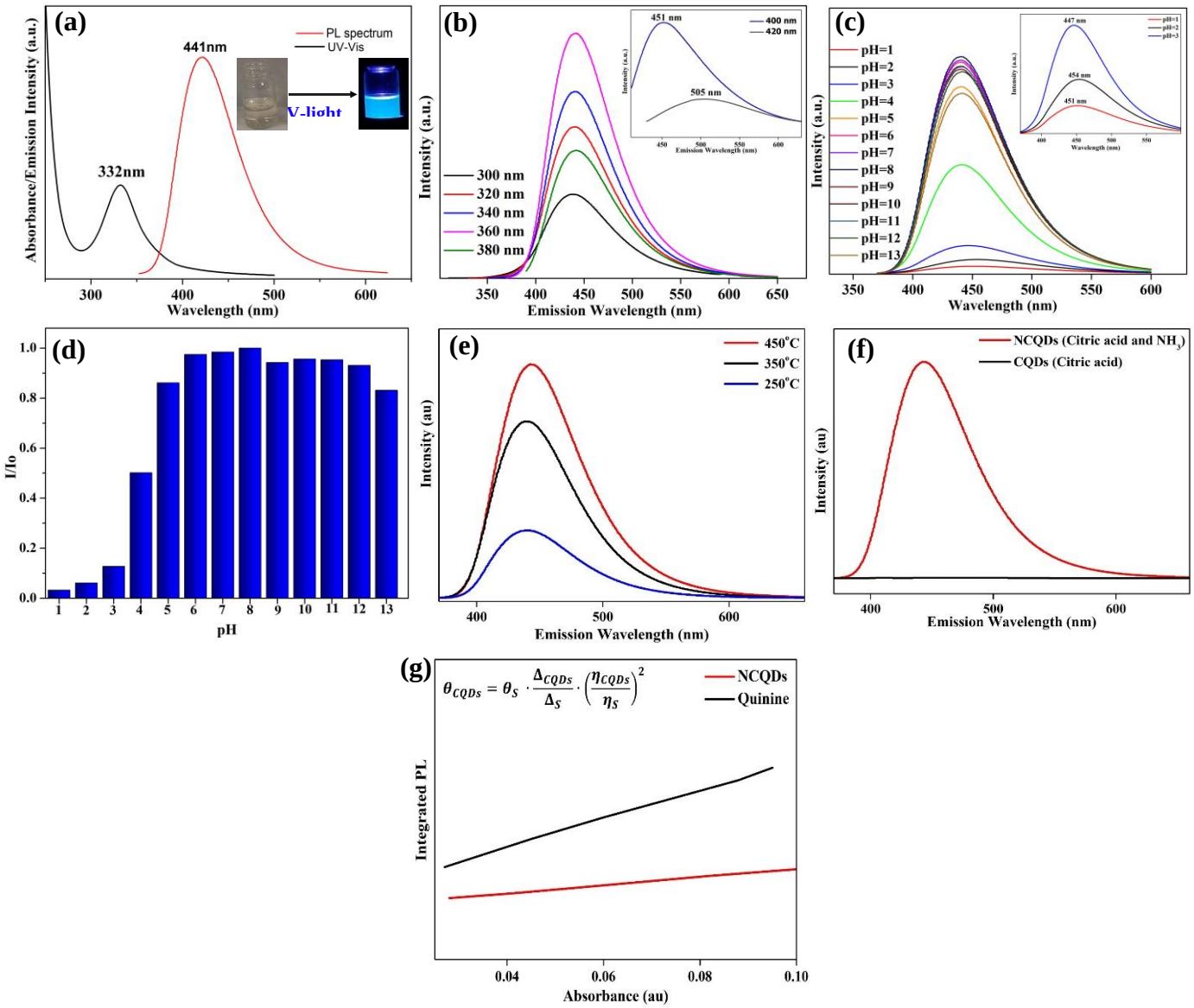

Figure 3.12: (a) UV-Vis absorption spectrum (black curve) and photoluminescence (PL) spectrum (red curve) of carbon quantum dots at 360 nm excitation wavelength. (b) NCQDs excitation at wavelengths 320 – 380 nm gave emission spectra showing excitation independent optical behaviour, but excitation from 400 - 420 nm showed excitation dependent behaviour (inset). (c) pH influence over the emission intensity and (d) histogram of pH effect on the emission spectrum and photoluminescence spectrum of N-doped carbon quantum dots at 360 nm excitation wavelength (e) showing the effect of CHFS reaction temperature (all other conditions were kept the same), (f) comparison of the PL spectra of N-doped CQD (synthesised using citric acid and ammonia) and control reaction (CQDs) synthesised from citric acid only showing negligible photoluminescence (the synthesis reaction temperature in both cases was kept at 450°C) and (g) quantum yield determination *via* integrated fluorescence intensity vs absorbance plot method.

The NCQDs were analysed with UV-Vis and the steady-state PL spectrophotometry. The characteristic specific absorption (black curve) and emission bands (red curve) recorded from aqueous solutions of NCQDs are shown in **Figure 3.12**. **Figure 3.12 (a)** shows the strongest absorbance and emission band for NCQDs produced via CHFS. The UV-Vis spectrum displays two absorption bands that are characteristic of NCQDs, the first at ~250 nm and the second peaking at 332 nm (broad absorption band from 300 nm tailing to 480 nm). The former band can be ascribed to π-π* transitions for aromatic sp^2 domains in the graphitic core and the latter to n-π* transitions for C=O in the NCQDs[344, 345]. The absorption band displayed below 250 nm can be attributed to the C=C and the C-C bonds.

Photoluminescence (PL) was observed for both the as-prepared NCQDs and the CQDs (control) under UV excitation with wavelengths ranging from 300 – 420 nm. The control material, CQDs synthesised from citric acid only, showed negligible photoluminescence (see **Figure 3.12f**). The NCQDs, on the other hand, displayed an optimum excitation at 360 nm corresponding to blue fluorescence emission at a consistent 441 nm for each excitation (**Figure 3.12b**) and a redshift lower intensity emission for lower energy excitation at 400 nm and 420 nm. The as-prepared NCQD material exhibited a rarely observed UV excitation independent emission behaviour[346,347]. We attribute this zero-tunability (320 - 380 nm) behaviour to surface state defects of the NCQDs, which is also commonly associated with a blue emission, a feature that has been reported for r-GO, GQDs and CNDs. The redshift character due to the observed emission for lower energy excitations may be ascribed to the π-π* transitions (of isolated sp^2 clusters) within the graphitic carbon cores[337]. The proportion of surface defects are correlated with the degree of surface oxidation with the increasing presence of oxygen atoms in the make-up of the surface structure of CQDs, which typically leads to further reducing the bandgap, *i.e.* a redshift of PL. However, given the excitation independent blue-luminescent for the as-prepared NCQDs, the process of nitrogen doping as compared to the control has had a significant impact on the optical properties (**Figure 3.12f**).

Since pH can play pivotal roles in various environmental and biological systems, the impact of pH on the NCQDs performance as a sensor is of significance. The pH-dependent behaviour of the NCQDs was explored (**Figure 3.12c and d**), were mildly acidic, and alkali media have had a small to negligible impact on fluorescence stability showing the NCQDs to be stable over a broad pH range of 5-12. However, the fluorescence intensity of the NCQDs is significantly reduced in acidic media to 50% (against control intensity) at pH=4 and reduced further to just 13% at pH=3 and 3% at pH=1. A small but significant redshift occurs from pH=3

to pH=1. Similar observations have been made by Zhu *et al.*[321] (for their excitation dependent N-doped CQDs hydrothermally synthesised from citric acid and ethylenediamine) and Dong e*t al.*[347] (for the N,S-CQDs), but neither adequately rationalise for the redshift. The diminishing intensity is a consequence of protonation of the nitrogen and carboxylate groups disrupting the surface charge and its associated emissivity, thus allowing emission from the graphitic core to come to prominence over that of the surface as reflected by the redshift of the PL. The red-shift feature of the luminescence highlighted earlier is excitation dependent. At pH=13 there is also a reduction in emission intensity versus control. Furthermore, the NCQD material exhibited resistance to photo-bleaching, with PL intensity remaining stable for 6 months. The quantum yield value of our sample was measured to be 14.91 ± 0.24% (see **Figure 3.12g** calibrated against quinine sulphate in 0.1 M H_2SO_4 as standard), comparable to many literature reports for CQDs[341].

Typically, excitation dependent emission is a common feature of N-doped CQDs but tend to display complex emission spectra that are difficult to decipher in practical applications. Thus, single emission NCQDs are highly desirable. Our CHFS synthesised material uniquely exhibits the following: excitation independence with a narrow FWHM (~78 nm, where 100 nm is typical for CQDs[344]) and remoteness of the fluorescence emission (441 nm) from the UV excitation range (320 – 380 nm) - that usefully avoids auto-luminescence. Each of which is desirable features for sensor applications and more so when combined. These characteristics will ultimately allow this material to be uniquely suitable in a range of practical applications, such as chromate anion (Cr (VI)) detection, for example, a severe and highly toxic environmental pollutant even at trace (low mg L^{-1}) levels.

3.3.2 Chromium (VI) ion-sensing

Given the fluorescent properties of the NCQDs and their stability over a broad pH range (pH 5-12), investigations with respect to their interactions with and selectivity for, were undertaken for a range of environmentally relative anions and cations. These included the metal ions Na^+, K^+, Fe^{2+}, Co^{2+}, Ni^{2+}, Cu^{2+}, Zn^{2+}, Ce^{3+}, Ag^+ and the anions: F^-, Cl^-, Br^-, I^-, NO_3^-, SO_4^{2-}, CH_3COO^-, HCO_3^-, and the Cr (VI) anions CrO_4^{2-} and $Cr_2O_7^{2-}$ at concentrations of 50 ppm each in aqueous solutions. These included the metal ions Na^+, K^+, Fe^{2+}, Co^{2+}, Ni^{2+}, Cu^{2+}, Zn^{2+}, Ce^{3+}, Ag^+ and the anions: F^-, Cl^-, Br^-, I^-, NO_3^-, SO_4^{2-}, CH_3COO, HCO_3^-, and the Cr (VI) anions, CrO_4^{2-} and $Cr_2O_7^{2-}$ at concentrations of 50 ppm each in aqueous solution.

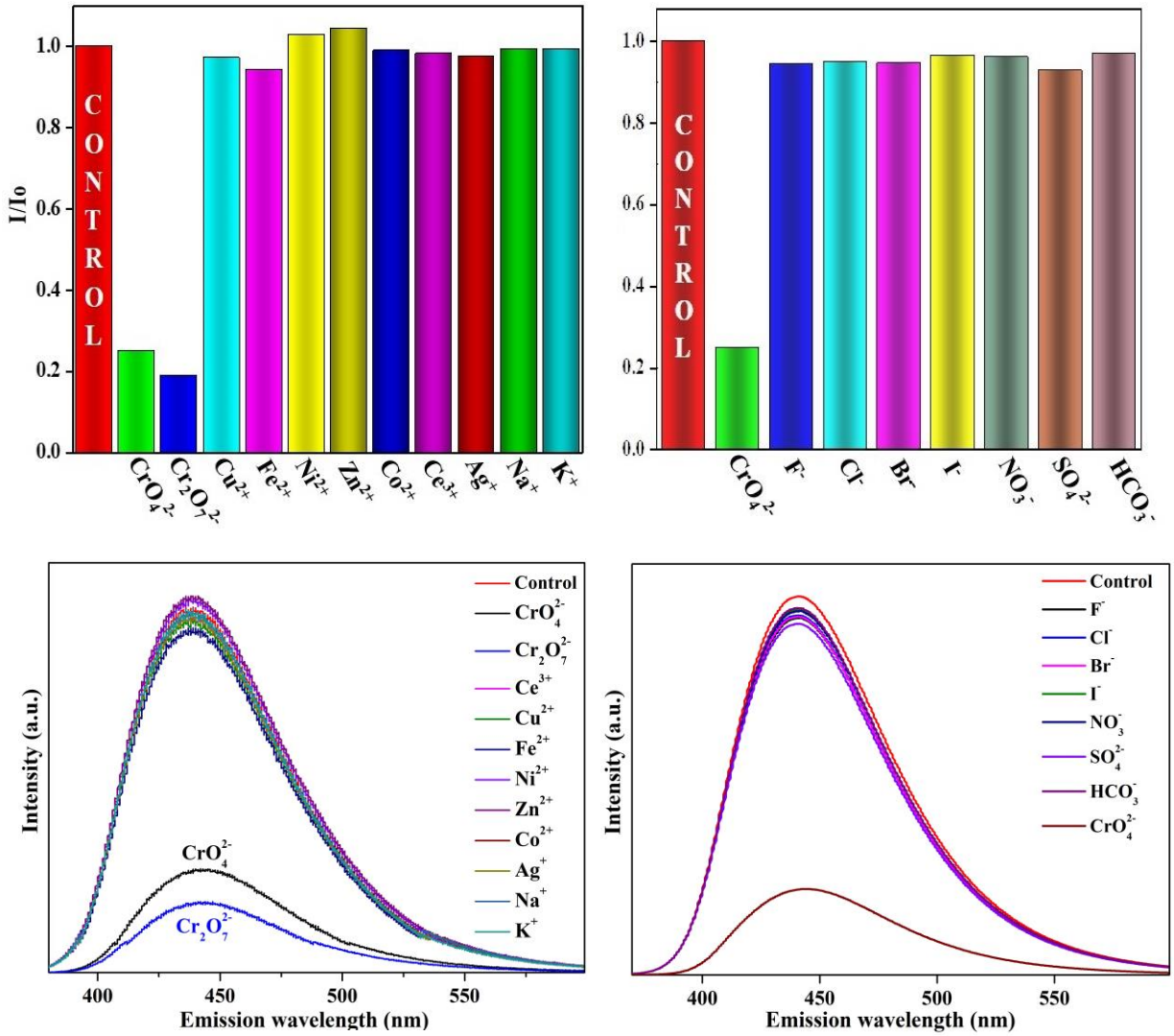

Figure 3.13: Selectivity of the N-doped CQDs based sensor over other ions and anions.

Sole selectivity for Cr (VI) detection was observed by significant fluorescence quenching of the NCQDs upon the addition of either Cr (VI) species (**Figure 4.13**), whilst the other ions exhibited limited/negligible quenching effect or fluorescence enhancement with minimal variation. This selectivity for Cr (VI) (CrO_4^{2-}/$Cr_2O_7^{2-}$) by the NCQDs fluorescent probe was further investigated regarding their sensitivity based on the PL spectra of NCQDs with a range of prepared concentrations of CrO_4^{2-}, each performed in triplicate. As shown in Figure 6 the fluorescence of NCQDs at around 441 nm is quenched after the addition of Cr (VI), with the emission intensity shown to be dependent on the concentration of Cr (VI) species. The fluorescence peaks of [CQDs-Cr (VI)] system was stable at 441 nm; no peak shifting was observed.

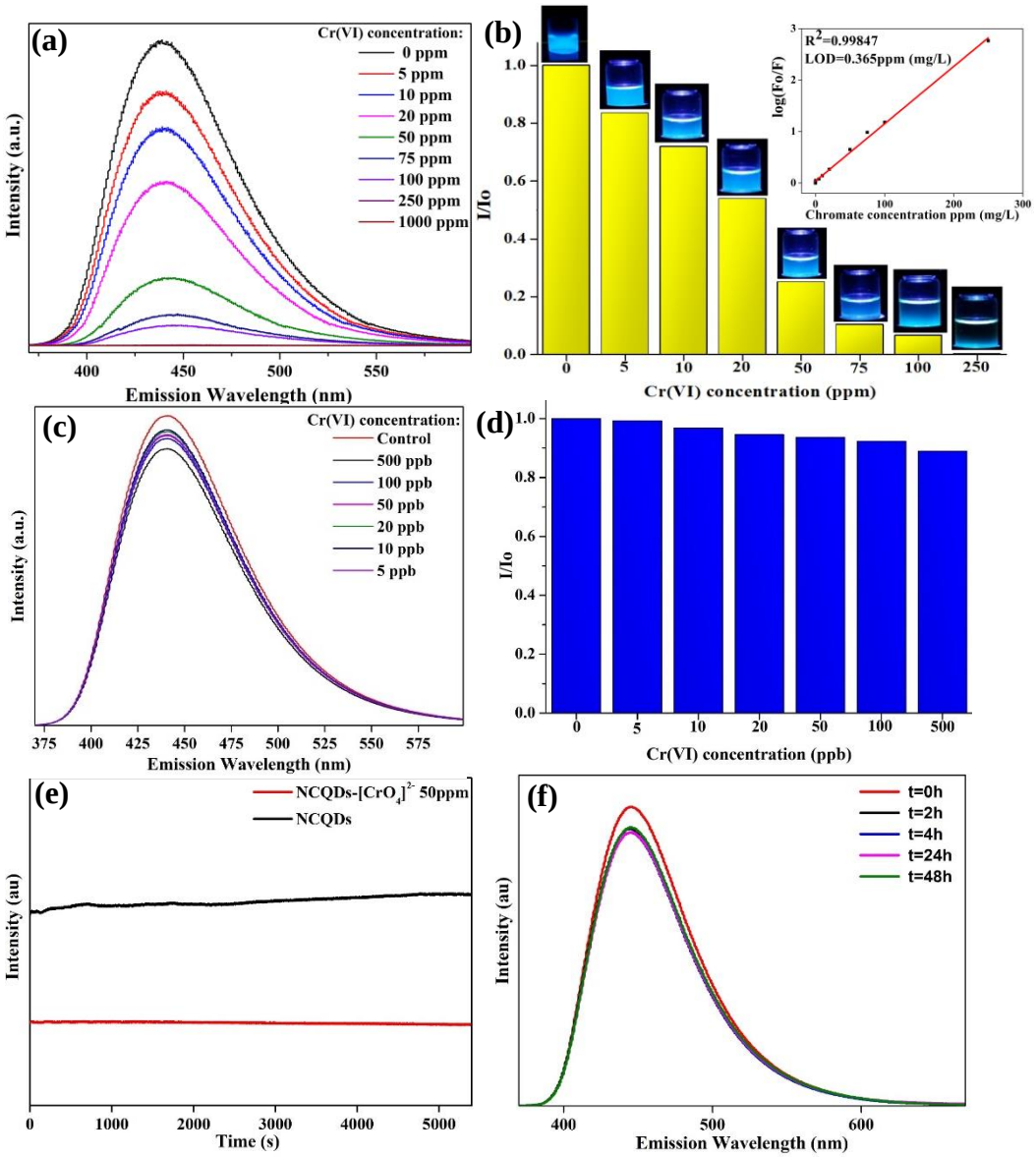

Figure 3.14: (a, b) Chromium (VI) ions influence on PL spectrum of N-doped CQDs in reflecting the intensity changes in ppm concentration range with (inset) showing Stem-Volmer plot, log(F_0/F) versus concentration, (c, d) chromium (VI) ions influence on PL spectrum of N-doped CQDs in reflecting the intensity changes in ppb concentration range and stability analysis of the NCQDs in the presence of chromium (VI) (50 ppm) were made by recording the fluorescence intensity at 441 nm emission wavelength of the mixture - (e) samples were initially exposed continuously for 5400 seconds (90 minutes) at 360 nm excitation, and (f) then at intervals of 2 hr, 4 hr, 24 hr and 48 hr.

The fluorescence intensity of NCQDs decreased linearly with the concentration of Cr (VI) (**Figure 3.14**). Stern-Volmer relation plot (inset **Figure 3.14 b**) showed a good correlation (R^2 = 0.998) giving a quenching constant K_{SV} value of 0.01113 (obtained from the slope of the

line y = 0.01113x + 0.03897). The limit of detection (LOD) is calculated as follows: LOD = $3\sigma/K_{SV}$, where σ is the standard error of the intercept. The LOD obtained value was 0.365 ppm, and the limit of quantification, LOQ = $10\sigma/K_{SV}$ was 1.218 ppm. Emission intensities at 441 nm for the pure NCQDs and [NCQDs-Cr^{6+}] solutions **(Figure 3.14c**) had shown negligible variation when the samples were continuously excited at 360 nm for 90 minutes. Further interval measurements of [NCQDs- Cr^{6+}] solution revealed just an 8.3% diminishment in emission intensity over 48 hours (see **Figure 3.14b**). This stability of the respective systems reflects the suitability of the material as a sensor for Cr (VI) detection.

Given that there was no observed red-shift for the Cr (VI) studies with the NCQDs, contrary to that to the findings of the NCQDs pH study, and no observed absorption peak shifts for UV–Vis spectra of the Cr(VI) and NCQDs mixture compared to Cr (VI) and NCQDs controls, suggests a mechanism other than that involving Cr(VI)-NCQD surface interactions. The selectivity of the CHFS-synthesised NCQD towards Cr (VI) can be attributed to the Inner Filter Effect (IFE). The IFE occurs where there exists a spectral overlap between the absorption bands of the chromate (CrO_4^{2-}) and the excitation band and/or emission band of the NCQDs as shown in **Figure 4.15**.

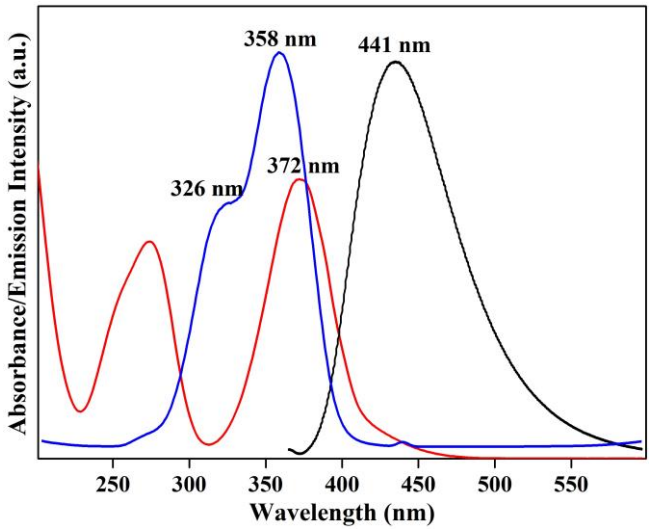

Figure 3.15: The Inner Filter Effect of Chromate (CrO_4^{2-}) representing the spectral overlap between the chromate normalised UV-Vis absorption band (red line), N-doped CQD's excitation spectrum (emission wavelength λ_{em} = 441 nm) (blue line), and the emission spectrum (excitation wavelength λ_{ext} = 360 nm) (black line).

The excitation spectrum for the NCQDs has two overlapping bands at 326 nm and 358 nm with its emission band centred at 441 nm (excitation at 360 nm), whereas the chromate (CrO_4^{2-}) has one of its absorption bands centred at 372 nm, with significant overlap of the

maximum excitation band of the NCQDs (see **Figure 3.15**). These factors generate an absorptive competition between anion units and NCQDs particles inside the solution, moreover, not only is the chromate effectively absorbing the radiation at 360 nm necessary for NCQDs to generate the transition to the excited state, but it can also absorb emitted light from the NCQDs, translating to a quenching of the NCQDs fluorescence. The quenching mechanism, IFE, has been previously reported as an effective on-off, rapid and enhanced sensitivity approach to chromium (VI) sensing [95,348].

3.3.3 Conclusions

In conclusion, a continuous hydrothermal flow synthesis route was developed for the synthesis of carbon rich, nitrogen-doped carbon quantum dots starting from citric acid and ammonia as precursors. The photoluminescence studies for the NCQDs demonstrated excitation independent behaviour with the emission peak at 441 nm due to the diversity of functional groups surface coverage from N-doping of the CQDs. Furthermore, we provide the proof of principle application that in aqueous solutions the materials display a high selectivity and sensitivity for Cr (VI), rendering our materials suitable for environmental applications. The materials may also be applied in a spectrum of applications including photovoltaics, bio-tagging, energy storage and beyond.

3.4 Summary conclusions

The green synthesis of nanomaterials with tailored properties oriented to specific applications has attracted high interest. In this work, we succeeded to expand the CHFS materials portfolio to the next generation of materials such as carbon quantum dots from biomass related carbon-source. The CHFS carbon quantum dots were tested for carcinogenic hexavalent chromium (Cr (VI)) ions nano-sensing. Using a CHFS approach we succeeded to synthesize carbon quantum dots (CQDs) from biomass related sources such as glucose and citric acid and accomplish the nitrogen-doping of rarely observed optical properties (excitation independent) CQDs using a simple and economical nitrogen source (NH_3) for the first time using this synthetic methodology.

The CHFS CQDs possess different optical properties by varying the carbon source: CQDs from citric acid exhibit intense excitation independent emission, meanwhile the CQDs from glucose have weak excitation dependent emission, but with similar mean particle size. The materials were successfully tested for carcinogenic Cr (VI) ions with a promising limit of detection (0.36 ppm for citric acid CQDs and 3.6 ppm for glucose CQDs) by only using their

optical properties. The CQDs nano-sensor manifest a high selectivity and sensitivity for Cr (VI), the mechanism behind the photoluminescence spectrum (PL) quenching phenomena was identified as the inner filter effect (IFE).

3.5 Future works

The continuous hydrothermal flow synthesis of carbon quantum dots achieved during this PhD research project has been recognized as an important progress in the field of hydrothermal synthesis of nanomaterials, and the research article was selected in the 2021 Journal of Materials Chemistry A and Materials Advances Editor's choice issue by Dr Miriam M. Unterlass[349]. This demonstrates the significance and the potential of this synthetic hydrothermal exploration for material science and biomass utilisation. The CHFS study can be easily expanded to other biomass-related molecules such as fructose, cellulose, lignin, or even raw biomass.

Another CHFS exploration in the CQDs field is the doping process, researching different nitrogen sources such as amine, imine, amino-alcohols, other dopants such as sulphur, phosphorus, boron, or co-doping. This study can provide more information about how the nature of dopants, or the doping source can influence the CQD's properties, such as particle size, solubility, optical and electronic properties, or cytotoxicity.

In terms of applications, the as-synthesised CQDs and NCQDs present promising characteristics to be tested for photocatalysis, photothermal conversion solar cells or bio-imaging. Some explorations have been already done; they will be subject of a future research article, the data collected so far was not enough to be included in the Thesis.

Chapter 4: Continuous hydrothermal flow synthesis of reduced graphene oxide for water treatment

4.1 Introduction

Graphene is the first discovered 2D material[51], made of a single layer of sp^2 carbon atoms, and it has unprecedented physical and chemical properties, including high surface area, extreme mechanical strength and flexibility, high chemical stability, exceptional optical and electronic properties and biocompatibility. All of these properties hold enormous potential for a wide range of applications in fields such as optoelectronics[350], electronic devices[351], catalysis[352], conductive ink[353], bio-applications[354], and environmental applications[228].

Graphene is currently synthesised using a variety of synthetic routes and methodologies, including chemical vapour deposition[187], wet[355] dry[356], chemical synthesis, mechanical exfoliation[83], microwave[357] and high-power ultrasound[358] assisted delamination. The synthetic methods are classified into two main strategies: top-down and bottom-up, or alternatively noted as graphite or non-graphite based synthetic process[359]. The material's key characteristics, such as morphology, defects, and elemental composition, are heavily influenced by the synthetic process[360]. Despite considerable progress, producing high-quality graphene-derived materials on a large scale remains difficult. As a result, preparing high-performance 2D graphene sheets through green synthetic routes is both desirable and critical because defects or doping atoms, as well as the C/O ratio, can affect the materials' properties and their end applications. Herein, in this work, we report the use of the Continuous Hydrothermal Flow Synthesis (CHFS) method as a unique approach towards 2D reduced graphene oxide manufacture via a top-down route that involves bulk modification/exfoliation of the currently available precursor, graphene oxide.

Continuous Hydrothermal Flow Synthesis (CHFS) is a single-step process, classified as environmentally friendly and green, and it employs the mixing (in a flow reactor) a feed of superheated water with one or more feeds of water-soluble precursor(s) to deliver a well-controlled, continuous, and fast synthesis of a variety of nanomaterials and nanocomposites[11]. A CHFS process provides real-time controls over the synthetic parameters such as temperature, residence time, pressure, reactant concentration to deliver a variety of surface functionalization of the 2D materials (through a chemical process such as oxidation, reduction, decomposition, condensation, etc.) in terms to reach the required characteristics for targeted applications[361]. To

the best of our knowledge, our group has pioneered and lead the utilization of the CHFS approach in 2D materials synthesis, including graphene quantum dots[298,303,307].

Characterised by a high physical and chemical stability and excellent mechanical and morphological properties, graphene, reduced graphene oxide and graphene oxide are ideal material candidates for membrane preparation for gas separation[362] and water treatment[363,364]. The reduced graphene oxide produced in a continuous hydrothermal flow synthesis process using a simple organic reducing agent can generate optimal surface chemistry of the material required in a solid-layer membrane preparation. Graphene in reduced form, with low oxygen content and controlled surface in oxygen-functionalities can act as an efficient building block material to assembly a performant barrier for pollutants[365,366].

According to the United Nations World Water Development Report[367] and International Water Association Report[368] on wastewater, approximately 80% of the worldwide wastewater volume is discharged untreated into waterways. This current situation is causing health emergencies, environmental issues, and/or climate-related hazards. The composition of wastewater varies depending on the source and can change over time, but it can be roughly described as 99% of water and 1% of suspended, colloidal and/or dissolved chemical compounds or biological-related components[369].

Traditional methods and technologies for cleaning wastewater, such as adsorption, chemical treatment, separation, and biological treatment, are costly and, in most cases, consume a large amount of energy, materials, and resources. Considering all these drawbacks, a new and improved water treatment technology is needed. The use of nanomaterials and nanocomposites to construct solid membranes is[370–372]. The pressure-assisted or pressure-driven solid membranes are the most widely used membrane technologies for water treatment applications.[373,374] Graphene-related materials[375] such as graphene oxide (GO)[376–378], reduced graphene oxide (r-GO)[379–382], and graphene derivatives[383–386] have been evaluated as solid membranes for wastewaters containing a variety of pollutants, and they are potential candidates for this application.

Particularly, the reduced graphene oxide can be considered one of the most promising candidates from the graphene family for water treatment applications due to its controlled oxygen content and functionalities over the surface[380]. The oxygen functionalities can play an important role in the membrane's assembly and stability due to the strong physical interaction generated between the r-GO layers and the controlled presence of oxygen functional groups.

This offers the r-GO membrane intermediate hydrophilicity, somewhere between graphene oxide and graphene[387–390]. The way reduced graphene oxide sheets interact with one another is reflected in the final membrane's performances; the stronger the interaction, the smaller the channels between, and this can lead to inferior performances when are compared to r-GO[391,392]. In graphite, the graphene layers are well packed through van der Waals interaction, resulting in a crystalline structure with a 0.335 nm spacing between the graphene layers[393]. The spacing between the layers within the membrane can vary from ca. 1 nm to a few nm when reduced graphene oxide is used as membrane material, and it can also alter during the process when the membrane is wet and/or under back pressure[374,380,387].

The CHFS synthesis of reduced graphene oxide with various functionalities is described in this chapter. It also describes the development of a membrane made of reduced graphene oxide that can operate at high pressure with promising rejection rates (defined as the ability of a membrane to partial or total block different components dissolved or suspended into a water feed when the feed crosses the membrane layer) for various pollutants like metal ions, organic molecules, and biological samples, as well as permeation (reveals how fast a liquid volume pass through a solid layer per unit of time).

4.2 Reduced graphene oxide via CHFS as a green alternative to the current synthesis processes

Zhou et al[394] reported the first time in 2009 that graphene oxide could be reduced using a hydrothermal method, and this achievement has been described as an alternative synthesis route to the toxic hydrazine method. Our group was the first to use a continuous hydrothermal flow synthesis process to reduce graphene oxide, with the first paper published in 2014 by Kellici *et al*.[303] as an alternative to the traditional batch hydrothermal method, confirming a higher efficiency of CHFS process over the traditional batch hydrothermal method.

Kellici et al[303] used KOH as a reductive environment and the same CHFS system; however, this time, the use of formic acid as a reducing agent has been reported. This synthetic approach enables adaptation to reaction chemistries that require a more reductive environment to complete (for example, formation of metals under CHFS conditions).

Previous research has shown that the pH can play an essential role in the hydrothermal reduction of the graphene oxide[395], with the material produced in an acidic pH described as more closely matching the requirements of graphene derived membrane used in a water treatment process such as easy to assembly in a stable form in water and the generation of

channels required for the water flow to travel through the membrane. In comparison to the use of hydrazine[396,397] as a reductive agent (another efficient method, but highly toxic for human health and the environment[398]), the CHFS approach proposed in this work is safer and greener due to the reductive agent (formic acid) used in the chemical process as well as short reaction time and lower energy consumption.

4.2.1 Results and discussions

Aiming to achieve reduced graphene oxide with synthetic process tunable oxygen functionalities, in this work, we succeeded to develop a new CHFS method by using a simple organic compound (formic acid) as a reducing agent and by varying the graphene oxide concentration. In our developed CHFS process (see schematic in **Figure 4.1a**), the graphene oxide precursor with different concentration (2 mg/mL, and 0.5 mg/mL) was mixed with a constant concentration of the formic acid solution (3 M) to understand the effect of the reducing agent over the oxygen functionalities, when graphene oxide was less in the reaction environment. Also, in-situ iron nanoparticles were generated with the purpose to catalyse the reduction process and studying if certain oxygen functionalities are selectively reduced.

The process parameters: flow rates, supercritical temperature, and pressure were kept constant during all the synthetic experiments, and the CHFS setup schematic is shown in **Figure 4.1b**. The formic acid solution was premixed with graphene oxide at room temperature and the mixture was delivered a single feed into the reaction area. When the precursor's feed meets the supercritical water feed, the reduction process starts, and it ends when the reaction mixture is cooled down inside the cold-water pipe in pipe heat-exchanger.

The as-synthesized 2D structures were characterised using a variety of techniques including XPS, FTIR and Raman to determine the surface chemistry and to confirm the oxygen functionalities and material defects evolution before and after the CFHS process, and TEM, and SEM to see if there is a change in the graphene morphology.

Table 4.1: Carbon high-resolution XPS spectra peak positions.

Sample label	XPS position (eV)					
	sp^2 C-C	**sp^3 C-C**	**C-O/ C-O-C**	**C=O**	**O-C=O**	**π-π***
GO	284.33	285.39	287.31	288.59	289.42	290.65
r-GO(1)	284.55	285.68	286.83	288.38	289.47	290.10
r-GO(2)	284.48	284.80	286.64	288.38	288.85	290.68
r-GO(3)	284.43	284.80	286.40	288.13	289.19	290.88

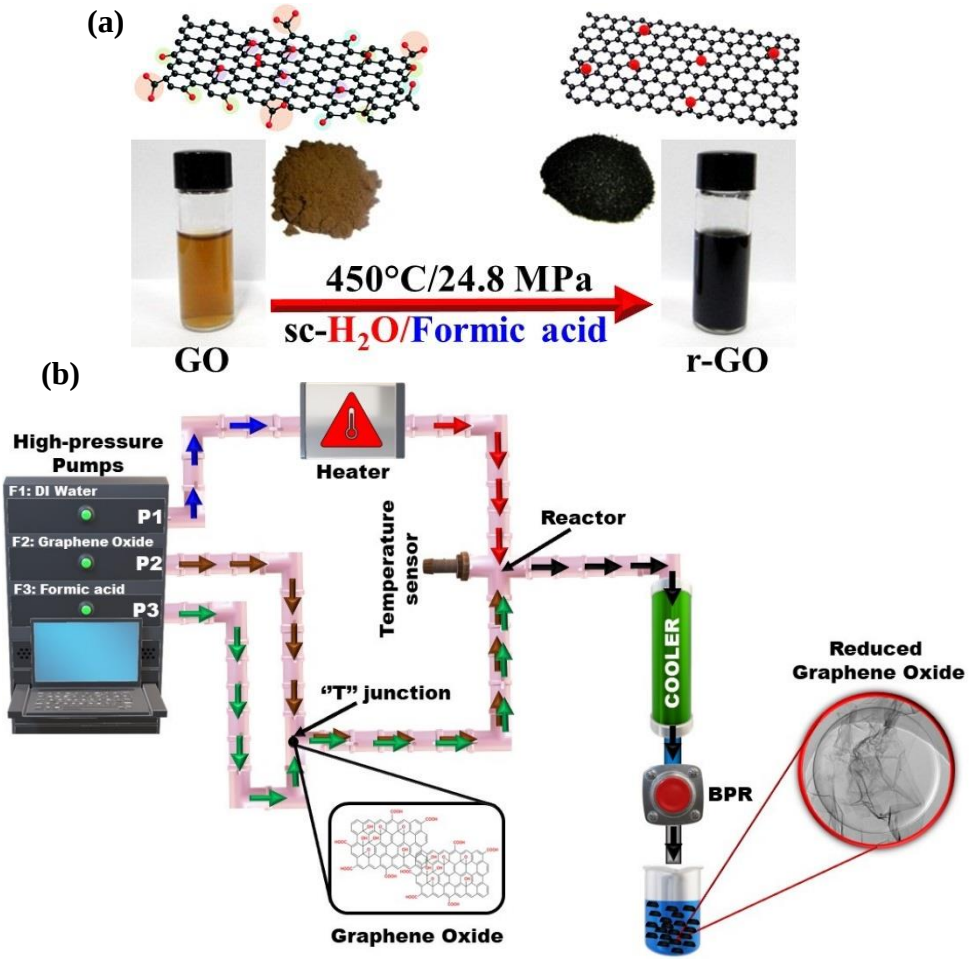

Figure 4.1: (a) Reduced graphene oxide synthesis schematic, and (b) simplified continuous hydrothermal flow reactor and process representation. Key: BPR – back pressure regulator, F – feed of DI water, aqueous dispersion of graphene oxide and formic acid solution, P = pump.

The X-ray photoelectron spectroscopy was performed to analyse the surface chemistry of the reduced graphene oxide produced by CHFS and to provide information about the oxygen functionalities present as well as the effectiveness of the CHFS process' reduction. The XPS survey reveals the presence of carbon (C 1s) and oxygen (O 1s). The high-resolution XPS spectrum of carbon of the CHFS products and graphene oxide (starting material) reveals the characteristic peaks of C-C sp^2 (~284.5 eV) and C-C sp^3 (~285 eV) hybridizations of carbon atoms, C-O. Carbon atoms in graphene oxide commonly have sp^2 and sp^3 hybridization at different ratio. The presence of sp^3 hybridized carbon atoms results from the formation of carbon-oxygen simple covalent bonds during the oxidation stage, and the sp^2 hybridization originates from unoxidized carbon atoms or the C=O bonds containing functionalities[399–401].

Other peaks assigned to hydroxyl (C–OH, ~286 eV), epoxide (C–O–C ~286 eV), carbonyl (>C=O ~288 eV), and carboxyl (O=C–OH ~289 eV) are also observed. The shake-up satellite peak of sp^2 bonds (π-π*) is responsible for the ~290 eV peak. The peaks' location for each compound is summarized and shown in **Table 4.1**.

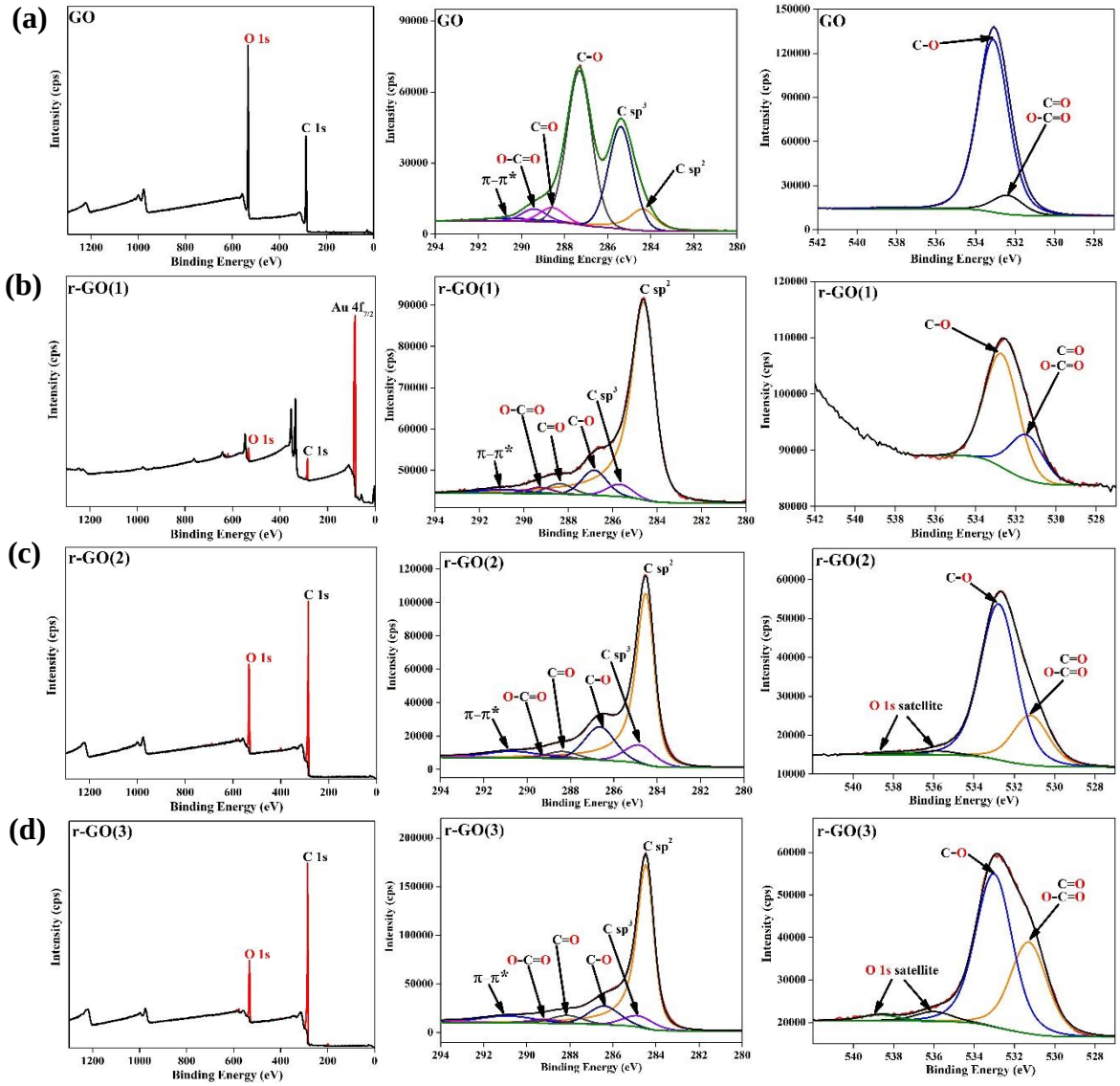

Figure 4.2: XPS survey and high-resolution of carbon and oxygen spectrum of (a) GO, (b) r-GO(1), (c) r-GO(2), and (d) r-GO(3).

The XPS spectra shown in **Figure 4.2** present a noticeable reduction of the oxygen functionalities and increased sp^2 carbon content. The oxygen content of graphene-based materials, which is usually expressed as carbon to oxygen ratio (C/O), is a commonly used criterion for assessing the reduction process[402]. **Figure 4.3** shows the sp^2, sp^3, oxygen, and carbon content evolution in each sample. The GO precursor contains 6.26 at% sp^2 carbon, while the r-GO(1), r-GO(2) and r-GO(3) exhibiting 65.95 at%, 52.43 at% and 57.64 at%,

respectively. There is also a significant decrease in carbon-oxygen sp^3 bonds. It decreased from 32.62 at% in graphene oxide precursor to 6.94 at%, 13.04 at% and 9.23 at% in r-GO(1), r-GO(2) and r-GO(3), respectively. In the XPS elemental composition, a decrease in the oxygen content was also observed (from 31.68 at% for GO to 17.37 at%, 16.82 at% and 13.3 at% for r-GO(1), r-GO(2) and r-GO(3), respectively). Based on these oxygen content values, is noted the-reduction of the oxygen functionalities in graphene oxide, the oxygen content in r-GO(1), r-GO(2) and r-GO(3) decreases to 45.15%, 46.91% and 58.02%, respectively. For the synthesis of r-GO materials, the CHFS process has proved its ability to generate the required conditions for the chemical reduction of commercial graphene oxide and its overall tunability to modify the product characteristics. From XPS elemental analysis it can be concluded that by decreasing the graphene oxide precursor concentration in the reaction environment, a decrease in the oxygen content is observed, as well as a significant increase in the content of sp^2 hybridized carbon atoms (characteristic of graphene materials). Also, by using in-situ generated iron nanoparticles, the oxygen content decreased further.

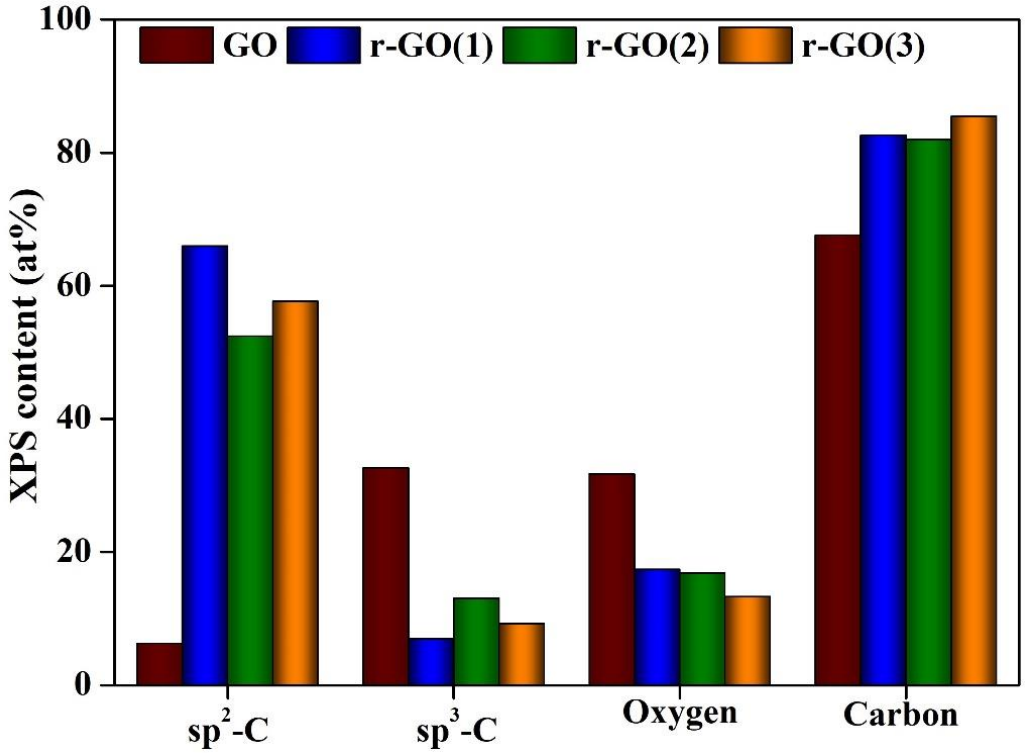

Figure 4.3: sp^2-C, sp^3-C, oxygen and carbon XPS atomic content evolution in GO, r-GO(1), r-GO(2), and r-GO(3).

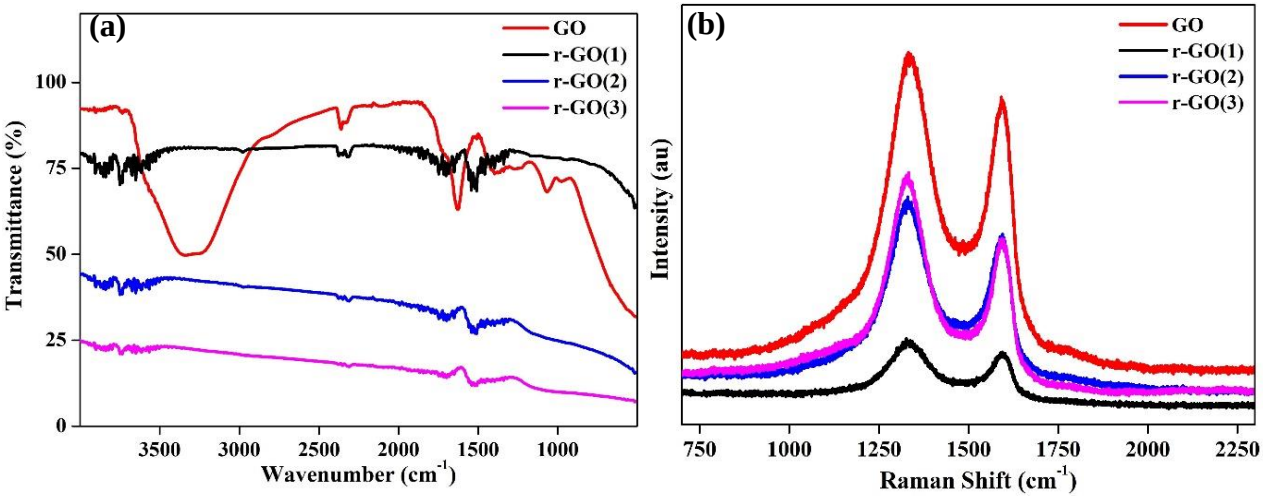

Figure 4.4: The (a) FTIR and (b) Raman spectra of graphene oxide and CHFS reduced graphene oxide materials.

The FT-IR spectra of graphene oxide precursor and CHFS synthesised reduced graphene oxide samples were obtained to further investigate the oxidation and reduction processes. The hydroxyl and epoxide groups attached to the graphene's basal plane, as well as carboxyl and carbonyl groups found at the edges, are generally recognised as the dominant functional groups in graphene-related materials such as graphene oxide, graphite oxide or reduced graphene oxide[403–406]. The FTIR spectra are shown in **Figure 4.4a** and are in good agreement with XPS data. It can be observed that graphene oxide has large peak between 3707-2411 cm^{-1} centred at 3338 cm^{-1} which is characteristic for -OH stretching vibrations. This band completely disappeared for r-GO(1), r-GO(2), and r-GO(3), indicating that hydroxyl functional groups were reduced during the CHFS process. It can also be assigned to the reduction of -COOH to C=O, which occurs through the reduction of the -OH bond[407]. This is also evident in the high-resolution XPS spectrum of carbon 1s, where C-OH and -COOH concentration on the surface of reduced graphene oxide is reduced. The peak at 1724.3 cm^{-1} is assigned to C=O stretching vibrations characteristic of the carbonyl group. The evidence from XPS data shows that the concentration of carbonyl does not change after the CHFS chemical reduction process. However, there is an increase from 3.03 % (r-GO(2)) to 4.05 % (sample r-GO(3)). This could be due to the use of iron nanoparticles aiding in the catalytic reduction of carboxylic groups on the GO surface via CHFS. The C=O peak appears in FT-IR plots ca. 1705 cm^{-1} for r-GO(1), r-GO(2), and r-GO(3) (3). Further, peaks located around 1390 cm^{-1} (O-H deformation), 1240 cm^{-1} (C–O epoxy), and 1070 cm^{-1} (C–O (alkoxy) present in the precursor FTIR spectrum (GO), these peaks have been reduced or diminish in the r-GO samples FTIR

spectra. To summarise, all the CHFS synthesised samples show a reduction in oxygen functionalities, indicating that the CHFS process is effective at reducing graphene oxide.

The Raman spectra shown in **Figure 4.4b** reveals the presence of D and G vibration bands characteristic of carbonaceous materials. The G band, which is generally located at ca.1580 cm^{-1} is related to the in-plane vibration of sp^2 carbon atoms, and the D peak located at ca.1350 cm^{-1} is related to the sp3 carbon atoms and network defects[335,408]. The ratio of I_D/I_G is often reported as an indicator of the disorder level in graphene-based materials.[409] Typically, the I_D/I_G ratio is expected to increase in value when the oxygen functionalities are reduced, associated with the sp^3 hybridized carbon content decreasing[335,409]. The precursor graphene oxide (GO) and the r-GO samples have no obvious D and G bands blue- or redshift, the peaks are located similar wavenumbers. The I_D/I_G ratio of the precursor is 1.15, and for the reduced graphene oxide samples: r-GO (1) 1.16, r-GO (2) 1.20 and r-GO (3) 1.34. The relative intensity of the D to G band (I_D/I_G ratio) of CHFS synthesised reduced graphene oxide increased progressively with the oxygen content drop off in the synthetic procedure with varying the graphene oxide concentration, or by adding the iron nanoparticles to reduction system), and this indicates the reduction of the sp^3 hybridized carbon atoms and the defects in graphene oxide precursor. The Raman data further supports and confirms the observations made by XPS and FTIR measurements.

Table 4.2: Raman peaks position and I_D/I_G ratio

Sample name	**Raman peak position [cm^{-1}]**		**I_D/I_G**
	D band	G band	
GO	1332.49	1594.43	1.15
r-GO(1)	1328.99	1593.41	1.16
r-GO(2)	1330.07	1594.18	1.2
r-GO(3)	1329.83	1593.4	1.34

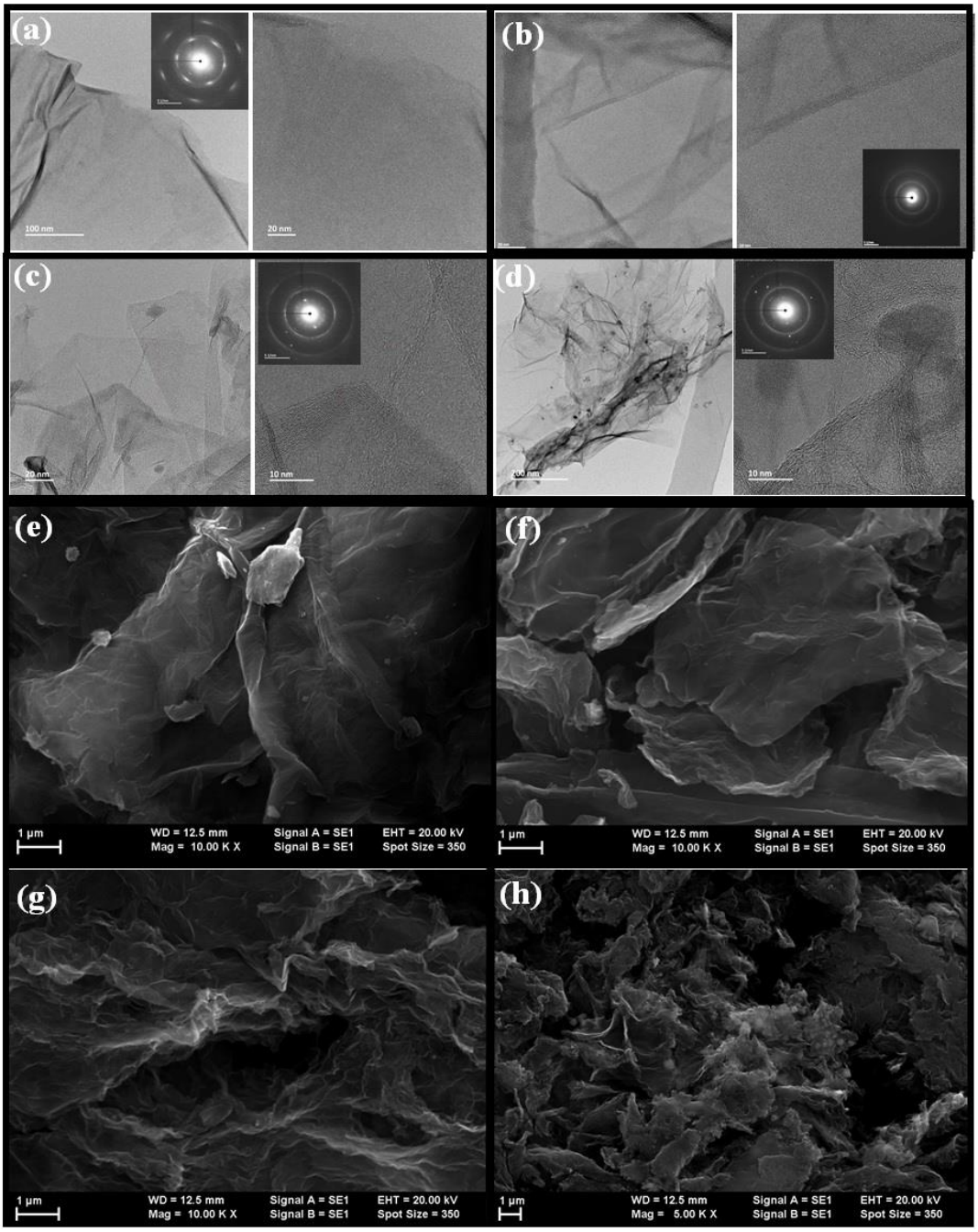

Figure 4.5: TEM images of (a) GO, (b) r-GO(1), (c) r-GO(2), and (d) r-GO(3) and SEM images of (e) GO, (f) r-GO(1) (g) r-GO(2), and (h) r-GO(3).

The transmission electron microscopy (TEM) images shown in **Figure 4.5 a-d** revealed a 2D morphology. The graphene oxide and the reduced graphene oxide CHFS products consist of graphene flakes made of less than 10 layers of graphene, some being made of 5-10 graphene layer (this was estimated using the edge counting method).[410] In **Figure 4.5 d** (the TEM images of rGO(3) sample) it can be observed that the graphene sheets are decorated with iron nanoparticles, confirming the presence of in-situ generated nanoparticle catalyst. The iron nanoparticles can be easily removed from the main material with a low concentration HCl acid

solution, but this was not the goal of this study. XPS detected the presence of iron, however, the concentration (0.06 XPS at%) was too low to be accurately quantified.

In the literature, oxidation/reduction methods are linked to the development of aggregated r-GO sheets.[411] In this work, SEM was employed to further study the morphology of CHFS synthesised reduced graphene oxide. The SEM images of GO and r-GO CHFS materials shown in **Figure 4.5 e-h** reveal the characteristic 2D morphology of graphene derived materials. The reduced graphene oxide flakes appear to be exfoliated and randomly oriented. In addition, the presence of iron nanoparticles decorating r-GO sheets can be seen in **Figure 4.5 g**, confirming the TEM observations. The iron nanoparticle catalysts were generated in-situ with the goal of improving the CHFS reduction environment. Overall, the sheets can be predicted to assemble together in a solid membrane-like film with nano-channels between the layers wide enough to allow a water flow to move through due to the presence of oxygen functionalities[366] (as verified by XPS and FTIR data). The graphene flakes (presented in **Figure 5.5e)** appear as a thin and large-surface area aggregated morphology, promising for the utilisation of the material as a membrane for water treatment processes.

To summarise, the use of complementary techniques revealed that the graphene oxide precursor was efficiently reduced through the continuous hydrothermal flow synthesis process. The results of the electron microscopy (HRTEM/SEM) showed that this process is capable of producing two-dimensional exfoliated reduced graphene oxide flakes. The XPS, FT-IR, Raman analyses confirmed the effective reduction of graphene oxide precursor in the presence of a reducing agent (formic acid), with one example exploring the presence of an in-situ synthesised iron catalyst. The synthesised product's characteristics and properties are comparable to those of other high-quality chemically reduced graphene oxide[355,394,412,413]. The rGO(1) was used as a membrane material for water treatment, and this proof-of-concept application will be discussed in the section that follows.

4.2.2 Water treatment process using reduced graphene oxide in-house produced high-pressure membranes

The water treatment processes can be divided into two main categories: chemical and physical processes.[414] The wastewater purification using solid membranes can be classified as a physical process as it proceeds through physical interaction between the pollutants, water and the membrane surface. The membrane technology for water treatment is one of the most desired methods because it involves no additional chemicals or side-products generated during the

process. It can also offer the recovery and capitalization of the containing pollutants if they represent an economic advantage of the industrial process or their proper storage before neutralisation[371,415].

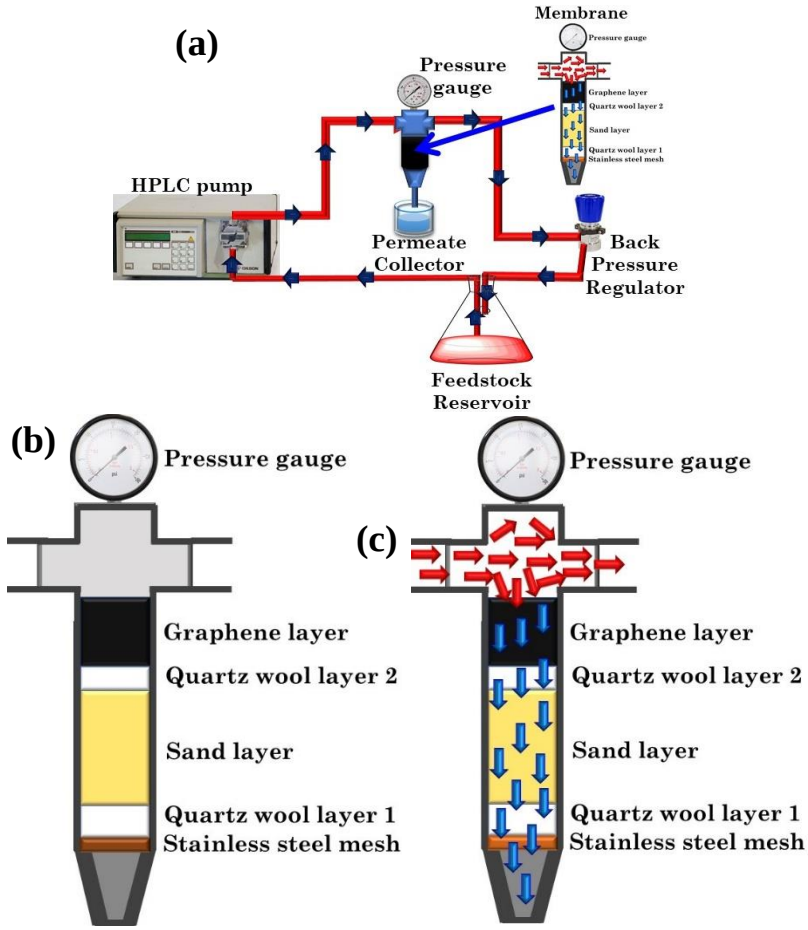

Figure 4.6: (a) Water treatment high-pressure membrane setup schematic, (b) a representation of the membrane materials' configuration and (c) schematic representation of the graphene-based high-pressure membrane water treatment process indicating the flow process.

The membrane preparation method and water treatment setup have been discussed in Chapter 2. Briefly, the water treatment setup consists of a high-pressure pump, a back-pressure regulator (BPR), pressure gauge, a membrane, and permeate collector and feedstock reservoir. Under normal operating conditions, the system is under pressure between the pump and the BPR, with the rest of the system operating at atmospheric pressure (see **Figure 5.6a**). The model wastewater is recirculated until half of the initial volume is collected in the permeate vessel.

The high-pressure membrane is made up of a multilayer system of support consisting of a top layer of graphene-based material (see **Figure 4.6b**). The purpose of a multilayer support design is to prevent graphene migration with the water flow and to sustain the high

pressure generated during the water treatment process. Depending on the chemical nature of the pollutant and the type of interactions that can occur, the graphene layer can act as a barrier against the pollutants within the wastewater flow or as an absorbent during the process[365,366]. The graphene-based layer consisted of the following configurations: (I) graphene oxide, (II) reduced graphene oxide, and (III) graphene oxide/reduced graphene oxide mixture. The outcomes of each configuration were compared, and the water treatment data are presented in the section that follows.

This study focused on the permeate feed, with the evolution of pollutant concentration measured over time and volume. The membrane performance for each configuration consisting of a different graphene layer (graphene oxide, reduced graphene oxide and a mixture of both) was determined as a result of the rejection rate (**Equation (4.1)**) and the permeation (**Equation (4.2)**). The results are presented in **Figure 4.7 a-g**. Various pollutant species were tested in this study to simulate a possible real-case scenario, ranging from metal ions and anions to dyes/organic molecules and biological samples (proteins). From highly toxic chemicals ($[CrO_4]^{2-}$) to stable and non-harmful ones ($[Fe(CN)_6]^{3-}$), divalent (Fe^{2+}) and trivalent (Fe^{3+}) metal ions commonly found in industrial wastewater or generated by human's activities, different organic dye such as methylene blue (blue) and rhodamine B (red-pink), or complex structures like proteins (cytochrome C) were successfully tested on all membranes, aiming to provide a better view over this new and innovative water treatment process.

$$\mathbf{R(\%)} = \frac{C_{stock} - C_{permeate}}{C_{stock}} \cdot 100 \qquad (\textit{Equation 2.1})$$

$$\mathbf{Permeation(mL/min)} = \frac{V_{permeate}}{t} \qquad (\textit{Equation 2.2})$$

Where:

R(%) is the rejection rate

$\mathbf{C_{stock}}$ is the stock concentration (the initial concentration)

$\mathbf{C_{permeate}}$ is the permeate concentration.

$\mathbf{V_{permeate}}$ is the volume of the permeate.

t is the time recorded to collect a certain volume of permeate.

The rejection rate defines the efficiency of the membrane to block different types of pollutants present in a wastewater flow. The rejection rate of a solid graphene-based membrane

can be affected by different parameters such as the pressure (inside the system), the pollutant concentration, the graphene layers dimension and oxygen content (which define the type of interaction and the size of the channels between the graphene layers).[416–419]

In terms of rejection rate performances, when comparing between anionic metallic complexes species $[CrO_4]^{2-}$ and $[Fe(CN)_6]^{3-}$, in general, all the membranes worked better for oxo-metallic anions ($[CrO_4]^{2-}$), with r-GO membrane exhibiting the best performances with 74.00 % rejection rate, followed by GO/r-GO membrane with 74.18% rejection rate and GO membrane with 70.00 % rejection rate. When it comes to ferrocyanide anions ($[Fe(CN)_6]^{3-}$), the best results were obtained for r-GO membrane with 10 % rejection rate, followed by GO/r-GO membrane (7 %) and GO membrane with only 5% rejection rate. It can be observed that when the negatively charged surface of graphene is boosted due to the increase in oxygen functionalities, the rejection rate (R(%)) of the membrane decreases[420]. The rejection rate is influenced if the interaction between the metallic complex anion and the graphene-based material surface is weak or if there is a repulsion between, due to the negatively charged surface through oxygen functionalities[420–423]. Overall these will be reflected in the GO and GO/r-GO membrane performances.

Similar behaviour was found for Fe^{2+} and Fe^{3+} ions. All membranes performed well for divalent iron (Fe^{2+}) with r-GO membrane showing the best performances with 96 % rejection rate, followed by GO/r-GO membrane with 93 % rejection rate and GO membrane with 92 %. In the case of trivalent iron ions (Fe^{3+}) the lowest rejection rate was obtained for GO membrane with just 40 %, the r-GO membrane recorded an intermediate performance of 65 %, compared with 87 % obtained for GO/r-GO membrane. The iron (II) and iron (III) ions tend to coordinate to the oxygen functionalities over the membrane surface[424], and Fe(II) has a stronger cation-π interactions[425] than Fe(III), which explains why all the membranes perform better for Fe(II). The hydration sphere of Fe(III) ions contains approximately 21 molecules of water. In contrast, the hydration sphere of Fe(II) contains about 14-15 molecules,[426–428], indicating that Fe(III) has a stronger interaction with water molecules in the wastewater flow than with the membrane surface. This lends support to the rejection rate behaviour of reduced graphene oxide membranes.

Methylene blue (MB) and rhodamine B (RB) were successfully tested as standards for organic dyes pollutants. All the membranes performed better for methylene blue, with 99 % rejection rate obtained for GO membrane, followed by GO/r-GO membrane with a similar rejection of 99 %, and the lowest rejection rate (87 %) was recorded for r-GO membrane. The

GO/r-GO hybrid membrane generated a 96 % rejection rate for rhodamine B, but when each corresponding material was used alone, the performances decreased to 78 % rejection rate for GO membrane and 67 % rejection rate for r-GO membrane. Similar performances for methylene blue and rhodamine B have been reported on GO and r-GO membranes[429,430]. The lower rejection rate for rhodamine B can be explained due to its higher solubility in water. Even though its structure is larger, the presence of ternary ammonium chloride and the carboxylic group makes the molecule highly stable and well hydrated in water[431].

When the wastewater feed contained proteins (cytochrome C), the GO/r-GO hybrid membrane performed the best with 99 % rejection rate, followed by r-GO membrane with 87 % and GO membrane with 82 %. Cytochrome C, which has a more complex structure and a larger molecular weight and molecular volume than dyes, can passthroug the graphene membrane layer due to the presence of large channels between layers, particularly in graphene oxide material rather than rGO material. According to the findings of the study, it can be concluded that the cytochrome C macromolecule is physically adsorbed stronger on reduced graphene oxide substrates than graphene oxide because more of the cytochrome C molecule interacts with the aromatic rings of rGO, providing a substrate with significantly reduced oxygen functionalities[432–434].

The r-GO membrane has the highest permeation (as determined by **Equation (4.2)**), followed by the GO membrane and the GO/r-GO membrane. All the tested membranes are stable over time for the majority of the pollutants, generating similar permeation rates when the pollutants were tested in series (one after another), the exception being $[CrO_4]^{2-}$ test, which performs very fast on the GO membrane (2.46 mL/min), and much slower for r-GO membrane (0.54 mL/min) and GO/r-GO membrane (0.29 mL/min). For r-GO membrane, a similar permeation rate value was obtained for Fe^{2+}(0.52 mL/min). For the rest of pollutants the data obtained are as follows: $[Fe(CN)_6]^{3-}$ (1.39 mL/min), Fe^{3+} (1.43 mL/min), methylene blue (1.41 mL/min), rhodamine B (1.44 mL/min) and cytochrome C (1.47 mL/min). The GO membrane performed much more slower for the rest of pollutants: $[Fe(CN)_6]^{3-}$ (0.4 mL/min), Fe^{2+}(0.66 mL/min), Fe^{3+} (0.79 mL/min), methylene blue (0.29 mL/min), rhodamine B (0.29 mL/min) and cytochrome C (0.82 mL/min). The permeation rates of GO and r-GO membranes are reflected for the r-GO/GO mixture and the membrane permeation rates are: $[CrO_4]^{2-}$ (0.29 mL/min) $[Fe(CN)_6]^{3-}$ (0.34 mL/min), Fe^{2+}(0.47 mL/min), Fe^{3+} (0.32 mL/min), methylene blue (0.31 mL/min), rhodamine B (0.27 mL/min) and cytochrome C (0.31 mL/min).

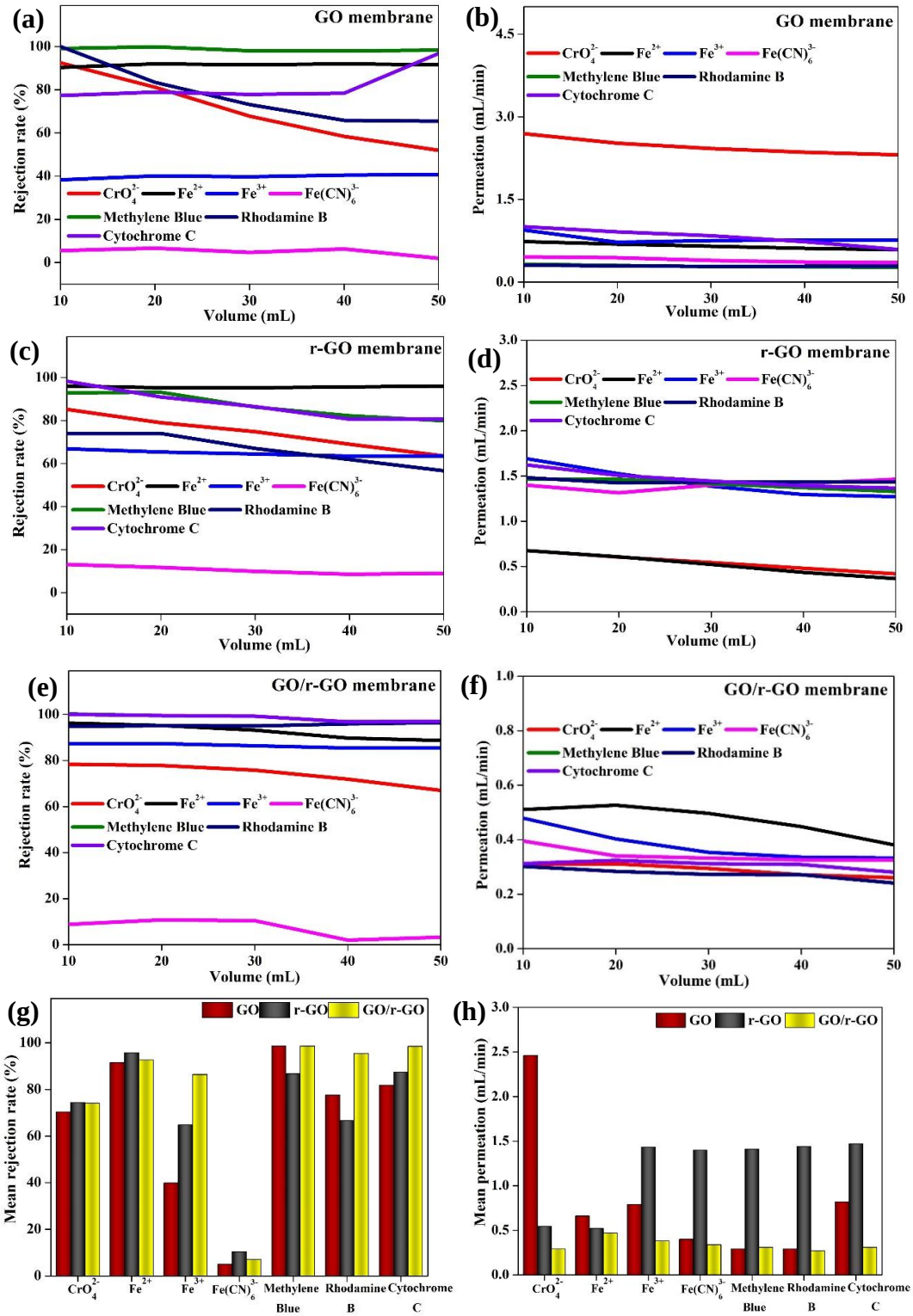

Figure 4.7: The membrane's performance for graphene oxide (GO): (a) rejection and (b) permeation, reduced graphene oxide (r-GO): (c) rejection and (d) permeation, and graphene oxide/reduced graphene oxide (GO/r-GO): (e) rejection and (f) permeation. The mean rejection rate and (g) and the mean permeation (h) of the GO, r-GO, and GO/r-GO membranes charts for a better visualization of the water treatment processes.

Taking into account the rejection rates, the order in which the membranes perform can be explained by the (a) interaction between the pollutants molecules with the water molecules, (b) the type of interaction they create with the membrane materials, and (c) the adsorption of the pollutants on the membrane's surface[435–441]. Further, the extraction process from their hydration sphere can slow down the speed of the water flow (the speed with the permeate flow pass through the membrane's layers), or if the extraction process is not very effective due to a large hydration sphere, the pollutant can pass through the membrane with the water flow[442–444]. The graphene oxide tends to interact stronger with water due to its rich oxygen functionalities surface[445,446]. These functional groups can form various hydrogen bonds, with water molecules slowing down the flow. The oxygen functionalities interact strongly with metal ions and organic molecules to form complexes[447–449]. These oxygen functionalities are higher in GO than in rGO materials, as evidenced by XPS and FTIR data. As a result, it is expected that GO will have stronger and more complex interactions with these species. A material with more functionalities will slow down the permeate flow through the membrane by creating more and more robust interactions with it.

4.3 Conclusions

Graphene and its derivatives have attracted a lot of interest over the last decade. Since its discovery, numerous methods, and strategies for producing 2D graphene derivatives with specific properties and characteristics have been developed. Wet chemical methods are widely used to produce large amounts of graphene by chemical reduction of graphene oxide. Most of these methods employ hazardous or toxic reductive agents or solvents, with hydrothermal methods offering a promising alternative.

In this study, new continuous hydrothermal flow synthesis methodology was developed, which involved the use of formic acid as a reductive agent to reduce graphene oxide. Starting with a raw material containing 31.7 at% oxygen, the CHFS process reduced the oxygen functionalities to 17.4 at%, 16.8 at%, and 13.3 at%, by using different concertation of graphene oxide or catalysts iron nanoparticles. These findings demonstrated the tunability of the CHFS process, which was used to produce reduced graphene oxide with varying levels of oxygen functionalities. The reduced graphene oxide produced via CHFS was employed to prepare high-pressure membranes which were successfully used for water treatment.

This study proposes a novel membrane prototype capable of operating in continuous flow and high-pressure conditions. The water treatment process proposed in this study still has

a few parameters (membrane composition, recirculation flow rate, pressure studies, and multiple pollutants wastewater test) to optimize in future tests, but the results obtained thus far indicate that the process is a promising alternative to traditional water treatment processes.

4.4 Future works

In terms of synthetic procedure, the CHFS formic acid method utilized for the reduction of graphene oxide precursor is very promising. It opens a new research avenue for further process optimization: flow rate, pressure, temperature, and formic acid concentration. Future studies can lead to a better understating of the CHFS formic acid method in selective reduction of the oxygen functionalities via a top-down approach. The optimization of the CHFS process may result in the development of a new large-scale synthetic alternative. Further, synthesizing rGO/Fe nanoparticles composite has been proved the ability of this innovative method to produce nanometals-rGO nanocomposite. This study can be expanded to different metals such as gold, platinum, palladium, copper, which can be explored, and their composite can be tested from catalysis to electronics and sensing.

The membrane design, the setup, and the water treatment method developed during this study can be used as proof of concept and the graphene layer can be replaced with other 2D materials or even their nanocomposite with graphene. The optimization of the currently tested membranes may result in the development of a commercial version of the product, which is highly required to provide a solution to a major global challenge, water treatment.

Chapter 5: Continuous hydrothermal flow synthesis of TiO_2-NCQDs-rGO nanocomposites as photocatalysts

5.1 Introduction

The continued exponential population growth and consequential industrial expansion and demands on planetary resources have unleashed unprecedented and unsustainable pressure on the environment as reflected by global water contamination (for instance, 80 - 90% of wastewater is released untreated in Asia and Pacific regions into surface-water bodies).[450] This is compounded by advancing climate change and is of great concern, prompting urgent scientific research into renewable, effective, and sustainable solutions. In this regard, photocatalysis can readily harness freely available clean solar energy to degrade organic contaminants[451], reduce CO_2 into renewable solar hydrocarbon fuels[452], and generate hydrogen and oxygen by the splitting of water when exposed to sunlight[453].

Since the first report of their photocatalytic bleaching of dyes in 1938[454], titanium dioxide (TiO_2) has been one of the most extensively studied metal oxides[455] and remains currently the most feasible photocatalyst for industrial-scale applications. It does, however, feature a large bandgap energy (3.2 eV for its anatase form), which remains a challenge in meeting the requirements of visible-light applications. Integration with an active catalytic surface that allows for efficient charge transfer and kinetics is additionally identified as a limiting factor in achieving outstanding photocatalytic performance.

To overcome these challenges have led to the design of new materials that have propagated the development of hybrid and/or heteroatom doped nanostructures that deliver visible light-responsive photocatalysts. For example, the addition of carbonaceous material to the surface of TiO_2 can induce and enhance visible-light photocatalytic activity. Graphene, the first 2D material made of a single or a few layers of sp^2 carbon atoms arranged in a hexagonal array and conjugated electronic structure, with a large surface area, can be hybridized in its reduced oxide form with TiO_2 to provide a photocatalytic system. These can be developed to offer enhanced charge separation in electron transfer processes and increases surface-adsorption of chemical substrates (via π–π interactions), including pollutant molecules[456]. An alternative approach has been found in the application of the critically small carbon quantum dots (CQDs) with dimensions < 10 nm. CQDs are composed of sp^2 graphitic carbon core with a shell surface consisting of a mixture of sp^2 and sp^3 carbon decorated entanglements with a variety of oxygen (and optional nitrogen) functionalities, with a poorly defined electronic

structure. The CQDs offer a variety of advantages that include conductivity, a tuneable size dependant bandgap (1.8-3.1 eV) tailored to match solar light adsorption, that along with their small size, facilitates short charge transfer.[457] As such, when hybridised with TiO_2, energy levels are aligned, forming heterojunctions (between p states of the CQDs and the conduction band of the semiconductor), resulting in enhancement of the charge lifetime separation[458].

Configuring new arrangements of carbonaceous mixtures with catalytic support (TiO_2) can provide unique solutions to the photocatalytic challenges discussed via novel mechanisms. The sp^2 carbon atoms from the CQDs core and graphene in its reduced oxide form could be very efficient in storing, and shuttling electrons, and the oxygen functional groups/dangling bonds can play an important role in interconnecting the solid components through hydrogen bonds and other physical interactions, whilst nitrogen functionalities can manipulate the ability of TiO_2 to harvest visible light.[236,459,460] These can be achieved by using a unique, versatile, continuous synthetic technology that produces consistently high quality and large quantities of nano-hybrids of choice, which would also offer a solution to one of the challenges in photocatalytic materials industrialization[457]: scale-up.

The primary focus of this research was to establish a suitable, fast, and effective strategy for the discovery of highly efficient visible-light photocatalysts. Herein, we report the rapid and tailored synthesis of nano-TiO_2 hybrids with nitrogen-doped carbon quantum dots and/or reduced graphene oxide (rGO) and their enhanced photocatalytic performance under solar light using methylene blue dye as a model pollutant. The materials were produced in continuous mode using a hydrothermal flow process that mixed supercritical water (450 °C, 24.8 MPa) with precursor solution(s) in a reactor to give the product in fractions of a second. In the perspective of a green, adaptive and economically efficient synthetic method, the continuous hydrothermal flow synthesis (CHFS) has attracted a growing interest for the production of a new generation of nanomaterials such as graphene, graphene quantum dots, carbon quantum dots and their nanocomposites, offering enhancement of their properties and expanding their area of applications.[11,298] Reproducibility, an assurance of complete real-time control over the reaction parameters, and delivering materials with optimised properties are just a few of the benefits of CHFS.[11,306,307,461–463] Our research has previously applied these particular synthetic properties to the production of different metal oxides[11] and various carbonaceous materials (reduced graphene oxide[303], carbon quantum dots[299,313,464], graphene quantum dots[298,307]). This research adds further to the development of continuous flow technology of photoactive related nanomaterials. A detailed analysis of the CHFS synthesised materials' charge behaviour

through a series of complementary techniques including transient photoluminescence, X-ray photoelectron spectroscopy, and density functional theory calculations, are reported. High-resolution transmission electron microscopy was employed to study the morphology and particle size of nano-hybrids, UV-Vis spectroscopy to provide information about optical properties and bandgap determination, and X-ray powder diffraction, Raman spectroscopy lend complementary information about the compositions and crystallinity of nano-TiO_2 hybrids. Surface area values were also determined using the nitrogen adsorption technique.

5.2 Results and discussions

In recent years, various methods have been used to improve the photocatalytic properties of titanium dioxide-carbonaceous nanocomposites by altering or extending the TiO_2 anatase photoactivity for radiation harvesting from UV to visible.[236,458,465] Whilst established synthetic processes are promising, they still suffer drawbacks such as high energy and time consumption demands, costly precursors or experimental setup, batch to batch quality discrepancies, and the inability to scale up the process from the laboratory to industrial production. The continuous hydrothermal flow synthesis approach reported herein addresses all the shortcomings of traditional methods due to the systems' inherent precision control of reaction parameters, which not only allows real-time tunability of the material production process but also reduces the time required to assess the material production process best synthetic experimental conditions considerably. CHFS has previously been applied to TiO_2 synthesis[466]; the uniqueness of this work is that we simultaneously and homogeneously generate titanium dioxide anatase nanoparticles, NCQDs, and reduce graphene oxide. We also compare these with a two-step process (using pre-made NCQDs). The experimental details are shown in **Figure 5.1 a-f**.

In general, pre-mixed (at the T-junction) feeds of titanium(IV) bis(ammonium lactate) dihydroxide and a carbon precursor (graphene oxide and/or citric acid, or pre-made N-doped carbon quantum dots) were delivered to meet concurrently with a flowing feed of sc-H_2O (450°C and a pressure of 24.8 MPa) in the mixing zone (reactor) for nanocomposite formation. After cooling, the product mixture was collected for isolation and purification (see **Figure 5.1 g**). The as-produced hybrid structures did not require any post-thermal processing; instead, the nanomaterials were characterized and used for further analysis and photocatalytic testing as described in the following.

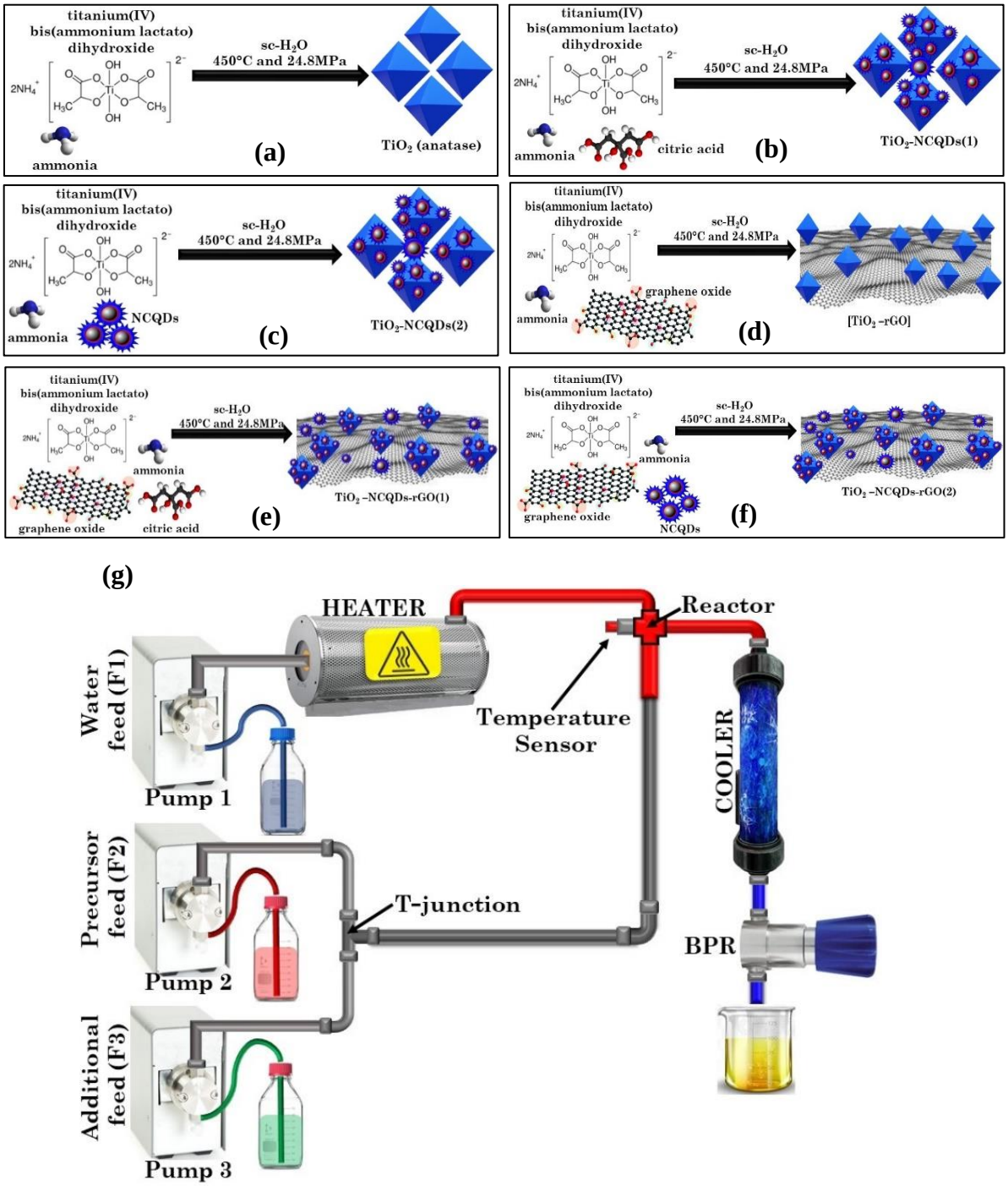

Figure 5.1: Continuous hydrothermal flow synthesis (CHFS) process detailing the synthetic protocols for: (a) -(f) production of TiO_2 and its nanocomposites with reduced graphene oxide (rGO) and/or N-doped carbon quantum dots (NCQD); (g) simplified representation of the CHFS process.

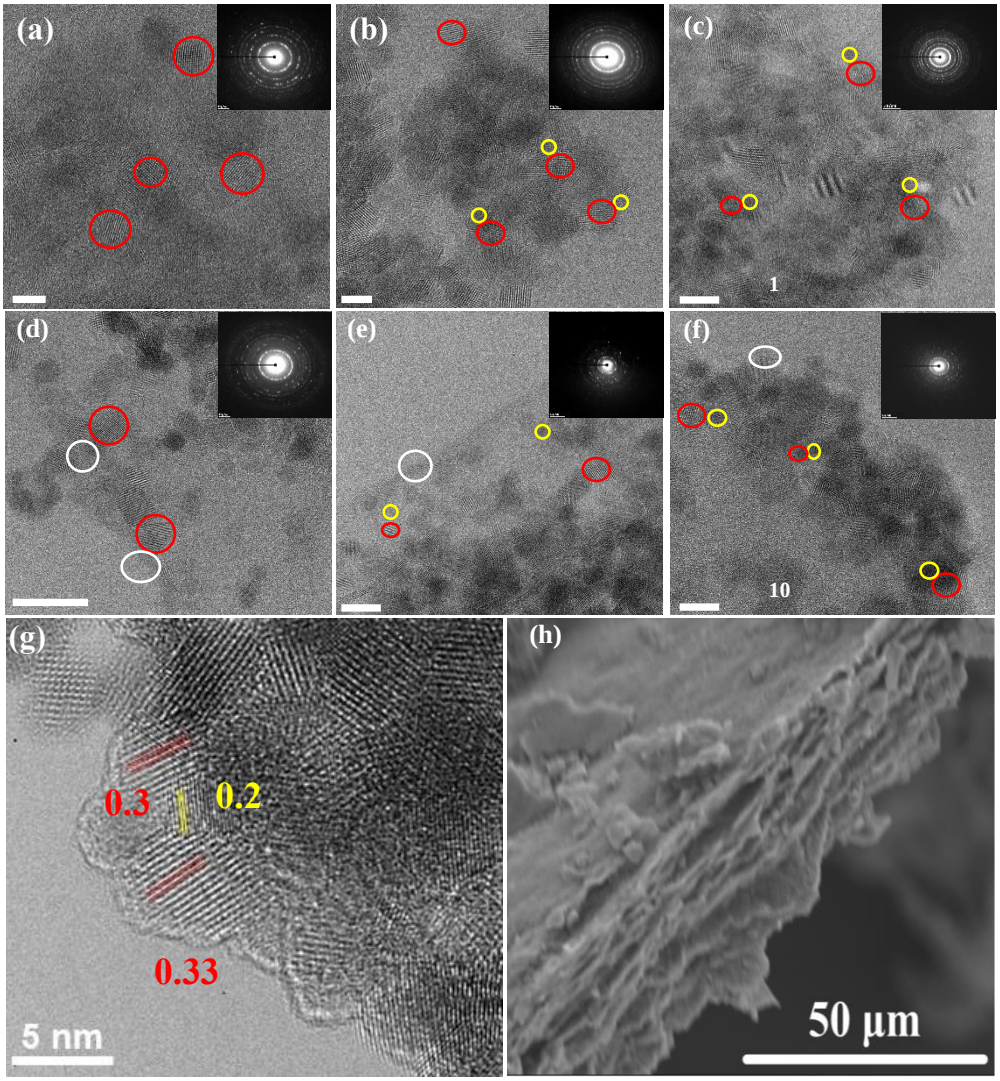

Figure 5.2: High-resolution transmission electron microscopy (HRTEM) images of: (a) TiO_2, (b) [TiO_2-NCQDs(1)], (c) [TiO_2-NCQDs(2)], (d) [TiO_2-rGO], (e) [TiO_2-NCQDs-rGO(1)], (f) [TiO_2-NCQDs-rGO(2)]. Each TEM image has an inset of a corresponding selected area electron diffraction pattern. (g) lattice fringes of TiO_2 and NCQDs in TiO_2-NCQDs(1), and (h) Scanning electron microscopy image of TiO_2-NCQDs-rGO(1) showing reduced graphene oxide (rGO) layers. Sample labelling key: yellow -NCQDS, red – TiO_2, white – rGO.

High-resolution transmission electron microscopy (HRTEM) reveals the morphological architecture of the TiO_2 and TiO_2-carbonaceous nanocomposites, as shown in **Figure 5.2 a-g**. The TiO_2 mean particle size is ~ 5.0 nm in diameter with a lattice spacing of *ca*. 0.33 nm (**Figure 5.2g**) and assigned to the (101) plane of anatase.[456] The NCQDs exhibited a spherical morphology with a mean particle size of ~ 3.4 nm with an in-plane lattice spacing of *ca.* 0.22 nm (**Figure 5.2g**) and identified as a graphitic core arrangement[313] with the graphene sheets consisting of 5-8 layers. The corresponding selected area electron diffraction pattern (insets in Figure 2) of each sample confirms the existence of the crystalline TiO_2 anatase phase and

influence due to the presence of an amorphous carbon phase in the TiO_2-carbonaceous nanocomposites. A close interaction between the TiO_2 nanoparticles and NCQDs as a solid-solid direct interface was observed, as shown in **Figure 5.2g**. In the case of TiO_2-rGO (**Figure 5.2d**) and TiO_2-NCQDs-rGO (**Figure 5.2e-f**), the TiO_2 nanoparticles and NCQDs are dispersed over the 2D layer, creating extensive interfacial interactions across the entire surface of the rGO layers and interlayers. Scanning electron microscopy (SEM) images for TiO_2-NCQDs-rGO (**Figure 5.2h**) supported HRTEM analysis for the layered structure of reduced graphene oxide.

The small particle sizes observed by HRTEM correlated with the large surface area of the as-synthesised CHFS materials measurements by SA_{BET} for the pristine titania and its hybrids (compiled in **Table 5.1**) ranging from 232 $m^2\ g^{-1}$ for TiO_2 to 253 $m^2\ g^{-1}$ for TiO_2 – NCQDs-rGO(1) nanocomposite. Such high specific area values would be expected to increase the activity of the nano-hybrids through increased adsorption of pollutant molecules (model methylene blue dye) and irradiation photons. Of course, other variables, including structural and surface properties of the photocatalysts, must be considered when comparing activities of different materials.

For further investigation of the structures and composition of TiO_2 photocatalysts and its hybrids, Raman spectroscopy (**Figure 5.3 a**), and XRD analysis (**Figure 5.3 b**) were undertaken. Characteristic Raman vibrations for the CHFS-synthesised samples of TiO_2 anatase presented an E_g band located at 146 cm^{-1} and 641 cm^{-1}, a B_{1g} band located at 398 cm^{-1}, and an A_{1g} band positioned 513 cm^{-1}, all in good agreement with the literature.[467] Adding a carbonic phase (reduced graphene oxide) to the material, not only were the expected appearance of the D (*ca.* 1345 cm^{-1}) and G (*ca.* 1595 cm^{-1}) vibrational bands observed, but these bands for all rGO containing hybrids were noticeably blue shifted (D-band) and red shifted (G band). It should also be noted that the standard E_g vibrational mode at 144 cm^{-1} was also red-shifted for TiO_2-rGO (150 cm^{-1}), TiO_2-NCQDs-rGO(1) (152 cm^{-1}) and TiO_2-NCQDs-rGO(2) (151 cm^{-1}), respectively. This red shift could be assigned to the charge transfer process occurring between the TiO_2 nanoparticles and its hybridised carbonaceous materials[468]; this would be in line with the XPS and modelling data discussed later. Interestingly, the D and G vibrational modes are missing for both TiO_2-NCQDs(1) and TiO_2-NCQDs(2), most likely due to a too low an NCQD content in the samples for Raman analysis, but nanocomposites NCQDs are accounted for in the XPS analysis later.

Lending further insight and complementary support for our findings, XRD analysis (**Figure 5.3b**) showed characteristic diffraction peaks for TiO_2 anatase (JCPDS 21-1272) in all cases. The diffraction peak at $2\theta = 12.2°$ indicated the presence of the carbonic phase [002] and was observed for all samples but two; TiO_2-NCQDs(2), which we assume as previously stated for its Raman analysis, is due to the low NCQD content and therefore below the limit of detection for both instruments. Critically, interactions between TiO_2 and NCQD and/or rGO are observed by X-ray photoelectron spectroscopy (XPS) and are discussed next.

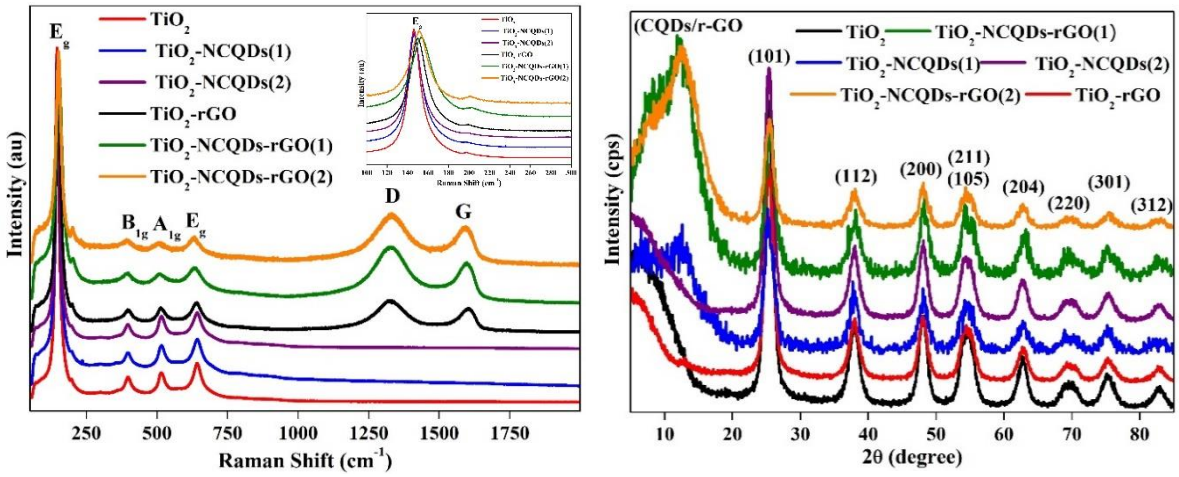

Figure 5.3:(a) the Raman spectra and (b) the XRD patterns of CHFS-synthesised nano-TiO_2 hybrids with nitrogen-doped carbon quantum dots and/or reduced graphene oxide.

The XPS analysis of TiO_2 nanoparticles (**Figure 5.4 a-p**) reveals the characteristic Ti(2p) spin-orbit split peaks, the binding energy of the Ti($2p_{3/2}$) peak recorded at 459.3 eV; the corresponding O(1s) peak is comprised of two peaks corresponding to Ti-O lattice oxygen (530.6 eV) and surface OH/CO_x (531.8 eV), a N(1s) signal at 400.7 eV is also found, consistent with fragments in the starting material for the synthesis of the nano-TiO_2.

For a better understanding of the interaction between the carbon phase and oxide phase, the high-resolution XPS spectrum of carbon (1s) was analyzed for all the samples (**Figure 5.4 a-e)**. It is worth noting that compared to the pure TiO_2, the survey spectra of all samples exhibited higher intensity in carbon originating from graphene and/or carbon quantum dots. The addition of NCQD to pristine TiO_2 resulted in asymmetry to the lower binding energy side of the C(1s) envelope, characteristic of the sp^2 graphitic core peaks at binding energies of 284.5 eV (sp^3 component was measured at 285.4 eV for both materials) for both NCQD(1) and (2). The difference in the binding energy of the sp^2 component is possibly indicative of the difference in the attachment of the NCQDs to the TiO_2 or the charge states of the TiO_2 and NCQDs on the surface. Additional C(1s) peaks at 286.7, and 289.4 eV were noted and ascribed

to C-O/C-N and COO moieties, respectively, whilst N(1s) species at 400.7 eV is again characteristic of C-N/NH_x functions.

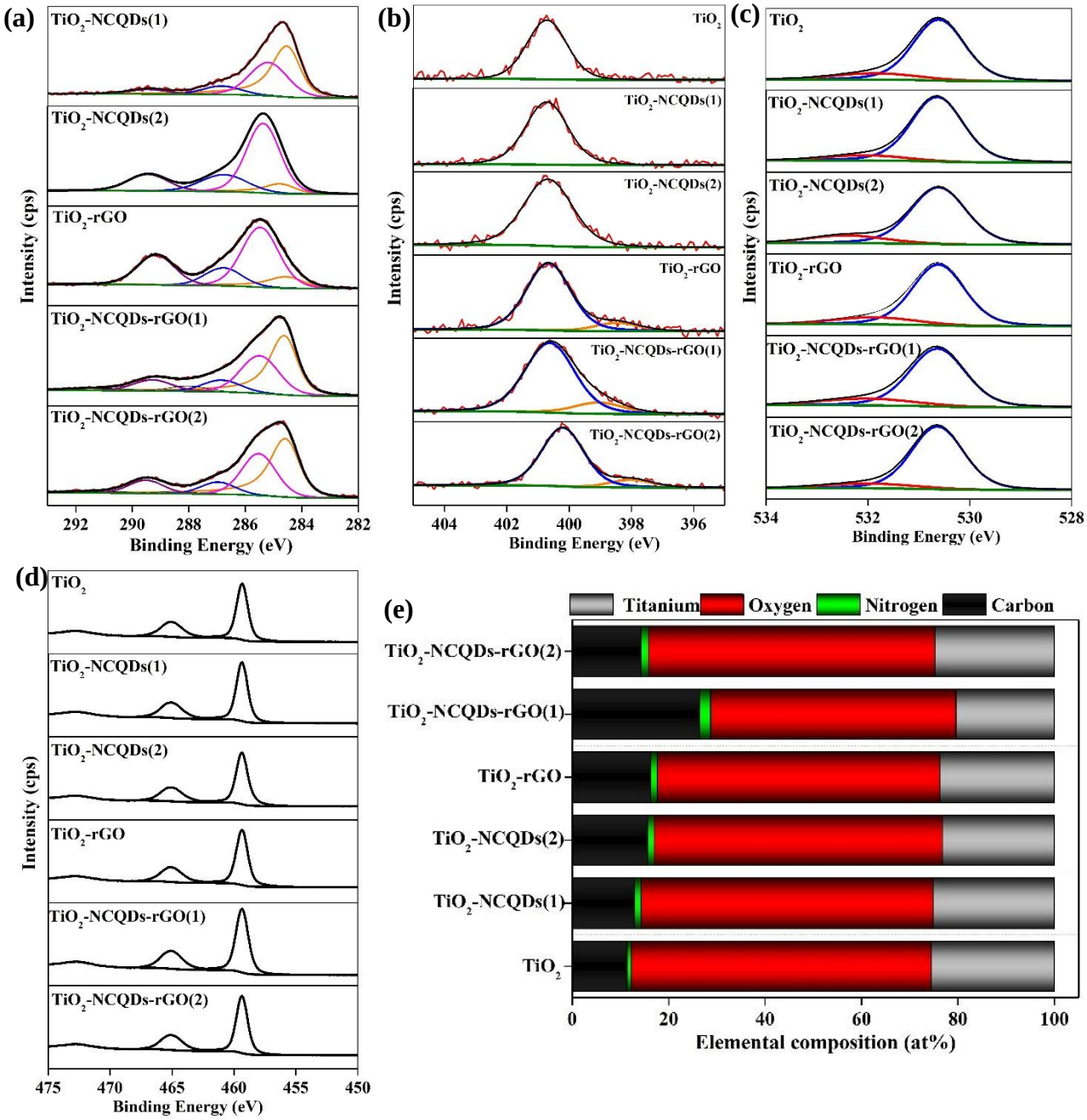

Figure 5.4: The high-resolution XPS spectra for**:** (a) carbon, (b) nitrogen, (c) oxygen, and (d) titanium of TiO_2, [TiO_2-NCQDs(1)], [TiO_2-NCQDs(2)], [TiO_2-rGO], [TiO_2-NCQDs-rGO(1)], and [TiO_2-CQDs-rGO(2)], and (e) the XPS elemental composition of TiO_2 and its carbonaceous nanocomposites.

The TiO_2-rGO complex has peaks centred at 284.5, 285.1, 286.8 and 289.4 eV, again characteristic of sp^2, sp^3, C-O/C-N and COO functionalities as noted previously. N(1s) signals are found at 398.5 and 400.7 eV, representative of C=N-C and C-N type functions. The N

presence in rGO is not unexpected as it is considered a consequence of the incorporation of ammonium from the reaction process. In the case of TiO_2-NCQDs-rGO materials, the high-resolution carbon spectra again show characteristic peaks for sp^2 (here, the p-p* shake up structure is particularly evident) and C–N/C-O bonds, together with sp^3 and the addition of C=O functions. For TiO_2-NCQDs-rGO(1) and TiO_2-NCQDs-rGO(2), the N(1s) spectra, whilst both showing the presence of the 400.7 eV, C-N/-NH_x peak, there is a 0.5 eV deviation in the lower binding energy species (399.0 and 398.5 eV, respectively), the lower peak typically ascribed to -NH- or C=N species[469]. XPS confirms the relationship between TiO_2 with NCQDs, and with rGO; despite signals absent from Raman spectroscopy mention earlier for both TiO_2-NCQDs (1) and (2), as well as from XRD for TiO_2-NCQDs(2) and TiO_2-rGO.

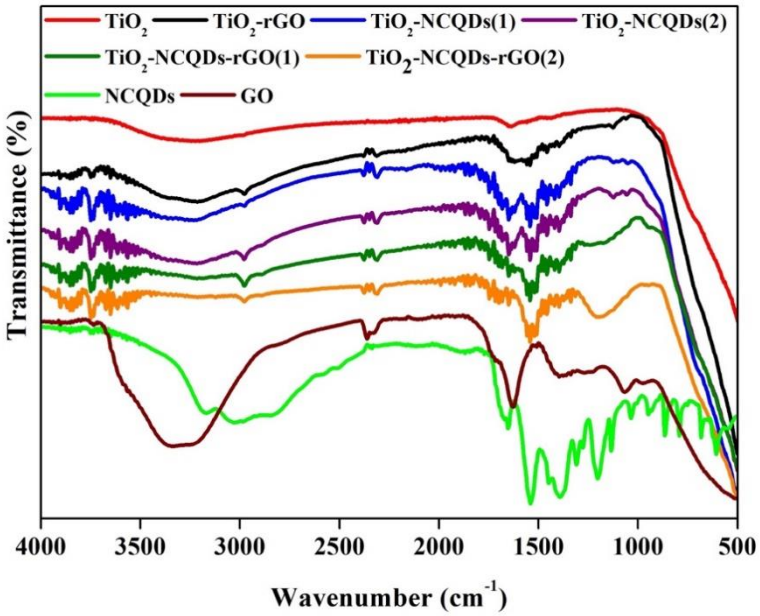

Figure 5.5: FT-IR spectra of the CHFS synthesised photocatalysts.

FT-IR spectroscopy analysis (**Figure 5.5**) reveals the distinctive overlapping stretches (2700–3500 cm^{-1}) due to the presence of hydroxyl groups (-OH, -COOH) on the surface of TiO_2, and its nanocomposites, as well as protonated amino groups for TiO_2 nanocomposites of NCQDs and/or rGO, along with the expected C–H stretching vibrations (2950 cm^{-1}). Additional peaks may be assigned for C=O/COO- (1641 cm^{-1}), C=N (1532 cm^{-1}), and C-N (1460 cm^{-1}) in the TiO_2-NCQDs supporting XPS data stated earlier. For the TiO_2-rGO related materials, the presence of oxygen functionalities on the rGO surface was supported by stretches for C=O/COO- (1627 cm^{-1}), C-OH (1396 cm^{-1}) and C–O–C vibrations (1068 cm^{-1}), which are diminished when compared to graphene oxide precursor indicating the reduced form being present. The absorption band at *ca.* 1543 cm^{-1} may be assigned for graphene-based hybrids that relate to their skeletal vibration of the sheets[250]; however, this peak may overlap the

characteristic stretch for C=N of NCQDs in TiO_2-NCQDs-rGO. The broadening of peaks observed for TiO_2 nanocomposites below 1000 cm^{-1} may correspond to TiO_2 coordinating through a combination of interactions, Ti−O−Ti and Ti−O−C, with the carbonaceous materials.[28]

A photocatalyst with a bandgap that corresponds to solar light and can efficiently maximise energy utilisation would as such be highly desirable. In this regard, the light absorption properties of the as-synthesized photocatalysts were investigated using diffuse reflectance UV-Vis spectrophotometry as profiled in **Figure 5.6**, where bandgap edge values were quantified based on collected measurements. Characteristically, the TiO_2 (**Figure 5.6 a**) nanoparticles demonstrated a strong UV-absorption below 400 nm; however, the absorption edge shifted from the UV to visible when TiO_2 was combined with reduced graphene oxide (rGO). This phenomenon was also observed for TiO_2-NCQDs but at a lower intensity. Significantly, it is by the incorporation of NCQDs into TiO_2-rGO that an appreciable increase in UV and visible radiation absorption was realised, offering the possibility of improved light-harvesting performance. The quantified bandgap edge values **(Figure 5.6 b-c)** were calculated using the Tauc plot, either for direct and indirect transitions (relationship of $[\alpha h\nu]^n$ versus photon energy, where n =2 for direct transition or n=1/2 for an indirect one) for each corresponding photocatalyst. The bandgap for anatase TiO_2 was calculated to be 3.2 eV, whereas the bandgap values of TiO_2-carbonaceous hybrids were noted to be substantially reduced. Extending photocatalyst absorption into the visible region of the electromagnetic spectrum by primarily narrowing the bandgap is generally regarded as one of the most difficult aspects of designing photocatalytic material. These optical studies have demonstrated that using CHFS to manufacture TiO_2 and its carbonaceous nanocomposites provided materials with improved properties when compared to anatase, such as enhanced ability to absorb visible radiation. Nevertheless, the photo-response of these modified catalysts is highly dependent on the characteristics of the type of dopant and as well as optimal dopant concentration. Crucially, fast interfacial electron transport that minimises electron-hole pair recombination (produced

when a photon is absorbed), as well as the lifetime of charge separation, play key roles in the photocatalytic activity of a material.

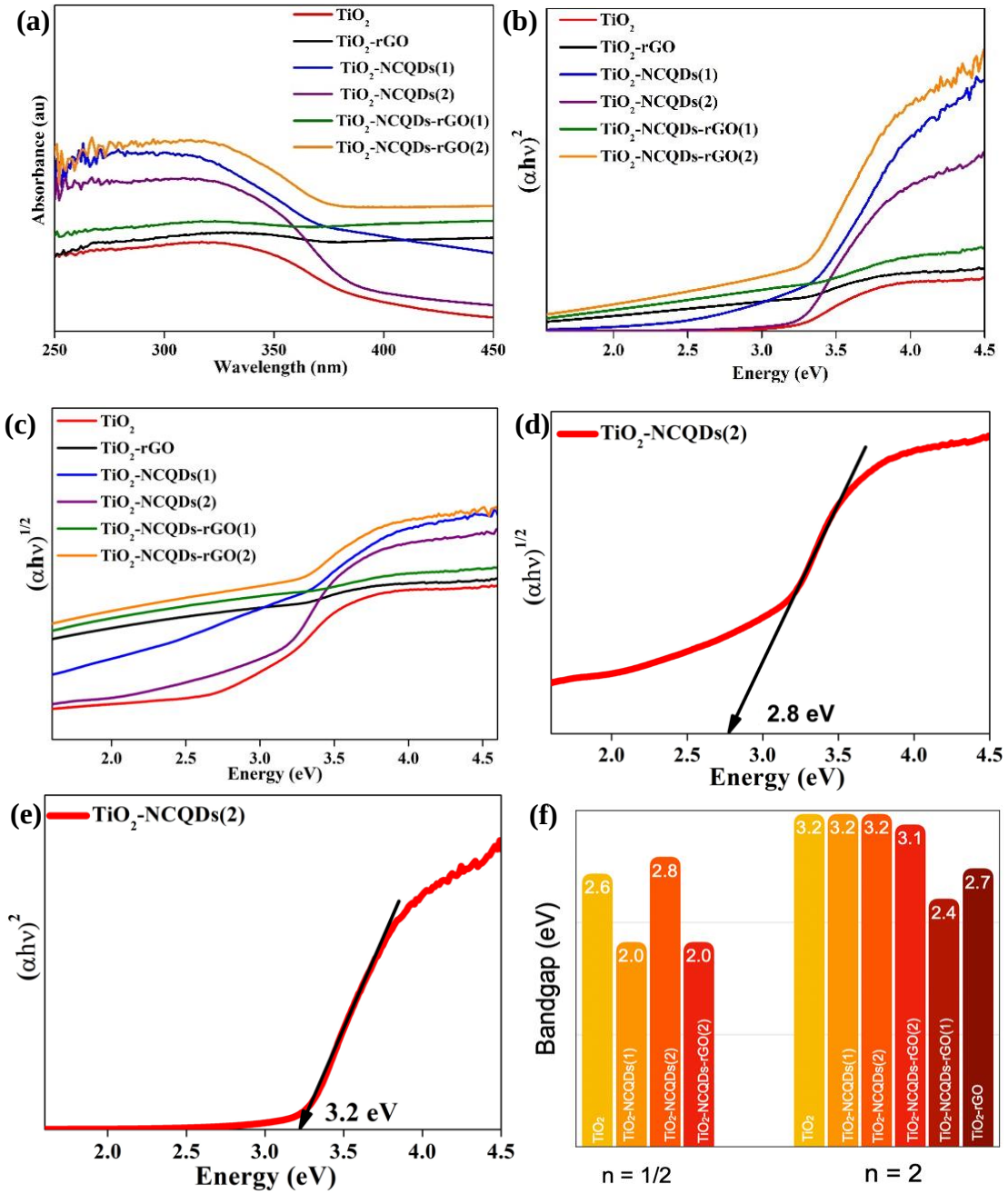

Figure 5.6: Optical properties of the CHFS synthesised materials: (a) UV-Vis absorption profiles, and Tauc plot profiles $(\alpha h\nu)^n$ versus photon energy hν are shown for (b) direct (n=2) and (c) indirect (n =1/2) bandgap transitions of all photocatalysts materials. (d-f) The resulting extrapolated bandgap edge values E_g (eV) values shown for all potential photocatalysts materials. Methodology of bandgap determination for the representative sample of TiO_2-NCQDs(2) and its quantified E_g values for (d) indirect and (f) direct transition.

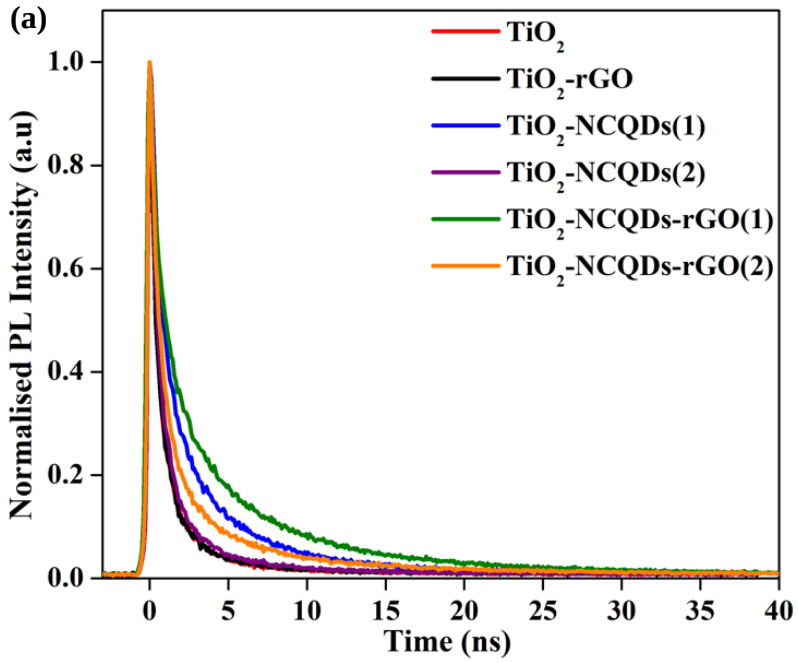

(b)

Photocatalyst name	Lifetime (ns)	Charge-transfer rate (10^8 s^{-1})
TiO_2	2.39	-
TiO_2-rGO	3.15	1
TiO_2-NCQDs(1)	4.37	1.9
TiO_2-NCQDs(2)	2.96	0.8
TiO_2-NCQD-rGO(1)	6.13	2.6
TiO_2-NCQDs-rGO(2)	5.07	2.2

Figure 5.7: (a) Transient photoluminescence spectrum of TiO_2 and TiO_2-carbonaceous nanocomposites and (b) tabulated data showing lifetime (ns) and charge transfer rate (sec^{-1}) values.

Transient photoluminescence spectroscopy was used to assess the emission lifetime of TiO_2 and its carbonaceous nanocomposites and to determine the charge transfer rate. To quantify the interfacial charge transfer process between TiO_2 and nitrogen-doped carbon quantum dots (NCQDs) and/or reduced graphene oxide, the transient photoluminescence (PL) studies were performed using time-correlated single-photon counting (TCSPC) at an excitation wavelength of 375 nm. The normalized PL decays (**Figure 5.7a**) show a decrease in the rate of decay for the nanocomposites of TiO_2 with rGO and NCQDs. The slowest decay is observed in the case of TiO_2-NCQDs-rGO(1) (6.13 ns). Since PL is the result of recombination of photo-generated electrons and holes; slower decay means that this recombination is suppressed in the presence of rGO and/or NCQDs due to efficient charge separation.[470]

If it is assumed that the difference of the TiO_2 emission lifetime (τ) is exclusively due to interfacial charge transfer between TiO_2 and NCQDs and/or rGO, then the rate constant for electron transfer, k_{ET}, can be determined. Previous studies[470] have estimated k_{ET} using:

$$\mathbf{k_{ET}} = \frac{\mathbf{1}}{\boldsymbol{\tau}(\mathbf{TiO_2})} - \frac{\mathbf{1}}{\boldsymbol{\tau}\left(\mathbf{TiO_2} - \frac{\mathbf{NCQDs}}{\mathbf{G}}\right)} \qquad \textbf{(Equation 5.1)}$$

To determine the emission lifetime, the experimental data were fitted with multiexponential decays, and the average lifetimes were calculated for all samples and were used to evaluate the electron transfer rate constants (**Figure 5.7b**) using **Equation 5.1**. Comparison of the interfacial charge transfer rate constants with trends for photocatalytic activities of the nanocomposites (**Figure 5.8**) was found to be complimentary. The greatest charge transfer rates were obtained when TiO_2 was combined with NCQDs and graphene, in particular for TiO_2-NCQDs-rGO(1) (2.6×10^{-8} s^{-1}). This reflects the photocatalytic performances of TiO_2 and its carbonaceous nanocomposites and the influence of intimate contact between TiO_2 with NCQDs, and/or rGO.

The presence of NCQDs not only improves the composite's interfacial charge transfer but the nature of NCQDs can influence the photolytic efficiency. This was highlighted by the longer lifetimes and charge transfer rates observed for TiO_2-NCQDs(1) and TiO_2-NCQDs-rGO(1) compared to TiO_2-NCQDs(2) and TiO_2-NCQDs-rGO(2) respectively, where the synthesis strategies for the respective materials (1) and (2) differed. For nanocomposite materials (1) citric acid was used as the carbon precursor for the synthesis of NCQDs in a single step CHFS reaction. For nanocomposite materials (2), the NCQDs[313] were pre-made, and introduced into the CHFS reaction with Ti(IV) precursors and graphene oxide. The observed diminished performances for nanocomposite materials (2) would most likely reflect CHFS induced modifications of the NCQDs' surface functional groups, disrupting their electronic structure.[459,471–473] Indeed, this is consistent with the evidence from XPS analysis where elemental composition details show that the oxygen content of the NCQDs in TiO_2-NCQDs(2) had increased by ca. 12% (from 31.8 at% to 36 at%), gaining ca. 7% more C-OH functionalities (from 7.7 at% to 8.2 at%), and 47% more C=O functionalities (from 9.7 at% to 14.3 at%) when compared to TiO_2-NCQDs(1) sample.

5.3 Photocatalytic activity measurements

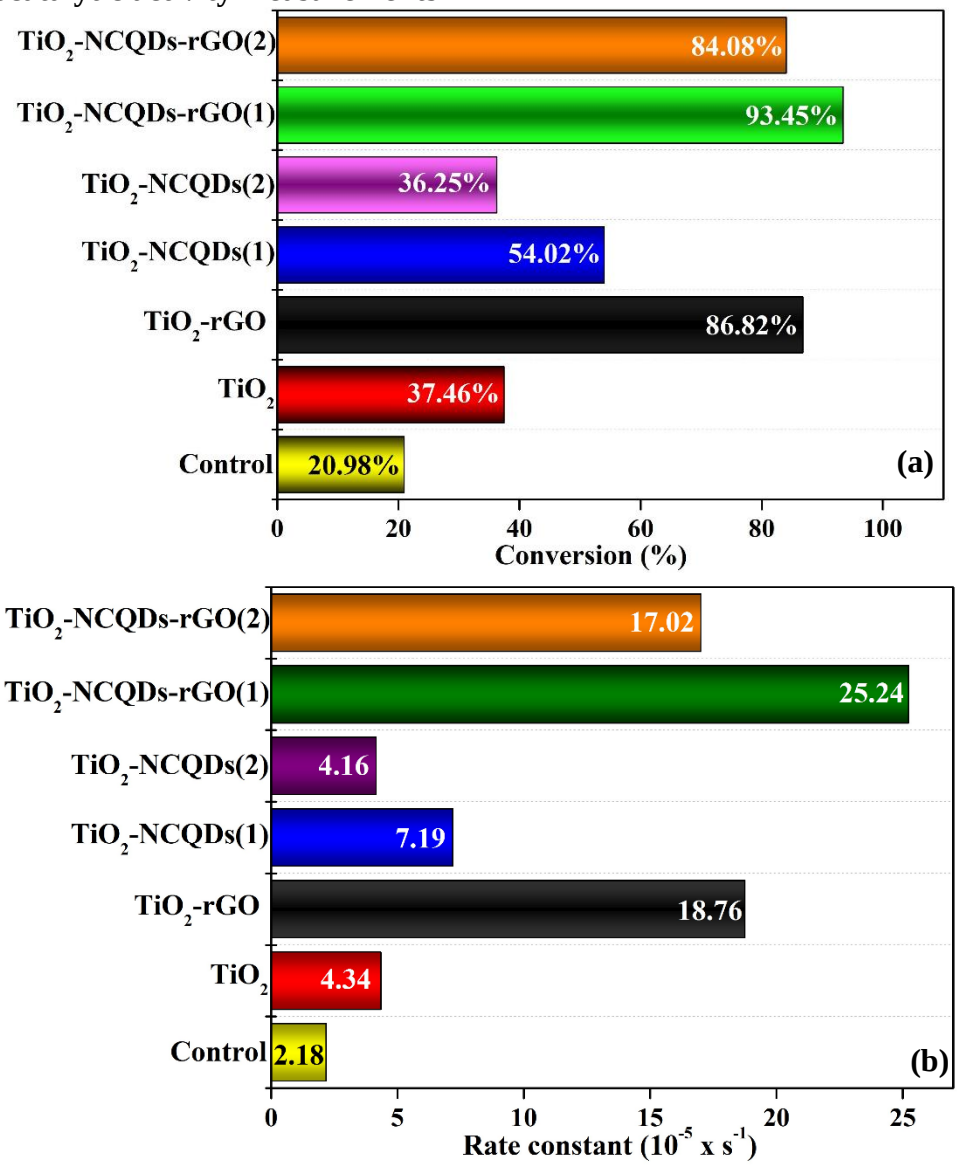

Figure 5.8: (a) Photo-response activities of TiO_2 and hybrid nanomaterials showing photodecomposition of methylene blue (a) the final % conversation (C= final concentration to C_0 = initial concentration, C/C_0 x100) for each photocatalyst during the total solar light exposure period and, (b) first-order rate constants. In both graphs, control = methylene blue.

The TiO_2 and its carbonaceous nanocomposites were examined for their ability to photodegrade a model dye pollutant (methylene blue, MB) under a solar light simulator. The photo-response was assessed by measuring the concentration of MB at 30 minutes intervals over a total irradiation time of 180 minutes. The conversion of MB (C= final concentration to C_0 = initial concentration, (C/C_0 x100)) for each of the photocatalytic nanomaterials during the total solar light exposure period was recorded (**Figure 5.8.a**). The photocatalytic reaction rate was determined using first-order kinetics ($\ln(C/C_0) = -k't$),[462] where $\ln(C/C_0)$ vs time exhibited

a linear relationship in all the cases, and the rate constant, k', was determined from the slope. A control experiment involved the direct photodegradation of MB dye in the absence of a catalyst under the same solar irradiation conditions.

Table 5.1: Adsorption coefficients (q_t) determined using Langmuir-Hinshelwood model and SA_{BET} values for each corresponding photocatalysts.

Photocatalyst	**q_t**	**SA_{BET}**
TiO_2	4.4	232 m^2/g
TiO_2-rGO	14.2	254 m^2/g
TiO_2-NCQDs(1)	5.5	238 m^2/g
TiO_2 - NCQDs(2)	2.4	239 m^2/g
TiO_2 –NCQDs-rGO(1)	11.2	253 m^2/g
TiO_2 –NCQDs-rGO(2)	11.2	241 m^2/g

Most of the carbonaceous TiO_2 nanocomposites (N-doped carbon quantum dots and/or reduced graphene oxide) revealed remarkable improvement on photocatalytic activity, in particular, TiO_2-NCQDs-rGO(1) with 93% conversion of MB in the allotted 180 minutes, and significantly, a 6 fold photocatalytic rate enhancement (25.24 $x10^{-5}$ s^{-1}) over that of TiO_2 alone (**Fig 8b**). The exception to the improved performances is TiO_2-NCQDs(2), a likely consequence of the CHFS induced modifications on the NCQDs described previously. The photocatalytic activities are comparable to the lifetimes of photogenerated charge carriers (as determined from TPS and shown in **Figure 5.7**), with longer lifetimes correlating with improved photocatalytic activity. Furthermore, the addition of rGO enhances the adsorption capacity towards methylene blue via either or combination of their respective anionic-cationic interactions and possible aromatic π–stacking and/or C-H-π interactions with the dye. As a consequence, the adsorbed reaction substrates can effectively react with photogenerated active species (e.g., electrons/ holes, hydroxyl radicals, and superoxide radicals) on the surface of nanohybrid, enhancing the photoredox activity. Indeed, a TiO_2-NCQDs-rGO(1)which exhibited the highest photocatalytic activity, also had a high adsorption coefficient (**Table 5.1**). In all cases, the formulations of hybrids, through one-step CHFS synthesis, have proven to be more efficient in delivering enhancement of catalytic activities when compared to a two-step process [TiO_2-NCQDs(2) and TiO_2-NCQDs-rGO(2)].

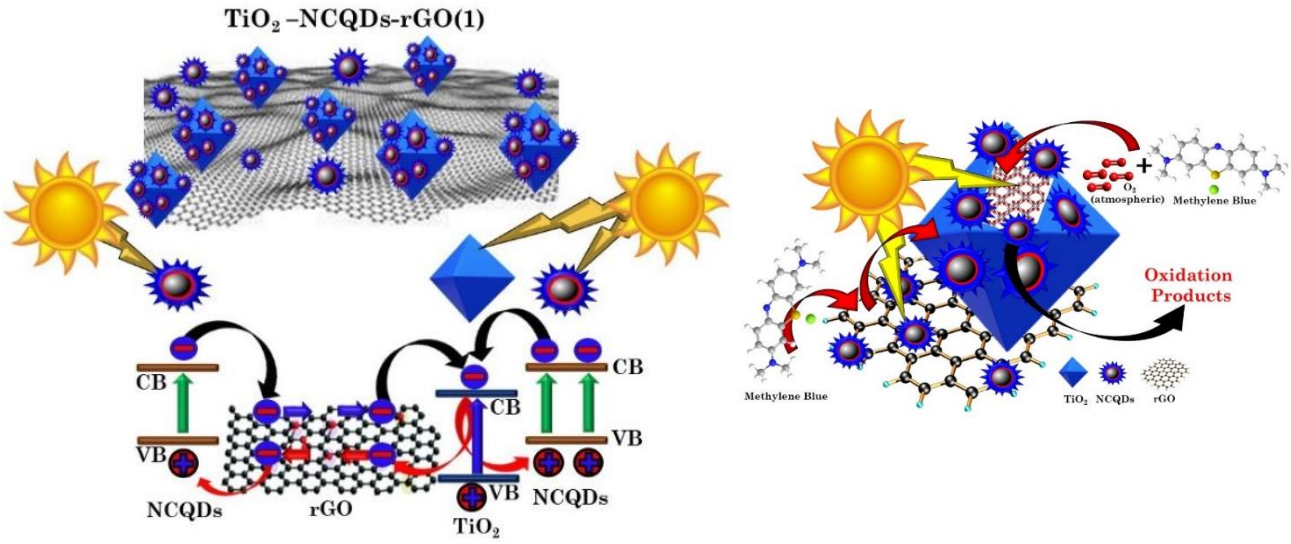

Schematic 5.1: showing the mechanism of the photocatalytic reaction between methylene blue and TiO_2-NCQDs-rGO(1) hybrid.

Tailoring the optical properties of titania and controlling their electronic structure has been the subject of research primarily because it relates to the optimisation of its functionalities. Hybridisation with other nanostructures such as carbon quantum dots results in the formation of a new electronic structure (type II heterojunctions) and an increase in photo-response. This form of arrangement has been shown to not only increase the visible light harvesting potential whilst also extending the lifetime of photogenerated carriers (electrons and holes) through internal charge transfer. These phenomena are further enhanced by the substitutional doping, and the addition of a heteroatom, N,[474] present in all CHFS synthesised materials discussed. Graphene can also act as a co-catalyst when hybridised with titanium dioxide. With an electron conductive nanosheet and a lower Fermi stage, 2D graphene can act as an electron reservoir in accepting, transporting, and shuttling the electrons produced by photoexcitation of TiO_2, enhancing charge carrier separation and transfer to participate in photo-redox processes (decomposition of methylene blue dye). Hence, multilevel/route electron transfer is possible with the hybrid structures of TiO_2 and carbonaceous materials reported herein **(**see **Schematic 5.1).**

5.4 Conclusions

Continuous hydrothermal flow synthesis enabled the rapid and efficient production of homogeneous nano-TiO_2 hybrid composites with nitrogen-doped carbon quantum dots and/or reduced graphene oxide with outstanding photocatalytic activities. Titania particles exhibited a particle size of < 5 nm, high crystallinity (anatase form) and large surface area (typically >

232 m^2 g^{-1}), NCQDs exhibited spherical morphology (mean particle size *ca.* 3.4 nm) with a graphitic core arrangement, and the graphene (r-GO) sheets consisted of 5-8 layers. The highlight of the TiO_2 hybrid nanocomposites remarkable photocatalytic activity was TiO_2-NCQDs-r-GO(1) providing 93% conversion of methylene blue with a 6 fold photocatalytic rate enhancement (25.24 x10^{-5} s^{-1}) over that of TiO_2 alone under solar light simulation, was facilitated by longer emission lifetimes (6.13 ns), faster charge transfer rates (2.6 x 10^{-8} s^{-1}), and a narrowed band gap. The combination of these two effects account for the considerable improvement in photocatalytic performance identified for TiO_2-rGO example (emission lifetime, 3.15 ns), charge transfer rate (1.0 x 10^{-8} s^{-1}). The model proposed for TiO_2-NCQDs-rGO would also incorporate this, facilitated by NCQDs further increasing the emission lifetimes and charge transfer rates via multilevel electron transfer thus significantly enhancing photocatalytic activity.

Effective nano level engineering coupled with a successful synthetic technique that delivers close interfacial interaction and tailored surface chemistry are thus critical for achieving the optimum performance and efficiency in terms of the charge carrier transfer to the surface of the photocatalyst, facilitating relevant photo-redox reactions to take place. These hybrid structures reported here have the potential to be explored in alternative fields, including energy storage, hydrogen generation, or environmental applications.

5.5 Future works

The CHFS approaches developed to synthesize TiO_2-carbonaceous nanocomposites can be further explored for new photoactive metal oxides such as ZnO, NiO or Cu_2O, which can be generated in situ via CHFS and combined with NCQDs and rGO. TiO_2 from the as-synthesized nanocomposites can be replaced by its more efficient solar light harvester version called black-TiO_2, considering the reductive capability of formic acid/supercritical water system, the CHFS reduction of the TiO_2 anatase surface and the conversion of it into black-TiO_2 can be explored.

The continuous hydrothermal flow synthesized TiO_2-carbonaceous nanocomposites demonstrated as being very efficient photocatalysts for dye photodegradation. The most efficient photocatalysts produced in this study can be tested for photothermal conversion, water splitting, hydrogen evolution reaction, or solar cell due to their demonstrated properties and characteristics.

Conclusions

The research developed during this PhD project consists of a journey from small molecules to nanomaterials and nanocomposite, synthesized using a green process, and the materials were successfully integrated into environmental-related applications.

The materials researched, synthesized, and studied were carbon quantum dots, reduced graphene oxide, and their nanocomposites with titanium dioxide. These nanomaterials and nanocomposites have a huge potential in various applications due to their fascinating properties such as rich surface chemistry, high physical and chemical stability, and superior optical and electronic properties. All of them are classified as not environmentally harmful or dangerous. These characteristics allow the integration of these materials into environmental-related applications such as toxic ion-sensing, water treatment processes, and photodegradation of dyes (photocatalysis).

The main novelty brought by this study is the synthetic method. For the first time, carbon quantum dots and their nanocomposites with TiO_2 were synthesized by developing and applying a continuous hydrothermal flow synthesis method (CHFS). The CHFS is one of the most promising hydrothermal methods ever developed for nanomaterial synthesis, being faster, cheaper, and greener than a traditional batch hydrothermal process, and it offers full real-time control over the reaction parameters. During this PhD project, ten new continuous hydrothermal flow synthesis methodologies were developed, and eleven new nanomaterials and nanocomposites were synthesized, characterised, and added to the CHFS materials' portfolio.

The carbon quantum dots were synthesized using glucose (CQDs) and citric acid (NCQDs), (biomass-related molecules) as carbon sources. In the case of the nitrogen-doped carbon quantum dots, one of the simplest nitrogen sources available (ammonia) was used as nitrogen dopant. The CQDs and NCQDs were successfully tested for toxic ion-sensing with promising results. The CQDs showed dual sensitivity for Cr(VI) and Fe(II) ions with a limit of detection of 3.62 ppm and 1.83 ppm, respectively. The nitrogen-doped carbon quantum dots (NCQDs) performed better in terms of Cr (VI) sensitivity with a limit of detection of 0.36 ppm, and present a lower selectivity for Fe (II) ions. The optical properties of NCQDs encouraged their use in the fabrication of carbonaceous-TiO_2 nanocomposites.

The novelty in the reduced graphene oxide continuous hydrothermal flow synthesis was the use of formic acid as a reducing agent in combination with graphite oxide (at concentration of 0.5 mg/mL and 2 mg/mL) comparing with the previous CHFS explorations[303,306]. The reduced graphene oxide obtained exhibited reduction in the oxygen functionalities. Starting from a graphene oxide precursor with 31.68 at% oxygen functionalities, the CHFS process achieved the chemical reduction of GO to 13.3 at% for r-GO(3) material. Because of its relatively low oxygen content but good oxygen functionality variety on the surface, the most suited material (r-GO(1)) was employed in membrane fabrication and tested for water treatment applications. The water treatment tests were performed using in-house designed high-pressure water treatment setup which makes use of an innovative multi-layered membrane prototype. During the study, three membranes were tested: GO, rGO, and rGO/GO; the purpose was to understand and optimize a newly developed water treatment membrane prototype.

The TiO_2-NCQDs, TiO_2-rGO and TiO_2-NCQDs-rGO nanocomposites were synthesized with the main purpose to enhance the photocatalytic performances of TiO_2 by expanding its light absorption ability to the visible domain and improving the charge transfer and electron mobility of the photocatalyst. A consistent band gap reduction was observed for TiO_2-NCQDs-rGO(1) photocatalyst to 2.4 eV from 3.2 eV of pristine TiO_2. The influence of NCQDs origin has been studied. In-situ CHFS generated and premade NCQDs were used, and their photocatalytic performances were tested. The TiO_2-NCQDs(1) nanocomposites performed better than TiO_2-NCQDs(2) (premade NCQDs), and have a conversion of 54.02% compared to 36.25% for methyelene blue photodegration. Further, TiO_2-NCQDs-rGO photocatalysts further confirmed this behaviour,: TiO_2-NCQDs-rGO(1) (93.45%) had a better conversion than TiO_2-NCQDs-rGO(2) (84.08%). Photocatalytic performances improvement for TiO_2-rGO and TiO_2-NCQDs-rGO were observed. This was assigned to the presence of NCQDs and rGO which offer suppression of the charge recombination processes and it offers optimised charge transfer and electron mobility between the phases. The optical studies concluded that that these nanocomposites can absorb visible light, expanding the ability of the materials to interact with solar light and convert it into photocatalytic energy.

Overall, this PhD project demonstrated that continuous hydrothermal flow synthesis is a very versatile synthetic method, and it can produce new materials with excellent properties for environmental applications and beyond.

References:

1. Esmaeilian, B., Behdad, S. & Wang, B. The evolution and future of manufacturing: A review. *J. Manuf. Syst.* **39**, 79–100 (2016).
2. Xu, Q. Thoughts on the development of new material technology. *IOP Conf. Ser. Mater. Sci. Eng.* **493**, (2019).
3. Almgren, R. & Skobelev, D. Evolution of technology and technology governance. *J. Open Innov. Technol. Mark. Complex.* **6**, (2020).
4. Huimin, L. The impact of human behavior on ecological threshold: Positive or negative?-Grey relational analysis of ecological footprint, energy consumption and environmental protection. *Energy Policy* **56**, 711–719 (2013).
5. Pensupa, N., Yunzi, S. L. & Chenyu, H. *Chemistry and Chemical Technologies in Waste Valorization*. (2018).
6. Adschiri, T., Lee, Y.-W., Goto, M. & Takami, S. Green materials synthesis with supercritical water. *Green Chem.* **13**, 1380 (2011).
7. Fang, L. *et al.* Turning bulk materials into 0D, 1D and 2D metallic nanomaterials by selective aqueous corrosion. *Chem. Commun.* **55**, 10476–10479 (2019).
8. Thangadurai, T. D., Manjubaashini, N., Thomas, S. & Maria, H. J. *Nanostructured Materials for Environmental Remediation*. (2020). doi:10.1007/978-3-030-26145-0_15
9. Varma, R. S. Biomass-Derived Renewable Carbonaceous Materials for Sustainable Chemical and Environmental Applications. *ACS Sustain. Chem. Eng.* **7**, 6458–6470 (2019).
10. Lee, S. & Park, S. TiO2 photocatalyst for water treatment applications. *J. Ind. Eng. Chem.* **19**, 1761–1769 (2013).
11. Darr, J. A., Zhang, J., Makwana, N. M. & Weng, X. Continuous Hydrothermal Synthesis of Inorganic Nanoparticles: Applications and Future Directions. *Chem. Rev.* **117**, 11125–11238 (2017).
12. Tyson, N. deGrasse. *Astrophysics for People in a Hurry*. (W. W. Norton & Company, 2017).
13. Harari, Y. N. *Sapiens: A Brief History of Humankind*. (Harper, 2015).

14. Emsley, J. *Nature's Building Blocks: An A-Z Guide to the Elements*. (Oxford University Press, 2011).

15. Namdari, P., Negahdari, B. & Eatemadi, A. Synthesis, properties and biomedical applications of carbon-based quantum dots: An updated review. *Biomed. Pharmacother.* **87**, 209–222 (2017).

16. Xu, X. *et al.* Electrophoretic analysis and purification of fluorescent single-walled carbon nanotube fragments. *J. Am. Chem. Soc.* **126**, 12736–12737 (2004).

17. Sun, Y. P. *et al.* Quantum-sized carbon dots for bright and colorful photoluminescence. *J. Am. Chem. Soc.* **128**, 7756–7757 (2006).

18. Yu, S. J., Kang, M. W., Chang, H. C., Chen, K. M. & Yu, Y. C. Bright fluorescent nanodiamonds: No photobleaching and low cytotoxicity. *J. Am. Chem. Soc.* **127**, 17604–17605 (2005).

19. Bottini, M. *et al.* Isolation and characterization of fluorescent nanoparticles from pristine and oxidized electric arc-produced single-walled carbon nanotubes. *J. Phys. Chem. B* **110**, 831–836 (2006).

20. Yuan, T. *et al.* Carbon quantum dots: An emerging material for optoelectronic applications. *J. Mater. Chem. C* **7**, 6820–6835 (2019).

21. Yuan, F. *et al.* Engineering triangular carbon quantum dots with unprecedented narrow bandwidth emission for multicolored LEDs. *Nat. Commun.* **9**, 1–11 (2018).

22. Gao, X., Du, C., Zhuang, Z. & Chen, W. Carbon quantum dot-based nanoprobes for metal ion detection. *J. Mater. Chem. C* **4**, 6927–6945 (2016).

23. Molaei, M. J. Principles, mechanisms, and application of carbon quantum dots in sensors: A review. *Anal. Methods* **12**, 1266–1287 (2020).

24. Qu, S., Wang, X., Lu, Q., Liu, X. & Wang, L. A biocompatible fluorescent ink based on water-soluble luminescent carbon nanodots. *Angew. Chemie - Int. Ed.* **51**, 12215–12218 (2012).

25. Chen, Z. *et al.* Foxtail millet-derived highly fluorescent multi-heteroatom doped carbon quantum dots towards fluorescent inks and smart nanosensors for selective ion detection. *New J. Chem.* **42**, 7326–7331 (2018).

26. Li, H. *et al.* Water-soluble fluorescent carbon quantum dots and photocatalyst design.

Angew. Chemie - Int. Ed. **49**, 4430–4434 (2010).

27. Zhang, Y. Q., Ma, D. K., Zhang, Y. G., Chen, W. & Huang, S. M. N-doped carbon quantum dots for TiO2-based photocatalysts and dye-sensitized solar cells. *Nano Energy* **2**, 545–552 (2013).

28. Zhou, Y. *et al.* Carbon Quantum Dot/TiO2 Nanohybrids: Efficient Photocatalysts for Hydrogen Generation via Intimate Contact and Efficient Charge Separation. *ACS Appl. Nano Mater.* **2**, 1027–1032 (2019).

29. Hu, C., Li, M., Qiu, J. & Sun, Y. P. Design and fabrication of carbon dots for energy conversion and storage. *Chem. Soc. Rev.* **48**, 2315–2337 (2019).

30. Li, W. *et al.* Carbon quantum dots enhanced the activity for the hydrogen evolution reaction in ruthenium-based electrocatalysts. *Mater. Chem. Front.* **4**, 277–284 (2020).

31. Li, G. *et al.* Carbon quantum dots decorated Ba0.5Sr0.5Co0.8Fe0.2O3-Δ perovskite nanofibers for boosting oxygen evolution reaction. *Appl. Catal. B Environ.* **257**, 117919 (2019).

32. Gao, J. *et al.* Carbon quantum dot-covered porous Ag with enhanced activity for selective electroreduction of CO2 to CO. *Inorg. Chem. Front.* **6**, 1453–1460 (2019).

33. Sahadev, N. & Anappara, A. A. Photo-to-thermal conversion: Effective utilization of futile solid-state carbon quantum dots (CQDs) for energy harvesting applications. *New J. Chem.* **44**, 10662–10670 (2020).

34. Zhang, M., Wang, J., Wang, W., Zhang, J. & Zhou, N. Magnetofluorescent photothermal micelles packaged with GdN@CQDs as photothermal and chemical dual-modal therapeutic agents. *Chem. Eng. J.* **330**, 442–452 (2017).

35. Javed, M. *et al.* Carbon quantum dots from glucose oxidation as a highly competent anode material for lithium and sodium-ion batteries. *Electrochim. Acta* **297**, 250–257 (2019).

36. Xu, J. *et al.* Carbon quantum dots/nickel oxide (CQDs/NiO) nanorods with high capacitance for supercapacitors. *RSC Adv.* **6**, 5541–5546 (2016).

37. Hoang, V. C., Dave, K. & Gomes, V. G. Carbon quantum dot-based composites for energy storage and electrocatalysis: Mechanism, applications and future prospects. *Nano Energy* **66**, 104093 (2019).

38. Ning, Z., Dong, H., Zhang, Q., Voznyy, O. & Sargent, E. H. Solar cells based on inks of n-type colloidal quantum dots. *ACS Nano* **8**, 10321–10327 (2014).

39. Parthiban, V., Panda, S. K. & Sahu, A. K. Highly fluorescent carbon quantum dots-Nafion as proton selective hybrid membrane for direct methanol fuel cells. *Electrochim. Acta* **292**, 855–864 (2018).

40. Wang, Q. *et al.* Hollow luminescent carbon dots for drug delivery. *Carbon N. Y.* **59**, 192–199 (2013).

41. Wu, F., Su, H., Wang, K., Wong, W. K. & Zhu, X. Facile synthesis of N-rich carbon quantum dots from porphyrins as efficient probes for bioimaging and biosensing in living cells. *Int. J. Nanomedicine* **12**, 7375–7391 (2017).

42. Devi, P., Saini, S. & Kim, K. H. The advanced role of carbon quantum dots in nanomedical applications. *Biosens. Bioelectron.* **141**, 111158 (2019).

43. Chan, K. K., Yap, S. H. K. & Yong, K. T. *Biogreen Synthesis of Carbon Dots for Biotechnology and Nanomedicine Applications*. *Nano-Micro Letters* **10**, (Springer Berlin Heidelberg, 2018).

44. Liu, M. L., Chen, B. Bin, Li, C. M. & Huang, C. Z. Carbon dots: Synthesis, formation mechanism, fluorescence origin and sensing applications. *Green Chem.* **21**, 449–451 (2019).

45. Pan, D., Zhang, J., Li, Z. & Wu, M. Hydrothermal Route for Cutting Graphene Sheets into Blue-Luminescent Graphene Quantum Dots. *Adv. Mater.* **22**, 734–738 (2010).

46. Bunch, J. S., Yaish, Y., Brink, M., Bolotin, K. & McEuen, P. L. Coulomb oscillations and hall effect in quasi-2D graphite quantum dots. *Nano Lett.* **5**, 287–290 (2005).

47. Silvestrov, P. G. & Efetov, K. B. Quantum dots in graphene. *Phys. Rev. Lett.* **98**, 1–4 (2007).

48. Brey, L. & Fertig, H. A. Electronic states of graphene nanoribbons studied with the Dirac equation. *Phys. Rev. B - Condens. Matter Mater. Phys.* **73**, 2–6 (2006).

49. Matulis, A. & Peeters, F. M. Quasibound states of quantum dots in single and bilayer graphene. *Phys. Rev. B - Condens. Matter Mater. Phys.* **77**, 1–7 (2008).

50. Trauzettel, B., Bulaev, D. V., Loss, D. & Burkard, G. Spin qubits in graphene quantum dots. *Nat. Phys.* **3**, 192–196 (2007).

51. Novoselov, K. S. *et al.* Electric Field Effect in Atomically Thin Carbon Films. *Science (80-.).* **306**, 666–669 (2004).

52. Pillar-Little, T. J. *et al.* Superior photodynamic effect of carbon quantum dots through both type I and type II pathways: Detailed comparison study of top-down-synthesized and bottom-up-synthesized carbon quantum dots. *Carbon N. Y.* **140**, 616–623 (2018).

53. Zhang, Q., Sun, X., Ruan, H., Yin, K. & Li, H. Production of yellow-emitting carbon quantum dots from fullerene carbon soot. *Sci. China Mater.* **60**, 141–150 (2017).

54. Luo, X. *et al.* Laser irradiated vortex fluidic mediated synthesis of luminescent carbon nanodots under continuous flow. *React. Chem. Eng.* (2018). doi:10.1039/C7RE00197E

55. A. J. Lynch, C. A. R. *The History of Grinding*. (2005).

56. Faraji, G., Kim, H. S. & Kashi, H. T. Introduction. *Sev. Plast. Deform.* 1–17 (2018). doi:10.1016/b978-0-12-813518-1.00020-5

57. Prasad Yadav, T., Manohar Yadav, R. & Pratap Singh, D. Mechanical Milling: a Top Down Approach for the Synthesis of Nanomaterials and Nanocomposites. *Nanosci. Nanotechnol.* **2**, 22–48 (2012).

58. Salver-Disma, F., Tarascon, J. M., Clinard, C. & Rouzaud, J. N. Transmission electron microscopy studies on carbon materials prepared by mechanical milling. *Carbon N. Y.* **37**, 1941–1959 (1999).

59. Ong, T. S. & Yang, H. Effect of atmosphere on the mechanical milling of natural graphite. *Carbon N. Y.* **38**, 2077–2085 (2000).

60. Imamura, H. *et al.* Carbon nanocomposites synthesized by high-energy mechanical milling of graphite and magnesium for hydrogen storage. *Acta Mater.* **51**, 6407–6414 (2003).

61. Welham, N. J., Berbenni, V. & Chapman, P. G. Increased chemisorption onto activated carbon after ball-milling. *Carbon N. Y.* **40**, 2307–2315 (2002).

62. Wang, C. S. Lithium Insertion in Carbon-Silicon Composite Materials Produced by Mechanical Milling. *J. Electrochem. Soc.* **145**, 2751 (1998).

63. Salver-Disma, F., Lenain, C., Beaudoin, B., Aymard, L. & Tarascon, J. M. Unique effect of mechanical milling on the lithium intercalation properties of different carbons. *Solid State Ionics* **98**, 145–158 (1997).

64. Wang, L., Chen, X., Lu, Y., Liu, C. & Yang, W. Carbon quantum dots displaying dual-wavelength photoluminescence and electrochemiluminescence prepared by high-energy ball milling. *Carbon N. Y.* **94**, 472–478 (2015).

65. Arepalli, S. Laser ablation process for single-walled carbon nanotube production. *J. Nanosci. Nanotechnol.* **4**, 317–325 (2004).

66. Amendola, V. & Meneghetti, M. Laser ablation synthesis in solution and size manipulation of noble metal nanoparticles. *Phys. Chem. Chem. Phys.* **11**, 3805–3821 (2009).

67. Fazio, E. *et al.* Iron oxide nanoparticles prepared by laser ablation: Synthesis, structural properties and antimicrobial activity. *Colloids Surfaces A Physicochem. Eng. Asp.* **490**, 98–103 (2016).

68. Sajti, C. L., Sattari, R., Chichkov, B. N. & Barcikowski, S. Gram scale synthesis of pure ceramic nanoparticles by laser ablation in liquid. *J. Phys. Chem. C* **114**, 2421–2427 (2010).

69. Xiao, J., Liu, P., Wang, C. X. & Yang, G. W. External field-assisted laser ablation in liquid: An efficient strategy for nanocrystal synthesis and nanostructure assembly. *Prog. Mater. Sci.* **87**, 140–220 (2017).

70. Amendola, V. & Meneghetti, M. What controls the composition and the structure of nanomaterials generated by laser ablation in liquid solution? *Phys. Chem. Chem. Phys.* **15**, 3027–3046 (2013).

71. Zhang, J. *et al.* The luminescent carbon nanoparticles with controllable oxygen-related functional groups prepared by pulsed laser ablation in water. *Mod. Phys. Lett. B* **30**, 3–6 (2016).

72. Hu, S., Liu, J., Yang, J., Wang, Y. & Cao, S. Laser synthesis and size tailor of carbon quantum dots. *J. Nanoparticle Res.* **13**, 7247–7252 (2011).

73. Arora, N. & Sharma, N. N. Arc discharge synthesis of carbon nanotubes: Comprehensive review. *Diam. Relat. Mater.* **50**, 135–150 (2014).

74. Sari, A. H., Khazali, A. & Parhizgar, S. S. Synthesis and characterization of long-CNTs by electrical arc discharge in deionized water and NaCl solution. *Int. Nano Lett.* **8**, 19–23 (2018).

75. Ya-Ping Sun. Arc-Discharge System for Carbon Nanotube Production: Production of single-walled carbon nanotubes (multiple grams per day with 30-40% purity), multi-walled carbon nanotubes, C60, and other carbon forms. *Laboratory for Emerging Materials and Technology, Clemson University* Available at: https://chemistry.sites.clemson.edu/lemt/Arc-Discharge.htm.

76. Berzelio. Carbon Nanotube Arc Discharge in Water. *youtube.com* (2013). Available at: https://www.youtube.com/watch?v=yInS9hcYgSc.

77. Iijima, S. Helical microtubules of graphitic carbon. *Nature* **354**, 56–58 (1991).

78. Kroto, H. W., Heath, J. R., O'Brien, S. C., Curl, R. F. & Smalley, R. E. C 60: buckminsterfullerene. *Nature* **318**, 162–163 (1985).

79. Su, Y. *et al.* Facile synthesis and photoelectric properties of carbon dots with upconversion fluorescence using arc-synthesized carbon by-products. *RSC Adv.* **4**, 4839–4842 (2014).

80. Kim, S., Song, Y. & Heller, M. J. Seamless aqueous arc discharge process for producing graphitic carbon nanostructures. *Carbon N. Y.* **120**, 83–88 (2017).

81. Ming, H. *et al.* Large scale electrochemical synthesis of high quality carbon nanodots and their photocatalytic property. *Dalt. Trans.* **41**, 9526–9531 (2012).

82. Lu, L., Zhu, Y., Shi, C. & Pei, Y. T. Large-scale synthesis of defect-selective graphene quantum dots by ultrasonic-assisted liquid-phase exfoliation. *Carbon N. Y.* **109**, 373–383 (2016).

83. Yi, M. & Shen, Z. A review on mechanical exfoliation for the scalable production of graphene. *J. Mater. Chem. A* 11700–11715 (2015). doi:10.1039/c5ta00252d

84. Li, L. L. *et al.* A facile microwave avenue to electrochemiluminescent two-color graphene quantum dots. *Adv. Funct. Mater.* **22**, 2971–2979 (2012).

85. Liu, X., Hao, J., Liu, J. & Tao, H. Green synthesis of carbon quantum dots from lignite coal and the application in Fe3+ detection. *IOP Conf. Ser. Earth Environ. Sci.* **113**, (2018).

86. Hu, C., Liu, Y., Lei, B., Zheng, M. & Xiao, Y. Extraction of graphitic carbon quantum dots by hydrothermal treatment commercially activated carbon: the role of cation–π interaction. *J. Nanoparticle Res.* **17**, 1–10 (2015).

87. Dong, Y. *et al.* Extraction of electrochemiluminescent oxidized carbon quantum dots from activated carbon. *Chem. Mater.* **22**, 5895–5899 (2010).

88. Han, B. *et al.* One-step extraction of highly fluorescent carbon quantum dots by a physical method from carbon black. *New J. Chem.* **41**, 5267–5270 (2017).

89. Cui, B. *et al.* Fluorescent carbon quantum dots synthesized by chemical vapor deposition: An alternative candidate for electron acceptor in polymer solar cells. *Opt. Mater. (Amst).* **75**, 166–173 (2018).

90. Tang, Q., Zhu, W., He, B. & Yang, P. Rapid Conversion from Carbohydrates to Large-Scale Carbon Quantum Dots for All-Weather Solar Cells. *ACS Nano* **11**, 1540–1547 (2017).

91. Xu, Y. *et al.* Nitrogen-doped carbon dots: A facile and general preparation method, photoluminescence investigation, and imaging applications. *Chem. - A Eur. J.* **19**, 2276–2283 (2013).

92. Shen, Z. *et al.* Microwave-assisted synthesis of cyclen functional carbon dots to construct a ratiometric fluorescent probe for tetracycline detection. *J. Mater. Chem. C* **6**, 9636–9641 (2018).

93. Dong, Y. *et al.* Blue luminescent graphene quantum dots and graphene oxide prepared by tuning the carbonization degree of citric acid. *Carbon N. Y.* **50**, 4738–4743 (2012).

94. Wang, J., Wei, J., Su, S. & Qiu, J. Novel fluorescence resonance energy transfer optical sensors for vitamin B12 detection using thermally reduced carbon dots. *New J. Chem.* **39**, 501–507 (2015).

95. Zheng, M. *et al.* On-off-on fluorescent carbon dot nanosensor for recognition of chromium(VI) and ascorbic acid based on the inner filter effect. *ACS Appl. Mater. Interfaces* **5**, 13242–13247 (2013).

96. Jing, S., Zhao, Y., Sun, R. C., Zhong, L. & Peng, X. Facile and High-Yield Synthesis of Carbon Quantum Dots from Biomass-Derived Carbons at Mild Condition. *ACS Sustain. Chem. Eng.* **7**, 7833–7843 (2019).

97. Das, R., Bandyopadhyay, R. & Pramanik, P. Carbon quantum dots from natural resource: A review. *Mater. Today Chem.* **8**, 96–109 (2018).

98. Briscoe, J., Marinovic, A., Sevilla, M., Dunn, S. & Titirici, M. Biomass-Derived Carbon

Quantum Dot Sensitizers for Solid-State Nanostructured Solar Cells. *Angew. Chemie - Int. Ed.* **54**, 4463–4468 (2015).

99. Zhao, W. B., Liu, K. K., Song, S. Y., Zhou, R. & Shan, C. X. Fluorescent nano-biomass dots: Ultrasonic-assisted extraction and their application as nanoprobe for FE3+ detection. *Nanoscale Res. Lett.* **14**, (2019).

100. Zhao, Y. *et al.* Synthesizing green carbon dots with exceptionally high yield from biomass hydrothermal carbon. *Cellulose* **27**, 415–428 (2020).

101. Bergius, F. C. R. *Anwendung hoher Drucke bei chemischen Vorgängen und die Nachbildung des Entstehungsprozesses der Steinkohle*. (Halle a.S. : W. Knapp, 1913).

102. Wu, P., Li, W., Wu, Q., Liu, Y. & Liu, S. Hydrothermal synthesis of nitrogen-doped carbon quantum dots from microcrystalline cellulose for the detection of Fe3+ ions in an acidic environment. *RSC Adv.* **7**, 44144–44153 (2017).

103. Li, D. *et al.* Far-Red Carbon Dots as Efficient Light-Harvesting Agents for Enhanced Photosynthesis. *ACS Appl. Mater. Interfaces* **12**, 21009–21019 (2020).

104. Cong, S. & Zhao, Z. Carbon Quantum Dots: A Component of Efficient Visible Light Photocatalysts. in *Visible-Light Photocatalysis of Carbon-Based Materials* (2018). doi:10.5772/intechopen.70801

105. Huang, P. *et al.* Carbon quantum dots improving photovoltaic performance of CdS quantum dot-sensitized solar cells. *Opt. Mater. (Amst).* **110**, (2020).

106. Zheng, J. *et al.* An efficient synthesis and photoelectric properties of green carbon quantum dots with high fluorescent quantum yield. *Nanomaterials* **10**, 1–15 (2020).

107. Cruz, R. A. T. *et al.* Functionalized Carbon-based Quantum Dots: Optical Characterization and Potential Application as Bio-fluorophore. *IOP Conf. Ser. Mater. Sci. Eng.* **559**, (2019).

108. Zhang, Z., Zheng, T., Li, X., Xu, J. & Zeng, H. Progress of Carbon Quantum Dots in Photocatalysis Applications. *Part. Part. Syst. Charact.* **33**, 457–472 (2016).

109. Molaei, M. J. The optical properties and solar energy conversion applications of carbon quantum dots: A review. *Sol. Energy* **196**, 549–566 (2020).

110. Wang, J. *et al.* Theoretical investigations of optical origins of fluorescent graphene quantum dots. *Sci. Rep.* **6**, 1–5 (2016).

111. Liqiang, J. *et al.* Review of photoluminescence performance of nano-sized semiconductor materials and its relationships with photocatalytic activity. *Sol. Energy Mater. Sol. Cells* **90**, 1773–1787 (2006).

112. Wang, L. *et al.* Common origin of green luminescence in carbon nanodots and graphene quantum dots. *ACS Nano* **8**, 2541–2547 (2014).

113. Wei, J. & Qiu, J. Unveil the fluorescence of carbon quantum dots. *Adv. Eng. Mater.* **17**, 132–142 (2015).

114. Zhu, S. *et al.* The photoluminescence mechanism in carbon dots (graphene quantum dots, carbon nanodots, and polymer dots): current state and future perspective. *Nano Research* (2015). doi:10.1007/s12274-014-0644-3

115. Mintz, K. J., Zhou, Y. & Leblanc, R. M. Recent development of carbon quantum dots regarding their optical properties, photoluminescence mechanism, and core structure. *Nanoscale* **11**, 4634–4652 (2019).

116. Tian, R. *et al.* Tailoring surface groups of carbon quantum dots to improve photoluminescence behaviors. *Appl. Surf. Sci.* **301**, 156–160 (2014).

117. Li, M. *et al.* Organic amine-grafted carbon quantum dots with tailored surface and enhanced photoluminescence properties. *Carbon N. Y.* **91**, 291–297 (2015).

118. Papaioannou, N. *et al.* Structure and solvents effects on the optical properties of sugar-derived carbon nanodots. *Sci. Rep.* **8**, 1–10 (2018).

119. Liu, Y., Liu, C. yan & Zhang, Z. ying. Synthesis and surface photochemistry of graphitized carbon quantum dots. *J. Colloid Interface Sci.* **356**, 416–421 (2011).

120. Dong, Y. *et al.* Graphene quantum dots, graphene oxide, carbon quantum dots and graphite nanocrystals in coals. *Nanoscale* **6**, 7410–7415 (2014).

121. Linehan, K. & Doyle, H. Size controlled synthesis of carbon quantum dots using hydride reducing agents. *J. Mater. Chem. C* **2**, 6025–6031 (2014).

122. Zhao, A. *et al.* Recent advances in bioapplications of C-dots. *Carbon N. Y.* **85**, 309–327 (2015).

123. Molaei, M. J. Carbon quantum dots and their biomedical and therapeutic applications: A review. *RSC Adv.* **9**, 6460–6481 (2019).

124. Li, M., Chen, T., Gooding, J. J. & Liu, J. Review of carbon and graphene quantum dots

for sensing. *ACS Sensors* **4**, 1732–1748 (2019).

125. Wang, R., Lu, K. Q., Tang, Z. R. & Xu, Y. J. Recent progress in carbon quantum dots: synthesis, properties and applications in photocatalysis. *J. Mater. Chem. A* **5**, 3717–3734 (2017).

126. Zhang, Q. Q., Chen, B. Bin, Zou, H. Y., Li, Y. F. & Huang, C. Z. Inner filter with carbon quantum dots: A selective sensing platform for detection of hematin in human red cells. *Biosens. Bioelectron.* **100**, 148–154 (2018).

127. Zhao, Y. *et al.* Simple and sensitive fluorescence sensor for methotrexate detection based on the inner filter effect of N, S co-doped carbon quantum dots. *Anal. Chim. Acta* **1047**, 179–187 (2019).

128. Lee, H. J., Jana, J., Chung, J. S. & Hur, S. H. Uncovering the actual inner-filter effect between highly efficient carbon dots and nitroaromatics. *Spectrochim. Acta - Part A Mol. Biomol. Spectrosc.* **236**, (2020).

129. Loo, A. H. *et al.* Carboxylic Carbon Quantum Dots as a Fluorescent Sensing Platform for DNA Detection. *ACS Appl. Mater. Interfaces* **8**, 1951–1957 (2016).

130. Zhang, Y.-L. *et al.* Graphitic carbon quantum dots as a fluorescent sensing platform for highly efficient detection of Fe3+ ions. *RSC Adv.* **3**, 3733–3738 (2013).

131. Yu, J., Xu, C., Tian, Z., Lin, Y. & Shi, Z. Facilely synthesized N-doped carbon quantum dots with high fluorescent yield for sensing Fe3+. *New J. Chem.* **40**, 2083–2088 (2016).

132. Singh, Jai, Williams, R. T. *Excitonic and Photonic Processes in Materials*. (Springer Singapore, 2015). doi:10.1007/978-981-287-131-2

133. Liao, C., Li, Y. & Tjong, S. C. Graphene nanomaterials: Synthesis, biocompatibility, and cytotoxicity. *Int. J. Mol. Sci.* **19**, (2018).

134. Pinto, A. M., Gonc, I. C. & Magalhães, F. D. Graphene-based materials biocompatibility : A review. *Colloids Surfaces B Biointerfaces* **111**, 188–202 (2013).

135. Martín, C., Kostarelos, K., Prato, M. & Bianco, A. Biocompatibility and biodegradability of 2D materials: Graphene and beyond. *Chem. Commun.* **55**, 5540–5546 (2019).

136. Wu, X., Ding, S. J., Lin, K. & Su, J. A review on the biocompatibility and potential applications of graphene in inducing cell differentiation and tissue regeneration. *J.*

Mater. Chem. B **5**, 3084–3102 (2017).

137. Ma, T. *et al.* Tailoring the thermal and electrical transport properties of graphene films by grain size engineering. *Nat. Commun.* **8**, 1–9 (2017).

138. Son, J. *et al.* Tailoring Surface Properties via Functionalized Hydrofluorinated Graphene Compounds. *Adv. Mater.* **31**, 1–7 (2019).

139. Liu, L. *et al.* Tailoring physical properties of graphene: Effects of hydrogenation, oxidation, and grain boundaries by atomistic simulations. *Comput. Mater. Sci.* **112**, 527–546 (2016).

140. Wang, N. *et al.* Tailoring the Thermal and Mechanical Properties of Graphene Film by Structural Engineering. *Small* **14**, 1–8 (2018).

141. Park, K. H. *et al.* Defect-free, size-tunable graphene for high-performance lithium ion battery. *Nano Lett.* **14**, 4306–4313 (2014).

142. Park, B. J. *et al.* Defect-Free Graphene Synthesized Directly at 150 °c via Chemical Vapor Deposition with No Transfer. *ACS Nano* **12**, 2008–2016 (2018).

143. Charlier, J. C., Gonze, X. & Michenaud, J. P. Graphite interplanar bonding: Electronic delocalization and van der waals interaction. *Epl* **28**, 403–408 (1994).

144. Yi, M. & Shen, Z. A review on mechanical exfoliation for the scalable production of graphene. *J. Mater. Chem. A* **3**, 11700–11715 (2015).

145. Jeon, I. Y. *et al.* Edge-carboxylated graphene nanosheets via ball milling. *Proc. Natl. Acad. Sci. U. S. A.* **109**, 5588–5593 (2012).

146. Nguyen, D. D. *et al.* Synthesis of ethanol-soluble few-layer graphene nanosheets for flexible and transparent conducting composite films. *Nanotechnology* **22**, 1–8 (2011).

147. Bai, H., Li, C. & Shi, G. Functional composite materials based on chemically converted graphene. *Adv. Mater.* **23**, 1089–1115 (2011).

148. Mahmoud, A. E. D., Stolle, A. & Stelter, M. Sustainable Synthesis of High-Surface-Area Graphite Oxide via Dry Ball Milling. *ACS Sustain. Chem. Eng.* **6**, 6358–6369 (2018).

149. Casallas Caicedo, F. M. *et al.* Synthesis of graphene oxide from graphite by ball milling. *Diam. Relat. Mater.* **109**, (2020).

150. Palei, B. B., Dash, T. & Biswal, S. K. Reduced graphene oxide synthesis by dry planetary ball milling technique under hydrogen atmosphere. *IOP Conf. Ser. Mater. Sci. Eng.* **872**, (2020).

151. Anderson, S. H. & Chung, D. D. L. Exfoliation of intercalated graphite. *Carbon N. Y.* **22**, 253–263 (1984).

152. Yoshida, A., Hishiyama, Y. & Inagaki, M. Exfoliation of vapor-grown graphite fibers as studied by scanning electron microscope. *Carbon N. Y.* **28**, 539–543 (1990).

153. Yoshida, A., Hishiyama, Y. & Inagaki, M. Exfoliated graphite from various intercalation compounds. *Carbon N. Y.* **29**, 1227–1231 (1991).

154. Viculis, L. M., Mack, J. J., Mayer, O. M., Hahn, H. T. & Kaner, R. B. Intercalation and exfoliation routes to graphite nanoplatelets. *J. Mater. Chem.* **15**, 974–978 (2005).

155. Bepete, G. *et al.* "Eau de graphene" from a KC8 graphite intercalation compound prepared by a simple mixing of graphite and molten potassium. *Phys. Status Solidi - Rapid Res. Lett.* **10**, 895–899 (2016).

156. Catheline, A. *et al.* Graphene solutions. *Chem. Commun.* **47**, 5470–5472 (2011).

157. Wada, T. *et al.* Evaluation of Layered Graphene Prepared via Hydroxylation of Potassium-Graphite Intercalation Compounds. *J. Nanomater.* **2014**, 1–6 (2014).

158. Setton, R. New developments in the use of graphite lamellar compounds as reagents in organic synthesis. *Mater. Sci. Eng.* **31**, 303–307 (1977).

159. Podall, H. & Foster, W. E. Catalytic Graphite Inclusion Compounds. II. Potassium Graphite as an Polymerization Catalyst. *J. Org. Chem.* **23**, 401–403 (1958).

160. Fredenhagen, K. & Cadenbach, G. Die Bindung von Kalium durch Kohlenstoff. *Zeitschrift für Anorg. und Allg. Chemie* **158**, 249–263 (1926).

161. Hennig, G. R. Optical transmission of graphite compounds. *J. Chem. Phys.* **43**, 1201–1206 (1965).

162. Nobuhara, K., Nakayama, H., Nose, M., Nakanishi, S. & Iba, H. First-principles study of alkali metal-graphite intercalation compounds. *J. Power Sources* **243**, 585–587 (2013).

163. Yang, S. *et al.* Ultrafast Delamination of Graphite into High-Quality Graphene Using Alternating Currents. *Angew. Chemie - Int. Ed.* **56**, 6669–6675 (2017).

164. Munuera, J. M. *et al.* Electrochemical Exfoliation of Graphite in Aqueous Sodium Halide Electrolytes toward Low Oxygen Content Graphene for Energy and Environmental Applications. *ACS Appl. Mater. Interfaces* **9**, 24085–24099 (2017).

165. Okotrub, A. V., Fedorovskaya, E. O., Senkovskiy, B. V. & Bulusheva, L. G. Nitrogen species in few-layer graphene produced by thermal exfoliation of fluorinated graphite intercalation compounds. *Phys. Status Solidi Basic Res.* **252**, 2444–2450 (2015).

166. Seiler, S. *et al.* Effect of friction on oxidative graphite intercalation and high-quality graphene formation. *Nat. Commun.* **9**, 1–9 (2018).

167. Brodie, B. C. On the atomic weight of graphite. *Philos. Trans. R. Soc.* **149**, 249–259 (1858).

168. Arsem, W. C. Transformation of other forms of carbon into graphite. *Ind. Eng. Chem. Res.* **3**, 799–804 (1911).

169. Hummers, W. S. & Offeman, R. E. Preparation of Graphitic Oxide. *J. Am. Chem. Soc.* **80**, 1339 (1958).

170. Staudenmaier, L. Verfahren zur Darstellung der Graphitsäure. *Eur. J. Inorg. Chem.* (1898).

171. Long, D. *et al.* Preparation of nitrogen-doped graphene sheets by a combined chemical and hydrothermal reduction of graphene oxide. *Langmuir* **26**, 16096–16102 (2010).

172. Zhou, Y. *et al.* One-pot synthesis of B-doped three-dimensional reduced graphene oxide via supercritical fluid for oxygen reduction reaction. *Green Chem.* **17**, 3552–3560 (2015).

173. Park, S. *et al.* Chemical structures of hydrazine-treated graphene oxide and generation of aromatic nitrogen doping. *Nat. Commun.* **3**, (2012).

174. Zhang, J. *et al.* Reduction of graphene oxide vial-ascorbic acid. *Chem. Commun.* **46**, 1112–1114 (2010).

175. Dey, R. S., Hajra, S., Sahu, R. K., Raj, C. R. & Panigrahi, M. K. A rapid room temperature chemical route for the synthesis of graphene: Metal-mediated reduction of graphene oxide. *Chem. Commun.* **48**, 1787–1789 (2012).

176. Fan, Z. *et al.* An environmentally friendly and efficient route for the reduction of graphene oxide by aluminum powder. *Carbon N. Y.* **48**, 1686–1689 (2010).

177. Pham, V. H. *et al.* Chemical reduction of an aqueous suspension of graphene oxide by nascent hydrogen. *J. Mater. Chem.* **22**, 10530–10536 (2012).

178. Rabchinskii, M. K. *et al.* Facile reduction of graphene oxide suspensions and films using glass wafers. *Sci. Rep.* **8**, 1–11 (2018).

179. Zhang, H., Kuila, T., Kim, N. H., Yu, D. S. & Lee, J. H. Simultaneous reduction, exfoliation, and nitrogen doping of graphene oxide via a hydrothermal reaction for energy storage electrode materials. *Carbon N. Y.* **69**, 66–78 (2014).

180. Chua, C. K. & Pumera, M. The reduction of graphene oxide with hydrazine: elucidating its reductive capability based on a reaction-model approach. *Chem. Commun.* **52**, 72–75 (2016).

181. Mohanty, N., Nagaraja, A., Armesto, J. & Berry, V. High-throughput, ultrafast synthesis of solutiondispersed graphene via a facile hydride chemistry. *Small* **6**, 226–231 (2010).

182. Matsumoto, K. *Frontiers of Graphene and Carbon Nanotubes*. (Springer, Tokyo, 2015). doi:https://doi.org/10.1007/978-4-431-55372-4_1

183. Joffrey Pijeat, J.-S. L. and S. C. Chapter 2: Bottom-up approach for the synthesis of graphene nanoribbons. in *Graphene Nanoribbons* 2.1-2.25 (IOP Publishing Ltd, 2019). doi:10.1088/978-0-7503-1701-6ch2

184. Li, X. *et al.* Large-area synthesis of high-quality and uniform graphene films on copper foils. *Science (80-.).* **324**, 1312–1314 (2009).

185. Berger, C. *et al.* Ultrathin epitaxial graphite: 2D electron gas properties and a route toward graphene-based nanoelectronics. *J. Phys. Chem. B* **108**, 19912–19916 (2004).

186. Kim, K. S. *et al.* Large-scale pattern growth of graphene films for stretchable transparent electrodes. *Nature* **457**, 706–710 (2009).

187. Tu, Z. *et al.* Controllable growth of 1 – 7 layers of graphene by chemical vapour deposition. *Carbon N. Y.* **73**, 252–258 (2014).

188. Mattevi, C., Kim, H. & Chhowalla, M. A review of chemical vapour deposition of graphene on copper. *J. Mater. Chem.* **21**, 3324–3334 (2011).

189. Liu, W., Li, H., Xu, C., Khatami, Y. & Banerjee, K. Synthesis of high-quality monolayer and bilayer graphene on copper using chemical vapor deposition. *Carbon N. Y.* **49**, 4122–4130 (2011).

190. Li, X., Colombo, L. & Ruoff, R. S. Synthesis of Graphene Films on Copper Foils by Chemical Vapor Deposition. *Adv. Mater.* **28**, 6247–6252 (2016).

191. Muñoz, R. & Gómez-Aleixandre, C. Review of CVD synthesis of graphene. *Chem. Vap. Depos.* **19**, 297–322 (2013).

192. Johánek, V., Nehasil, V., Skála, T. & Tsud, N. Carbon Chain Length Dependence of Graphene Formation via Thermal Decomposition of Alkenes on Pt(111). *J. Phys. Chem. C* **123**, 7911–7921 (2019).

193. An, H., Lee, W. J. & Jung, J. Graphene synthesis on Fe foil using thermal CVD. *Curr. Appl. Phys.* **11**, S81–S85 (2011).

194. Jiang, L. *et al.* Low-temperature, bottom-up synthesis of graphene via a radical-coupling reaction. *J. Am. Chem. Soc.* **135**, 9050–9054 (2013).

195. Yang, Y. *et al.* Bottom-up Fabrication of Graphene on Silicon/Silica Substrate via a Facile Soft-hard Template Approach. *Sci. Rep.* **5**, 1–7 (2015).

196. Moreno, C. *et al.* Bottom up synthesis of multifunctional nanoporous graphene. *Science (80-.).* **203**, 23–28 (2018).

197. Li, Q., Zhang, C., Zheng, J. Y., Zhao, Y. S. & Yao, J. Large-scale production of high-quality graphene using glucose and ferric chloride. *Chem. Sci.* **5**, 4656–4660 (2014).

198. Yan, Q., Li, J., Zhang, X., Zhang, J. & Cai, Z. Synthetic bio-graphene based nanomaterials through different Iron catalysts. *Nanomaterials* **8**, (2018).

199. Huang, D. *et al.* Bottom-up synthesis and structural design strategy for graphene quantum dots with tunable emission to the near infrared region. *Carbon N. Y.* **142**, 673–684 (2019).

200. Titirici, M. M. Hydrothermal Carbons: Synthesis, Characterization, and Applications. in *Novel Carbon Adsorbents* 351–399 (2012). doi:10.1016/B978-0-08-097744-7.00012-0

201. Hou, I. C., Hu, Y., Narita, A. & Müllen, K. Diels – Alder polymerization : a versatile synthetic method toward functional polyphenylenes , ladder polymers and graphene nanoribbons. *Nat. Publ. Gr.* **50**, 3–20 (2017).

202. Shifrina, Z. B., Averina, M. S., Rusanov, A. L., Wagner, M. & Müllen, K. Branched polyphenylenes by repetitive Diels-Alder cycloaddition. *Macromolecules* **33**, 3525–3529 (2000).

203. Narita, A. *et al.* Synthesis of structurally well-defined and liquid- phase-processable graphene nanoribbons. *Nat. Chem.* **6**, 126–132 (2014).

204. Jacobse, P. H., Hoogenband, A. Van Den, Moret, M., Gebbink, R. J. M. K. & Swart, I. Aryl Radical Geometry Determines Nanographene Formation on Au (111). *Angew. Chemie - Int. Ed.* **55**, 13052–13055 (2016).

205. Morimoto, N., Kubo, T. & Nishina, Y. Tailoring the Oxygen Content of Graphite and Reduced Graphene Oxide for Specific Applications. 4–11 (2016). doi:10.1038/srep21715

206. Sergio, A. P., Xu, X. & Ulises, A. M. Functionalized reduced graphene oxide with tunable band gap and good solubility in organic solvents. **146**, 491–502 (2019).

207. Ma, Y. *et al.* Highly doped graphene with multi-dopants for high-capacity and ultrastable sodium-ion batteries. *Energy Storage Mater.* **13**, 134–141 (2018).

208. Zhang, L. *et al.* Fe , N co-doped graphene as a multi-functional anchor material for lithium- sulfur battery. *J. Phys. Chem. Solids* **126**, 280–286 (2019).

209. Zhao, A. *et al.* Green and controllable synthesis of multi-heteroatoms co-doped graphene fiber as flexible and biocompatible microelectrode for in situ electrochemical detection of biological samples. *Sensors Actuators B. Chem.* **335**, 129683 (2021).

210. Sforzini, J. *et al.* Structural and Electronic Properties of Nitrogen-Doped Graphene. *Phys. Rev. Lett.* **116**, 126805 (2016).

211. Geng, D. *et al.* Nitrogen doping effects on the structure of graphene. *Appl. Surf. Sci.* **257**, 9193–9198 (2011).

212. Zhao, Y. *et al.* A Versatile , Ultralight , Nitrogen-Doped Graphene Framework **. *Angew. Chemie - Int. Ed.* **51**, 11371–11375 (2012).

213. Wang, L., Sofer, Z. & Pumera, M. Will Any Crap We Put into Graphene Increase Its Electrocatalytic Effect? *ACS Nano* **14**, 21–25 (2020).

214. Konios, D., Stylianakis, M. M., Stratakis, E. & Kymakis, E. Dispersion behaviour of graphene oxide and reduced graphene oxide. *J. Colloid Interface Sci.* **430**, 108–112 (2014).

215. Yi, M., Shen, Z., Zhang, X. & Ma, S. Achieving concentrated graphene dispersions in water/acetone mixtures by the strategy of tailoring Hansen solubility parameters. *J.*

Phys. D. Appl. Phys. **46**, 025301 (2012).

216. Cao, G. Atomistic Studies of Mechanical Properties of Graphene. *Polymers (Basel).* **6**, 2404–2432 (2014).

217. Ovid'ko, I. A. Mechanical properties of graphene. *Rev. Adv. Mater. Sci.* **34**, 1–11 (2013).

218. Bae, S., Kim, S. J., Shin, D., Ahn, J. H. & Hong, B. H. Towards industrial applications of graphene electrodes. *Phys. Scr.* **T146**, 014024 (2012).

219. Wolf, E. L. *Applications of Graphene: An Overview*. *Applications of Graphene* (2014).

220. Smith, A. T., LaChance, A. M., Zeng, S., Liu, B. & Sun, L. Synthesis, properties, and applications of graphene oxide/reduced graphene oxide and their nanocomposites. *Nano Mater. Sci.* **1**, 31–47 (2019).

221. Politou, M. *et al.* Single- and multilayer graphene wires as alternative interconnects. *Microelectron. Eng.* **156**, 131–135 (2016).

222. Abbasi, E., Akbarzadeh, A., Kouhi, M. & Milani, M. Graphene: Synthesis, bio-applications, and properties. *Artif. Cells, Nanomedicine Biotechnol.* **44**, 150–156 (2016).

223. Chung, C. *et al.* Biomedical Applications of Graphene and Graphene Oxide. *Acc. Chem. Res.* **46**, 2211–2224 (2013).

224. Yang, Y., Asiri, A. M., Tang, Z., Du, D. & Lin, Y. Graphene based materials for biomedical applications. *Mater. Today* **16**, 365–373 (2013).

225. Kim, J. Applications of Graphene and Graphene-Related Materials. *Int. J. Nanomedicine* **11**, 1927–1945 (2016).

226. Li, F., Jiang, X., Zhao, J. & Zhang, S. Graphene oxide: A promising nanomaterial for energy and environmental applications. *Nano Energy* **16**, 488–515 (2015).

227. Perreault, F., Fonseca De Faria, A. & Elimelech, M. Environmental applications of graphene-based nanomaterials. *Chem. Soc. Rev.* **44**, 5861–5896 (2015).

228. Kemp, K. C. *et al.* Environmental applications using graphene composites: Water remediation and gas adsorption. *Nanoscale* **5**, 3149–3171 (2013).

229. Zhang, H. & Banfield, J. F. Structural characteristics and mechanical and thermodynamic properties of nanocrystalline TiO2. *Chem. Rev.* **114**, 9613–9644 (2014).

230. Eibner, A. Action of light on pigments I. *Chem. Zeitung* **35**, 753–755 (1911).

231. Shin-ichi Kato, F. M. Titanium Dioxide-Photocatalyzed Liquid Phase Oxidation of Tetralin. *J. Soc. Chem. Ind. Japan* **67**, 1136–1140 (1964).

232. Kumar, S. G. & Devi, L. G. Review on modified TiO2 photocatalysis under UV/visible light: Selected results and related mechanisms on interfacial charge carrier transfer dynamics. *J. Phys. Chem. A* **115**, 13211–13241 (2011).

233. Tang, Q., Zhu, W., He, B. & Yang, P. Rapid Conversion from Carbohydrates to Large-Scale Carbon Quantum Dots for All-Weather Solar Cells. *ACS Nano* **11**, 1540–1547 (2017).

234. Meng, A., Zhang, L., Cheng, B. & Yu, J. Dual Cocatalysts in TiO2 Photocatalysis. *Adv. Mater.* **31**, 1–31 (2019).

235. Ramadoss, A., Kim, G. S. & Kim, S. J. Fabrication of reduced graphene oxide/TiO2 nanorod/reduced graphene oxide hybrid nanostructures as electrode materials for supercapacitor applications. *CrystEngComm* (2013). doi:10.1039/c3ce41517a

236. Khalid, N. R., Majid, A., Tahir, M. B., Niaz, N. A. & Khalid, S. Carbonaceous-TiO2 nanomaterials for photocatalytic degradation of pollutants: A review. *Ceram. Int.* **43**, 14552–14571 (2017).

237. Luttrell, T. *et al.* Why is anatase a better photocatalyst than rutile? - Model studies on epitaxial TiO2 films. *Sci. Rep.* **4**, 1–8 (2015).

238. Scanlon, D. O. *et al.* Band alignment of rutile and anatase TiO2. *Nat. Mater.* **12**, 798–801 (2013).

239. Jin, C. *et al.* Hydrothermal synthesis and characterization of phosphorous-doped TiO2 with high photocatalytic activity for methylene blue degradation. *J. Mol. Catal. A Chem.* **313**, 44–48 (2009).

240. Hanaor, D. A. H. & Sorrell, C. C. Review of the anatase to rutile phase transformation. *J. Mater. Sci.* **46**, 855–874 (2011).

241. Malekshahi Byranvand, M., Nemati Kharat, A., Fatholahi, L. & Malekshahi Beiranvand, Z. A Review on Synthesis of Nano-TiO2 via Different Methods. *J. Nanostructures* **3**, 1–9 (2013).

242. Murugan, A. V., Samuel, V. & Ravi, V. Synthesis of nanocrystalline anatase TiO2 by microwave hydrothermal method. *Mater. Lett.* **60**, 479–480 (2006).

243. Kellici, S. Cleaner Routes to Nanoparticle Synthesis from Supercritical Fluid Mixtures. (Queen Mary University of London, 2006).

244. Zhang, Z. *et al.* Direct continuous hydrothermal synthesis of high surface area nanosized titania. *J. Alloys Compd.* **476**, 451–456 (2009).

245. Kawasaki, S. ichiro *et al.* Continuous supercritical hydrothermal synthesis of controlled size and highly crystalline anatase TiO2 nanoparticles. *J. Supercrit. Fluids* **50**, 276–282 (2009).

246. Williams, G., Seger, B. & Kamt, P. V. TiO2-graphene nanocomposites. UV-assisted photocatalytic reduction of graphene oxide. *ACS Nano* **2**, 1487–1491 (2008).

247. Akhavan, O. & Ghaderi, E. Photocatalytic reduction of graphene oxide nanosheets on TiO2 thin film for photoinactivation of bacteria in solar light irradiation. *J. Phys. Chem. C* **113**, 20214–20220 (2009).

248. Manga, K. K., Zhou, Y., Yan, Y. & Loh, K. P. Multilayer hybrid films consisting of alternating graphene and titania nanosheets with ultrafast electron transfer and photoconversion properties. *Adv. Funct. Mater.* **19**, 3638–3643 (2009).

249. Lambert, T. N. *et al.* Synthesis and Characterization of Titania - Graphene Nanocomposites. *J. Phys. Chem. C* **113**, 19812–19823 (2009).

250. Zhang, H., Lv, X., Li, Y., Wang, Y. & Li, J. P25-graphene composite as a high performance photocatalyst. *ACS Nano* **4**, 380–386 (2010).

251. Zhu, C. *et al.* One-pot, water-phase approach to high-quality graphene/TiO2 composite nanosheets. *Chem. Commun.* **46**, 7148–7150 (2010).

252. Sharavath, V., Sarkar, S. & Ghosh, S. One-pot hydrothermal synthesis of TiO2/graphene nanocomposite with simultaneous nitrogen-doping for energy storage application. *J. Electroanal. Chem.* **829**, 208–216 (2018).

253. Leng, Y., Gao, Y., Wang, W. & Zhao, Y. Continuous supercritical solvothermal synthesis of TiO2-pristine-graphene hybrid as the enhanced photocatalyst. *J. Supercrit. Fluids* **103**, 115–121 (2015).

254. Sun, M. *et al.* A nanocomposite of carbon quantum dots and TiO2 nanotube arrays: Enhancing photoelectrochemical and photocatalytic properties. *RSC Adv.* **4**, 1120–1127 (2014).

255. Sharma, S., Kumar, S., Arumugam, S. M. & Elumalai, S. Promising photocatalytic degradation of lignin over carbon quantum dots decorated TiO2 nanocomposite in aqueous condition. *Appl. Catal. A Gen.* **602**, 117730 (2020).

256. Yu, J. *et al.* Lignite-derived carbon quantum dot/TiO2 heterostructure nanocomposites: photoinduced charge transfer properties and enhanced visible light photocatalytic activity. *New J. Chem.* **43**, 18355–18368 (2019).

257. Choi, D., Ham, S. & Jang, D. J. Visible-light photocatalytic reduction of Cr(VI) via carbon quantum dots-decorated TiO2 nanocomposites. *J. Environ. Chem. Eng.* **6**, 1–8 (2018).

258. Trapalis, A. *et al.* TiO2/graphene composite photocatalysts for NOx removal: A comparison of surfactant-stabilized graphene and reduced graphene oxide. *Appl. Catal. B Environ.* **180**, 637–647 (2016).

259. Zhou, G. *et al.* Ti3+ self-doped mesoporous black TiO2/graphene assemblies for unpredicted-high solar-driven photocatalytic hydrogen evolution. *J. Colloid Interface Sci.* **505**, 1031–1038 (2017).

260. Sargin, I., Yanalak, G., Arslan, G. & Patir, I. H. Green synthesized carbon quantum dots as TiO2 sensitizers for photocatalytic hydrogen evolution. *Int. J. Hydrogen Energy* **44**, 21781–21789 (2019).

261. Kumar, K. Y. *et al.* Controllable synthesis of TiO2 chemically bonded graphene for photocatalytic hydrogen evolution and dye degradation. *Catal. Today* **340**, 170–177 (2020).

262. Bhanvase, B. A., Shende, T. P. & Sonawane, S. H. A review on graphene–TiO2 and doped graphene–TiO2 nanocomposite photocatalyst for water and wastewater treatment. *Environ. Technol. Rev.* **6**, 1–14 (2017).

263. Kusiak-Nejman, E. & Morawski, A. W. TiO2/graphene-based nanocomposites for water treatment: A brief overview of charge carrier transfer, antimicrobial and photocatalytic performance. *Appl. Catal. B Environ.* **253**, 179–186 (2019).

264. Liu, X. *et al.* Black titania/graphene oxide nanocomposite films with excellent photothermal property for solar steam generation. *J. Mater. Res.* **33**, 674–684 (2018).

265. Xiang, C. *et al.* Lightweight and ultrathin TiO 2 -Ti 3 C 2 T X /graphene film with electromagnetic interference shielding. *Chem. Eng. J.* **360**, 1158–1166 (2019).

266. Ou, G. *et al.* Photothermal therapy by using titanium oxide nanoparticles. *Nano Res.* **9**, 1236–1243 (2016).

267. Mirtchev, P., Henderson, E. J., Soheilnia, N., Yip, C. M. & Ozin, G. A. Solution phase synthesis of carbon quantum dots as sensitizers for nanocrystalline TiO 2 solar cells. *J. Mater. Chem.* **22**, 1265–1269 (2012).

268. Zhu, G. *et al.* Graphene-incorporated nanocrystalline TiO2 films for CdS quantum dot-sensitized solar cells. *J. Electroanal. Chem.* **650**, 248–251 (2011).

269. Yoon, D. *et al.* One-pot route for uniform anchoring of TiO2 nanoparticles on reduced graphene oxides and their anode performance for lithium-ion batteries. *J. Supercrit. Fluids* **125**, 66–78 (2017).

270. Cheng, L. *et al.* Template-free synthesis of mesoporous succulents-like TiO 2 /graphene aerogel composites for lithium-ion batteries. *Electrochim. Acta* **300**, 417–425 (2019).

271. Yang, S., Li, Y., Sun, J. & Cao, B. Laser induced oxygen-deficient TiO2/graphene hybrid for high-performance supercapacitor. *J. Power Sources* **431**, 220–225 (2019).

272. Yang, S., Lin, Y., Song, X., Zhang, P. & Gao, L. Covalently Coupled Ultrafine H-TiO2 Nanocrystals/Nitrogen-Doped Graphene Hybrid Materials for High-Performance Supercapacitor. *ACS Appl. Mater. Interfaces* **7**, 17884–17892 (2015).

273. Yan, Y. *et al.* Carbon quantum dot-decorated TiO2 for fast and sustainable antibacterial properties under visible-light. *J. Alloys Compd.* **777**, 234–243 (2019).

274. Malmir, S. *et al.* Antibacterial properties of a bacterial cellulose CQD-TiO2 nanocomposite. *Carbohydr. Polym.* **234**, 115835 (2020).

275. Fan, Y. *et al.* Hydrothermal preparation and electrochemical sensing properties of TiO2-graphene nanocomposite. *Colloids Surfaces B Biointerfaces* **83**, 78–82 (2011).

276. Galstyan, V. *et al.* Reduced Graphene Oxide-TiO2 Nanotube Composite: Comprehensive Study for Gas-Sensing Applications. *ACS Appl. Nano Mater.* **1**, 7098–7105 (2018).

277. Mehta, A., Mishra, A., Kainth, S. & Basu, S. Carbon quantum dots/TiO2 nanocomposite for sensing of toxic metals and photodetoxification of dyes with kill waste by waste concept. *Mater. Des.* **155**, 485–493 (2018).

278. Shuai, C., Wang, B., Bin, S., Peng, S. & Gao, C. TiO2-Induced in Situ Reaction in

Graphene Oxide-Reinforced AZ61 Biocomposites to Enhance the Interfacial Bonding. *ACS Appl. Mater. Interfaces* **12**, 23464–23473 (2020).

279. Bröll, D. *et al.* Chemistry in supercritical water. *Angew. Chemie - Int. Ed.* **38**, 2998–3014 (1999).

280. Kritzer, P. Corrosion in high-temperature and supercritical water and aqueous solutions: A review. *J. Supercrit. Fluids* **29**, 1–29 (2004).

281. Choudhry, K. I., Guzonas, D. A., Kallikragas, D. T. & Svishchev, I. M. On-line monitoring of oxide formation and dissolution on alloy 800H in supercritical water. *Corros. Sci.* **111**, 574–582 (2016).

282. Hayashi, H. & Hakuta, Y. Hydrothermal Synthesis of metal oxide nanoparticles in supercritical water. *Materials (Basel).* **3**, 3794–3817 (2010).

283. Weingärtner, H. & Franck, E. U. Supercritical water as a solvent. *Angew. Chemie - Int. Ed.* **44**, 2672–2692 (2005).

284. Woodcock, L. V. Gibbs Density Surface of Water and Steam: 2nd Debate on the Absence of Van Der Waals' "Critical Point". *Nat. Sci.* **06**, 411–432 (2014).

285. Kritzer, P., Boukis, N. & Dinjus, E. Factors controlling corrosion in high-temperature aqueous solutions: A contribution to the dissociation and solubility data influencing corrosion processes. *J. Supercrit. Fluids* **15**, 205–227 (1999).

286. Tadafumi Adschiri, Katsuhito Kanazawa, K. A. Rapid and Continuous Hydrothermal Crystallization of Metal Oxide Particles in Supercritical Water. *J. Am. Ceram. Soc.* **75**, 1019–1022 (1992).

287. Tadafumi Asdchiri; Satoru Hirose; Roberto Malaluan; and Kunio Arai. Noncatalytic conversion of cellulose in supercirtical and subcritical water. *J. Chem. Eng. JAPAN* **26**, 676–680 (1993).

288. Cabanas, A., Darr, J. A., Lester, E. & Poliakoff, M. A continuous and clean one-step synthesis of nano-particulate CeZrO solid solutions in near-critical water. *Chem. Commun.* 901–902 (2000). doi:10.1039/B001424I

289. Blood, P. J., Denyer, J. P., Azzopardi, B. J., Poliakoff, M. & Lester, E. A versatile flow visualisation technique for quantifying mixing in a binary system: Application to continuous supercritical water hydrothermal synthesis (SWHS). *Chem. Eng. Sci.* **59**,

2853–2861 (2004).

290. Tighe, C. J. *et al.* Investigation of counter-current mixing in a continuous hydrothermal flow reactor. *J. Supercrit. Fluids* **62**, 165–172 (2012).

291. Dunne, P. W., Munn, A. S., Starkey, C. L., Huddle, T. A. & Lester, E. H. Continuous-flow hydrothermal synthesis for the production of inorganic nanomaterials. *Philos. Trans. R. Soc. A Math. Phys. Eng. Sci.* **373**, (2015).

292. Sierra-Pallares, J. *et al.* Understanding bottom-up continuous hydrothermal synthesis of nanoparticles using empirical measurement and computational simulation. *Nano Res.* **9**, 3377–3387 (2016).

293. Lester, E. *et al.* Reaction engineering: The supercritical water hydrothermal synthesis of nano-particles. *J. Supercrit. Fluids* **37**, 209–214 (2006).

294. Gruar, R. I., Tighe, C. J. & Darr, J. A. Scaling-up a confined jet reactor for the continuous hydrothermal manufacture of nanomaterials. *Ind. Eng. Chem. Res.* **52**, 5270–5281 (2013).

295. Mi, J. L. *et al.* Highly controlled crystallite size and crystallinity of pure and iron-doped anatase-TiO2 nanocrystals by continuous flow supercritical synthesis. *J. Mater. Res.* **28**, 333–339 (2013).

296. Breslow, R. The Principles of and Reasons for Using Water as a Solvent for Green Chemistry. in *Handbook of Green Chemistry* (ed. Anastas, P. T.) **42**, (Wiley-VCH Verlag GmbH & Co. KGaA, 2011).

297. Caramazana-Gonzalez, P. *et al.* Assessing the life cycle environmental impacts of titania nanoparticle production by continuous flow solvo/hydrothermal syntheses. *Green Chem.* **19**, 1536–1547 (2017).

298. Kellici, S. *et al.* Continuous hydrothermal flow synthesis of graphene quantum dots. *React. Chem. Eng.* **3**, 949–958 (2018).

299. Baragau, I. A. *et al.* Efficient Continuous Hydrothermal Flow Synthesis of Carbon Quantum Dots from a Targeted Biomass Precursor for On-Off Metal Ions Nanosensing. *ACS Sustain. Chem. Eng.* **9**, 2559–2569 (2021).

300. Stieberova, B. *et al.* Sustainability assessment of continuous-flow hydrothermal synthesis of nanomaterials in the context of other production technologies. *J. Clean.*

Prod. **241**, (2019).

301. Beyer, J., Mamakhel, A., Søndergaard-Pedersen, F., Yu, J. & Iversen, B. B. Continuous flow hydrothermal synthesis of phase pure rutile TiO2 nanoparticles with a rod-like morphology. *Nanoscale* **12**, 2695–2702 (2020).

302. Makwana, N. M., Tighe, C. J., Gruar, R. I., McMillan, P. F. & Darr, J. A. Pilot plant scale continuous hydrothermal synthesis of nano-titania; Effect of size on photocatalytic activity. *Mater. Sci. Semicond. Process.* **42**, 131–137 (2016).

303. Kellici, S. *et al.* A single rapid route for the synthesis of reduced graphene oxide with antibacterial activities. *RSC Adv.* **4**, 14858–14861 (2014).

304. Tian, J. *et al.* Environmentally Friendly, One-Pot Synthesis of Ag Nanoparticle-Decorated Reduced Graphene Oxide Composites and Their Application to Photocurrent Generation. *Inorg. Chem.* **2**, 4742–4746 (2012).

305. Middelkoop, V. *et al.* Next frontiers in cleaner synthesis: 3D printed graphene-supported CeZrLa mixed-oxide nanocatalyst for CO2 utilisation and direct propylene carbonate production. *J. Clean. Prod.* **214**, 606–614 (2019).

306. Kellici, S. *et al.* Calixarene Assisted Rapid Synthesis of Silver-Graphene Nanocomposites with Enhanced Antibacterial Activity. *ACS Appl. Mater. Interfaces* **8**, 19038–19046 (2016).

307. Kellici, S. *et al.* Rapid synthesis of graphene quantum dots using a continuous hydrothermal flow synthesis approach. *RSC Adv.* **7**, 14716–14720 (2017).

308. Pei, S. & Cheng, H. M. The reduction of graphene oxide. *Carbon N. Y.* **50**, 3210–3228 (2012).

309. Park, S. *et al.* Hydrazine-reduction of graphite- and graphene oxide. *Carbon N. Y.* **49**, 3019–3023 (2011).

310. Mei, X., Meng, X. & Wu, F. Hydrothermal method for the production of reduced graphene oxide. *Phys. E Low-Dimensional Syst. Nanostructures* **68**, 81–86 (2015).

311. Yu, J. & Savage, P. E. Decomposition of Formic Acid under Hydrothermal Conditions. *Ind. Eng. Chem. Res.* **37**, 2–10 (1998).

312. Bjerre, A. B. & Sørensen, E. Thermal Decomposition of Dilute Aqueous Formic Acid Solutions. *Ind. Eng. Chem. Res.* **31**, 1574–1577 (1992).

313. Baragau, I. A. *et al.* Continuous hydrothermal flow synthesis of blue-luminescent, excitation-independent nitrogen-doped carbon quantum dots as nanosensors. *J. Mater. Chem. A* **8**, 3270–3279 (2020).

314. Nguyen-Phan, T. D. *et al.* The role of graphene oxide content on the adsorption-enhanced photocatalysis of titanium dioxide/graphene oxide composites. *Chem. Eng. J.* **170**, 226–232 (2011).

315. Makuła, P., Pacia, M. & Macyk, W. How To Correctly Determine the Band Gap Energy of Modified Semiconductor Photocatalysts Based on UV-Vis Spectra. *J. Phys. Chem. Lett.* **9**, 6814–6817 (2018).

316. Zuo, P., Lu, X., Sun, Z., Guo, Y. & He, H. A review on syntheses, properties, characterization and bioanalytical applications of fluorescent carbon dots. *Microchim. Acta* **183**, 519–542 (2016).

317. Luo, X. *et al.* Laser irradiated vortex fluidic mediated synthesis of luminescent carbon nanodots under continuous flow. *React. Chem. Eng.* **3**, 164–170 (2018).

318. Yang, Shengtao; Cao, Li; Luo, Pengju G; Lu, Fushen; Wang, xin; Wang, Haifeng; Meziani, Mohammed J.; Liu, Yuanfang, Qi, Gang; Sun, Y. Carbon Dots for Optical Imaging in Vivo. *J. Am. Chem. Soc.* **131**, 11308–11309 (2009).

319. Ma, Z., Ming, H., Huang, H., Liu, Y. & Kang, Z. One-step ultrasonic synthesis of fluorescent N-doped carbon dots from glucose and their visible-light sensitive photocatalytic ability. *New J. Chem.* **36**, 861 (2012).

320. Ding, H., Du, F., Liu, P., Chen, Z. & Shen, J. DNA-carbon dots function as fluorescent vehicles for drug delivery. *ACS Appl. Mater. Interfaces* **7**, 6889–6897 (2015).

321. Zhu, S. *et al.* Highly photoluminescent carbon dots for multicolor patterning, sensors, and bioimaging. *Angew. Chemie - Int. Ed.* **52**, 3953–3957 (2013).

322. Qu, K., Wang, J., Ren, J. & Qu, X. Carbon dots prepared by hydrothermal treatment of dopamine as an effective fluorescent sensing platform for the label-free detection of iron(III) ions and dopamine. *Chem. - A Eur. J.* **19**, 7243–7249 (2013).

323. Guo, X., Wang, C.-F., Yu, Z.-Y., Chen, L. & Chen, S. Facile access to versatile fluorescent carbon dots toward light-emitting diodes. *Chem. Commun.* **48**, 2692 (2012).

324. Mashtalir, O., Lukatskaya, M. R., Zhao, M. Q., Barsoum, M. W. & Gogotsi, Y. Amine-

assisted delamination of Nb2C MXene for li-ion energy storage devices. *Adv. Mater.* **27**, 3501–3506 (2015).

325. Marinovic, A., Kiat, L. S., Dunn, S., Titirici, M.-M. & Briscoe, J. Carbon-Nanodot Solar Cells from Renewable Precursors. *ChemSusChem* **10**, 1004–1013 (2017).

326. Li, Y., Zhong, X., Rider, A. E., Furman, S. A. & Ostrikov, K. Fast, energy-efficient synthesis of luminescent carbon quantum dots. *Green Chem.* **16**, 2566–2570 (2014).

327. Ehrat, F. *et al.* Tracking the Source of Carbon Dot Photoluminescence: Aromatic Domains versus Molecular Fluorophores. *Nano Lett.* **17**, 7710–7716 (2017).

328. Chen, W., Hu, C., Yang, Y., Cui, J. & Liu, Y. Rapid synthesis of carbon dots by hydrothermal treatment of lignin. *Materials (Basel).* **9**, 184 (2016).

329. Qu, D. *et al.* Formation mechanism and optimization of highly luminescent N-doped graphene quantum dots. *Sci. Rep.* **4**, 1–11 (2014).

330. Tighe, C. J., Cabrera, R. Q., Gruar, R. I. & Darr, J. A. Scale Up Production of Nanoparticles: Continuous Supercritical Water Synthesis of Ce–Zn Oxides. *Ind. Eng. Chem. Res.* **52**, 5522–5528 (2013).

331. Darr, J. A. & Poliakoff, M. New Directions in Inorganic and Metal-Organic Coordination Chemistry in Supercritical Fluids. *Chem. Rev.* **99**, 495–542 (1999).

332. Cabanas, A., Darr, J. A., Lester, E. & Poliakoff, M. Continuous hydrothermal synthesis of inorganic materials in a near-critical water flow reactor; the one-step synthesis of nano-particulate CeZrO ([space]=[space]0-1) solid solutions. *J. Mater. Chem.* **11**, 561–568 (2001).

333. Middelkoop, V. *et al.* Next frontiers in cleaner synthesis: 3D printed graphene-supported CeZrLa mixed-oxide nanocatalyst for CO 2 utilisation and direct propylene carbonate production. *J. Clean. Prod.* **214**, 606–614 (2019).

334. da Silva Souza, D. R., Caminhas, L. D., de Mesquita, J. P. & Pereira, F. V. Luminescent carbon dots obtained from cellulose. *Mater. Chem. Phys.* **203**, 148–155 (2018).

335. López-Díaz, D., López Holgado, M., García-Fierro, J. L. & Velázquez, M. M. Evolution of the Raman Spectrum with the Chemical Composition of Graphene Oxide. *J. Phys. Chem. C* **121**, 20489–20497 (2017).

336. Moon, I. K., Lee, J., Ruoff, R. S. & Lee, H. Reduced graphene oxide by chemical

graphitization. *Nat. Commun.* **1**, 1–6 (2010).

337. Ding, H., Yu, S. B., Wei, J. S. & Xiong, H. M. Full-color light-emitting carbon dots with a surface-state-controlled luminescence mechanism. *ACS Nano* **10**, 484–491 (2016).

338. Yang, Z. C. *et al.* Intrinsically fluorescent carbon dots with tunable emission derived from hydrothermal treatment of glucose in the presence of monopotassium phosphate. *Chem. Commun.* **47**, 11615–11617 (2011).

339. Guo, Y. *et al.* Hydrothermal synthesis of nitrogen and boron doped carbon quantum dots with yellow-green emission for sensing Cr(VI), anti-counterfeiting and cell imaging. *RSC Adv.* **7**, 48386–48393 (2017).

340. Sun, W., Du, Y. & Wang, Y. Study on fluorescence properties of carbogenic nanoparticles and their application for the determination of ferrous succinate. *J. Lumin.* **130**, 1463–1469 (2010).

341. Li, F., Yang, D. & Xu, H. Non-Metal-Heteroatom-Doped Carbon Dots: Synthesis and Properties. *Chem. - A Eur. J.* **25**, 1165–1176 (2019).

342. Jin, S. H., Kim, D. H., Jun, G. H., Hong, S. H. & Jeon, S. Tuning the photoluminescence of graphene quantum dots through the charge transfer effect of functional groups. *ACS Nano* **7**, 1239–1245 (2013).

343. Lazar, P., Mach, R. & Otyepka, M. Spectroscopic Fingerprints of Graphitic, Pyrrolic, Pyridinic, and Chemisorbed Nitrogen in N-Doped Graphene. *J. Phys. Chem. C* **123**, 10695–10702 (2019).

344. Wang, R., Lu, K.-Q., Tang, Z.-R. & Xu, Y.-J. Recent progress in carbon quantum dots: synthesis, properties and applications in photocatalysis. *J. Mater. Chem. A* **5**, 3717–3734 (2017).

345. Zhou, M., Zhou, Z., Gong, A., Zhang, Y. & Li, Q. Synthesis of highly photoluminescent carbon dots via citric acid and Tris for iron(III) ions sensors and bioimaging. *Talanta* **143**, 107–113 (2015).

346. Yang, C. *et al.* Nitrogen-doped carbon dots with excitation-independent long-wavelength emission produced by a room-temperature reaction. *Chem. Commun.* **52**, 11912–11914 (2016).

347. Dong, Y. *et al.* Carbon-based dots co-doped with nitrogen and sulfur for high quantum

yield and excitation-independent emission. *Angew. Chemie - Int. Ed.* **52**, 7800–7804 (2013).

348. Huang, S., Qiu, H., Zhu, F., Lu, S. & Xiao, Q. Graphene quantum dots as on-off-on fluorescent probes for chromium(VI) and ascorbic acid. *Microchim. Acta* **182**, 1723–1731 (2015).

349. Unterlass, M. M. Journal of Materials Chemistry A and Materials Advances Editor's choice web collection: 'Recent advances in hydrothermal materials synthesis'. *J. Mater. Chem. A* **9**, 661–662 (2021).

350. Jin, Z., Owour, P., Lei, S. & Ge, L. Graphene, graphene quantum dots and their applications in optoelectronics. *Curr. Opin. Colloid Interface Sci.* **20**, 439–453 (2015).

351. Schwierz, F., Pezoldt, J. & Granzner, R. Two-dimensional materials and their prospects in transistor electronics. *Nanoscale* **7**, 8261–8283 (2015).

352. Fu, Q. & Bao, X. Surface chemistry and catalysis confined under two-dimensional materials. *Chem. Soc. Rev.* **46**, 1842–1874 (2017).

353. Koutsioukis, A., Georgakilas, V., Belessi, V. & Zboril, R. Highly conductive water-based polymer / graphene nanocomposites for printed electronics. *Chem. Eur. J.* (2017). doi:10.1002/chem.201700997

354. Tian, F., Lyu, J., Shi, J. & Yang, M. Graphene and graphene-like two-denominational materials based fluorescence resonance energy transfer (FRET) assays for biological applications. *Biosens. Bioelectron.* **89**, 123–135 (2017).

355. De Silva, K. K. H., Huang, H. H., Joshi, R. K. & Yoshimura, M. Chemical reduction of graphene oxide using green reductants. *Carbon N. Y.* **119**, 190–199 (2017).

356. Liu, X., Giordano, C. & Antonietti, M. A Facile Molten-Salt Route to Graphene Synthesis. *Small* **10**, 193–200 (2014).

357. Iskandar, F., Hikmah, U., Stavila, E. & Aimon, A. H. Microwave-assisted reduction method under nitrogen atmosphere for synthesis and electrical conductivity improvement of reduced graphene oxide (rGO) †. *RSC Adv.* **7**, 52391–52397 (2017).

358. Krishnamoorthy, K., Kim, G. & Jae, S. Graphene nanosheets : Ultrasound assisted synthesis and characterization. *Ultrason. Sonochem.* **20**, 644–649 (2013).

359. Whitener, K. E. & Sheehan, P. E. Graphene synthesis. *Diam. Relat. Mater.* **46**, 25–34

(2014).

360. Edwards, R. S. & Coleman, K. S. Graphene synthesis : relationship to applications. *Nanoscale* **5**, 38–51 (2013).

361. Alli, U., Hettiarachchi, S. J. & Kellici, S. Chemical Functionalisation of 2D Materials by Batch and Continuous Hydrothermal Flow Synthesis. *Chem. - A Eur. J.* **26**, 6447–6460 (2020).

362. Yoo, B. M., Shin, J. E., Lee, H. D. & Park, H. B. Graphene and graphene oxide membranes for gas separation applications. *Curr. Opin. Chem. Eng.* **16**, 39–47 (2017).

363. Jiang, Y., Biswas, P. & Fortner, J. D. A review of recent developments in graphene-enabled membranes for water treatment. *Environ. Sci. Water Res. Technol.* **2**, 915–922 (2016).

364. Tabish, T. A., Memon, F. A., Gomez, D. E., Horsell, D. W. & Zhang, S. A facile synthesis of porous graphene for efficient water and wastewater treatment. *Sci. Rep.* **8**, 1–14 (2018).

365. Zhang, L. *et al.* Effect of physical and chemical structures of graphene oxide on water permeation in graphene oxide membranes. *Appl. Surf. Sci.* **520**, (2020).

366. Yu, H. *et al.* The roles of oxygen-containing functional groups in modulating water purification performance of graphene oxide-based membrane. *Chem. Eng. J.* **389**, (2020).

367. Michela Miletto, Richard Connor, Engin Koncagul, Valentina Abete, Marco Tonsini, and S. L. *The United Nations World Water Development Report 2021: Valuing water*. *Water Politics* (2021). doi:10.4324/9780429453571-2

368. Yasser Hanaqtah, Hotaf Yassien, Pathan Banjongproo, Tantikom Supachai, Mr. Kuixiao Li, Shri Roy, Mr. Rajamohan Teddy Gounden, Rose Kaggwa, Karina Valenzuela, B. E. *The Reuse Opportunity*. *Wastewater Report* (2018).

369. Simone Grego, Michela Miletto, Engin Koncagul, Alice Franek, Diwata Hunziker, Valentina Abete, and R. C. *Water for a sustainable world*. *The United Nations World Water Development Report* (2015).

370. Li, R., Zhang, L. & Wang, P. Rational design of nanomaterials for water treatment. *Nanoscale* **7**, 17167–17194 (2015).

371. MaryTheresa M. Pendergast, and E. M. V. H. A review of water treatment membrane nanotechnologies. *Energy Environ. Sci.* **4**, 1946–1971 (2011).

372. Lee, A., Elam, J. W. & Darling, S. B. Membrane materials for water purification: Design, development, and application. *Environ. Sci. Water Res. Technol.* **2**, 17–42 (2016).

373. Van Der Bruggen, B., Vandecasteele, C., Van Gestel, T., Doyen, W. & Leysen, R. A review of pressure-driven membrane processes in wastewater treatment and drinking water production. *Environ. Prog.* **22**, 46–56 (2003).

374. Xia, S., Ni, M., Zhu, T., Zhao, Y. & Li, N. Ultrathin graphene oxide nanosheet membranes with various d-spacing assembled using the pressure-assisted filtration method for removing natural organic matter. *Desalination* **371**, 78–87 (2015).

375. Dervin, S., Dionysiou, D. D. & Pillai, S. C. 2D nanostructures for water purification: Graphene and beyond. *Nanoscale* **8**, 15115–15131 (2016).

376. Fathizadeh, M., Xu, W. L., Zhou, F., Yoon, Y. & Yu, M. Graphene Oxide: A Novel 2-Dimensional Material in Membrane Separation for Water Purification. *Adv. Mater. Interfaces* **4**, 1–16 (2017).

377. Goh, K. *et al.* Graphene oxide as effective selective barriers on a hollow fiber membrane for water treatment process. *J. Memb. Sci.* **474**, 244–253 (2015).

378. Huang, H., Ying, Y. & Peng, X. Graphene oxide nanosheet: An emerging star material for novel separation membranes. *J. Mater. Chem. A* **2**, 13772–13782 (2014).

379. Wang, L., Williams, C. M., Boutilier, M. S. H., Kidambi, P. R. & Karnik, R. Single-Layer Graphene Membranes Withstand Ultrahigh Applied Pressure. *Nano Lett.* **17**, 3081–3088 (2017).

380. Liu, H., Wang, H. & Zhang, X. Facile fabrication of freestanding ultrathin reduced graphene oxide membranes for water purification. *Adv. Mater.* **27**, 249–254 (2015).

381. Pei, J., Zhang, X., Huang, L., Jiang, H. & Hu, X. Fabrication of reduced graphene oxide membranes for highly efficient water desalination. *RSC Adv.* **6**, 101948–101952 (2016).

382. Zhang, P., Li, J., Lv, L., Zhao, Y. & Qu, L. Vertically Aligned Graphene Sheets Membrane for Highly Efficient Solar Thermal Generation of Clean Water. *ACS Nano* **11**, 5087–5093 (2017).

383. Song, N. *et al.* A review of graphene-based separation membrane: Materials, characteristics, preparation and applications. *Desalination* **437**, 59–72 (2018).

384. Sun, P., Wang, K. & Zhu, H. Recent Developments in Graphene-Based Membranes: Structure, Mass-Transport Mechanism and Potential Applications. *Adv. Mater.* **28**, 2287–2310 (2016).

385. Safarpour, M., Vatanpour, V., Khataee, A. & Esmaeili, M. Development of a novel high flux and fouling-resistant thin film composite nanofiltration membrane by embedding reduced graphene oxide/TiO2. *Sep. Purif. Technol.* **154**, 96–107 (2015).

386. Xianfu Chen, Minghui Qiu, Hao Ding, K. F. and Y. F. Reduced graphene oxide nanofiltration membrane intercalated by well-dispersed carbon nanotubes for drinking water purification. *Nanoscale* **10**, 5696–5705 (2016).

387. Anand, A., Unnikrishnan, B., Mao, J. Y., Lin, H. J. & Huang, C. C. Graphene-based nanofiltration membranes for improving salt rejection, water flux and antifouling–A review. *Desalination* **429**, 119–133 (2018).

388. Xu, Z. *et al.* Reversible hydrophobic to hydrophilic transition in graphene via water splitting induced by UV irradiation. *Sci. Rep.* **4**, 1–9 (2014).

389. Chang, H. *et al.* Highly Reversible and Recyclable Absorption under Both Hydrophobic and Hydrophilic Conditions using a Reduced Bulk Graphene Oxide Material. *Adv. Mater.* **28**, 3504–3509 (2016).

390. Dong, J., Yao, Z., Yang, T., Jiang, L. & Shen, C. Control of superhydrophilic and superhydrophobic graphene interface. *Sci. Rep.* **3**, 1–6 (2013).

391. Alayande, A. B., Park, H. D., Vrouwenvelder, J. S. & Kim, I. S. Implications of Chemical Reduction Using Hydriodic Acid on the Antimicrobial Properties of Graphene Oxide and Reduced Graphene Oxide Membranes. *Small* **15**, 1–12 (2019).

392. Huang, L. *et al.* Reduced Graphene Oxide Membranes for Ultrafast Organic Solvent Nanofiltration. *Adv. Mater.* **28**, 8669–8674 (2016).

393. Chung, D. D. L. Review: Graphite. *J. Mater. Sci.* **37**, 1475–1489 (2002).

394. Zhou, Y., Bao, Q., Tang, L. A. L., Zhong, Y. & Loh, K. P. Hydrothermal dehydration for the ‘green’ reduction of exfoliated graphene oxide to graphene and demonstration of tunable optical limiting properties. *Chem. Mater.* **21**, 2950–2956 (2009).

395. Bai, Y., Rakhi, R. B., Chen, W. & Alshareef, H. N. Effect of pH-induced chemical modification of hydrothermally reduced graphene oxide on supercapacitor performance. *J. Power Sources* **233**, 313–319 (2013).

396. Tung, V. C., Allen, M. J., Yang, Y. & Kaner, R. B. High-throughput solution processing of large-scale graphene. *Nat. Nanotechnol.* **4**, 25–29 (2009).

397. Stankovich, S. *et al.* Synthesis of graphene-based nanosheets via chemical reduction of exfoliated graphite oxide. *Carbon N. Y.* **45**, 1558–1565 (2007).

398. Arvidsson, R., Kushnir, D., Sanden, B. A. & Molander, S. Prospective life cycle assessment of graphene production by ultrasonication and chemical reduction. *Environ. Sci. Technol.* **48**, 4529–4536 (2014).

399. Mkhoyan, K. A. *et al.* Atomic and electronic structure of graphene-oxide. *Nano Lett.* **9**, 1058–1063 (2009).

400. Galande, C. *et al.* Science and engineering of graphene oxide. *Part. Part. Syst. Charact.* **31**, 619–638 (2014).

401. Lesiak, B. *et al.* C sp 2 /sp 3 hybridisations in carbon nanomaterials – XPS and (X)AES study. *Appl. Surf. Sci.* **452**, 223–231 (2018).

402. Chua, C. K. & Pumera, M. Chemical reduction of graphene oxide: a synthetic chemistry viewpoint. *Chem. Soc. Rev.* **43**, 291–312 (2014).

403. Li, M., Cushing, S. K., Zhou, X., Guo, S. & Wu, N. Fingerprinting photoluminescence of functional groups in graphene oxide. *J. Mater. Chem.* **22**, 23374–23379 (2012).

404. Yan, J. A. & Chou, M. Y. Oxidation functional groups on graphene: Structural and electronic properties. *Phys. Rev. B - Condens. Matter Mater. Phys.* **82**, 21–24 (2010).

405. Gao, W., Alemany, L. B., Ci, L. & Ajayan, P. M. New insights into the structure and reduction of graphite oxide. *Nat. Chem.* **1**, 403–408 (2009).

406. Szabó, T. *et al.* Evolution of surface functional groups in a series of progressively oxidized graphite oxides. *Chem. Mater.* **18**, 2740–2749 (2006).

407. Xu, C., Yuan, R. S. & Wang, X. Selective reduction of graphene oxide. *Xinxing Tan Cailiao/New Carbon Mater.* **29**, 61–66 (2014).

408. Ferrari, A. C. & Basko, D. M. Raman spectroscopy as a versatile tool for studying the properties of graphene. *Nat. Nanotechnol.* **8**, 235–246 (2013).

409. Eigler, S., Dotzer, C. & Hirsch, A. Visualization of defect densities in reduced graphene oxide. *Carbon N. Y.* **50**, 3666–3673 (2012).

410. Abdolhosseinzadeh, S., Asgharzadeh, H. & Kim, H. S. Fast and fully-scalable synthesis of reduced graphene oxide. *Sci. Rep.* **5**, 1–7 (2015).

411. Chowdhury, I., Mansukhani, N. D., Guiney, L. M., Hersam, M. C. & Bouchard, D. Aggregation and Stability of Reduced Graphene Oxide: Complex Roles of Divalent Cations, pH, and Natural Organic Matter. *Environ. Sci. Technol.* **49**, 10886–10893 (2015).

412. Akhavan, O., Azimirad, R., Gholizadeh, H. T. & Ghorbani, F. Hydrogen-rich water for green reduction of graphene oxide suspensions. *Int. J. Hydrogen Energy* **40**, 5553–5560 (2015).

413. Guex, L. G. *et al.* Experimental review: Chemical reduction of graphene oxide (GO) to reduced graphene oxide (rGO) by aqueous chemistry. *Nanoscale* **9**, 9562–9571 (2017).

414. Hsien, C., Low, J. S. C., Chung, S. Y. & Tan, D. Z. L. Quality-based water and wastewater classification for waste-to-resource matching. *Resour. Conserv. Recycl.* **151**, (2019).

415. Fryer, P. J. & Asteriadou, K. A prototype cleaning map: A classification of industrial cleaning processes. *Trends Food Sci. Technol.* **20**, 255–262 (2009).

416. Lin, H., Mehra, N., Li, Y. & Zhu, J. Graphite oxide/boron nitride hybrid membranes: The role of cross-plane laminar bonding for a durable membrane with large water flux and high rejection rate. *J. Memb. Sci.* **593**, 1–9 (2020).

417. Choi, W., Chun, K. Y., Kim, J. & Han, C. S. Ion transport through thermally reduced and mechanically stretched graphene oxide membrane. *Carbon N. Y.* **114**, 377–382 (2017).

418. Jang, J. H., Woo, J. Y., Lee, J. & Han, C. S. Ambivalent Effect of Thermal Reduction in Mass Rejection through Graphene Oxide Membrane. *Environ. Sci. Technol.* **50**, 10024–10030 (2016).

419. Su, P., Wang, F., Li, Z., Tang, C. Y. & Li, W. Graphene oxide membranes: Controlling their transport pathways. *J. Mater. Chem. A* **8**, 15319–15340 (2020).

420. Saha, B. & Bhattacharyya, P. K. Anion···π interaction in oxoanion-graphene complex

using coronene as model system: A DFT study. *Comput. Theor. Chem.* **1147**, 62–71 (2019).

421. Zeraatkar Moghaddam, A., Esmaeilkhanian, E. & Shakourian-Fard, M. Immobilizing magnetic glutaraldehyde cross-linked chitosan on graphene oxide and nitrogen-doped graphene oxide as well-dispersible adsorbents for chromate removal from aqueous solutions. *Int. J. Biol. Macromol.* **128**, 61–73 (2019).

422. Shojaipour, M. & Ghaemy, M. Highly efficient and antibacterial ion exchanger based on graphene oxide for removal of chromate and nitrate from water: Synthesis, characterization and application. *New J. Chem.* **45**, 268–281 (2021).

423. Kumar, A. S. K., Kakan, S. S. & Rajesh, N. A novel amine impregnated graphene oxide adsorbent for the removal of hexavalent chromium. *Chem. Eng. J.* **230**, 328–337 (2013).

424. Liu, T., Yang, B., Graham, N., Yu, W. & Sun, K. Trivalent metal cation cross-linked graphene oxide membranes for NOM removal in water treatment. *J. Memb. Sci.* **542**, 31–40 (2017).

425. Chen, L. *et al.* Ion sieving in graphene oxide membranes via cationic control of interlayer spacing. *Nature* **550**, 1–4 (2017).

426. Böhm, F., Sharma, V., Schwaab, G. & Havenith, M. The low frequency modes of solvated ions and ion pairs in aqueous electrolyte solutions: iron(ii) and iron(iii) chloride. *Phys. Chem. Chem. Phys.* **17**, 19582–19591 (2015).

427. Park, J., Bazylewski, P. & Fanchini, G. Porous graphene-based membranes for water purification from metal ions at low differential pressures. *Nanoscale* **8**, 9563–9571 (2016).

428. Sun, P. *et al.* Selective ion penetration of graphene oxide membranes. *ACS Nano* **7**, 428–437 (2013).

429. Fan, X., Cai, C., Gao, J., Han, X. & Li, J. Hydrothermal reduced graphene oxide membranes for dyes removing. *Sep. Purif. Technol.* **241**, 116730 (2020).

430. Sundaran, S. P., Reshmi, C. R., Sagitha, P., Manaf, O. & Sujith, A. Multifunctional graphene oxide loaded nanofibrous membrane for removal of dyes and coliform from water. *J. Environ. Manage.* **240**, 494–503 (2019).

431. Fang, Y. *et al.* Complex Formation via Hydrogen bonding between Rhodamine B and

Montmorillonite in Aqueous Solution. *Sci. Rep.* **8**, 1–10 (2018).

432. Zhao, D., Li, L. & Zhou, J. Simulation insight into the cytochrome c adsorption on graphene and graphene oxide surfaces. *Appl. Surf. Sci.* **428**, 825–834 (2018).

433. Kowalska, A. M., Trzaskowski, B. & Osella, S. Assessing the Charge Transfer at the Cytochrome c553/Graphene Interface: A Multiscale Investigation. *J. Phys. Chem. C* **122**, 29405–29413 (2018).

434. Wu, L. & Jiang, X. Enhancing Peroxidase Activity of Cytochrome c by Modulating Interfacial Interaction Forces with Graphene Oxide. *Langmuir* **36**, 1094–1102 (2020).

435. Titov, A. V, Kra, P. & Pearson, R. Sandwiched Graphene-Membrane Superstructures. *ACS Nano* **4**, 229–234 (2010).

436. Frost, R., Svedhem, S., Langhammer, C. & Kasemo, B. Graphene Oxide and Lipid Membranes: Size-Dependent Interactions. *Langmuir* **32**, 2708–2717 (2016).

437. Sun, P. *et al.* Selective ion transport through functionalized graphene membranes based on delicate ion-graphene interactions. *J. Phys. Chem. C* **118**, 19396–19401 (2014).

438. Katsnelson, M. I. & Fasolino, A. Graphene as a prototype crystalline membrane. *Acc. Chem. Res.* **46**, 97–105 (2013).

439. Hu, M. & Mi, B. Layer-by-layer assembly of graphene oxide membranes via electrostatic interaction. *J. Memb. Sci.* **469**, 80–87 (2014).

440. Bunch, J. S. & Dunn, M. L. Adhesion mechanics of graphene membranes. *Solid State Commun.* **152**, 1359–1364 (2012).

441. Liu, G. *et al.* Graphene oxide for high-efficiency separation membranes: Role of electrostatic interactions. *Carbon N. Y.* **110**, 56–61 (2016).

442. Kommu, A. & Singh, J. K. A review on graphene-based materials for removal of toxic pollutants from wastewater. *Soft Mater.* **18**, 297–322 (2020).

443. Sun, C. *et al.* Mechanisms of molecular permeation through nanoporous graphene membranes. *Langmuir* **30**, 675–682 (2014).

444. Köhler, M. H., Bordin, J. R. & Barbosa, M. C. 2D nanoporous membrane for cation removal from water: Effects of ionic valence, membrane hydrophobicity, and pore size. *J. Chem. Phys.* **148**, (2018).

445. Boukhvalov, D. W., Katsnelson, M. I. & Son, Y. W. Origin of anomalous water permeation through graphene oxide membrane. *Nano Lett.* **13**, 3930–3935 (2013).

446. Chen, B., Jiang, H., Liu, X. & Hu, X. Observation and Analysis of Water Transport through Graphene Oxide Interlamination. *J. Phys. Chem. C* **121**, 1321–1328 (2017).

447. Sitko, R. *et al.* Adsorption of divalent metal ions from aqueous solutions using graphene oxide. *Dalt. Trans.* **42**, 5682–5689 (2013).

448. Wu, W. *et al.* Highly efficient removal of Cu(II) from aqueous solution by using graphene oxide. *Water. Air. Soil Pollut.* **224**, (2013).

449. Dong, Y. *et al.* Graphene oxide-iron complex: Synthesis, characterization and visible-light-driven photocatalysis. *J. Mater. Chem. A* **1**, 644–650 (2013).

450. Nations, U. *The United Nations World Water Development Report 2019: Leaving no one behind*. (2019).

451. Nguyen, C. H., Tran, M. L., Tran, T. T. Van & Juang, R. S. Enhanced removal of various dyes from aqueous solutions by UV and simulated solar photocatalysis over TiO2/ZnO/rGO composites. *Sep. Purif. Technol.* **232**, (2020).

452. Liu, Y. *et al.* Enhanced photocatalytic activities of commercial P25 TiO2 by trapping holes and transferring electrons for CO2 conversion and 2,4-dichlorophenol degradation. *Mater. Res. Bull.* **92**, 23–28 (2017).

453. Chen, S., Takata, T. & Domen, K. Particulate photocatalysts for overall water splitting. *Nat. Rev. Mater.* **2**, 1–17 (2017).

454. Goodeve, C. F. & Kitchener, J. A. Photosensitisation by titanium dioxide. *Trans. Faraday Soc.* **34**, 570–579 (1938).

455. Hoffmann, M. R., Martin, S. T., Choi, W. & Bahnemann, D. W. Environmental Applications of Semiconductor Photocatalysis. *Chem. Rev.* **95**, 69–96 (1995).

456. Lee, J. S., You, K. H. & Park, C. B. Highly photoactive, low bandgap TiO 2 nanoparticles wrapped by graphene. *Adv. Mater.* **24**, 1084–1088 (2012).

457. Yang, X. & Wang, D. Photocatalysis: From Fundamental Principles to Materials and Applications. *ACS Appl. Energy Mater.* **1**, 6657–6693 (2018).

458. Luo, H. *et al.* Nitrogen-Doped Carbon Dots/TiO2 Nanoparticle Composites for Photoelectrochemical Water Oxidation. *ACS Appl. Nano Mater.* **3**, 3371–3381 (2020).

459. Zhang, N., Yang, M. Q., Liu, S., Sun, Y. & Xu, Y. J. Waltzing with the Versatile Platform of Graphene to Synthesize Composite Photocatalysts. *Chem. Rev.* **115**, 10307–10377 (2015).

460. Mahmood, A. *et al.* Carbon quantum dots-TiO2 nanocomposite as an efficient photocatalyst for the photodegradation of aromatic ring-containing mixed VOCs: An experimental and DFT studies of adsorption and electronic structure of the interface. *J. Hazard. Mater.* **401**, (2021).

461. Middelkoop, V. *et al.* Imaging the continuous hydrothermal flow synthesis of nanoparticulate CeO2 at different supercritical water temperatures using in situ angle-dispersive diffraction. *J. Supercrit. Fluids* **87**, 118–128 (2014).

462. Goodall, J. B. M. *et al.* Optical and photocatalytic behaviours of nanoparticles in the Ti-Zn-O binary system. *RSC Adv.* **4**, 31799–31809 (2014).

463. Alli, U., Hettiarachchi, S. J. & Kellici, S. Chemical functionalisation of 2D materials via batch and continious hydrothermal flow synthesis. *Chem. – A Eur. J.* (2020). doi:10.1002/chem.202000383

464. Baragau, I.-A. *et al.* Continuous Hydrothermal Flow Synthesis of S-Functionalised Carbon Quantum Dots for Enhanced Oil Recovery. *Chem. Eng. J.* **405**, 126631 (2020).

465. Zhao, L. *et al.* One-step solvothermal synthesis of a carbon @TiO2 dyade structure effectively promoting visible-light photocatalysis. *Adv. Mater.* **22**, 3317–3321 (2010).

466. Thompson, K. *et al.* Screening tests for the evaluation of nanoparticle titania photocatalysts. *J. Chem. Technol. Biotechnol.* **84**, 1717–1725 (2009).

467. Allen, N. S., Mahdjoub, N., Vishnyakov, V., Kelly, P. J. & Kriek, R. J. The effect of crystalline phase (anatase, brookite and rutile) and size on the photocatalytic activity of calcined polymorphic titanium dioxide (TiO2). *Polym. Degrad. Stab.* **150**, 31–36 (2018).

468. Vallejo, W., Rueda, A., Díaz-Uribe, C., Grande, C. & Quintana, P. Photocatalytic activity of graphene oxide-TiO 2 thin films sensitized by natural dyes extracted from Bactris guineensis. *R. Soc. Open Sci.* **6**, (2019).

469. Alexander Naumkin, Anna Kraut-Vass, Stephen Gaarenstroom, and C. P. NIST X-ray Photoelectron Spectroscopy Database. *NIST Stand. Ref. Database 20, Version 4.1* (2012).

470. Liu, L. *et al.* Engineering the TiO2-graphene interface to enhance photocatalytic H2 production. *ChemSusChem* **7**, 618–626 (2014).

471. Luo, H. *et al.* Manipulating the Optical Properties of Carbon Dots by Fine-Tuning their Structural Features. *ChemSusChem* **12**, 4335–4335 (2019).

472. Luo, H. *et al.* Nitrogen-Doped Carbon Dots/TiO 2 Nanoparticle Composites for Photoelectrochemical Water Oxidation. *ACS Appl. Nano Mater.* (2020). doi:10.1021/acsanm.9b02412

473. Jia, J. *et al.* Facile and Efficient Fabrication of Bandgap Tunable Carbon Quantum Dots Derived From Anthracite and Their Photoluminescence Properties. *Front. Chem.* **8**, 1–10 (2020).

474. Štengl, V., Popelková, D. & Vláčil, P. TiO 2-graphene nanocomposite as high performace photocatalysts. *J. Phys. Chem. C* **115**, 25209–25218 (2011).